

Chemical Analysis of Biomarkers and Silver Nanoparticles

A thesis submitted for the degree of
Doctor of Philosophy
in Physical and Theoretical Chemistry

Kamonwad Ngamchuea

St John's College

University of Oxford

Trinity Term 2018

Chemical Analysis of Biomarkers and Silver Nanoparticles

Kamonwad Ngamchuea
St John's College, University of Oxford
A thesis submitted for the degree of D.Phil. in Physical and Theoretical Chemistry
Trinity Term, 2018

Abstract

This thesis is focused on the development of chemical sensors for the detection of molecular biomarkers and silver nanoparticles, and the application of the techniques to *authentic* saliva samples.

As an important antioxidant in humans, the first aim of this thesis is to develop sensors for the detection of *glutathione*. Two different assays for glutathione detection based on electrochemical and spectrophotometric techniques are developed. The spectrophotometric assay is further applied to authentic human plasma and saliva samples, where the stability of glutathione is investigated *in-vitro*. The copper(II)-catalysed oxidation process which is the major cause of the loss of reduced glutathione from biological samples is next investigated and the mechanism is proposed. The spectrophotometric glutathione assay is then employed to study the potential of salivary glutathione as a biomarker for bipolar disorder.

An electroanalytical assay is also developed for the detection of salivary *uric acid*, a potential biomarker for gout, oral cavity cancer and other several diseases. The significantly different electrochemical behaviour in authentic as compared to synthetic saliva of commonly used redox mediators such as ferrocenemethanol and ferrocyanide is further highlighted in this thesis.

In addition to molecular biomarkers such as glutathione and uric acid, an electrochemical sensor is developed for the detection of ensembles and individual *silver nanoparticles* (AgNPs). The oxidative dissolution of AgNPs is first investigated by two electrochemical techniques: nano-impacts and anodic stripping voltammetry, where the results reveal the relative kinetics of the process. The electrochemical techniques are then directly applied to investigate the physicochemical properties of AgNPs in authentic human saliva.

Acknowledgements

First of all, I would like to thank Professor Richard G. Compton for his extraordinary support and guidance throughout my D.Phil. studies as well as the Part II year. It has been a real privilege to be a part of your research group. I am very grateful for the open-door policy and the constructive advice you give in every meeting. Many thanks for always believing in the capabilities of your students and for offering many opportunities for me to experience all these years.

I am also very thankful to Dr. Christopher Batchelor-McAuley for his very helpful advice and encouragement throughout the years. Thank you for always kindly answering my random questions. From chemistry, Python to potentiostat circuits, I have really learned so much from you over the years.

I would also like to thank Professor Philip J. Cowen and Clare Williams for very helpful discussions and their assistance with ethic application and biological sample collection. Special thanks go to Dr. Chuhong Lin for her help with the simulation of the supported microwire electrode studies. Many thanks to Dr. Neil P. Young and Dr. Stanislav V. Sokolov for their help with the imaging of silver nanoparticles. Thanks to Korbua Chaisiwamongkhol for her collaboration in the writing of the saliva review article. I am also thankful to Philip Hurst for his help and advice with electronics.

I would like to express my gratitude to the Development and Promotion of Science and Technology Talents Project (DPST), the Royal Thai Government, who provides full funding for my studies since 2006, from high school in Thailand to A-levels, Bachelor-Master and PhD in the UK. Special thanks also go to all the staffs at the OEA London and the DPST office in Thailand for their help and kindness over the years.

I am also indebted to all the tutors at University College, Oxford for all the excellent tutorials provided during the three years of my undergraduate degree.

To Her Shuang, Patty, Jeffrey, Chuhong, Xiuting, Ivana, Korbua, Tulip and every member of the Compton group past and present, thank you very much for the memorable lunches, trips, and the great time in the lab.

My heartfelt thanks also go to P.Kate, P.Bee, P.Kul, P.Tong, P.Pong, P.Pui, P.Plum, P.Nodd, P.Mind, Oat, Noo.d, and the friends who have been with me all these years. Most importantly, to my parents, thank you for all the love, care and never ending support!

Contents

Abstract i
Acknowledgements ii
Contents iii
Glossary vi
Chapter 1 Introduction to electrochemistry 1
1.1 Principles of electrochemistry 1
1.2 Electrochemical methods 12
1.3 Conclusions 26
Chapter 2 Introduction to UV-visible spectrophotometry 28
2.1 Properties of UV and visible radiation 28
2.2 Absorption of electromagnetic radiation 29
2.3 Optical properties of nanoparticles 32
2.4 Instrumentation 36
2.5 Conclusions 36
Bibliography 37
Chapter 3 Introduction to saliva and salivary biomarkers 39
3.1 Functions of saliva 40
3.2 Components of human saliva and synthetic saliva recipes 40
3.3 Biomarkers in saliva – what correlations exist, do not exist 45
3.4 Potential problems of measurements in saliva 54
3.5 Conclusions 55
Bibliography 55
Chapter 4 Experimental 58
4.1 Chemical reagents 58
4.2 Biological samples 59
4.3 Electrochemical instrumentation 60
4.4 Non-electrochemical instrumentation 61
Bibliography 61

Chapter 5 Sensitive amperometric detection of reduced glutathione and the development of supported microwire electrodes for electroanalysis 62
5.1 Introduction 63
5.2 Experimental 65
5.3 Theory and simulation 68
5.4 Results and discussions 71
5.5 Conclusions 90
Bibliography 90
Chapter 6 Rapid method for the quantification of reduced and oxidised glutathione in human plasma and saliva 92
6.1 Introduction 93
6.2 Experimental 96
6.3 Results and discussions 97
6.4 Conclusions 113
Chapter 7 The copper(II)-catalysed oxidation of glutathione 116
7.1 Introduction 117
7.2 Experimental methods 119
7.3 Results and discussions 120
7.4 Conclusions 139
Bibliography 139
Chapter 8 Salivary glutathione in bipolar disorder 141
8.1 Introduction 142
8.2 Experimental procedures 144
8.3 Results 150
8.4 Discussion 161
8.5 Conclusions 162
Bibliography 162
Chapter 9 Understanding electroanalytical measurements in authentic human saliva leading to the detection of salivary uric acid 164
9.1 Introduction 165
9.2 Experimental 167

9.3 Results and discussion....168
9.4 Conclusions....178
Bibliography....178
Chapter 10 Electrochemical detection of silver nanoparticles....180
10.1 Introduction....181
10.2 Experimental....183
10.3 Results....185
10.4 Discussion....207
10.5 Conclusions....212
Bibliography....213
Chapter 11 The fate of silver nanoparticles in authentic human saliva....216
11.1 Introduction....217
11.2 Experimental....218
11.3 Results and discussion....220
11.4 Conclusions....232
Bibliography....233
Chapter 12 Overall conclusions....234
Appendix A....237
A1 Cyclic voltammetry at a supported microwire electrode in the irreversible electron-transfer limit....237
A2 Cyclic voltammetry at a microdisc electrode as provided by the supplier....239
Appendix B....240
B1 Characterisation of the carbon microdisc electrode....240
B2 Cyclic voltammetry of hexaammineruthenium(III) reduction in authentic *vs.* synthetic saliva....241
B3 Cyclic voltammetry of uric acid, ascorbic acid and dopamine....242
Bibliography....244

Glossary

Where appropriate, symbols are defined in terms of the generic species i or the reduction process A + ne$^-$ ⇄ B.

Roman Symbols

Symbol	Definition	Units
A	Electrode area	m^2
A_r	Relative atomic mass	Dimensionless
c_i	Concentration of species *i*	mol m^{-3}
c_i^*	Bulk concentration of species *i*	mol m^{-3}
$c_{i,0}$	Concentration of species *i* at the electrode surface	mol m^{-3}
D_i	Diffusion coefficient of species *i*	m^2 s^{-1}
E	Potential applied to the working electrode	V
E_f^0	Formal potential	V
E^0	Standard potential	V
E_{photon}	Energy of photon	J
F	Faraday constant ≈ 96485	C mol^{-1}
f	Frequency	s^{-1}
G	Gibbs energy	J mol^{-1}
$\Delta G^{\#}$	Gibbs energy of activation	J mol^{-1}
I	Current	A
i	Current density	A m^{-2}
I_0	Intensity of incident radiation	W m^{-2}
$I_{\text{transmitted}}$	Intensity of transmitted radiation	W m^{-2}
I_λ	Intensity of a beam of monochromatic radiation of wavelength λ	W m^{-2}
J	Flux	mol m^{-2} s^{-1}

k^0	Standard electrochemical rate constant	m s^{-1}
$k_{\mathrm{f/b}}$	Rate constants of the forward/backward reactions	m s^{-1}
k_{B}	Boltzmann constant ≈ 1.381×10^{-23}	J K^{-1}
L	Length of sample	m
n	Number of moles of electrons transferred per mole of reaction	Dimensionless
N	Atomic number density	atoms m^{-3}
$\mathrm{N_A}$	Avogadro's number ≈ 6.022×10^{23}	mol^{-1}
Q	Charge	C
R	Molar gas constant ≈ 8.314	J K^{-1} mol^{-1}
r_{e}	Electrode radius	m
T	Temperature	K
t	Time	s
v	Velocity	m s^{-1}
z_i	Charge on species *i*	Dimensionless

Greek Symbols

Symbol	**Definition**	**Units**
α	Transfer coefficient for reduction	Dimensionless
β	Transfer coefficient for oxidation	Dimensionless
δ	Diffusion layer thickness	m
ε	Extinction coefficient	M^{-1} cm^{-1}
η	Overpotential ($E - E_f^0$)	V
γ	Activity coefficient	Dimensionless
λ	Wavelength	m
$\bar{\mu}$	Electrochemical potential	J mol^{-1}
μ	Chemical potential	J mol^{-1}
τ	Dimensionless time	Dimensionless

v	Scan rate	V s^{-1}
ϕ	Electrical potential	J
ρ	Density of solution	kg m^{-3}
σ	Cross section (extinction, absorption, scattering)	m^2
θ	Surface coverage	Dimensionless

Abbreviations

Abbreviation	Definition
AA	Ascorbic acid
AgNP	Silver nanoparticle
BQ	Benzoquinone
C	Carbon
CE	Counter electrode
CNT-SPE	Carbon nanotube modified screen-printed electrode
CV	Cyclic voltammetry
DA	Dopamine
DLS	Dynamic light scattering
DTNB	5,5′-dithiobis(2-nitrobenzoic acid) or Ellman's reagent
GC	Glassy carbon electrode
GR	Glutathione reductase (enzyme)
GSH	Glutathione (reduced)
GSSG	Glutathione (oxidised)
MSAD	Mean scaled absolute deviation
RDS	Rate-determining step
RE	Reference electrode
TEM	Transmission electron microscope
TNB	2-nitro-5-thiobenzoate
UA	Uric acid
WE	Working electrode

Chapter 1 Introduction to electrochemistry

This introductory chapter gives an overview of the fundamentals of electrochemistry and the principles underlying the electrochemical techniques used in this thesis.

1.1 Principles of electrochemistry

Electrochemistry studies chemical reactions and electron transfer at an electrode/solution interface. Both equilibrium (section 1.1.1) and dynamic electrochemistry (section 1.1.2) are discussed herein. Mass transport in solutions is then considered in section 1.1.3.

1.1.1 Equilibrium electrochemistry

When a metal electrode is immersed in a solution containing solution-phase species A and B, the metal can act as a *source* or *sink* of electrons, resulting in the *reduction* or *oxidation* of the species, as shown in the forward and backward reactions in eqn. 1.1 respectively.

$$\mathrm{A\ (aq)} + \mathrm{e^-\ (metal)} \underset{k_\mathrm{b}}{\overset{k_\mathrm{f}}{\rightleftarrows}} \mathrm{B\ (aq)};\quad E_f^0 \qquad (1.1)$$

The thermodynamic and kinetic parameters associated with the above electrochemical reaction are ***i)*** E_f^0: the formal potential of the A/B redox couple, and ***ii)*** k_f and k_b: the electrochemical rate constants of the forward and backward reactions. These parameters will be discussed later.

In a metal, electron energy levels exist in a continuum and are filled up to the Fermi level, shown schematically in Figure 1.1. Meanwhile, the energy levels of the solution-phase species (A and B) are discrete. If the Fermi energy of the metal is higher than the lowest unoccupied molecular orbital (LUMO) of A, it is energetically favourable for an electron to

transfer from the metal to the LUMO of A, decreasing the energy of the Fermi level. The reduction of A to B thus occurs. If the energy of the highest occupied molecular orbital (HOMO) of species B is higher than the Fermi energy, the reverse *oxidation* process occurs. Both oxidation and reduction can take place until the Fermi energy of the metal is intermediate between the energy levels of A and B such that the rates of the forward and backward reactions are equal and a dynamic equilibrium is established.[1,2]

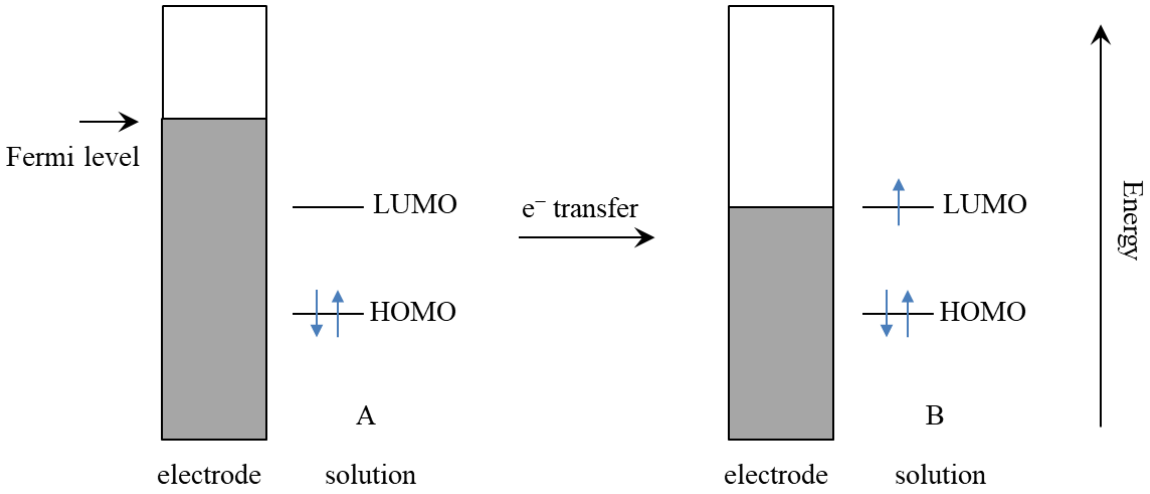


Figure 1.1: Schematic representation of the energy levels of a metal electrode and solution-phase species A and B.

As a result of the electron transfer processes, there is likely a built-up of net electrical charges at the electrode/solution interface. The net charge separation at equilibrium between the electrode and the solution phase gives rise to an *electrode potential*. This electrode potential is dependent upon the activities (or concentrations) of the relevant solution-phase species at the electrode surface according to the Nernst equation (eqn. 1.10), which can be derived from the thermodynamic description of electrochemical equilibrium as will be discussed next.[2]

At equilibrium, the electrochemical potentials of the reactants and products are equal. The electrochemical potential ($\bar{\mu}_i$) of a chemical species i is defined as:

$$\bar{\mu}_i = \mu_i + z_i \mathrm{F} \phi_{\mathrm{m/s}} \tag{1.2}$$

where μ_i and z_i denote the chemical potential and the charge of species i. F is a Faraday constant (96485 C mol^{-1}). ϕ_{m} and ϕ_{s} are the electrical potentials of the electron (metal-phase) and the chemical species (solution-phase) respectively.

For an equilibrium in eqn. 1.1, the balance of the electrochemical potentials is

$$(\mu_{\mathrm{A}} + z_{\mathrm{A}} \mathrm{F} \phi_{\mathrm{s}}) + (\mu_{\mathrm{e}^-} - \mathrm{F} \phi_{\mathrm{m}}) = (\mu_{\mathrm{B}} + (z_{\mathrm{A}} - 1) \mathrm{F} \phi_{\mathrm{s}}) \tag{1.3}$$

$$\mathrm{F}(\phi_{\mathrm{s}} - \phi_{\mathrm{m}}) = \mu_{\mathrm{B}} - \mu_{\mathrm{A}} - \mu_{\mathrm{e}^-} \tag{1.4}$$

The chemical potential (μ_i) is defined as

$$\mu_i = \mu_i^0 + \mathrm{R}T \ln a_{i,0} \tag{1.5}$$

where μ_i^0 is the standard chemical potential. R and T are the molar gas constant (8.314 J K^{-1} mol^{-1}) and absolute temperature (K) respectively. $a_{i,0}$ is the activity of species i at the electrode surface.

By substituting eqn. 1.5, eqn. 1.4 can be rearranged to

$$(\phi_{\mathrm{m}} - \phi_{\mathrm{s}}) = (\phi_{\mathrm{m}}^0 - \phi_{\mathrm{s}}^0) - \frac{\mathrm{R}T}{\mathrm{F}} \ln \frac{a_{\mathrm{B},0}}{a_{\mathrm{A},0}} \tag{1.6}$$

or

$$E = E^0 - \frac{\mathrm{R}T}{\mathrm{F}} \ln \frac{a_{\mathrm{B},0}}{a_{\mathrm{A},0}} \tag{1.7}$$

where E is the applied potential. E^0 is the standard potential.

In practice, it is the absolute *concentrations* of the chemical species, rather than activities, that are often known, easily controlled and measured. The two properties are related by[3]

$$a_i = \gamma_i c_i \tag{1.8}$$

where γ_i is the *activity coefficients* of species i, and is the factor accounting for the non-ideality of the solution, for example due to the long-range electrostatic interaction between charged species/ions.

By defining the *formal potential* (E_f^0) as

$$E_f^0 = E^0 - \frac{\mathrm{R}T}{\mathrm{F}} \ln \frac{\gamma_\mathrm{B}}{\gamma_\mathrm{A}} \tag{1.9}$$

Equation 1.7 can be written as

$$E = E_f^0 - \frac{\mathrm{R}T}{\mathrm{F}} \ln \frac{c_{\mathrm{B},0}}{c_{\mathrm{A},0}} \tag{1.10}$$

where $c_{i,0}$ is the concentration at the surface of the electrode of species i. This is the Nernst equation used to describe electrochemical equilibrium at the electrode surface.[4]

1.1.2 Dynamic electrochemistry

If instead of allowing equilibrium to establish a potential is **applied** to the electrode, the energy of the Fermi level is perturbed. The application of a negative potential increases the Fermi energy, causing electrons to flow from the metal to the solution. The reduction of A is thus enhanced relative to the oxidation of B. The opposite occurs if a positive potential is applied.[5]

The unequal rates of reduction and oxidation results in a non-zero net flux of electrons between the electrode and the solution-phase species. For an electrochemical reaction in eqn. 1.1, the net flux (J, mol m^2 s^{-1}) at the electrode is

$$J = k_{\mathrm{f}} c_{\mathrm{A},0} - k_{\mathrm{b}} c_{\mathrm{B},0} \tag{1.11}$$

where k_{f} and k_{b} are the electrochemical rate constants of the forward (reduction) and backward (oxidation) reactions respectively. $c_{i,0}$ is the concentration at the surface of the electrode of species i, which may differ from that in the bulk solution.

The number of electrons flowing across the entire electrode surface in unit time or *current* (I) is given by

$$I = \mathrm{F}AJ \tag{1.12}$$

where A is the surface area of the electrode.

Combining equations 1.11 and 1.12, the current is therefore

$$I = \mathrm{F}A(k_{\mathrm{f}} c_{\mathrm{A},0} - k_{\mathrm{b}} c_{\mathrm{B},0}) \tag{1.13}$$

Figure 1.2 demonstrates a typical reaction profile including the positions of the reactants, products and the transition state (#). The reaction profile is sensitive to the potentials ϕ_{m} and ϕ_{s}. According to the transition state theory, the electrochemical rate constant ($k_{\mathrm{f/b}}$) can be related to the Gibbs energies of activation ($\Delta \mathrm{G}_{\mathrm{f/b}}^{\#}$) according to the Arrhenius equation:[6,7]

$$k_{\mathrm{f/b}} = \mathrm{A}' \exp\left\{\frac{-\Delta \mathrm{G}_{\mathrm{f/b}}^{\#}}{\mathrm{R}T}\right\} \tag{1.14}$$

where $\Delta G_f^{\#}$ and $\Delta G_b^{\#}$ are the Gibbs energies of activation of the forward and backward reactions respectively. A′ is a frequency factor relating to the rate of collisions of the electroactive species with the electrode surface.

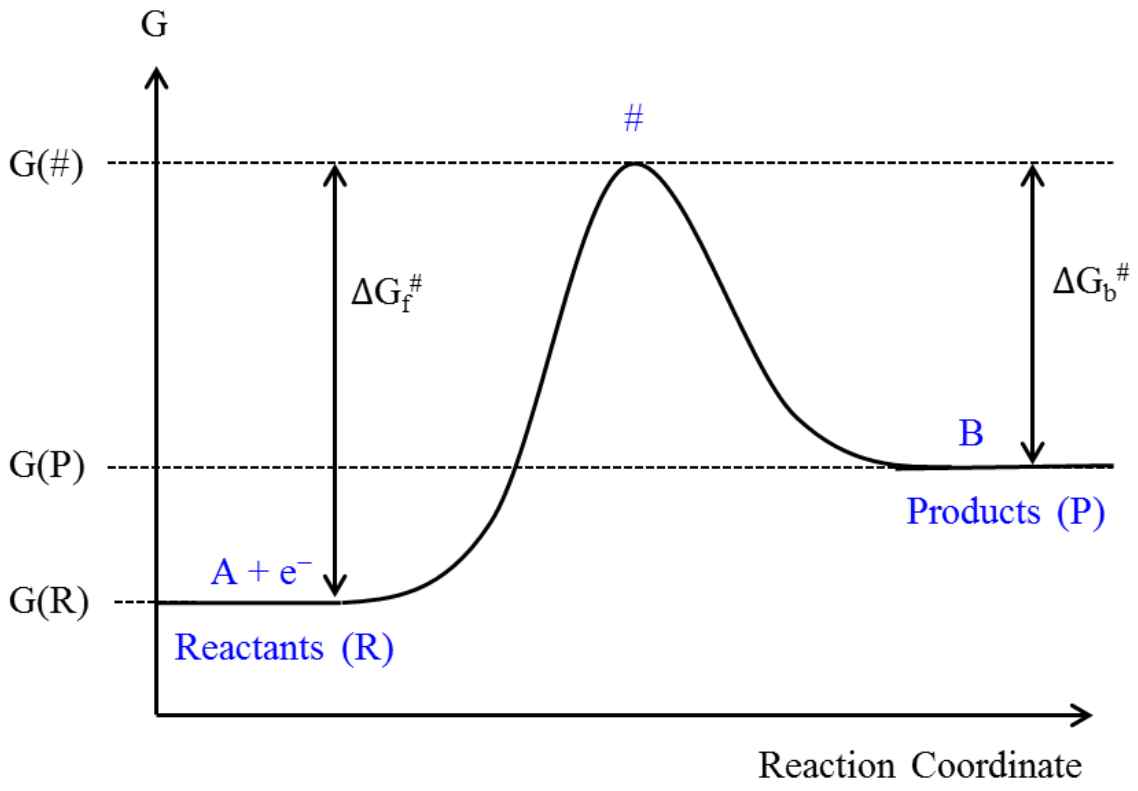


Figure 1.2: A reaction profile for a general electrode process: A + e^- ⇄ B. # denotes the transition state.

For a fixed temperature and pressure, the Gibbs energies of activation of the forward (cathodic, $\Delta G_f^{\#}$) and backward (anodic, $\Delta G_b^{\#}$) reactions are given by

$$\Delta G_f^{\#} = \Delta G^{\#}_0 + \alpha F(E - E_f^0) \qquad (1.15)$$

$$\Delta G_b^{\#} = \Delta G^{\#}_0 - \beta F(E - E_f^0) \qquad (1.16)$$

where $\Delta G^{\#}_0$ is the standard Gibbs energy change. E and E_f^0 are the applied and formal potentials respectively. α is the *cathodic* transfer coefficient, taking the value between 0 and 1. For an *anodic* process, the transfer coefficient is given by β, where $\alpha + \beta = 1$. The transfer coefficients reflect the position of the transition state.[8] If α is close to 0 (i.e. β is close to 1), the transition state resembles A + e^-. If α is close to 1, the transition state resembles B. The value of α is found to be ~0.5 for a number of reactions, suggesting the intermediate nature of the transition state.[5,9]

Substituting eqns. 1.15 and 1.16 into eqn. 1.14 gives

$$k_\mathrm{f} = \mathrm{A}' \exp\left\{\frac{-\Delta G_0^{\#}}{RT}\right\} \exp\left\{\frac{-\alpha F(E-E_f^0)}{RT}\right\} \tag{1.17}$$

$$k_\mathrm{b} = \mathrm{A}' \exp\left\{\frac{-\Delta G_0^{\#}}{RT}\right\} \exp\left\{\frac{\beta F(E-E_f^0)}{RT}\right\} \tag{1.18}$$

By defining the standard electrochemical rate constant (k^0) as

$$k^0 = \mathrm{A}' \exp\left\{\frac{-\Delta G_0^{\#}}{RT}\right\} \tag{1.19}$$

the following equations result:[10,11]

$$k_\mathrm{f} = k^0 \exp\left\{\frac{-\alpha F(E-E_f^0)}{RT}\right\} \tag{1.20}$$

$$k_\mathrm{b} = k^0 \exp\left\{\frac{\beta F(E-E_f^0)}{RT}\right\} \tag{1.21}$$

where $E - E_f^0$ is known as the overpotential (η) of a redox process.

Consequently, the flux (J) can be described by the following equation:

$$J = k^0 c_{\mathrm{A},0} \exp\left\{\frac{-\alpha \mathrm{F}(E-E_f^0)}{\mathrm{R}T}\right\} - k^0 c_{\mathrm{B},0} \exp\left\{\frac{\beta \mathrm{F}(E-E_f^0)}{\mathrm{R}T}\right\} \qquad (1.22)$$

This Butler-Volmer equation will further be discussed in relation to the mass transport in the interpretation of the results of electrochemical measurements in Section 1.2.

1.1.3 Mass transport in solution

When a suitable potential is applied, a reactant is consumed at an electrode, lowering the concentration of this species in the vicinity of the electrode. Three mass transport processes, *diffusion, migration and convection*, can transfer the species from bulk solution to the electrode surface.[12]

Diffusion and migration occur as a result of an electrochemical potential gradient. If the electrochemical potential is non-uniform, the solution will adjust in a way that the electrochemical potential gradient will be minimised and that the system reaches equilibrium. The electrochemical potential, introduced in eqn. 1.2, is the sum of the chemical potential (relating to concentration, $\mathrm{R}T\ln c + \mu_i^0$) and the electrical potential ($z\mathrm{F}\phi$). Diffusion is an entropic process driven by concentration gradients, while migration is driven by the electric field gradients.

The addition of sufficiently large amount of inert (supporting) electrolyte to the system minimises the effect of migration, typically when the support ratios are over 30 for steady-state[13] and 100 for transient measurements.[14-19] The meaning of steady-state and transient will be discussed later in the next section. At high support ratios, most of the currents in the bulk solution are carried by the supporting electrolyte. The potential drop between the metal (ϕ_{m})

and the solution phase (ϕ_s) is also restricted to a very thin layer (< 20 Å), where tunnelling can take place outside of this layer at sufficiently fast rates.[20] The migration of the electroactive species to the electrode is thus negligible at high concentrations of supporting electrolytes.

Convection is the movement of a species due to a mechanical force. There are two general forms of convection: forced and natural (free). The former is induced by an external mechanical force applied to the system, for example, stirring, flowing or the use of a rotating electrode. This type of convection is not considered in this thesis. Natural convection is an intrinsic property of electrochemical reaction. It is generated by density or temperature (thermal) gradients in solution.[21] The effect of density-driven natural convection is minimal at short time (typically < 10 s).[22] Meanwhile, the effect of the temperature gradient can be minimised by thermostating of the electrochemical system, as is the case in this thesis.

Under suitable experimental conditions such as that described above, the effects of migration and convection can be neglected, and the mass transport of the redox-active species to the electrode is exclusively diffusion. In the following, diffusion will thus be the only mode of mass transport considered. The variation in concentrations with space and time due to diffusion is described by Fick's laws of diffusion.[23,24]

Fick's 1st law describes how the flux (J) through a unit area in a unit time (mol m^{-2} s^{-1}) is related to the concentrations (c):

$$J = -D\nabla c \tag{1.23}$$

where D is the diffusion coefficient. ∇c is the local concentration gradient.

Fick's 2nd law describes the change in concentrations with time:

$$\frac{\partial c}{\partial t} = D\nabla^2 c \tag{1.24}$$

These laws of diffusion can be understood from a microscopic model, described next.

Consider a linear diffusion in the direction perpendicular (x-axis) to the plane (yz-plane) of area 'A,' refer to Figure 1.3. On both sides of the plane, there is an infinitesimally small thickness (δx) of solution containing particles (e.g. molecules, ions) with concentrations c_1 and c_2 on the left and the right hand sides of the plane respectively. The concentrations are constant in the yz-plane. These particles move freely in solutions and across the plane of interest in a random walk process. The probabilities of the particles moving to the left and the right compartments are equal. In time δt, the number of particles moving to the left of the plane is $c_2 A\delta x/2$, and the number of particles moving to the right of the plane is $c_1 A\delta x/2$.

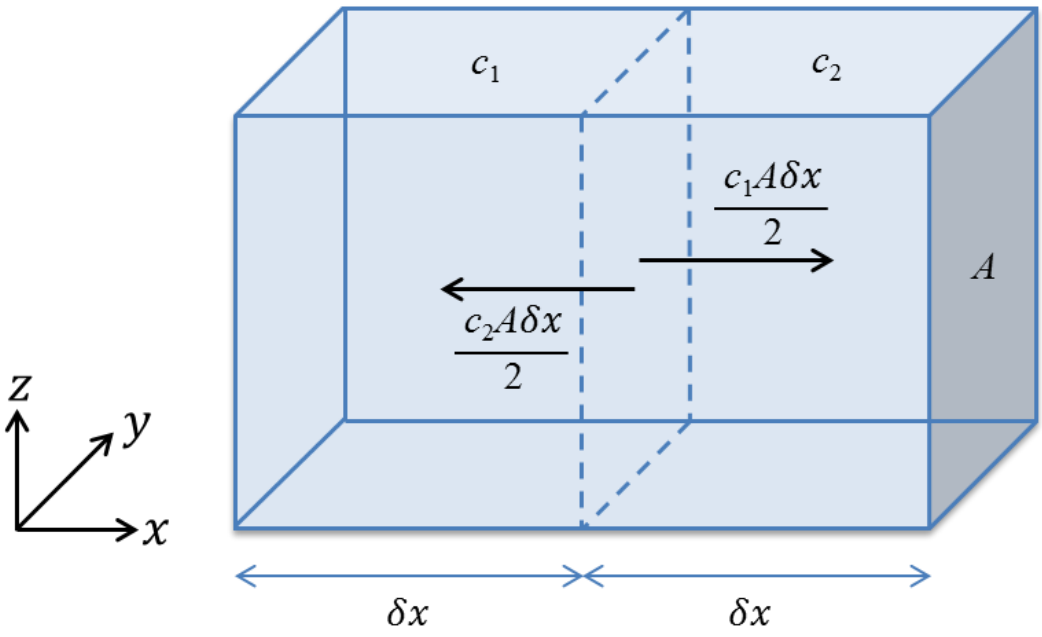


Figure 1.3: A microscopic model used in the interpretation of Fick's law of diffusion for one-dimensional linear diffusion through a planar plane.

Overall, the net number of particles (N) moving through a plane of area 'A' in time δt is thus

$$N = \frac{(c_1 - c_2) A \delta x}{2} \tag{1.25}$$

The flux (J) of particles per unit area per unit time is

$$J = \frac{1}{A\delta t} \frac{A \delta c \delta x}{2} \tag{1.26}$$

where $\delta c = c_1 - c_2$

$$J = \frac{\delta c \delta x}{2\delta t} \tag{1.27}$$

By multiplying $\delta x/\delta x$ and approximating $\delta c/\delta x$ as $\partial c/\partial x$, equation 1.27 can be written as

$$J = -\frac{(\delta x)^2}{2\delta t} \frac{\partial c}{\partial x} \tag{1.28}$$

The negative sign reflects the movement of particles from high to low concentrations (i.e. the flux down the concentration gradient).

The mean-square of the distance ($\langle x^2 \rangle$) travelled by a particle in time t is related to the *diffusion coefficient* (D) by the Einstein-Smoluchowski equation:[25,26]

$$D = \frac{\langle x^2 \rangle}{2t} = \frac{(\delta x)^2}{2\delta t} \tag{1.29}$$

Substituting eqn. 1.29 into eqn. 1.28 thus yields the Fick's first law as given in eqn. 1.23, connecting the microscopic random walk process to the macroscopic law of diffusion.

1.2 Electrochemical methods

In most electrochemical cells (including in all of the electrochemical measurements in this thesis), a three-electrode set-up is used, refer to Figure 1.4. The potential is applied to a working electrode (WE) relative to a reference electrode (RE). The redox chemistry of interest then takes place at a working electrode (WE), where a current is also drawn and measured. Minimal negligible current is passed through the RE to maintain its constant potential. A third electrode, counter electrode (CE), is required to complete the circuit and allow the current to flow.

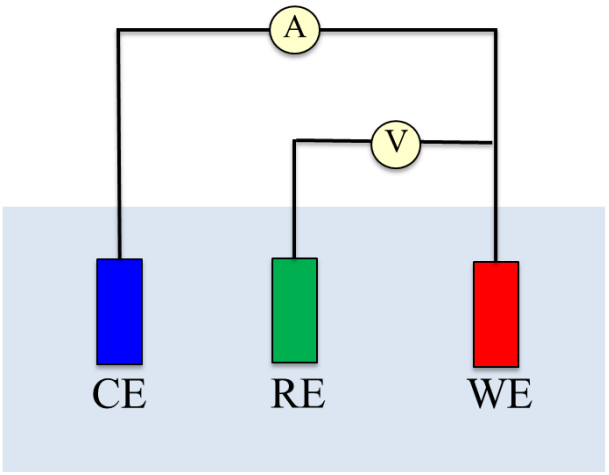


Figure 1.4: An electrochemical three-electrode cell set-up

Two electrochemical techniques are used in this thesis: cyclic voltammetry and chronoamperometry. In both techniques, the potential(s) are applied to the electrode and the resulting currents of the redox processes are measured. Voltammetry is often used to study the interplay between the electrode kinetics and mass transport in solution. Chronoamperometry is usually used to explicitly study mass transport in the solution.

1.2.1 Cyclic voltammetry

In cyclic voltammetry, the potential is swept linearly with time ($E_1 \rightarrow E_2$ in Figure 1.5), reversed at a certain point (E_2 in Figure 1.5) and then swept linearly back to the initial potential ($E_2 \rightarrow E_1$ in Figure 1.5).[27,28] The potential is decreased (made more negative) for the study of a reduction process, and increased (made more positive) for an oxidation process. The rate at which the potential is swept ($v = \mathrm{d}E/\mathrm{d}t$) is called 'scan rate' (V s^{-1}). The initial potential (E_1) in voltammetric measurements is typically chosen to be at a point where no Faradaic (oxidation or reduction) process takes place and the currents are near-zero. The only contribution to the current at this initial potential is predominantly non-Faradaic or capacitative currents due to the built-up of charges at the electrified surface.[29] The potential E_2 at which the scan is reversed is typically chosen to be at a high overpotential ($\eta = \left|E - E_f^0\right|$). At this high overpotential, the electron transfer reaction occurs almost instantaneously when the electroactive species reaches the electrode surface.

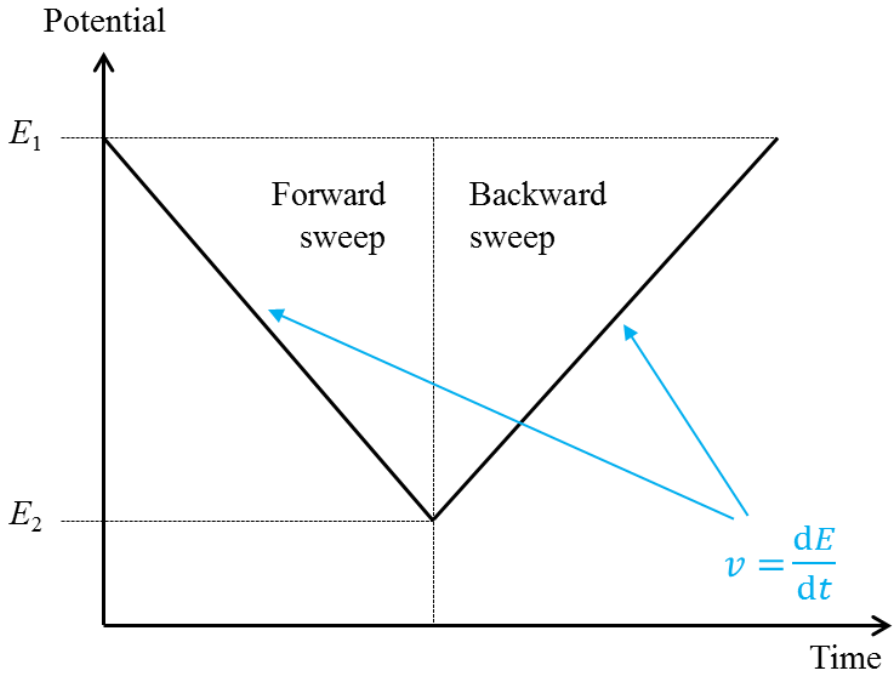


Figure 1.5: The waveform of the potential applied during a typical cyclic voltammetry experiment.

The cyclic voltammetric behaviour changes with the electrode geometry. Herein, only macrodisc and microdisc electrodes which are relevant to the context of this thesis will be considered. A cylindrical electrode is used in Chapter 5 and will be discussed in the chapter. In the followings, we will consider the cyclic voltammetric responses of a reaction $A + e^- \leftrightarrow B$, with only A present in the bulk solution.

a) Macrodisc electrode

The voltammetric response reflects an interplay between diffusion, electrode kinetics and scan rates. In the forward (cathodic) sweep (refer to Figure 1.5), as potentials become more negative than the formal potential (E_f^0), reductive cathodic currents flow. The electrochemical reaction rates at the different potentials can be determined by the Butler-Volmer equations (eqn. 1.22). The flux of electron transfer however does not continue to increase indefinitely with the overpotential as predicted by the Butler-Volmer kinetics. This is because as the reaction progresses, A in the region near the electrode is consumed. At the same time, the concentration of B builds up near the electrode surface. The flux starts to decrease when the surface concentration of A becomes near-zero, resulting in a *peak-shaped* response in the cyclic voltammetry at a macrodisc electrode.

In the backward sweep, the reverse oxidation process ($B \rightarrow A + e^-$) occurs when the potentials are higher (more positive) than the formal potential E_f^0. Note that although the bulk concentration of B is zero, B has been formed from the cathodic reaction in the forward sweep. The flux increases with increasing potentials according to the Butler-Volmer kinetics. However when the concentration of B at the electrode becomes near-zero, the flux starts to decrease, giving a peak-shaped response similar to the cathodic reaction described above. There are thus two peaks of opposite currents in a cyclic voltammogram at a macrodisc

electrode, refer to Figure 1.7. The difference in the potentials of the two peaks is often known as peak-to-peak separation, the importance of which will be discussed later.

The concentration gradient formed near the electrode induces diffusion. A macrodisc electrode is often approximated as a plane with infinite dimensions. The diffusion is therefore one-dimensional or linear in the direction perpendicular to the electrode, as also described in Section 1.1.3. In practice, the electrode has finite dimension and the diffusion at the edge of the electrode can be non-linear, refer to Figure 1.6a. This effect however is very small, contributing to less than 2% of the currents at a macrodisc electrode of size larger than 2 mm.[30]

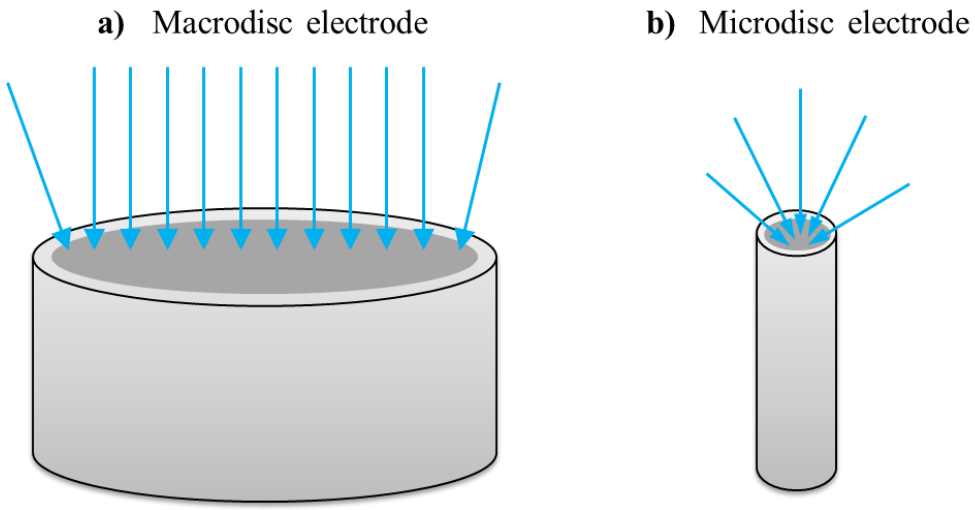


Figure 1.6: The diffusional mass transport regimes: **a)** *linear* diffusion at a macrodisc electrode and **b)** *convergent* diffusion a microdisc electrode.

This diffusional mass transport influences the availability of the redox-active species at the electrode surface. The extent to which the diffusion controls the consumption of the electroactive species determines the voltammetric responses. The electrochemical rate

constant (k_0) can be insightfully compared with the diffusional mass transport coefficient (m_T), which is defined as

$$m_T = D/\delta \tag{1.30}$$

where δ is the time-dependent diffusion layer thickness. $\delta \sim \sqrt{2Dt}$ for a macrodisc electrode, refer to eqn. 1.29 ($\delta \equiv \delta x$).[2]

For *fast* electrode kinetics,

$$m_T \ll k^0 \tag{1.31}$$

the rate of electron transfer significantly outweighs the diffusion rate. In this case, the system is in an electrochemically *reversible* limit. The concentrations of the electroactive species at the electrode surface obey the Nernst equation (eqn. 1.10). According to the Nernst equation, the peak-to-peak separation in the cyclic voltammetry is expected to be ~57 mV at 298 K and is independent of scan rate.

On the other hand, for relatively *slow* electrode kinetics,

$$m_T \gg k^0 \tag{1.32}$$

the system is in an *irreversible* limit. Due to the small k^0, the amount of the electroactive species consumed at the electrode is also relatively small at low overpotential. The peak in the cyclic voltammetry occurs when the surface concentration is near-zero. The peak thus occurs at higher overpotential. This is the case for both oxidation and reduction processes, and hence the peak-to-peak potential is larger than 57 mV of the reversible limit (at 298 K). The peak-to-peak separation of the irreversible process is also dependent on the scan rates. At fast scan rates, the system is allowed to be reduced or oxidised in a short period of time, and hence the diffusion layer is relatively thin. The mass transport to the electrode is thus more

efficient relative to the electrode kinetics, and the system is more *irreversible* (i.e. larger peak-to-peak separation).

In practice, many systems are in between the two limits, known as *quasi-reversible*. At very slow scan rates, the systems behave more reversible-like, and at very fast scan rates as irreversible-like.

The system is typically classified as reversible, quasi-reversible or irreversible according to the parameter Λ, introduced by Matsuda and Ayabe, defined as:[31]

$$\Lambda = \frac{k^0}{\sqrt{\frac{FDv}{RT}}} \tag{1.33}$$

This parameter essentially summarises the interplay between the rates of electron transfer (k^0) and (diffusional) mass transport ($\sqrt{\frac{FDv}{RT}}$). The system is considered to be a reversible process if,

$$\Lambda \geq 15 \qquad \text{or} \qquad k^0 \geq 0.3v^{0.5} \text{ cm s}^{-1} \tag{1.34}$$

a quasi-reversible process if,

$$10^{-3} < \Lambda < 15 \qquad \text{or} \qquad 2 \times 10^{-5}v^{0.5} < k^0 < 0.3v^{0.5} \text{ cm s}^{-1} \tag{1.35}$$

and irreversible if,

$$\Lambda \leq 10^{-3} \qquad \text{or} \qquad k^0 \leq 2 \times 10^{-5}v^{0.5} \text{ cm s}^{-1} \tag{1.36}$$

Figure 1.7 displays the characteristic peak-shaped cyclic voltammetry of a one-electron transfer process with different electrochemical rate constant (k^0) at a fixed scan rate and at

the same (macro)electrode size. The parameters used in the simulation of the voltammetry are given in the caption of the figure. The system changes from reversible at large k^0 to irreversible at small k^0, as noticeable from the more distorted shape of the voltammograms and the larger peak-to-peak separation as k^0 decreases.

The effect of scan rate on the cyclic voltammetry is demonstrated in Figure 1.8, showing the constant and increased peak-to-peak separation with scan rate for the reversible and irreversible limits respectively.

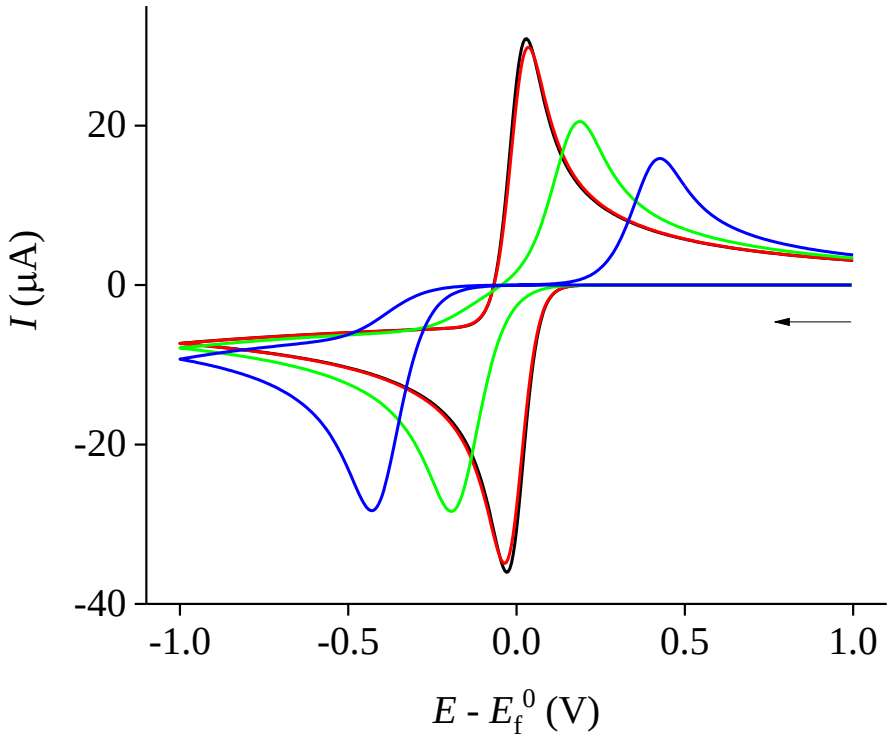


Figure 1.7: Cyclic voltammograms at a macrodisc electrode (A = 0.3 cm^2) of a one-electron transfer process (A + e$^-$ ↔ B; E_f^0 = 0 V, c_A = 1 mM, c_B = 0 mM, $D_A = D_B = 1\times10^{-5}$ cm^2 s^{-1}) starting from cathodic scan at the scan rate of 20 mV s^{-1} at a range of electrochemical rate constants (k^0): **(Black)** $k^0 = 1\times10^4$ cm s^{-1}; **(Red)** $k^0 = 1\times10^{-2}$ cm s^{-1}; **(Green)** $k^0 = 1\times10^{-4}$ cm s^{-1}; **(Blue)** $k^0 = 1\times10^{-6}$ cm s^{-1}.

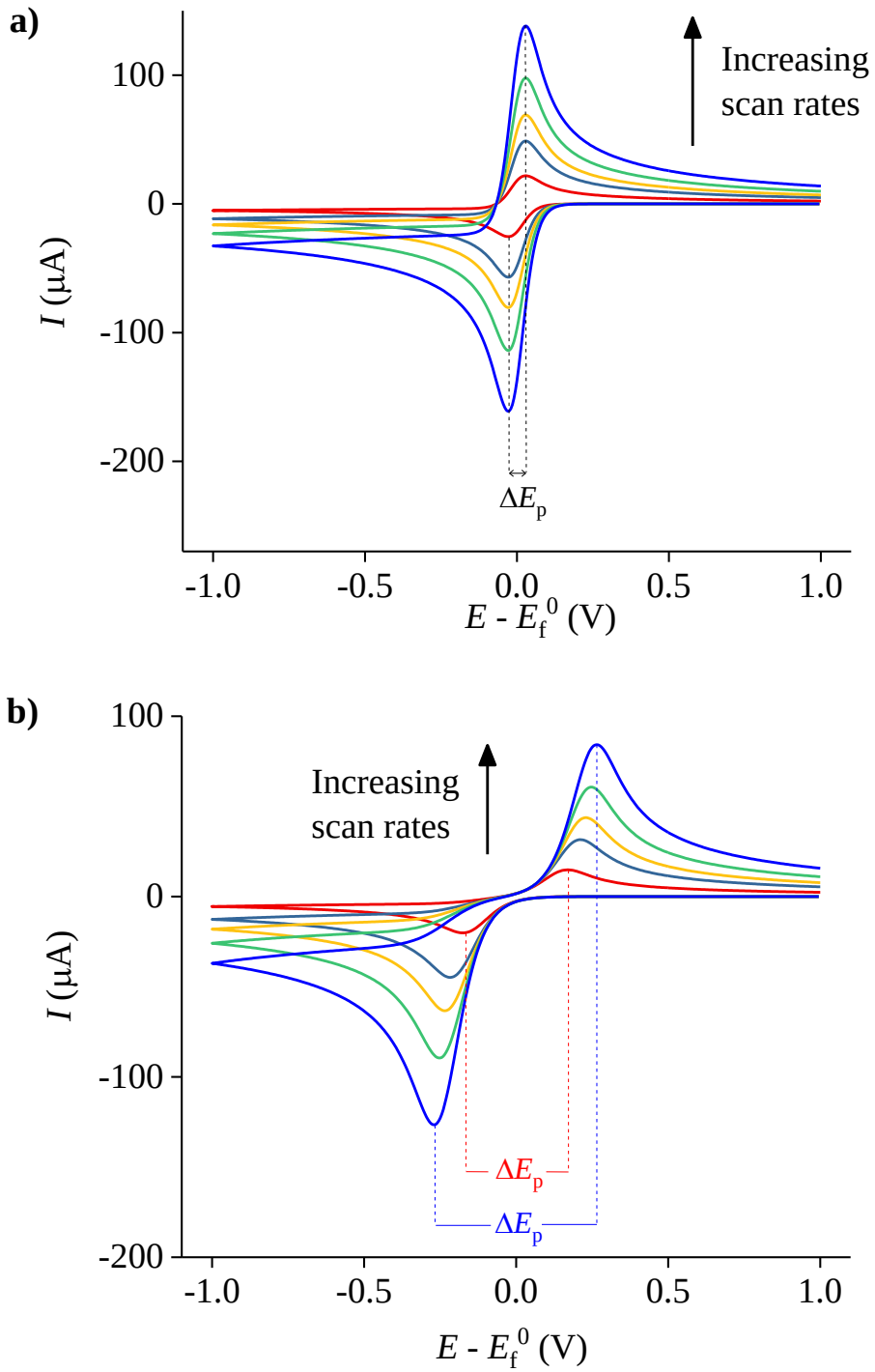


Figure 1.8: Cyclic voltammograms at a macrodisc electrode (A = 0.3 cm^2) of a one-electron transfer process (A + e$^-$ ↔ B; E_f^0 = 0 V, c_A = 1 mM, c_B = 0 mM, $D_A = D_B = 1\times10^{-5}$ cm^2 s^{-1}) starting from cathodic scan at a range of scan rates (10 – 400 mV s^{-1}) for **a)** a reversible process (large $k^0 = 1\times10^4$ cm s^{-1}) showing constant peak-to-peak separation and **b)** an irreversible process (small $k^0 = 1\times10^{-4}$ cm s^{-1}) showing larger peak-to-peak separation as the scan rate increases.

In addition to the peak potentials and peak-to-peak separation, the voltammetric peak currents (I_p) contain important information related to the diffusion coefficient (D) and the bulk concentrations (c) of the redox species. In both the reversible and irreversible limits, the peak currents increase with the square root of the scan rates. At faster scan rates, the diffusion layer at the electrode has a shorter amount of time to develop. The higher concentration gradient in the thin diffusion layer thus enhances the flux, according to Fick's first law (eqn. 1.23). At slow scan rates, the converse is observed.

In the followings, a more general electrochemical reaction involving n-electron transfer will be considered.

$$\text{A (aq)} + n\,\text{e}^- \text{ (metal)} \;\rightleftarrows\; \text{B (aq)} \qquad (1.37)$$

In the reversible limit, the expression for the peak currents (I_p) derived from the solving of the Nernst and the diffusion equations is given by[32]

$$I_p = 0.446 n\text{F}Ac^* \sqrt{\frac{nFDv}{RT}} \qquad (1.38)$$

where n is the number of electrons transfer. A is the surface area of the electrode. c^* and D are the bulk concentration and diffusion coefficient of the electroactive species respectively. v is the voltage scan rate. F, R and T have their usual meanings.

In the irreversible limit, the electrode reaction is controlled by the Butler-Volmer kinetics (eqn. 1.22), instead of the Nernst equation. There is thus an additional kinetic term in the peak currents expression (eqn. 1.39), reflecting the significant contribution of the rate of electron transfer on the voltammetric response.[2]

$$I_{\mathrm{p}} = 0.496\sqrt{n' + \alpha_{n'+1}}\, nFAc^{*}\sqrt{\frac{FDv}{RT}} \qquad (1.39)$$

where n' is the total number of electrons transferred before the rate-determining step (RDS). $\alpha_{n'+1}$ is the transfer coefficient of the RDS.

For a one-electron transfer process, eqn. 1.39 can be simplified to:

$$I_{\mathrm{p}} = 0.496\sqrt{\alpha}FAc^{*}\sqrt{\frac{FDv}{RT}} \qquad (1.40)$$

where α is the transfer coefficient of the electron transfer process.

b) Microdisc electrode

At a microdisc electrode, the diffusion regime is different from the linear diffusion at a macrodisc. At very short times when the diffusion layer thickness ($\delta \sim \sqrt{Dt}$) is significantly smaller than the radius of the electrode (r_{e}), linear diffusion is still the dominant form of diffusional mass transport. However at longer times ($\delta \gg r_{\mathrm{e}}$), radial diffusion becomes dominant, refer to Figure 1.6b. The concentration gradients are not only established perpendicular to the electrode surface, but also along the axes parallel to the electrode. The diffusion in this case is *convergent*. As a result of convergent diffusion, the diffusion layer is approximately hemi-spherical in shape, allowing once developed a constant flux of the chemical species to the electrode surface.[33] A *steady-state* response is thus observed in the cyclic voltammetry at a microdisc electrode, provided that the scan rate is sufficiently slow for the convergent diffusion.[34-36]

Similar to the macrodisc electrode described in the previous section, the shape of the voltammetry reflects the *reversibility* and *irreversibility* (i.e. rate of electrode kinetics vs. mass transport) of the process. In the case that the diffusional mass transport is fast, i.e. $m_T \gg k_0$ (eqn. 1.32), the system is in a reversible limit. Otherwise, the system is irreversible if $m_T \ll k_0$ (eqn. 1.31). For a microdisc electrode, the mass transport coefficient is approximated by[2]

$$m_T \sim \frac{D}{r_\mathrm{e}} \tag{1.41}$$

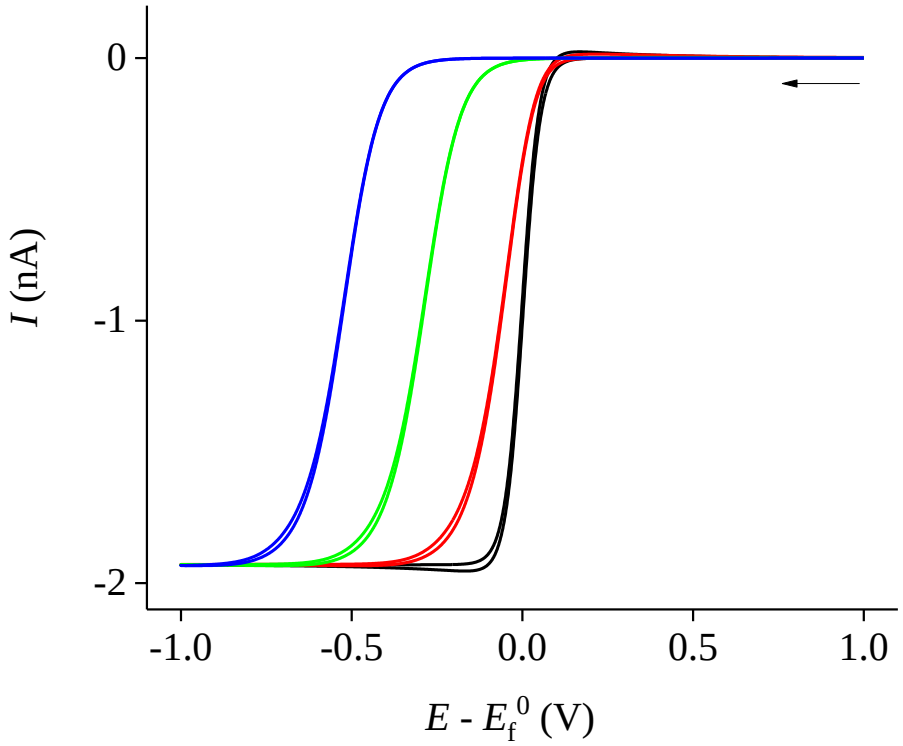


Figure 1.9: Cyclic voltammograms at a *microdisc* electrode (r_e = 5 μm) of a one-electron transfer process (A + e^- ↔ B; E_f^0 = 0 V, c_A = 1 mM, c_B = 0 mM, $D_\mathrm{A} = D_\mathrm{B} = 1\times10^{-5}$ cm^2 s^{-1}) starting from cathodic scan at the scan rate of 10 mV s^{-1} at a range of electrochemical rate constants (k^0): **(Black)** k^0 = 1×10^4 cm s^{-1}; **(Red)** k^0 = 1×10^{-2} cm s^{-1}; **(Green)** k^0 = 1×10^{-4} cm s^{-1}; **(Blue)** k^0 = 1×10^{-6} cm s^{-1}.

Figure 1.9 gives an example of cyclic voltammetry at a microdisc electrode at the different electrochemical rate constant (k_0). For a small k_0, higher overpotentials are required to induce the net flux of currents at the electrode. The cyclic voltammetry is thus more distorted as the values of k_0 becomes smaller.

At sufficiently slow scan rates at which steady-state is reached, the steady-state currents (I_{ss}) at a microdisc electrode correspond to the concentration (c^*) and diffusion coefficients (D) of the redox-active species according to the following equation:[37]

$$I_{ss} = 4nFc^*Dr_e \tag{1.42}$$

where all the parameters have their usual meanings, as previously described.

1.2.2 Chronoamperometry

In chronoamperometry, the potential applied to the electrode is changed instantaneously ('stepped') from some initial potential (E_1) to another (E_2), refer to Figure 1.10. E_1 is typically chosen to correspond to near-zero currents (i.e. only non-Faradaic/capacitative currents). The potential E_2 usually provides a sufficiently high overpotential ($\eta = \left|E - E_f^0\right|$) such that the rate of electron transfer, according to the Butler-Volmer kinetics (eqn. 1.22), is large enough that all the electroactive species of interest that arrive at the electrode is immediately reduced or oxidised. The concentration of the redox species at the electrode surface is thus effectively zero. The chronoamperometric currents therefore reflect exclusively the mass transport of the electroactive species from the bulk solution to the electrode surface. An example of the current-time responses of a chronoamperometric measurement is given in Figure 1.11,

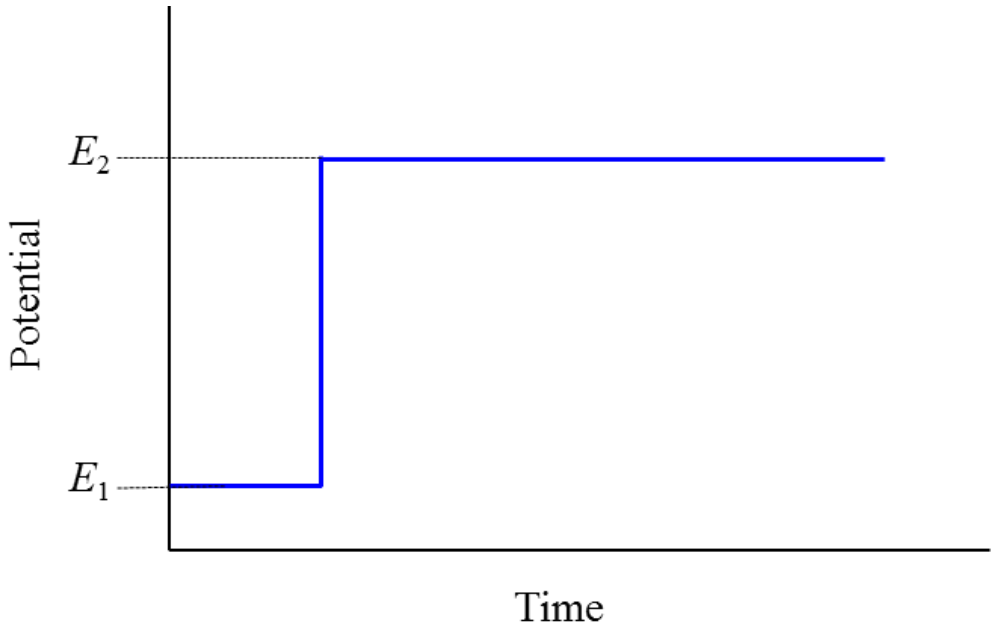


Figure 1.10: The potential step applied during a chronoamperometry experiment.

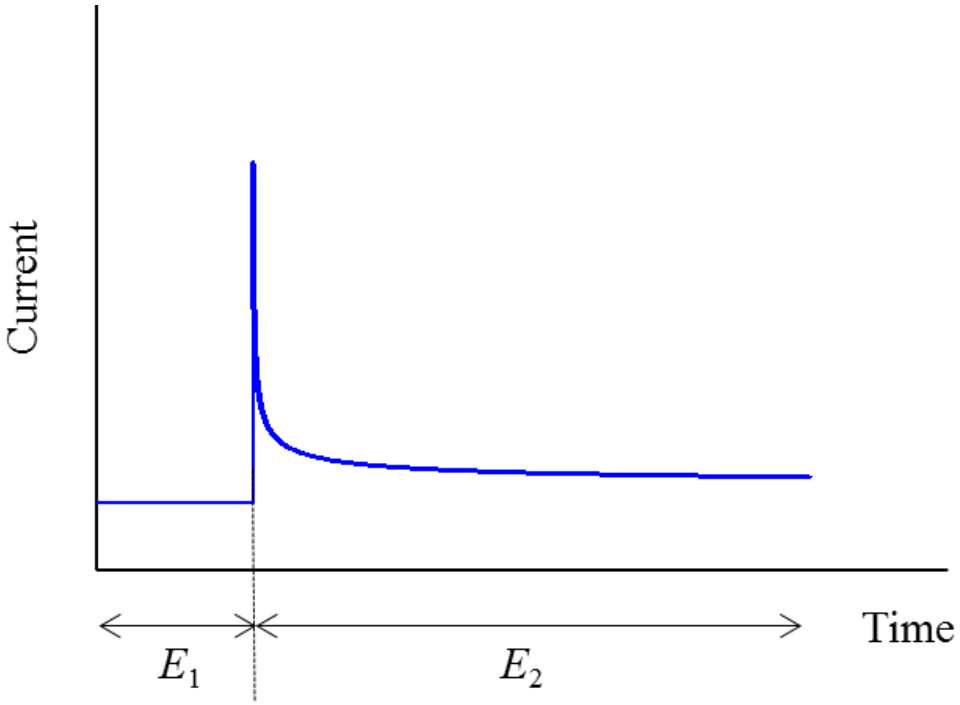


Figure 1.11: A typical chronoamperogram produced by the application of the potential waveform in Figure 1.10.

a) Macrodisc electrode

At a macrodisc electrode, the diffusional transport to the electrode surface can be assumed to be one-dimensional or linear, as discussed previously. By solving Fick's second law and the application of appropriate boundary conditions (at $t = 0$, $c = c^*$; at $t > 0$, $c(x = 0) = 0$ and $c(x \to \infty) = c^*$), an analytical expression of the current transient at a macrodisc electrode can be derived. The current-time (I-t) response resulting from a potential step from zero current to diffusion-limited conditions is thus given by the Cottrell equation:[38]

$$I = \frac{n\mathrm{F}Ac^*\sqrt{D}}{\sqrt{\pi t}} \tag{1.43}$$

where n is the number of electrons transfer and A is the surface area of the electrode.

b) Microdisc electrode

At a microdisc electrode, both linear and radial diffusion contributes significantly to the currents. The transient currents in this case can be analysed by the Shoup and Szabo equations:[39,40]

$$I = 4n\mathrm{F}c^*Dr_\mathrm{e}f(\tau) \tag{1.44}$$

where c^* is the bulk concentration of electroactive species. r_e is the radius of the electrode. $f(\tau)$ is given by:

$$f(\tau) = 0.7854 + 0.8863\,\tau^{-0.5} + 0.2146\exp(-0.7823\,\tau^{-0.5}) \tag{1.45}$$

τ is the dimensionless time, defined as

$$\tau = 4Dtr_\mathrm{e}^{-2} \tag{1.46}$$

1.3 Conclusions

This chapter has provided a brief overview of the fundamentals of electrochemistry and electrochemical techniques. The contents of this chapter will be used in the interpretation of the results that will be presented from chapter 5 onwards. Having discussed the electrochemical methods, the next chapter will describe the principle of UV-visible spectrophotometry, which is another technique used in this thesis.

Bibliography

(1) Compton, R. G.; Sanders, G. H. W. *Electrode Potentials*; Oxford University Press, Oxford, UK, **1996**.
(2) Compton, R. G.; Banks, C. E. *Understanding Voltammetry*, 2nd ed.; Imperial College Press, London, UK, **2011**.
(3) Gamsjäger, H.; Lorimer, J. W.; Scharlin, P.; Shaw, D. G. *Pure Appl. Chem.* **2008**, *80*, 233-276.
(4) Nernst, W. *Ber. Deutsche. Chem.* **1897**, 1547.
(5) Fisher, A. C. *Electrode Dynamics*; Oxford University Press, Oxford, UK, **1996**.
(6) Eyring, H. *J. Chem. Phys.* **1935**, *3*, 107.
(7) Laidler, K. J. *J. Chem. Educ.* **1984**, *61*, 494-498.
(8) Guidelli, R.; Compton, R. G.; Feliu, J. M.; Gileadi, E.; Lipkowski, J.; Schmickler, W.; Trasatti, S. *Pure Appl. Chem.* **2014**, *86*, 245-258.
(9) Marcus, R. *J. Phys. Chem.* **1963**, *67*, 853-857.
(10) Butler, J. A. V. *Trans. Faraday Soc.* **1924**, *19*, 729-733.
(11) Butler, J. A. V. *Trans. Faraday Soc.* **1924**, *19*, 734-739.
(12) Agar, J. N. *Discuss. Faraday Soc.* **1947**, *1*, 26-37.
(13) Oldham, K. B.; Zoski, C. G. *Chapter 2 Mass Transport to Electrodes; in Comprehensive Chemical Kinetics;* Elsevier, **1986**, *26*, 79-143.
(14) Toh, H. S.; Batchelor-McAuley, C.; Tschulik, K.; Uhlemann, M.; Crossley, A.; Compton, R. G. *Nanoscale* **2013**, *5*, 4884-4893.
(15) Ward Jones, S. E.; Campbell, F. W.; Baron, R.; Xiao, L.; Compton, R. G. *J. Phys. Chem. C* **2008**, *112*, 17820-17827.
(16) Batley, G. E. *Mar. Chem.* **1983**, *12*, 107-117.
(17) Wang, J.; Lu, J.; Hocevar, S. B.; Farias, P. A. M.; Ogorevc, B. *Anal. Chem.* **2000**, *72*, 3218-3222.
(18) Dai, X.; Nekrassova, O.; Hyde, M. E.; Compton, R. G. *Anal. Chem.* **2004**, *76*, 5924-5929.
(19) Dickinson, E. J. F.; Limon-Petersen, J. G.; Rees, N. V.; Compton, R. G. *J. Phys. Chem. C* **2009**, *113*, 11157-11171.
(20) Albery, J. *Electrode kinetics*; Clarendon Press, Oxford, UK, **1975**.
(21) Novev, J. K.; Compton, R. G. *Curr. Opin. Electrochem.* **2018**, *7*, 118-129.
(22) Ngamchuea, K.; Eloul, S.; Tschulik, K.; Compton, R. G. *Anal. Chem.* **2015**, *87*, 7226-7234.
(23) Fick, A. *Ann. Phys. (Berlin, Ger.)* **1855**, *170*, 59-86.
(24) Fick, A. *Science* **1855**, *16*, 30.
(25) Bockris, J. *Modern Electrochemistry: An Introduction to An Interdisciplinary Area*; Springer, US, **2012**.
(26) Islam, M. *Phys. Scr.* **2004**, *70*, 120-125.
(27) Nicholson, R. S.; Shain, I. *Anal. Chem.* **1964**, *36*, 706-723.
(28) Nicholson, R. S.; Shain, I. *Anal. Chem.* **1965**, *37*, 178-190.
(29) Cinková, K.; Clark, M.; Sokolov, S. V.; Batchelor-McAuley, C.; Švorc, Ľ.; Compton, R. G. *Electroanalysis* **2017**, *29*, 1006-1013.
(30) Ngamchuea, K.; Eloul, S.; Tschulik, K.; Compton, R. G. *J. Solid State Electrochem.* **2014**, *18*, 3251-3257.
(31) Matsuda, H.; Ayabe, Y. *Z. Elektrochem* **1955**, *59*, 494-503.

(32) Mabbott, G. A. *J. Chem. Educ.* **1983**, *60*, 697-702.
(33) Bond, A. M.; Oldham, K. B.; Zoski, C. G. *J. Electroanal. Chem. Interfacial Electrochem.* **1988**, *245*, 71-104.
(34) Oldham, K. B.; Zoski, C. G. *J. Electroanal. Chem. Interfacial Electrochem.* **1988**, *256*, 11-19.
(35) Wightman, R. M. *Anal. Chem.* **2008**, *53*, 1125A-1134A.
(36) Bond, A. M.; Oldham, K. B.; Zoski, C. G. *Anal. Chim. Acta* **1989**, *216*, 177-230.
(37) Saito, Y. *Rev. Polarogr.* **1968**, *15*, 177-187.
(38) Cottrell, F. G. *Z. Phys. Chem.* **1902**, *42*, 385.
(39) Shoup, D.; Szabo, A. *J. Electroanal. Chem. Interfacial Electrochem.* **1982**, *140*, 237-245.
(40) Xiong, L.; Aldous, L.; Henstridge, M. C.; Compton, R. G. *Anal. Methods* **2012**, *4*, 371-376.

Chapter 2 Introduction to UV-visible spectrophotometry

This chapter describes the principles underlying UV-visible spectrophotometry. The technique allows the identification of analyte and the measurement of concentrations based on the absorption of electromagnetic radiation of the target species in the ultraviolet-visible spectral region (200 – 800 nm).

2.1 Properties of UV and visible radiation

Ultraviolet (UV) and visible radiation is a part of electromagnetic spectrum, which is described by both 'wave' and 'particle' properties, so called *wave-particle duality*.[1] That is, electromagnetic radiation can be considered as a wave of alternating electric and magnetic fields defined by frequency (f), wavelength (λ) and velocity (v) which are related by:[2]

$$f = \mathrm{v}/\lambda \tag{2.1}$$

At the same time, electromagnetic radiation can be considered as *photon*, a stream of zero rest mass particles or packages of radiation, with associated energy (E_{photon}) of

$$E_{\mathrm{photon}} = hf \tag{2.2}$$

where h is Planck's constant (6.626176×10^{-34} J s).

In the event of interaction between electromagnetic radiation and atomic or molecular levels, the radiation is more generally considered as photon, as described next.

2.2 Absorption of electromagnetic radiation

Electromagnetic radiation can interact with matter via various processes such as absorption, scattering and fluorescence (absorption and re-emission). In UV-visible spectrophotometry, only absorption plays a significant role. Scattering is negligible for atomic and molecular species significantly smaller than the wavelength of the radiation. Absorption of photons causes the energy of the atoms or molecules to increase, and the electrons promoted to higher energy states. As electrons can only occupy discrete energy levels in molecules, only photons of certain energy can be absorbed.[3] For radiation in the UV and visible range (λ = 200 - 800 nm), the transition typically involves bonding electrons i.e. transition between electronic states, for example, d-d transitions in transition metals or $\pi \rightarrow \pi^*$ transitions in molecular species.

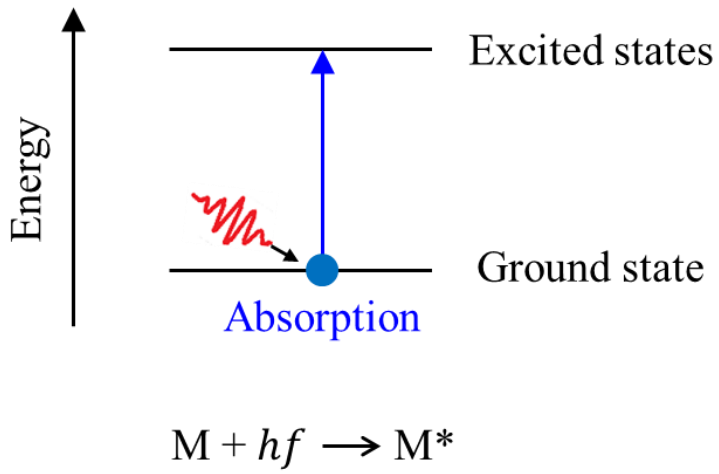


Figure 2.1: A diagram showing the absorption of radiation and the transition of electron from ground to excited state.

In the spectrophotometric measurement, the amount of radiation absorbed is determined from the difference in the intensities of the incident radiation (I_0) and the transmitted radiation

after passing through a sample ($I_{\text{transmitted}}$), refer to Figure 2.2. The relation of this change in intensities to concentration of the absorbing species is derived next.

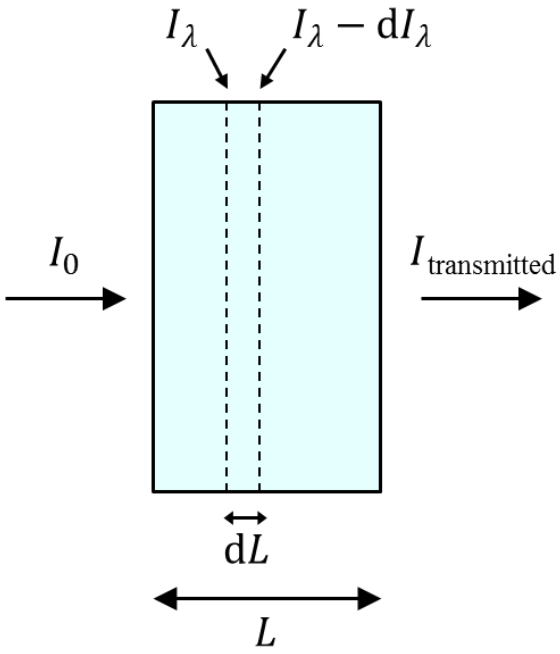


Figure 2.2: A diagram showing the path of the radiation and the intensities of radiation at different points in the sample

According to Figure 2.2, let I_λ be the intensity of a beam of monochromatic radiation of wavelength λ, and $\mathrm{d}I_\lambda$ be the change in its intensity after passing through a sample of thickness $\mathrm{d}L$. The rate of *decrease* (reflected as the *negative* sign in equation 2.3) in the intensity of radiation as it passes through the sample is proportional to the intensity of the incident radiation, as first suggested by Lambert.[4] As $\mathrm{d}L$ increases, the drop in the intensity ($\mathrm{d}I_\lambda$) becomes larger. The value of $\mathrm{d}I_\lambda$ can be determined from

$$\frac{\mathrm{d}I_\lambda}{I_\lambda} = -k'\mathrm{d}L \qquad (2.3)$$

where k' is a wavelength-dependent proportionality constant.

The total drop in intensity across all sample length L is determined from the integration of equation 2.3 in the range between 0 to L.

$$\int_{I_0}^{I_{\text{transmitted}}} \frac{\mathrm{d}I_\lambda}{I_\lambda} = -k' \int_0^L \mathrm{d}L \tag{2.4}$$

$$[\ln(I_\lambda)]_{I_0}^{I_{\text{transmitted}}} = -k'[L]_0^L \tag{2.5}$$

$$\ln \frac{I_{\text{transmitted}}}{I_0} = -k'L \tag{2.6}$$

$$\log_{10} \frac{I_0}{I_{\text{transmitted}}} = \frac{k'L}{2.303} \tag{2.7}$$

Similar to the dependence on the length of sample, the radiation intensity decreases exponentially with the number of absorbing molecules and hence concentration (c), as demonstrated by Beer:[4]

$$\log_{10} \frac{I_0}{I_{\text{transmitted}}} = \frac{k''c}{2.303} \tag{2.8}$$

where k'' is a wavelength-dependent proportionality constant.

By defining absorbance (Abs) as $\log_{10}(I_0/I_{\text{transmitted}})$, the combination of Beer's and Lambert's derivations yields the following *Beer-Lambert* law:[5]

$$Abs = \varepsilon Lc \tag{2.9}$$

where ε is the molar extinction coefficient (M^{-1} cm^{-1}). The parameter $I_{\text{transmitted}}/I_0$ is also known as transmittance. The Beer-Lambert law thus suggests that the amount of light absorbed, inversely proportional to the amount of light transmitted, is linearly dependent on the thickness and concentration of the absorbing species.

The Beer-Lambert law is generally true for sufficiently dilute solutions (typically <0.01 M).[6] Deviation from Beer-Lambert law is observed when the target species ionise, dissociate or form complexes in solutions at high concentrations. The relation between absorbance and concentration can thus become non-linear in concentrated solutions. The addition of small amount of electrolytes usually has no effects on the spectra, although at high concentrations, the electrolytes can shift the position of the spectral peaks or induce reactions of the analytes.[7]

2.3 Optical properties of nanoparticles

In addition to atomic and molecular species, UV-visible spectrophotometry can be extended to the characterisation of nanoparticles. This thesis will solely focus on *metallic* nanoparticles. Metal nanoparticles absorb and scatter light with extinction coefficients several orders of magnitude larger than other types of chromophores.[8] For example, the extinction coefficients of silver nanoparticles ($\varepsilon_{\mathrm{per\,NP}}$) are ~$10^8$ - 10^{11} M^{-1} cm^{-1},[9] compared with ~10^4 M^{-1} cm^{-1} of molecular dyes.[10,11]

The different optical properties of metal nanoparticles from that of the bulk metal can be explained by two phenomena. First is a *surface* effect. Atoms on the surface of a metal exhibit significantly different properties from atoms in the bulk due to the incomplete set of nearest neighbours (i.e. low coordination number). The surface area to volume ratios of nanoparticles are large and the ratios increase as the sizes of the particles decrease. The surface atoms therefore contribute significantly to the nanoparticle size-dependent properties. Second is the *quantum confinement* effect. Nanoparticles can be approximately described by a 'particle in a box' model. Due to the finite dimensions, the energies of the nanoparticles are quantized and electrons can only occupy discrete energy levels. For nanoparticles larger than

~2-3 nm, the nanoparticles are still metallic; that is, the band gap is smaller than the thermal energy ($k_B T$). At smaller sizes, such as quantum dots (not considered in this work), the particles become insulators/semi-conductors due to the gap between conduction and valence bands being larger than the thermal energy $k_B T$.[12]

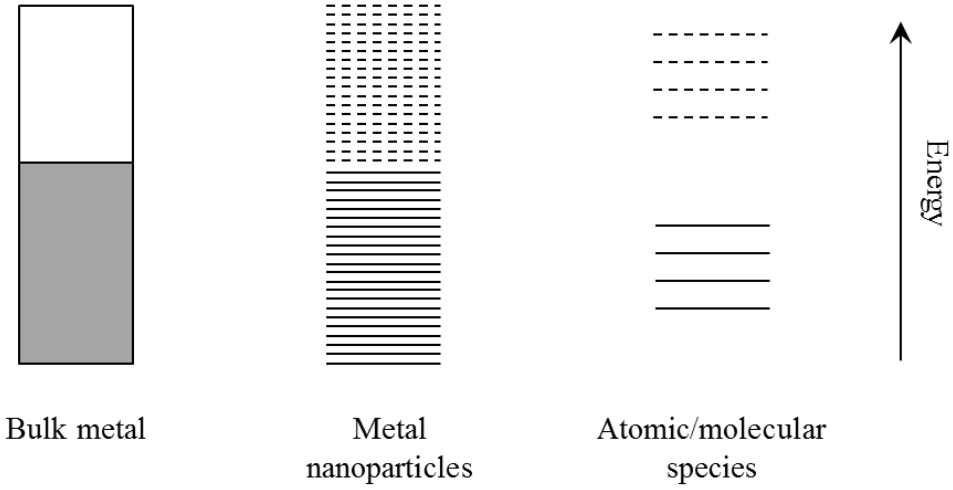


Figure 2.3: A diagram showing the energy levels of bulk metal, metal nanoparticles and atomic/molecular species.

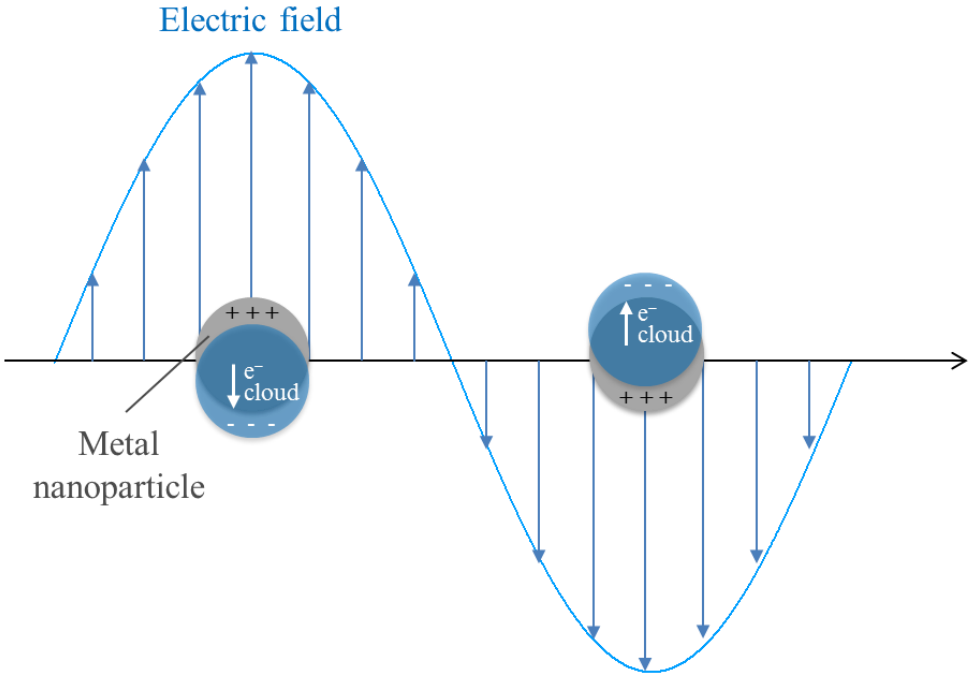


Figure 2.4: Surface plasmon resonance of spherical metal nanoparticles.

In the interaction with light, nanoparticles display strong *surface plasmon resonance*, refer to Figure 2.4. The electric field of the radiation induces free (conduction) electrons in the metal to oscillate coherently.[13] When the electron clouds move away from the core, the electrons are attracted to the positively charged nucleus by electrostatic force, causing the electron clouds to move back and forth leading to oscillations. The oscillation frequencies of metal nanoparticles such as gold and silver are often in the visible range, resulting in their red or yellow colours.[14]

UV-visible spectrophotometry has been used in the characterisation of a number of metallic nanoparticles.[15-17] The colours and extinction spectra of the nanoparticles are dependent upon the atomic constituents, size, shape, aggregation and the relative permittivity of the local environment.[14,18-21] The complete description of the extinction spectra of spherical particles is the solution of Maxwell's equations, which was first solved by Mie in 1908.[22] The full theoretical solution of Mie theory is beyond the scope of this work.

For spherical particles significantly smaller than the wavelength of the radiation, the electric field of the radiation can be approximated to be constant or static. Under the quasi-static approximation, the absorption (σ_{abs}) and scattering (σ_{scatt}) cross sections can be given by[23]

$$\sigma_{\text{abs}} = 4\pi k r^3 \text{Im}\left[\frac{\epsilon_{\text{in}}-\epsilon_{\text{out}}}{\epsilon_{\text{in}}+2\epsilon_{\text{out}}}\right] \tag{2.10}$$

$$\sigma_{\text{scatt}} = \frac{8}{3}\pi k^4 r^6 \left|\frac{\epsilon_{\text{in}}-\epsilon_{\text{out}}}{\epsilon_{\text{in}}+2\epsilon_{\text{out}}}\right|^2 \tag{2.11}$$

where r is the radius of the particle. ϵ_{in} and ϵ_{out} are the dielectric functions of the particle and the medium respectively. k is the wavevector in the medium:

$$k = \frac{2\pi}{\lambda} \tag{2.12}$$

where λ is the wavelength of the radiation.

The cross section is defined as the loss of energy from the incident optical flux due to absorption or scattering by the particle. The sum of σ_{abs} and σ_{scatt} gives the total extinction (attenuation) cross section, σ_{ext}:

$$\sigma_{\text{ext}} = \sigma_{\text{scatt}} + \sigma_{\text{abs}} \tag{2.13}$$

Note that σ_{abs} scales with r^3 ($\propto$ volume), while σ_{scatt} scales with r^6 ($\propto$ volume^2). The cross sections become zero if the nanoparticles and the medium are the same. For very small nanoparticles (< 2 nm), the effect of scattering is negligible.[24] For silver nanoparticles of size ~50 nm considered in this thesis, both scattering and absorption contribute to the extinction coefficient to the similar extents.[24]

To quantify the concentrations of nanoparticles by Beer-Lambert equation (eqn. 2.9), the value of molar extinction coefficient (ε_{ext}, M^{-1} cm^{-1}) is required. This quantity is related to σ_{ext} (cm^2) by:

$$\varepsilon_{\text{ext}} = \sigma_{\text{ext}} N \tag{2.14}$$

where N is the atomic number density (atoms cm^{-3}) of the particles.

The extinction coefficients of the nanoparticles ($\varepsilon_{\text{ext per NP}}$) are size-dependent. On the other hand, the extinction coefficients calculated on a per atom basis ($\varepsilon_{\text{ext per atom}}$) are constant, provided that the nanoparticles are no larger than ~50 nm diameter.[25]

The ε_{ext} on a per atom basis is related to $\varepsilon_{\text{ext per NP}}$ by

$$\varepsilon_{\text{ext per NP}} = \varepsilon_{\text{ext per atom}} \cdot \frac{4\pi r^3 \rho N_A}{3A_r} \tag{2.15}$$

where r is the radius of the nanoparticles, ρ and A_r are the density and atomic mass of the metal respectively. N_A is the Avogadro's number.

The Beer-Lambert plots of maximum absorbance against concentration of *silver atoms* gives the value of $\varepsilon_{\text{ext per atom}}$ of 15,300 ± 300 (Ag atom) M^{-1} cm^{-1}.[25] This value of $\varepsilon_{\text{ext per atom}}$ will be used later in the thesis in the characterisation of silver nanoparticles.

2.4 Instrumentation

Figure 2.5 displays the main components of a UV-visible spectrometer. The typical radiation sources of the UV-visible spectrometer, as also used in this thesis, are deuterium lamp (typically 190 - 390 nm) and halogen lamp (340 - 800 nm). The radiation from the sources is first passed through an entrance slit to improve the definition of the incident beam, and then passed through a prism to provide continuous spectrum which is dispersed in space. The radiation is then split into two equal beams passing through the test sample and the reference sample. The use of reference sample minimises the variation in the intensity of the radiation source, the absorption of radiation of the container (cuvette) and other variables. The radiation is then focused at the exit slit (where the required wavelength can also be isolated), passed through the sample, and reached the detector.[5]

2.5 Conclusions

The first two introductory chapters have described the fundamentals of the main techniques used in this thesis. These techniques will be employed in the development of saliva sensors and in the studies of silver nanoparticles in human saliva samples. The next chapter will provide a short review of salivary compounds, the biological functions of saliva and the use of saliva as a diagnostic fluid.

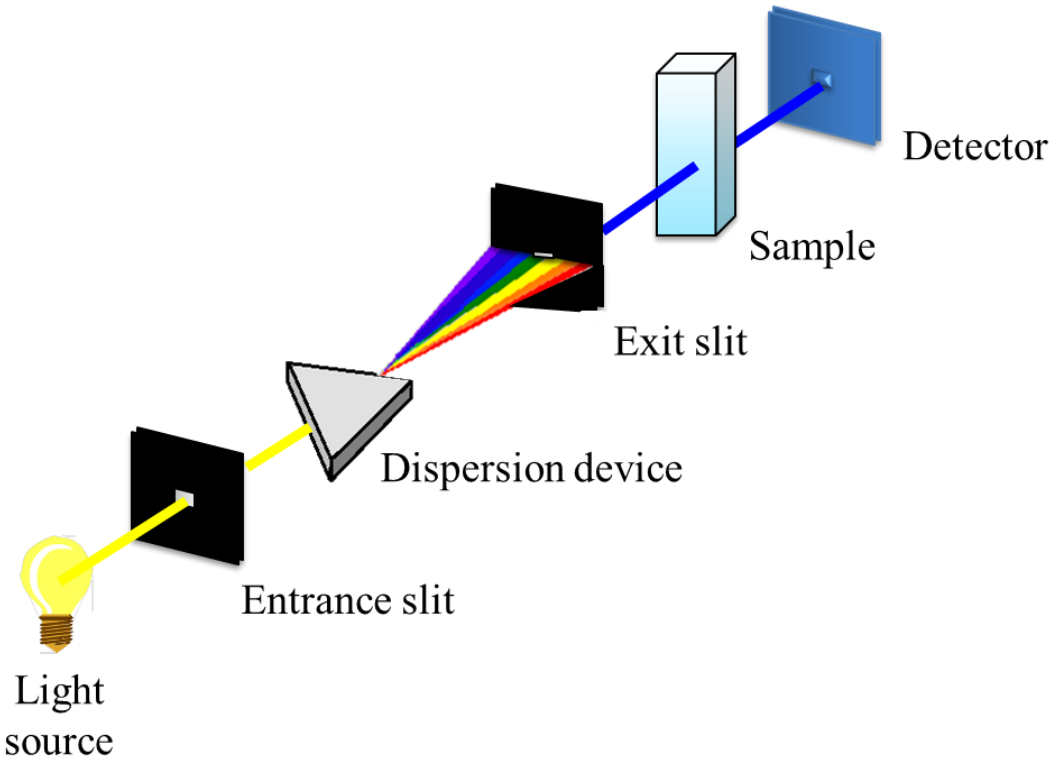


Figure 2.5: A diagram showing the main components of a UV-visible spectrometer

Bibliography

(1) Cassidy, D. C. *Ann. Phys. (Berlin, Ger.)* **2005**, *14*, 15-22.
(2) Atkins, P.; de Paula, J. *Atkins' Physical Chemistry*; Oxford University Press, Oxford, UK, **2010**.
(3) Einstein, A. *Ann. Phys. (Berlin, Ger.)* **1906**, *325*, 199-206.
(4) Ball, D. W. *The Basics of Spectroscopy*; SPIE- The International Society for Optical Engineering, Bellingham, USA, **2001**.
(5) Clark, B. J.; Frost, T.; Russell, M. A. *UV Spectroscopy: Techniques, Instrumentation and Data Handling*; Springer, Dordrecht, Netherlands, **1993**.
(6) Harris, D. C. *Quantitative Chemical Analysis, Sixth Edition*; W. H. Freeman and Company, New York, USA, **2003**.
(7) Vogel, A. *Textbook of Quantitative Chemical Analysis*; Pearson Education, London, UK, **2009**.
(8) Eustis, S.; el-Sayed, M. A. *Chem. Soc. Rev.* **2006**, *35*, 209-217.
(9) Paramelle, D.; Sadovoy, A.; Gorelik, S.; Free, P.; Hobley, J.; Fernig, D. G. *Analyst* **2014**, *139*, 4855-4861.
(10) Chen, H.; Huang, H.; Huang, X.; Clifford, J. N.; Forneli, A.; Palomares, E.; Zheng, X.; Zheng, L.; Wang, X.; Shen, P.; Zhao, B.; Tan, S. *J. Phys. Chem. C* **2010**, *114*, 3280-3286.
(11) Choi, H.; Raabe, I.; Kim, D.; Teocoli, F.; Kim, C.; Song, K.; Yum, J. H.; Ko, J.; Nazeeruddin, M. K.; Gratzel, M. *Chem. Eur. J.* **2010**, *16*, 1193-1201.
(12) Roduner, E. *Chem. Soc. Rev.* **2006**, *35*, 583-592.
(13) Kelly, K. L.; Coronado, E.; Zhao, L. L.; Schatz, G. C. *J. Phys. Chem. B* **2003**, *107*, 668-677.
(14) Creighton, J. A.; Eadon, D. G. *J. Chem. Soc., Faraday Trans.* **1991**, *87*, 3881-3891.
(15) Bhui, D. K.; Bar, H.; Sarkar, P.; Sahoo, G. P.; De, S. P.; Misra, A. *J. Mol. Liq.* **2009**, *145*, 33-37.
(16) Haiss, W.; Thanh, N. T.; Aveyard, J.; Fernig, D. G. *Anal. Chem.* **2007**, *79*, 4215-4221.
(17) Evanoff, D. D., Jr.; Chumanov, G. *ChemPhysChem* **2005**, *6*, 1221-1231.

(18) Burda, C.; Chen, X.; Narayanan, R.; El-Sayed, M. A. *Chem. Rev.* **2005**, *105*, 1025-1102.
(19) Hao, E.; Schatz, G. C.; Hupp, J. T. *J. Fluoresc.* **2004**, *14*, 331-341.
(20) Orendorff, C. J.; Sau, T. K.; Murphy, C. J. *Small* **2006**, *2*, 636-639.
(21) Noguez, C. *J. Phys. Chem. C* **2007**, *111*, 3806-3819.
(22) Mie, G. *Ann. Phys. (Berlin, Ger.)* **1908**, *330*, 377-445.
(23) Pelton, M.; Bryant, G. W. *Introduction to Metal-Nanoparticle Plasmonics*; Wiley, New Jersey, USA, **2013**.
(24) Evanoff, D. D.; Chumanov, G. *J. Phys. Chem. B* **2004**, *108*, 13957-13962.
(25) Ngamchuea, K.; Batchelor-McAuley, C.; Sokolov, S. V.; Compton, R. G. *Anal. Chem.* **2017**, *89*, 10208-10215.

Chapter 3 Introduction to saliva and salivary biomarkers

Saliva testing offers advantages over blood analysis due to its non-invasive nature, the ease of collection, storage and shipment of specimens, as well as the possibility of collecting multiple samples. Compared with other non-invasive procedures, saliva overcomes the problems of intrusion of privacy of urine and limited access to sweat and tears. Areas where saliva biomarkers may become particularly advantageous include point-of-care analysis, mass detection, epidemiologic surveillance, situations where the sample volume is limited e.g. in newborn babies and cases where self-monitoring may be desirable. For example in psychiatry, most diseases have persistent life-long symptoms and long-term monitoring is needed. Many neurological disorders can currently be assessed by behaviour observations as definitive causes and molecular markers are not known. Saliva tests may be able to offer alternative methods to aid the diagnosis of such diseases and disorders. Other potential uses of saliva are the detection of drugs of abuse and doping substances in forensics and sports.

This chapter gives a short description of the functions of saliva and how salivary components play important roles in maintaining the normal functions of the body. Details of saliva composition and available recipes for synthetic saliva are further provided. The chapter then summarises the existing diagnostic uses of salivary biomarkers and any correlation with blood plasma and other bodily fluids.

This chapter is part of the review article published in *Analyst*.[1]

3.1 Functions of saliva

There are five major functions of saliva: lubrication and protection, buffering, maintaining tooth integrity, antibacterial activity, and taste and digestion.[2] *"Lubrication and protection"*: the lubricating compounds in saliva such as mucins (complex protein molecules) protect the oral tissues against irritating agents and helps with mastication, speech, and swallowing processes.[3] "*Buffering"* maintains the pH of saliva to a normal range of 6.7 - 7.3 by three major components: bicarbonate, phosphate, and protein buffers.[4] Enzymes such as carbonic anhydrase also participate in controlling the pH of saliva.[5] The third main function of saliva is *"maintaining tooth integrity,"* by balancing demineralization and remineralization processes. The former happens when acids diffuse into the enamel and cause crystalline dissolution, usually at pH below 5.5. The minerals in the tooth structure may be recovered by remineralization of ions dissolved in the saliva.[6] *"Antibacterial activity"* is another important function of saliva. Several proteins in saliva such as immunoglobulin A (IgA) can neutralize bacterial products such as enzymes and toxins, and hence act as anti-bacterial agents. For *"taste and digestion"*, the main roles of saliva are the transport of taste substances and the protection of taste receptors.[7] The salivary enzyme amylase also plays a role in the digestion of carbohydrates.[8]

3.2 Components of human saliva and synthetic saliva recipes

Saliva is a complex bodily fluid consisting of ca. 99% water, inorganic and organic substances and a variety of proteins such as enzymes, mucus and glycoproteins.[9] It is secreted by three major pairs of salivary glands and other minor mucous glands surrounded by capillaries.[10] Many blood components enter saliva via either active transport requiring chemical energy from adenosine triphosphate (ATP) or passive diffusion (no energy required;

movement down a concentration gradient) through cell membranes. Accordingly, the presence, or the change in concentrations, of salivary components may be used in the diagnosis of diseases and the analysis of the state of health. Examples of commercial uses of saliva tests include HIV detection and steroid hormone monitoring.

The compositions of saliva vary during the day and between individuals.[11] Attempts to report saliva constituents and concentrations mainly use average compositions that can be found in healthy subjects. Components of authentic human saliva and the comparison of the normal concentration ranges between saliva and other biological fluids are summarised in Table 3.1. Briefly, saliva is composed of a variety of ions including sodium, potassium, calcium, bicarbonate, thiocyanate and phosphate. Also found in saliva are low molecular weight organic substances such as uric acid and lactate, immunoglobulins, enzymes, mucins and some important hormones such as cortisol. The viscosity of human whole saliva is ca. 1.30 relative to distilled water.[12]

In research studies such as in the initial development of chemical sensors, the use of a large amount of saliva is required. Accordingly, synthetic saliva was developed for use in such *in-vitro* studies. Synthetic saliva is further used in the treatment of dry mouth symptoms.[13] Table 3.2 presents examples of synthetic saliva recipes. Some of these formulae contain exclusively inorganic compounds,[14-18] while some further include organic components and proteins.[19,20] The composition of synthetic saliva is designed to mimic the average composition of human saliva. These recipes have been employed in the studies of electrochemical behaviour and corrosion resistance of materials in dental applications.[14-18]

Table 3.1 Components of authentic human saliva and the comparison of normal concentration ranges between saliva and other biological fluids

Authentic saliva compositions		Normal range		Ref
		Saliva	Other biological fluids	
1. Inorganic species	Na^+	20 – 80 mM	Plasma 145 mM	11
	K^+	20 mM	4 mM	
	Ca^{2+}	1 – 4 mM	2.2 mM	
	Cl^-	30 – 100 mM	120 mM	
	HCO_3^-	15 – 80 mM	25 mM	
	Phosphate	4 mM	1.2 mM	
	Mg^{2+}	0.2 mM	1.2 mM	
	SCN^-	2 mM	< 0.2 mM	
	NH_3	3 mM	0.05 mM	
2. Organic compounds (non-protein and lipids)	Uric acid	3.38 ± 0.21 mg/dL	Serum 6.31 ± 0.24 mg/dL	21-23
		217.2 ± 110.3 µM		
		0.1 – 7.5 mg/dL		
	Bilirubin	0.5 – 5.0 µM	Serum 0.2 – 1.2 mg/dL	24
	Creatinine	0.12 ± 0.06 mg/dL	Serum 0.89 ± 0.17 mg/dL	25
		0.05 – 0.2 mg/dL	Serum 0.6 – 1.5 mg/dL	
	Glucose	4 – 13 mg/dL	Blood 80 – 120 mg/dL	22,26
			Blood 88.6 ± 8.0 mg/dL	
	Cholesterol	0.02 – 5.46 µM	Serum <5 mM	27

	Lactate	0.3 – 1.8 mM	Serum 0.5 – 1.0 mM	[28,29]
		0.1 – 2.5 mM		
3. Protein/Polypeptide compounds	α-Amylase	19 – 308 U/mL*	Serum 0.05 – 0.125 U/mL*	[23,30]
		93 ± 62 U/L *		
		2.64 ± 1.8 mg/mL		
	Albumin	0.2 ± 0.1 mg/mL	Serum 3.5 – 5.5 g/dL	[31]
	Secretory-IgA	80 – 717 mg/dL	Serum 70 – 400 mg/dL	[23,32]
		124.3 – 333.5 µg/mL		
	Mucins group	1.19 ± 0.17 mg/mL	Serum 9.9 ± 0.8 ng/ml	[31,33]
	Lysozyme	3 – 50 µg/mL	Serum 7.4 ± 1.8 mg/mL	[23,32,34]
		59.7 – 1062.3 µg/ml	Serum 4 – 9 µg/mL	
	Total proteins	7.1 – 223.2 mg/dL	Serum 6 – 8 g/dL	[23,31]
		0.9 ± 0.2 mg/mL		
4. Hormones	Cortisol (unbound)	0.99 ± 0.42 µg/dL	Serum 1.56 ± 0.54 µg/dL	[35]
	Testosterone	32 – 55 pg/mL	Serum 320 – 600 ng/dL	[36]
	Progesterone (unbound)	Proliferative phase 126.8 ± 6.9 pg/mL	Plasma proliferative phase 88.5 ± 11.2 pg/mL	[37]
		Secretory phase 196.8 ± 18.8 pg/mL	Plasma secretory phase 332.2 ± 39.2 pg/mL	

* U/mL refers to Somogyi's unit/mL, a measure of the level of the activity of amylase. One Somogyi's unit is defined as the amount of amylase required to produce the equivalent of 1 mg of glucose when acting on a standard starch solution in 30 minutes incubation time at 40°C.[38]

Table 3.2 Compositions of different synthetic saliva recipes

Synthetic saliva compositions		Concentration (g/L)				
		AFNOR [14,15]	**Fusayama -Meyer** [16]	**SAGF** [17,18]	**Klimek** [19]	**Shellis** [20]
1. Inorganic compounds	NaCl	6.70	0.40	0.13	0.58	-
	KCl	1.20	0.40	0.96	1.27	1.16
	Na_2HPO_4	0.26	-	-	0.34	0.375
	KH_2PO_4	0.20	-	0.66	0.33	0.35
	$NaHCO_3$	1.50	0.10	0.63	-	0.54
	KSCN	0.33	-	0.19	0.16 (NaSCN)	0.22
	$CaCl_2.2H_2O$	-	0.69	0.23	0.17	0.21
	$Na_2S.9H_2O$	-	0.005	-	-	-
	Urea	-	1.00	0.20	0.20	0.17
	$NaH_2PO_4.H_2O$	-	0.69	-	-	-
	NH_4Cl	-	-	-	0.16	0.233
	$Na_2SO_4.10H_2O$	-	-	0.76	-	-
	$MgCl_2.6H_2O$	-	-	-	-	0.043
	Sodium citrate	-	-	-	-	0.013
2. Organic compounds	Ascorbic acid	-	-	-	0.002	-
	Glucose	-	-	-	0.03	-
	Uric acid	-	-	-	-	0.0105
	Creatinine	-	-	-	-	0.0001

	Choline	-	-	-	-	0.013
	Mixture of vitamins	-	-	-	-	0.0008
3. Protein/Polypeptide compounds	Mucin	-	-	-	2.70	-
	Glycoprotein	-	-	-	-	2.5
	α-Amylase	-	-	-	-	300 U/mL*
	Albumin	-	-	-	-	0.025
	Mixture of amino acids	-	-	-	-	0.041

* U/mL refers to Somogyi's unit/mL, a measure of the level of the activity of amylase. One Somogyi's unit is defined as the amount of amylase required to produce the equivalent of 1 mg of glucose when acting on a standard starch solution in 30 minutes incubation time at 40°C.[38]

3.3 Biomarkers in saliva – what correlations exist, do not exist

Biomarkers may be classified into three different categories based on their origins and mechanisms of action: exposure, effect (response) and susceptibility.[39] Any substances coming or arising from a source outside the organism or cell are referred to as 'exposure.' 'Effect' is a change in a biological system corresponding to impairment in the organism or cell, and is potentially related to diseases. The ability of the system to defend itself from toxic events is known as 'susceptibility.' For example, antioxidants reflect a type of susceptibility that responds to reactive oxidising species and prevents oxidation processes that may otherwise damage important organisms or cells.

A compound, ion or metabolite is considered a good biomarker when it is representative of a *specific* condition of the target cell, disease or the health state of an individual. In other words, it should not be affected by other factors unrelated to the disease or condition under studies. For ease of detection, biomarkers should be present and measurable in samples which can be readily collected, and easily processed and stored. The concentrations of the biomarker in the normal control population should be well-examined and preferably invariant in the control group such that any small change can be detected with reliability.[39]

Prior to diagnostic use, the applicability of the biomarkers for a specific disease has to be validated. Ideally, the aetiology of the disease - that is the mechanisms by which the biomarker takes part in the development of diseases or the action of the biomarker during the diseases - should be understood. However, the mechanistic detail is often unknown or not adequately known. Hence, the relevance of the biomarker to a specific disease has to be investigated based on a statistical model.[40]

The potential of a salivary component as a biomarker may be evaluated by the correlation of the presence/absence or the concentrations of the biomarker in saliva samples between a control population and the patients. Additionally, it is recommended that the correlation between matched blood plasma and saliva samples is investigated alongside the correlation with diseases.[41,42]

Hitherto, the potential of salivary inorganic constituents, anti-oxidants, hormones, antibodies and antigens as biomarkers in the diagnosis of several oral and systemic diseases have been recognized. In oral diseases, saliva has been used to detect oral cavity cancer, dental caries, periodontal disease and oral dryness; see Table 3.3. In systemic diseases (i.e. diseases that affect the entire body), saliva has been demonstrated to have strong correlations with plasma or serum for many cell components, and hence can act as a mirror reflecting the health states

of the body.[43] Examples of reported uses of saliva in systemic conditions, diseases, disorders and infections include the monitoring of hormone levels, pregnancy, risks for preterm labour, psychological disorders, neurological disorders, the condition of the immune system, smoking status, virus infections and nutritional status (Table 3.3).

It has also been shown that therapeutic drugs and drugs of abuse can be detected in saliva, the levels of which exhibit strong correlations with those in plasma or serum. In addition to providing an alternative choice of specimen for drug monitoring, the ability to detect therapeutic drugs in saliva allows the studies of pharmacokinetics and facilitates individualisation of pharmacotherapy as multiple non-invasive saliva samples can be readily collected. The saliva tests of drugs of abuse and prohibited doping substances provide convenient, accessible and lower cost methods for vehicle checkpoints, quarantine stations, sport competitions and in other screening tests. Table 3.3 provides examples of the current diagnostic uses of salivary biomarkers, together with any *correlations* with serum, plasma and other bodily fluids.

Note that the correlation between two sets of data may be determined by the Pearson correlation coefficient (r) and/or the p-value (p). The former measures the linear relationship between two random variables.[44] The positive value of r means that when the value of one parameter increases, it is likely the value of the other parameter will also increase. The higher magnitude of r ($|r| \leq 1$), the greater probability that this is true. For example, $r = 0$: no correlation, $r = +0.5$: moderately positive correlation, $r = +0.8$: strong positive correlation and $r = +1$: perfectly positive correlation. In Table 3.3, all correlations presented refer to positive correlations. Alternatively, the correlation may be assessed by the p-value which is based on hypothesis testing.[45,46] First, a null hypothesis (H_0) is assumed. For example in the correlation studies, the null hypothesis is that there is no correlation between the two sets of data. The p-

value quantifies the possibility that the null hypothesis is true. The lower the p-value, the more likely we can reject the null hypothesis. If p-value is smaller than the designated significant level (α) of usually 0.05, H_0 is rejected with less than 5% chance that this is the incorrect rejection of H_0. In other words, usually when $p < 0.05$, the correlation is considered to be statistically significant. Note the difference between *strong* correlation which is based on '*r*' and *significant* correlation which is based on '*p.*'

Table 3.3 Examples of the diagnostic uses of salivary biomarkers and their correlations with blood plasma, serum and other bodily fluids

Biomarker	Diagnostic use	Bodily fluid	Correlation	Detection method	Ref
Chemicals					
Cotinine	cigarette usage	saliva / plasma	strong correlation (*r*=0.99)	GC	[47]
	cigarette usage	saliva / serum	strong correlation	HPLC/ MS	[48]
Nicotine	cigarette usage	saliva / urine	-	single-drop microextraction / GC-FID	[49]
	nicotine skin patch users	saliva / plasma	strong correlation (*r*=0.82)	-	[50]
Anabasine	cigarette usage	saliva / urine	-	single-drop microextraction / GC-FID	[49]
Nitrates and nitrites	gastric cancer	saliva	-	colorimetric	[51]
	periodontal disease	saliva	-	colorimetric	[52]

Biomarker	Diagnostic use	Bodily fluid	Correlation	Detection method	Ref
Caffeine	caffeine clearance: liver function	saliva / serum	strong correlation (r>0.98)	enzyme immunoassay	[53]
	probe for CYP1A2	saliva / plasma /urine	strong correlation with plasma (r=0.97)	-	[54]
	drug monitoring	saliva / plasma	strong correlation (r=0.98)	HPLC	[55,56]
SCN^-	smoking status	saliva / plasma / urine	-	colorimetric	[57]
	cystic fibrosis	saliva	-	colorimetric	[58]
Anti-oxidants					
Glutathione (GSH, GSSG)	head and neck squamous cell carcinoma (GSH)	saliva	-	HPLC	[59]
	oral squamous cell carcinoma (GSH)	saliva	-	colorimetric	[60]
	health monitoring (GSH + GSSG)	saliva / whole blood	weak correlation (r=0.43)	colorimetric	[61]
	diabetic / parenteral drug addict (GSH, GSSG)	saliva	-	fluorometric	[62]
Ascorbic acid	correlation studies	saliva / plasma / white blood cell (WBC)	significant correlation with WBC (p<0.001)	-	[63]

Biomarker	Diagnostic use	Bodily fluid	Correlation	Detection method	Ref
Uric acid	oral cavity cancer	saliva	-	colorimetric	64
	gout	saliva / blood	-	colorimetric	65
	diabetes	saliva / serum	-	colorimetric	66
	metabolic syndrome	saliva	-	colorimetric	67
Therapeutic drugs					
Anticonvulsants / antiepileptic	drug monitoring	saliva / plasma	strong correlation	GLC, immunoassay	68-70
	drug monitoring	saliva / plasma / cerebrospinal fluid	strong correlation	GC-FID	71
Theophylline	drug monitoring	saliva / plasma	strong correlation (r>0.9)	HPLC, immunoassay	72-74
	drug monitoring	saliva / plasma	strong correlation (r>0.88)	immunoassay	75
Acetaminophen (paracetamol)	drug monitoring	saliva / plasma	strong correlation (r=0.95)	colorimetric	76
Lithium	drug monitoring	saliva / serum	strong correlation (r=0.83)	-	77
	drug monitoring	saliva / plasma / RBC	strong correlation	flame photometry	78

Biomarker	Diagnostic use	Bodily fluid	Correlation	Detection method	Ref
Drugs of abuse					
Ethanol	drug monitoring	saliva / serum, whole blood / urine	strong correlation	GC-FID, colorimetric	[79-82]
Cocaine	drug monitoring	saliva / plasma	significant correlation ($p \leq 0.05$)	-	[83,84]
Heroin	drug monitoring	saliva / plasma	-	GC-MS, immunoassay	[85-87]
Marijuana	drug monitoring	saliva	-	fluorometric, immunoassay	[88,89]
Prohibited doping substances					
Amphetamine, metham-phetamine, etc.*	detection	saliva / urine	-	GC-MS	[90]
Hormones					
Cortisol	chronic fatigue syndrome, depression	saliva / plasma	strong correlation	immunoassay	[91, 92]
	evaluation of adrenal function	saliva / plasma / serum	strong correlation	immunoassay	[93,94]
	correlation studies	saliva / serum	strong correlation (r=0.89)	immunoassay	[35]
Aldosterone	correlation studies	saliva / plasma	strong correlation (r=0.84,[95] 0.93[96])	dialysis, immunoassay	[95]

Biomarker	Diagnostic use	Bodily fluid	Correlation	Detection method	Ref
Testosterone	correlation studies	saliva / plasma	strong correlation (r>0.7)	dialysis, immunoassay	97,98
	correlation studies	saliva / serum	strong correlation (r>0.8)	immunoassay	99,100
17-hydroxyprotesterone	assessing endocrine function	saliva / plasma / parotid fluid	strong correlations (r>0.9)	immunoassay	101
	21-Hydroxylase deficiency	saliva / serum	strong correlation (r=0.93)	immunoassay	102
Progesterone	correlation during late pregnancy	saliva / serum	weak correlation	immunoassay	103
	correlation during the menstrual cycle	saliva / plasma	significant correlation (r=0.58, p=0.001)	-	37
Estradiol	correlation studies in postmenopausal women	saliva / serum	strong correlation in users on estrogen therapy (r=0.81)	immunoassay	104
	monitoring follicular stimulation	saliva / serum	strong correlation (r=0.77)	immunoassay	105
Estriol	correlation during normal pregnancy	saliva / plasma	strong correlation (r≥0.79)	-	106,107

Biomarker	Diagnostic use	Bodily fluid	Correlation	Detection method	Ref
Estriol (continued)	correlation during third trimester pregnancy	saliva / serum	strong correlation (r=0.99)	immunoassay	[108]
Insulin	normal and Type I diabetic subjects	saliva / serum	strong correlation (r=0.81)	immunoassay	[109]
Melatonin	correlation studies	saliva / serum	strong correlation (r=0.95,[110] r=0.81[111])	immunoassay	[110,111]
	circadian phase marker	saliva / plasma	strong correlation of time of onset (r=0.70)	immunoassay	[112]
Antibodies / Antigens					
HIV antibody	HIV infection	saliva / serum		immunoassay	[113,114]
Immunoglobulin A (IgA)	systemic sicca syndrome and rheumatoid arthritis	saliva / serum	strong correlation ($p<0.001$)	immunoassay	[115]
pH					
pH	dental caries	saliva	-	-	[116]

* Prohibited doping substances that have been demonstrated to be detectable in saliva include amphetamine, metham-phetamine, norselegiline, ephedrine / norephedrine, ephedrine-d3, selegiline, pentetrazol, crotetamide, cropropamide, sibutramine, codeine / dihydrocodeine, modafinil, ISTD1, cocaina, cocaine-d3, BEG, BEG-d3, EME, EME-d3.[90]

Detection methods:

FID: flame ionisation detector, GC: gas chromatography, GLC: gas-liquid chromatography, HPLC: high performance liquid chromatography, MS: mass spectrometry

3.4 Potential problems of measurements in saliva

Saliva is a viscous fluid due to the presence of mucopolysaccharides and mucoproteins. The difficulty in measuring precise volumes of viscous saliva samples can decrease the accuracy of analytical measurements. Importantly, most potential biomarkers are present in saliva at low concentrations. Any error in volume may give rise to large errors in the concentrations measured. Due to the low concentrations, assays with high sensitivity and low limit of detection are required, in addition to high selectivity and specificity.

The components of saliva may depend on the area in the oral cavity in which the sample is collected as well as the collection methods (unstimulated vs. stimulated). If stimulation is used, the effects of the collection tools (e.g. cotton pads, polyester swabs, paraffin wax) and/or the chemicals (e.g. citric acid) have to be carefully assessed; the significance of this will be demonstrated in Chapter 8. Oral diseases such as gingivitis, the change in pH and other potential interferences such as smoking, fasting and hydration level can also influence the levels of the biomarkers of interest.[117]

There are relatively large variations in metabolite concentrations between different individuals. Calcium and phosphate concentrations in unstimulated whole saliva vary significantly between individuals (ca. 4-fold and 6-fold ranges of calcium and phosphate concentrations respectively) although the samples are collected at the same time of the day and have similar pH and buffer capacity.[118] The marked inter-individual variation is likely because many salivary components play multifunctional roles and in some cases, have overlapping functions.[119] For example, glutathione, ascorbic acid and uric acid are all antioxidants. Amylases, cystatins, histatins, mucins and peroxidases are all involved in anti-bacterial activity in the oral cavity. Diurnal fluctuation, seasons (temperature) and other intra-

individual inconsistency may also have to be considered. Accordingly, single salivary analysis could be unreliable. Multiple saliva samples and follow-up tests are desirable.

3.5 Conclusions

Saliva contains various potential biomarkers that exhibit strong correlations with the concentrations in blood plasma or serum. The use of saliva as a diagnostic fluid however has to date been relatively limited. This thesis thus focuses on the development of chemical sensors for the detection of these biomarkers as well as studies the spectrophotometric and electrochemical behaviours of several redox species in *authentic* saliva samples.

Bibliography

(1) Ngamchuea, K.; Chaisiwamongkhol, K.; Batchelor-McAuley, C.; Compton, R. G. *Analyst* **2018**, *143*, 81-99.
(2) Kaplan, M. D.; Baum, B. J. *Dysphagia* **1993**, *8*, 225-229.
(3) Slomiany, B. L.; Murty, V. L. N.; Piotrowski, J.; Slomiany, A. *Gen. Pharmacol.* **1996**, *27*, 761-771.
(4) Bardow, A.; Moe, D.; Nyvad, B.; Nauntofte, B. *Arch. Oral Biol.* **2000**, *45*, 1-12.
(5) Kivelä, J.; Parkkila, S.; Parkkila, A.-K.; Leinonen, J.; Rajaniemi, H. *J. Physiol.* **1999**, *520*, 315-320.
(6) Manjunatha, B. S. *Textbook of Dental Anatomy and Oral Physiology*, JP Medical Ltd, New Delhi, India, **2012**.
(7) Mese, H.; Matsuo, R. *J. Oral Rehabil.* **2007**, *34*, 711-723.
(8) Moss, S. J. *J. Esthet. Restor. Dent.* **1995**, *7*, 197-203.
(9) de Almeida Pdel, V.; Gregio, A. M.; Machado, M. A.; de Lima, A. A.; Azevedo, L. R. *J. Contemp. Dent. Pract.* **2008**, *9*, 72-80.
(10) Chicharro, J. L.; Lucía, A.; Pérez, M.; Vaquero, A. F.; Ureña, R. *Sports Med.* **2012**, *26*, 17-27.
(11) Aps, J. K. M.; Martens, L. C. *Forensic Sci. Int.* **2005**, *150*, 119-131.
(12) NordbÖ, H.; Darwish, S.; Bhatnagar, R. S. *Eur. J. Oral Sci.* **1984**, *92*, 306-314.
(13) Silvestre, F. J.; Minguez, M. P.; Sune-Negre, J. M. *Med. Oral Patol. Oral Cir. Bucal.* **2009**, *14*, E8-E11.
(14) Elagli, K.; Traisnel, M.; Hildebrand, H. F. *Electrochim. Acta* **1993**, *38*, 1769-1774.
(15) Giacomelli, F. C.; Giacomelli, C.; Spinelli, A. *J. Braz. Chem. Soc.* **2004**, *15*, 541-547.
(16) Meyer, J.-M. *Corros. Sci.* **1977**, *17*, 971-982.
(17) Levallois, B.; Fovet, Y.; Lapeyre, L.; Gal, J. Y. *Dent. Mater.* **1998**, *14*, 441-447.
(18) Gal, J.-Y.; Fovet, Y.; Adib-Yadzi, M. *Talanta* **2001**, *53*, 1103-1115.
(19) Klimek, J.; Hellwig, E.; Ahrens, G. *Caries Res.* **1982**, *16*, 156-161.
(20) Shellis, R. P. *Arch. Oral Biol.* **1978**, *23*, 485-489.
(21) Shibasaki, K.; Kimura, M.; Ikarashi, R.; Yamaguchi, A.; Watanabe, T. *Metabolomics* **2012**, *8*, 484-491.
(22) Soukup, M.; Biesiada, I.; Henderson, A.; Idowu, B.; Rodeback, D.; Ridpath, L.; Bridges, E. G.; Nazar, A. M.; Bridges, K. G. *Diabetol. Metab. Syndr.* **2012**, *4*, 14-14.
(23) Hershkovich, O.; Nagler, R. M. *Arch. Oral Biol.* **2004**, *49*, 515-522.
(24) De Corso, E.; Baroni, S.; Agostino, S.; Cammarota, G.; Mascagna, G.; Mannocci, A.; Rigante, M.; Galli, J. *Ann. Surg.* **2007**, *245*, 880-885.
(25) Venkatapathy, R.; Govindarajan, V.; Oza, N.; Parameswaran, S.; Pennagaram Dhanasekaran, B.; Prashad, K. V. *Int. J. Nephrol.* **2014**, *2014*, 6.
(26) Kumar, S.; Padmashree, S.; Jayalekshmi, R. *Contemp. Clin. Dent.* **2014**, *5*, 312-317.
(27) Karjalainen, S.; Sewón, L.; Soderling, E.; Larsson, B.; Johansson, I.; Simell, O.; Lapinleimu, H.; Seppänen, R. *J. Dent. Res.* **1997**, *76*, 1637-1643.

(28) Segura, R.; Javierre, C.; Ventura, J. L.; Lizarraga, M. A.; Campos, B.; Garrido, E. *Br. J. Sports Med.* **1996**, *30*, 305-309.
(29) Schabmueller, C. G. J.; Loppow, D.; Piechotta, G.; Schütze, B.; Albers, J.; Hintsche, R. *Biosens. Bioelectron.* **2006**, *21*, 1770-1776.
(30) Mandel, A. L.; Peyrot des Gachons, C.; Plank, K. L.; Alarcon, S.; Breslin, P. A. S. *PLoS One* **2010**, *5*, e13352.
(31) Almståhl, A.; Wikström, M.; Groenink, J. *Oral Microbiol. Immunol.* **2001**, *16*, 345-352.
(32) Ng, V.; Koh, D.; Fu, Q.; Chia, S.-E. *Clin. Chim. Acta* **2003**, *338*, 131-134.
(33) Kejriwal, S.; Bhandary, R.; Thomas, B.; Kumari, S. *J. Clin. Diagn. Res.* **2014**, *8*, ZC56-ZC60.
(34) Tomita, H.; Sato, S.; Matsuda, R.; Sugiura, Y.; Kawaguchi, H.; Niimi, T.; Yoshida, S.; Morishita, M. *Lung* **1999**, *177*, 161-167.
(35) Teruhisa, U.; Ryoji, H.; Taisuke, I.; Tatsuya, S.; Fumihiro, M.; Tatsuo, S. *Clin. Chim. Acta* **1981**, *110*, 245-253.
(36) Yasuda, M.; Honma, S.; Furuya, K.; Yoshii, T.; Kamiyama, Y.; Ide, H.; Muto, S.; Horie, S. *J. Mens Health* **2008**, *5*, 56-63.
(37) Choe, J. K.; Khan-Dawood, F. S.; Yusoff-Dawood, M. *Am. J. Obstet. Gynecol.* **1983**, *147*, 557-562.
(38) Somogyi, M. *J. Biol. Chem.* **1938**, *125*, 399-414.
(39) Silbergeld, E. K. *Ann. N.Y. Acad. Sci.* **1993**, *694*, 62-71.
(40) Read, G. F. *Ann. N.Y. Acad. Sci.* **1993**, *694*, 146-160.
(41) Villiger, M.; Stoop, R.; Vetsch, T.; Hohenauer, E.; Pini, M.; Clarys, P.; Pereira, F.; Clijsen, R. *Eur. J. Clin. Nutr.* **2018**, *72*, 69-76.
(42) Williamson, S.; Munro, C.; Pickler, R.; Grap, M. J.; Elswick, R. K., Jr. *Nurs. Res. Pract.* **2012**, *2012*, 246178.
(43) Mandel, I. D. *Ann. N.Y. Acad. Sci.* **1993**, *694*, 1-10.
(44) Zou, K. H.; Tuncali, K.; Silverman, S. G. *Radiology* **2003**, *227*, 617-622.
(45) Lang, T. A.; Secic, M. *How to Report Statistics in Medicine: Annotated Guidelines for Authors, Editors, and Reviewers*, American College of Physicians, Pennsylvania, USA, **2006**.
(46) Ramachandran, K. M.; Tsokos, C. P. *Mathematical Statistics with Applications*, Elsevier Science, New York, USA, **2009**.
(47) Jarvis, M.; Primatesta, P.; Erens, B.; Feyerabend, C.; Bryant, A. *Nicotine Tobacco Res.* **2003**, *5*, 349-355.
(48) Bernert, J. T.; McGuffey, J. E.; Morrison, M. A.; Pirkle, J. L. *J. Anal. Toxicol.* **2000**, *24*, 333-339.
(49) Kardani, F.; Daneshfar, A.; Sahrai, R. *J. Chromatogr. B Analyt. Technol. Biomed. Life Sci.* **2010**, *878*, 2857-2862.
(50) Rose, J. E.; Levin, E. D.; Benowitz, N. *Ther. Drug Monit.* **1993**, *15*, 431-435.
(51) Forman, D.; Al-Dabbagh, S.; Doll, R. *Nature* **1985**, *313*, 620-625.
(52) Sanchez, G. A.; Miozza, V. A.; Delgado, A.; Busch, L. *Nitric Oxide* **2014**, *36*, 31-35.
(53) Wahllnder, A.; Mohr, S.; Paumgartner, G. *J. Hepatol.* **1990**, *10*, 129-137.
(54) Carrillo, J. A.; Christensen, M.; Ramos, S. I.; Alm, C.; Dahl, M. L.; Benitez, J.; Bertilsson, L. *Ther. Drug Monit.* **2000**, *22*, 409-417.
(55) Zylber-Katz, E.; Granit, L.; Levy, M. *Clin. Pharmacol. Ther.* **1984**, *36*, 133-137.
(56) Alkaysi, H. N.; Salem, M. S.; El-Sayed, Y. M. *J. Clin. Phar. Ther.* **1988**, *13*, 109-115.
(57) Maliszewski, T. F.; Bass, D. E. *J. Appl. Physiol.* **1955**, *8*, 289-291.
(58) Minarowski, L.; Sands, D.; Minarowska, A.; Karwowska, A.; Sulewska, A.; Gacko, M.; Chyczewska, E. *Folia Histochem. Cytobiol.* **2008**, *46*, 245-246.
(59) Almadori, G.; Bussu, F.; Galli, J.; Limongelli, A.; Persichilli, S.; Zappacosta, B.; Minucci, A.; Paludetti, G.; Giardina, B. *Head Neck* **2007**, *29*, 648-654.
(60) Shivashankara, A. R.; Prabhu, M. K. *Biomed Res-India* **2011**, *22*, 355-359.
(61) Ngamchuea, K.; Batchelor-McAuley, C.; Cowen, P. J.; Williams, C.; Goncalves, L. M.; Compton, R. G. *Analyst* **2016**, *141*, 4707-4712.
(62) Arana, C.; Cutando, A.; Ferrera, M. J.; Gomez-Moreno, G.; Worf, C. V.; Bolanos, M. J.; Escames, G.; Acuna-Castroviejo, D. *J. Oral Pathol. Med.* **2006**, *35*, 554-559.
(63) Bates, J. F.; Hughes, R. E.; Hurley, R. J. *Arch. Oral Biol.* **1972**, *17*, 1017-1020.
(64) Giebultowicz, J.; Wroczynski, P.; Samolczyk-Wanyura, D. *J. Oral Pathol. Med.* **2011**, *40*, 726-730.
(65) Owen-Smith, B.; Quiney, J.; Read, J. *Lancet* **1998**, *351*, 1932.
(66) Zloczower, M.; Reznick, A. Z.; Zouby, R. O.; Nagler, R. M. *Antioxid. Redox Signal.* **2007**, *9*, 765-773.
(67) Soukup, M.; Biesiada, I.; Henderson, A.; Idowu, B.; Rodeback, D.; Ridpath, L.; Bridges, E. G.; Nazar, A. M.; Bridges, K. G. *Diabetol. Metab. Syndr.* **2012**, *4*, 14.
(68) McAuliffe, J. J.; Sherwin, A. L.; Leppik, I. E.; Fayle, S. A.; Pippenger, C. E. *Neurology* **1977**, *27*, 409-413.
(69) Knott, C.; Reynolds, F. *Ther. Drug Monit.* **1984**, *6*, 35-41.
(70) Goldsmith, R. F.; Ouvrier, R. A. *Ther. Drug Monit.* **1981**, *3*, 151-157.

(71) Schmidt, D.; Kupferberg, H. J. *Epilepsia* **1975**, *16*, 735-741.
(72) Galant, S. P. *Arch. Pediatr. Adolesc. Med.* **1977**, *131*, 970.
(73) Aviram, M.; Tal, A.; Benzvi, Z.; Gorodischer, R. *Pediatrics* **1987**, *80*, 894-897.
(74) Levy, G.; Ellis, E. F.; Koysooko, R. *Pediatrics* **1974**, *53*, 873-876.
(75) Knott, C.; Bateman, M.; Reynolds, F. *Br. J. Clin. Pharmacol.* **1984**, *17*, 9-14.
(76) Wade, H.; McCoubrie, D. L.; Fatovich, D. M.; Ryan, J.; Vasikaran, S.; Daly, F. F. *Clin. Toxicol. (Phila.)* **2008**, *46*, 534-538.
(77) Perry, R.; Campbell, M.; Grega, D. M.; Anderson, L. *J. Clin. Psychopharmacol.* **1984**, *4*, 199-202.
(78) Evrard, J. L.; Baumann, P.; Pera-Bally, R.; Peters-Haefeli, L. *Acta Psychiatr. Scand.* **1978**, *58*, 67-79.
(79) Degutis, L. C. *Acad. Emerg. Med.* **2004**, *11*, 885-887.
(80) Gubala, W.; Zuba, D. *Pol. J. Pharmacol.* **2002**, *54*, 161-165.
(81) Tu, G.-c.; Kapur, B.; Israel, Y. *Alcohol.: Clin. Exp. Res.* **1992**, *16*, 222-227.
(82) Bates, M. E.; Martin, C. S. *J. Stud. Alcohol* **1997**, *58*, 531-538.
(83) Cone, E. J.; Kumor, K.; Thompson, L. K.; Sherer, M. *J. Anal. Toxicol.* **1988**, *12*, 200-206.
(84) Thompson, L. K.; Yousefnejad, D.; Kumor, K.; Sherer, M.; Cone, E. J. *J. Anal. Toxicol.* **1987**, *11*, 36-38.
(85) Gorodetzky, C. W.; Kullberg, M. P. *Clin. Pharmacol. Ther.* **1974**, *15*, 579-587.
(86) Wang, W.-L.; Darwin, W. D.; Cone, E. J. *J. Chromatogr. B: Biomed. Sci. Appl.* **1994**, *660*, 279-290.
(87) Jenkins, A. J.; Oyler, J. M.; Cone, E. J. *J. Anal. Toxicol.* **1995**, *19*, 359-374.
(88) Valentine, J. L.; Psaltis, P. *Anal. Lett.* **1979**, *12*, 855-866.
(89) Niedbala, R. S.; Kardos, K. W.; Fritch, D. F.; Kardos, S.; Fries, T.; Waga, J.; Robb, J.; Cone, E. J. *J. Anal. Toxicol.* **2001**, *25*, 289-303.
(90) Strano-Rossi, S.; Colamonici, C.; Botre, F. *Anal. Chim. Acta* **2008**, *606*, 217-222.
(91) Strickland, P.; Morriss, R.; Wearden, A.; Deakin, B. *J. Affect. Disord.* **1998**, *47*, 191-194.
(92) Vedhara, K.; Miles, J.; Bennett, P.; Plummer, S.; Tallon, D.; Brooks, E.; Gale, L.; Munnoch, K.; Schreiber-Kounine, C.; Fowler, C.; Lightman, S.; Sammon, A.; Rayter, Z.; Farndon, J. *Biol. Psychol.* **2003**, *62*, 89-96.
(93) Kahn, J.-P.; Rubinow, D. R.; Davis, C. L.; Kling, M.; Post, R. M. *Biol. Psychiatry* **1988**, *23*, 335-349.
(94) Vining, R. F.; McGinley, R. A.; Maksvytis, J. J.; Ho, K. Y. *Ann. Clin. Biochem.* **1983**, *20 (Pt 6)*, 329-335.
(95) Few, J. D.; Wallis, P. J. W.; James, V. H. T. *Clin. Endocrinol. (Oxf.)* **1986**, *24*, 119-126.
(96) McVie, R.; Levine, L. S.; New, M. I. *Pediatr. Res.* **1979**, *13*, 755-759.
(97) Khan-Dawood, F. S.; Choe, J. K.; Dawood, M. Y. *Am. J. Obstet. Gynecol.* **1984**, *148*, 442-445.
(98) Ohzeki, T.; Manella, B.; Campo, G.; uuml; belin, D.; Zachmann, M. *Hormone Res.* **1991**, *36*, 235-237.
(99) Johnson, S. G.; Joplin, G. F.; Burrin, J. M. *Clin. Chim. Acta* **1987**, *163*, 309-318.
(100) Wang, C.; Plymate, S.; Nieschlag, E.; Paulsen, C. A. *J. Clin. Endocrinol. Metab.* **1981**, *53*, 1021-1024.
(101) Walker, R. F.; Hughes, I. A.; Riad-Fahmy, D. *Clin. Endocrinol. (Oxf.)* **1979**, *11*, 631-637.
(102) Zerah, M.; Pang, S. Y.; New, M. I. *J. Clin. Endocrinol. Metab.* **1987**, *65*, 227-232.
(103) Perry, L. A.; Wathen, N.; Chard, T. *Horm. Metab. Res.* **1987**, *19*, 444-447.
(104) Tivis, L. J.; Richardson, M. D.; Peddi, E.; Arjmandi, B. *Prog. Neuropsychopharmacol. Biol. Psychiatry* **2005**, *29*, 727-732.
(105) Belkien, L. D.; Bordt, J.; Möller, P.; Hano, R.; Nieschlag, E. *Fertil. Steril.* **1985**, *44*, 322-327.
(106) Evans, J. J.; Wilkinson, A. R.; Aickin, D. R. *Clin. Chem.* **1984**, *30*, 120-121.
(107) Preti, M. S.; Lodi, S.; Busacchi, P.; Filicori, M.; Flamigni, C. *Steroids* **1984**, *43*, 469-479.
(108) Kundu, N.; Novak, N.; Petersen, L. P. *Steroids* **1983**, *41*, 145-153.
(109) Pasic, J.; Pickup, J. C. *Diabetes Care* **1988**, *11*, 489-494.
(110) Laakso, M.-L.; Porkka-Heiskanen, T.; Alila, A.; Stenberg, D.; Johansson, G. *J. Pineal Res.* **1990**, *9*, 39-50.
(111) Nowak, R.; McMillen, I. C.; Redman, J.; Short, R. V. *Clin. Endocrinol. (Oxf.)* **1987**, *27*, 445-452.
(112) Voultsios, A.; Kennaway, D. J.; Dawson, D. *J. Biol. Rhythms* **1997**, *12*, 457-466.
(113) Frerichs, R. R.; Htoon, M. T.; Eskes, N.; Lwin, S. *Lancet* **1992**, *340*, 1496-1499.
(114) Major, C. J.; Read, S. E.; Coates, R. A.; Francis, A.; McLaughlin, B. J.; Millson, M.; Shepherd, F.; Fanning, M.; Calzavara, L.; MacFadden, D.; et al. *J. Infect. Dis.* **1991**, *163*, 699-702.
(115) Elkon, K. B.; Gharavi, A. E.; Patel, B. M.; Hughes, G. R.; Frankel, A. *Clin. Exp. Immunol.* **1983**, *52*, 75-84.
(116) Bradshaw, D. J.; Marsh, P. D. *Caries Res.* **1998**, *32*, 456-462.
(117) von Knorring, L.; Mörnstad, H. *Neuropsychobiology* **2008**, *15*, 146-154.
(118) Larsen, M. J.; Jensen, A. F.; Madsen, D. M.; Pearce, E. I. F. *Arch. Oral Biol.* **1999**, *44*, 111-117.
(119) Levine, M. J. *Ann. N.Y. Acad. Sci.* **1993**, *694*, 11-16.

Chapter 4 Experimental

This chapter provides the experimental detail of the reagents and instrumentation used throughout this thesis.

4.1 Chemical reagents

All reagents were obtained from Sigma-Aldrich, UK and used as received without further purification. All solutions were prepared using deionised water (Millipore, UK) with a resistivity of 18.2 MΩ cm at 298 K.

Table 4.1: List of chemicals used in this thesis. The chemical structures of complex organic molecules are provided in the relevant chapters.

Chemical Name	Formula	Purity
L-glutathione reduced (GSH)	$C_{10}H_{17}N_3O_6S$	≥98.0%
L-glutathione oxidised (GSSG)	$C_{20}H_{32}N_6O_{12}S_2$	≥98.0%
5,5′-dithiobis(2-nitrobenzoic acid) (DTNB)	$C_{14}H_8N_2O_8S_2$	≥98%
ethylenediaminetetraacetic acid disodium salt dihydrate (EDTA)	$C_{10}H_{14}N_2Na_2O_8 \cdot 2H_2O$	99.0-101.0%
β-nicotinamide adenine dinucleotide 2′-phosphate reduced tetrasodium salt hydrate (NADPH)	$C_{21}H_{26}N_7Na_4O_{17}P_3 \cdot xH_2O$	≥97%
glutathione reductase from baker's yeast (S. cerevisiae)	-	100-300 units/mg protein (biuret)
1,4-benzoquinone	$C_6H_4O_2$	≥98%
1,4-naphthoquinone	$C_{10}H_6O_2$	97%
2-chloro-1,4-benzoquinone	$C_6H_3ClO_2$	95%

Chemical Name	Formula	Purity
2,6-dichloroquinone-4-chloroimide	$C_6H_2Cl_3NO$	≥95%
sodium phosphate dibasic	Na_2HPO_4	≥99.0%
sodium phosphate monobasic dihydrate	$NaH_2PO_4 \cdot 2H_2O$	≥99.0%
copper(II) nitrate trihydrate	$CuNO_3 \cdot 3H_2O$	puriss. p.a., 99-104%
ferrocenemethanol	$C_{11}H_{12}FeO$	97%
potassium ferrocyanide trihydrate	$K_4Fe(CN)_6 \cdot 3H_2O$	≥99%
uric acid	$C_5H_4N_4O_3$	≥99%
L-ascorbic acid	$C_6H_8O_6$	99%
dopamine hydrochloride	$C_8H_{11}NO_2$	≥98%
potassium nitrate	KNO_3	≥99.0%
potassium chloride	KCl	≥99.5%
potassium bromide	KBr	≥99.0%
potassium iodide	KI	≥99.5%

4.2 Biological samples

Synthetic saliva (according to DIN 53160-1) was purchased from Synthetic Urine e.K., Germany. The synthetic saliva contains Mg^{2+}, Ca^{2+}, K^+, Cl^-, CO_3^{2-} and HPO_4^{2-} ions. It has the ionic strength of ca. 43 mM and pH of ca. 6.8. Note that the synthetic saliva contains only some of the inorganic consituents of the authentic saliva, and *excludes* organic components, proteins and other polypeptides present in the real saliva samples.

Authentic saliva samples were donated by consenting volunteers and collected using Salivette® (Sarstedt, Germany), a commercial device that facilitates the stimulated collection of whole saliva, refer to Figure 4.1. A Salivette comprises of a conical swab made of either cotton or synthetic material (such as polystyrene) for saliva absorption. The participants were given the swabs to chew for 1 min. Saliva samples were then retrieved from the conical swab by centrifugation at 1000g for 2 min.

The work involving human participants was granted ethical approval by The Central University Research Ethics Committee (CUREC2). All risk assessments (COSHH) associated with biomaterial have been completed and approved by the biological safety committee of the Department of Chemistry, University of Oxford, prior to commencement of the work.

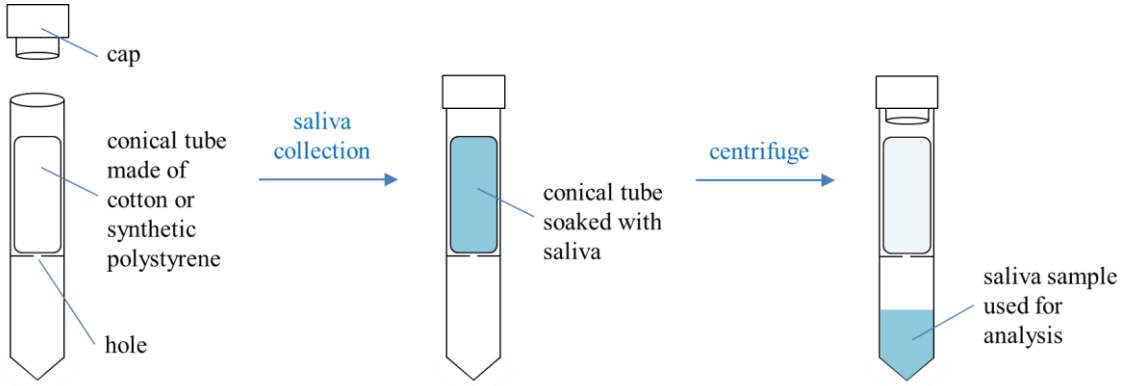


Figure 4.1: Schematic representation of saliva collection process using a Salivette®.

4.3 Electrochemical instrumentation

Nano-impact experiments were performed with a low noise potentiostat that was built in-house, using the Bessel filters which have been demonstrated to conserve the total charge transferred in an impact event.[1-3] All other electrochemical experiments were performed using a µAutolab Type III potentiostat (Utrecht, Netherlands). All measurements were conducted in a thermostated (25.0 ± 0.2 °C) Faraday cage, using standard three electrode

setups. The details of working, reference and counter electrodes used are different from chapter to chapter and will be discussed in the relevant chapter. In the case of the carbon microdisc working electrode (used in chapters 5, 9, 10 and 11), the size of the electrode is determined using the voltammetric responses of 1.0 mM $[Ru(NH_3)_6]^{3+}$ reduction in the presence of 0.10 M KCl, as further described in Appendix B1.

4.4 Non-electrochemical instrumentation

All ultra-violet visible (UV-vis) measurements were performed with a Shimadzu UV-1800 UV-visible spectrophotometer in disposable cuvettes (Eppendorf UVette, Sigma-Aldrich, UK) using a 10 mm optical path length.

The size of nanoparticles was determined by transmission electron microscopy (TEM), using a JEOL JEM-3000F instrument with an accelerating voltage of 300 kV. The samples were prepared by dropcasting nanoparticle suspensions onto carbon grids (Agar Scientific, UK) and allowing the modified grids to dry. The resulting nanoparticles images were sized using ImageJ software.

The hydrodynamic sizes of nanoparticles were determined using dynamic light scattering (DLS, ZEN3600 Nano-ZS Zetasizer, Malvern Instruments Ltd, UK) at 25 °C with a red laser of 633 nm.

Bibliography

(1) Batchelor-McAuley, C.; Ellison, J.; Tschulik, K.; Hurst, P. L.; Boldt, R.; Compton, R. G. *Analyst* **2015**, *140*, 5048-5054.
(2) Ngamchuea, K.; Clark, R. O. D.; Sokolov, S. V.; Young, N. P.; Batchelor-McAuley, C.; Compton, R. G. *Chem. Eur. J.* **2017**, *23*, 16085-16096.
(3) Kätelhön, E.; Tanner, E. E. L.; Batchelor-McAuley, C.; Compton, R. G. *Electrochim. Acta* **2016**, *199*, 297-304.

Chapter 5 Sensitive amperometric detection of reduced glutathione and the development of supported microwire electrodes for electroanalysis

The main biomarker compound considered in this thesis is glutathione, an important water-soluble antioxidant. This chapter develops an electroanalytical sensor for the detection of reduced glutathione (GSH) as well as introducing new electrode design for analytical applications. The fabricated sensor based on a surface-supported carbon microfiber (7 μm diameter, Figure 5.1) is cheap, disposable and requires only 150 μL of samples. The carbon fiber is surface-mounted onto an inert surface to overcome the problems of the fragility of the microwire and the possible interference of convective force due to the non-rigid nature of the wires, as well as to improve the reproducibility in length and the amperometric responses. As the cylindrical electrode is supported on a surface, the diffusion of redox-active species to the electrode is partially blocked by the substrate. A theoretical model is further developed to account for this restricted diffusion. The fabricated microwire electrode is then applied to the system of irreversible 2-nitro-5-thiobenzoate oxidation used in the detection of GSH. The microwire electrode shows significantly higher ratio of Faradaic to non-Faradaic currents as compared to microdisc, macrodisc or carbon nanotube modified electrodes. Using the fabricated microwire, GSH can be detected with the sensitivity of 0.7 nA μM^{-1} and the limit of detection of 0.5 μM ($3s_B/m$).

The work presented in this chapter has been published in *Analytical Chemistry*.[1]

5.1 Introduction

Providing rapid and potentially inexpensive analysis, electrochemical sensors have found extensive analytical application in areas ranging from environmental and industrial detectors to medical diagnosis.[2-6] However, the limit of detection of such devices is often restricted by the presence of relatively large non-Faradaic (capacitative) currents associated with the charging of the electrode surface.[7] In an attempt to resolve this problem, electrodes with microscopic (μm) dimension have been employed to first enhance the mass-transport of the redox-active analyte to the electrode surface (altering the mass-transport regime from linear to convergent), and second to decrease the non-Faradaic contribution to the electrochemical response. Examples of such electrode designs include microdisc,[8] microband electrodes,[9,10] and microelectrode arrays.[11-15] In comparison to more conventional macroelectrodes, these devices are relatively expensive, difficult to fabricate and can require calibration. Hence, such devices are not ideal for disposable use. More importantly, despite the theoretical expectations of the performance of these small electrodes, in practice they encounter difficulties relating to the presence of stray and/or parasitic capacitances arising from faults in the manufacturing process. The resulting capacitative currents are often found to be greater than that predicted on the basis of the geometric area of the electrode and hence limits the analytical sensitivity of the system.[16-18]

In this work, surface-supported carbon fiber microwires are presented as an alternative choice of electrode for analytical applications. These electrodes are shown to be accurate, reliable and appropriate for disposable use. Recent work in the literature has reported low limits of detection when using *isolated* microcylinder electrodes, for example in the detection of oxygen (~10 μM)[18] and nanoparticles (~0.1 pM).[19,20] However the application of such electrodes has been limited by their fragility and issues in reproducibly producing electrodes

of the same length. So far due to the use as isolated microcylinder these electrodes have been limited to being shorter than 1 mm in length as importantly, the use of long non-rigid electrodes moving freely in solution can give rise to a significant level of convective mass-transport, affecting the accuracy of the analytical procedure. In this work to overcome this problem and enhance the durability of the microwire, the carbon fiber is surface mounted on a glass slide, alongside a conducting wire and a silver wire as counter and reference electrodes respectively forming a sensor platform (Figure 5.1) which requires only a small sample volume (ca. 150 μL) for analysis.

The supported microwires are used to quantify the concentration of a solution phase analyte via two electrochemical techniques: chronoamperometry and cyclic voltammetry. Quantitative analysis of the resulting voltammogram is made by the solving of the diffusion equation for the system's geometry subjected to appropriate boundary conditions. Although the theoretical response of an isolated (azimuthally symmetric) microcylinder electrode is well established, in the present case of supported microwires, diffusion to the electrode is partially blocked by the supporting surface. The amperometric response of this system differs from that of an isolated electrode, where for the latter case the current-time response (chronoamperometry) and the voltammetric peak currents (cyclic voltammetry) can be predicted on the basis of the work of Szabo et al. (eqn. 5.5)[21] and Aoki et al. (eqn. 5.7)[22] respectively. Consequently, herein a theoretical model is developed for the diffusion-only response of a surface supported microwire electrode. This model is validated experimentally using the ideal outer-sphere redox probe ferrocene methanol.[23] Working curves of the peak currents predicted for cyclic voltammetry as a function of scan rates and for chronoamperoamperometry as a function of transient times are also presented for prospective future applications without the need for resource to further simulation.

This chapter continues by demonstrating the analytical application of the newly developed electrochemical system. Specifically, the solution phase concentration of glutathione (GSH) is quantified electrochemically at micromolar concentrations (5 μM to 65 μM range, LOD 0.5 μM ($3s_B/m$)), via its reaction with Ellman's reagent, 5,5′-dithiobis(2-nitrobenzoic acid) (DTNB). The irreversible reaction between DTNB and GSH results in the formation of 2-nitro-5-thiobenzoate (TNB), the latter is electrochemically detectable at the carbon fibre electrode. GSH is an important anti-oxidant in humans and is present in biological samples at low micromolar concentrations (~4 μM in plasma,[24] and ~3 μM in saliva[25]).[26-28] At these low levels, measurements using macro- or micro-disc electrodes are demonstrated to be unrealisable.

5.2 Experimental

5.2.1 Electrochemical instrumentation

All electrochemical measurements were conducted using standard three electrode setups employing different working electrodes in order to compare the voltammetric responses obtained at electrodes of different geometry. The different set-ups used are summarised in Table 5.1.

Table 5.1: The different three-electrode setups used in electrochemical measurements

Working electrode		Reference electrode	Counter electrode
Material	**Diameter**		
Glassy carbon (CH Instruments)	3 mm	Saturated calomel (BASi)	Platinum mesh
Carboxyl functionalised multi-walled carbon nanotube screen-printed (Dropsens)	4 mm	Silver wire	Carbon
Micro carbon fiber (microdisc, ALS)	7 µm	Saturated calomel (BASi)	Platinum mesh
Fabricated surface-mounted carbon microwire	7 µm	**Ferrocenemethanol experiments:** saturated calomel (BASi)	Tinned copper wire
		GSH/TNB experiments: silver wire	

5.2.2 Cell design of supported microwire electrodes

A carbon fiber, a silver wire and a metal conducting (tinned copper) wire were used as the working, reference and counter electrodes respectively. Carbon fiber (7 µm diameter) was obtained from Goodfellow, UK. The carbon fiber was attached to a conducting wire (0.2 mm diameter) of ca. 4 cm in length using the electrically conducting silver loaded epoxy adhesive (RS, USA) to allow the microfiber working electrode to be connected to electrochemical measurements. All electrodes were placed on a glass slide and sealed on both sides with the electrically insulating Kapton® tape to give the length of the electrodes of 1.0 cm. Nail polish (nitrocellulose in a mixture of organic solvents) was used to form a hydrophobic barrier and make a well surrounding the electrodes. With the well size of 1.4 x 1.4 cm^2, a droplet of ca. 150 µL of solution is required to cover the electrodes and enable electrochemical measurement.

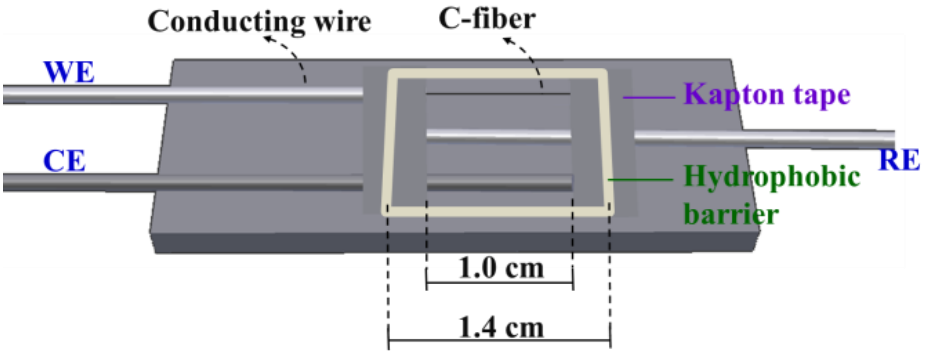


Figure 5.1: Design of the electrodes set-up on top of a non-conducting substrate with a C-fiber (7 μm diameter), a Ag wire and a metal conducting wire as working, reference and counter electrodes respectively.

5.2.3 Characterisation of the supported microwire electrodes: ferrocenemethanol ($FcCH_2OH$) experiments

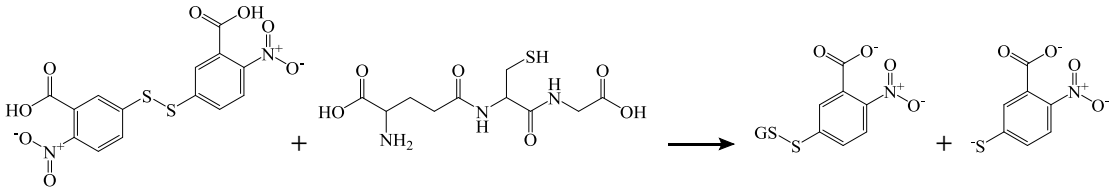
The ferrocenemethanol/ferrocenium methanol ($FcCH_2OH/FcCH_2OH^+$) redox couple was used to characterise the fabricated wire electrodes. Cyclic voltammetry (E = -0.2 → 0.6 → -0.2 V vs. SCE) of 1.0 mM $FcCH_2OH$ in the presence of 0.1 M potassium chloride (KCl) supporting electrolyte was performed at the carbon microfiber wire electrodes at varied scan rates (25 – 400 mV s^{-1}). The position of the anodic peak potential of the voltammogram is noted and the overpotential is selected for chronoamperometric measurements. Hence for chronoamperometry, the potential of 0.35 V vs. SCE is applied and the transient currents recorded for 10 s at a sampling rate of 1×10^4 Hz.

5.2.4 Reduced glutathione (GSH) measurement

The use of the surface supported microwire electrodes are demonstrated for the analysis of an irreversible system, 5-thio-2-nitrobenzoate (TNB) oxidation. This species is significant for the detection of reduced glutathione (GSH). GSH cannot be electrochemically detected

directly in aqueous media. Solutions of GSH (5 – 65 μM) were first reacted with excess 5,5′-dithiobis(2-nitrobenzoic acid) (DTNB, 170 μM); see eqn. 5.1. The reaction produces 5-thio-2-nitrobenzoate (TNB) which is detected electrochemically using the microwire electrodes.

DTNB + GSH ⟶ GS–TNB + TNB (5.1)



Note that the measurement of free thiol concentration requires the presence of a buffer for the thermodynamically-driven reaction of thiols with DTNB.[29] Hence, the chemical reactions were performed in the phosphate buffer pH 7.5 and allowed to mix for 2 minutes prior to the electrochemical measurements.[30] The resulting reaction mixtures are then subjected to cyclic voltammetry (E = 0.2 → 0.8 → 0.2 V vs. Ag, at the scan rate of 25 mV s^{-1}) or chrono-amperometry (E = 0.75 V vs. Ag) at the glassy carbon, carbon nanotube screen-printed, carbon microdisc or supported microwire electrode.

5.3 Theory and simulation

All simulation reported in this chapter was performed by Dr. Chuhong Lin.

Numerical simulation is applied to understand the electrochemical behaviour of a microcylinder located flat and lengthened on an inert substrate. The geometry of the simulation model is shown in Figure 5.2 and the concentration of the reactant c is calculated as a function of time t in the Cartesian coordinate system (x, y, z). The microclyinder is assumed long enough that only the circumference of the microcylinder electrode need to be considered in the simulation, reducing the problem to two-dimensions (x, z). Assuming that the mass-transport of the reactant in the solution is only due to diffusion and that a reversible

one-electron transfer reaction occurs at the surface of the supported microcylinder surface, the whole system can be described by the equations listed in Table 5.2. For a fast one-electron oxidation reaction, the concentration of the reactant on the electrode surface c_{surf} can be calculated via the Nernst equation:

$$c_{\mathrm{surf}} = \frac{1}{1+\exp\left(\frac{F(E-E_{\mathrm{f}})}{RT}\right)} \tag{5.2}$$

where F is the Faraday constant, R is the gas constant and T is the absolute temperature. E is the applied potential on the electrode, E_{f} is the formal potential of a redox reaction, and the difference between E and E_{f} is the overpotential for a redox reaction. The simulation grids are built in the same way as applied for a sphere on a plate, details of which can be found in refs. 31 and 32.[31,32]

In this work, two electrochemical techniques, chronoamperometry and cyclic voltammetry, are used to explore the electrochemical reaction at the microcylinder electrode on a flat plate. Chronoamperometry measures the current varying as a function of the experimental time at a fixed electrode potential. All the chronoamperometry results are simulated at a high overpotential, where the surface concentration of the reactant is effectively zero. Cyclic voltammetry reflects the current response at a time varying electrode potentials. The potential E is expressed by the following function of the experimental time t and the scan rate v:

$$E = \begin{cases} E_{\mathrm{ini}} + vt, & t \leq \frac{|E_{\mathrm{rev}} - E_{\mathrm{ini}}|}{v} \\ E_{\mathrm{rev}} - v\left(t - \frac{E_{\mathrm{rev}} - E_{\mathrm{ini}}}{v}\right), & t > \frac{|E_{\mathrm{rev}} - E_{\mathrm{ini}}|}{v} \end{cases} \tag{5.3}$$

where $[E_{\mathrm{ini}}, E_{\mathrm{rev}}]$ defines the potential window of the cyclic voltammogram and $E_{\mathrm{ini}} < E_{\mathrm{rev}}$ for an oxidation process. For a microcylinder on a plate with the length of l, the current I can be calculated from the gradient of the reactant concentration c at the electrode surface:

$$I = -FD \iint_S \frac{\partial c}{\partial n} dS \qquad (5.4)$$

where n is the unit normal vector pointing away from the microcylinder surface and S refers to the area of the microcylinder excluding the ends of the electrode.

The resulting problem was solved numerically by means of the Newton-Raphson method and the Alternating Direction Implicit (ADI) method.[33] The simulation programmes were written in Matlab R2016a and performed using an Intel(R) Xeon(R) 3.60G CPU.

Table 5.2: Conditions and equations used in the simulation of the microcylinder on a flat plate system

Condition	Equation
$t = 0$	$c = c^*$ (c^* is the concentration in the bulk solution)
$z \to \infty$	$c = c^*$
$x \to \infty$	$c = c^*$
$z = 0$	$\frac{\partial c}{\partial z} = 0$
$x = 0, z > 2r_{\mathrm{el}}$ (r_{el} is the radius of the microcylinder)	$\frac{\partial c}{\partial x} = 0$
$(z - r_{\mathrm{el}})^2 + x^2 = {r_{\mathrm{el}}}^2$	$c = \frac{1}{1+\exp\left(\frac{F(E-E_f)}{RT}\right)}$
x, z in the solution	$\frac{\partial c}{\partial t} = D\left(\frac{\partial^2 c}{\partial x^2} + \frac{\partial^2 c}{\partial z^2}\right)$ (D is the diffusion coefficient of the reactant)

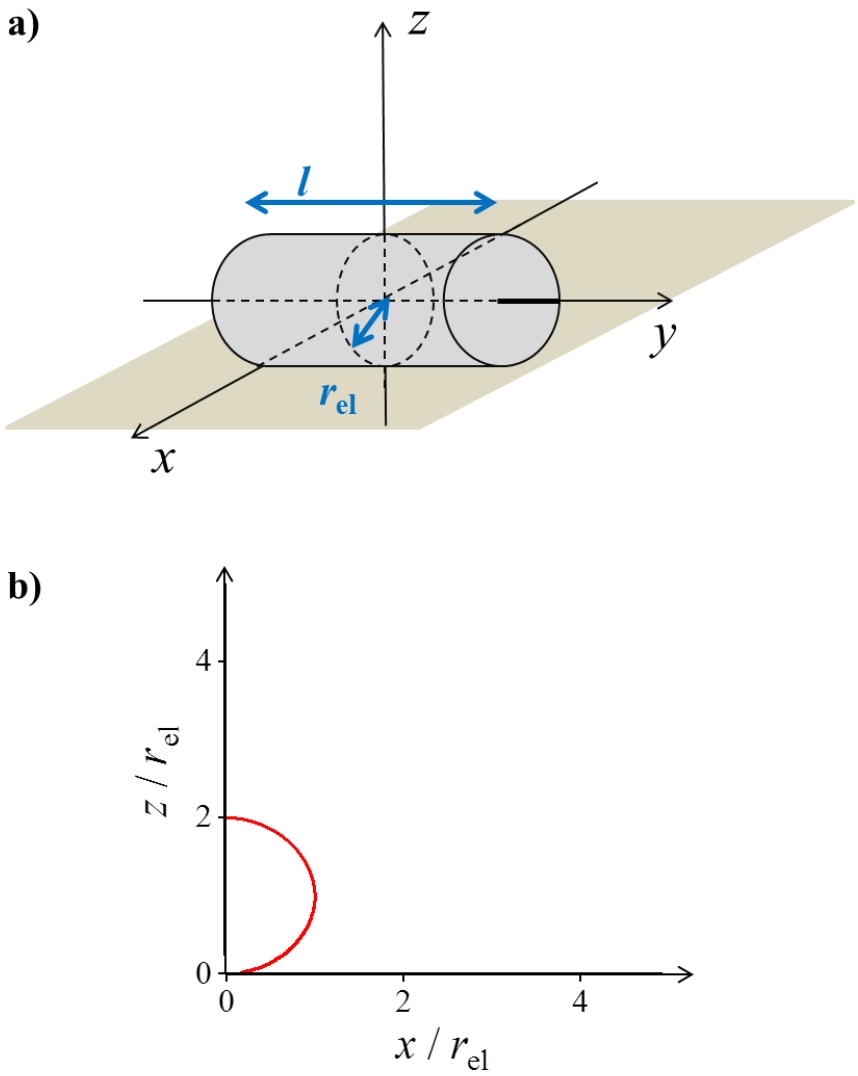


Figure 5.2: a) Geometry of the microcylinder electrode; **b)** Simulation model of the microcylinder electrode supported on the substrate. The red curve refers to the electroactive surface in the two-dimension (x, z) coordinate. r_{el} is the radius of the microcylinder.

5.4 Results and discussions

Two electrochemical techniques, chronoamperometry and cyclic voltammetry, are studied at the surface supported microwire electrodes. Both numerical simulation and experimental results are presented. First, the results of the simulation are detailed and compared to the responses of both a hemi and full (free standing) microcylinder. The simulation results are

subsequently experimentally validated using a reversible one-electron transfer process ($FcCH_2OH/FcCH_2OH^+$). Finally, the well-characterised surface supported microwire electrodes and cell design is then employed in the analysis of the more complicated system of irreversible TNB (from GSH + DTNB) oxidation.

5.4.1 Chronoamperometry

The chronoamperometric response of a fast one-electron transfer reaction at a surface mounted microwire electrode is explored via simulation and experiment. The effect of the wire geometry on the current-time responses is explored in relation to the response of an isolated free standing cylinder and a hemi-cylindrical electrode.

- **Theory**

The predicted chronoamperometry of the fast one-electron transfer reaction at high overpotential on the surface supported microwire electrode is shown in Figure 5.3. For clarity, the axes in Figure 5.3 are normalised current $I / (2FlDc^*)$ and normalised time Dt / r_{el}^2. Figure 5.3 contains the chronoamperograms at the supported microwire electrode (black line), the isolated free standing full cylinder microwire (blue line) and the hemi-microcylinder (red line). The radii of the three microwire electrodes are all the same. The chronoamperogram of the supported microwire is obtained from the simualtion. The current-time responses of the other two geometries have been analytically approximated in the literature:[21]

$$\frac{I}{2\pi lnFDc^*} = \sigma_{geo}\left(\frac{e^{-\sqrt{\pi\tau}/10}}{\sqrt{\pi\tau}} + \frac{1}{ln\left((4\tau e^{-\gamma})^{0.5}+e^{5/3}\right)}\right), \tau = \frac{Dt}{r_{el}^2} \qquad (5.5)$$

where n is the number of electrons transferred in the redox reaction (n = 1 for the one-electron-transfer reaction). γ is determined by Szabo et al. to be approximately 0.5772156.[21] σ_{geo} reflects the geometry area of the microwire being 0.5 for a hemicylinder and 1 for a full cylinder.

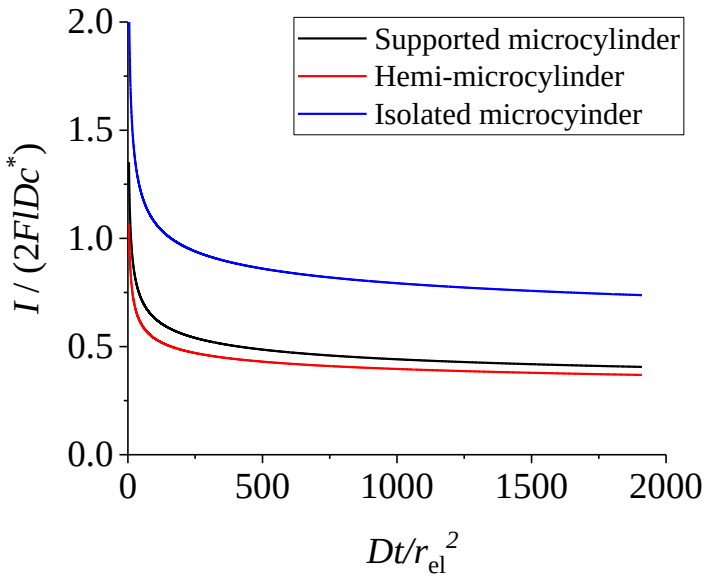


Figure 5.3: Chronoamperograms of a fast one-electron transfer reaction at high overpotential on microcylinder electrodes with various geometries. The black, red and blue solid lines are the simulation for the supported microwire, the hemi-microcylinder, and the isolated microwire respectively.

As shown in Figure 5.3, the current-time responses for the one-electron transfer reaction are distinguished by the geometry of the microcylinder. The reaction current of the supported microcylinder is between the currents expected from the hemi-microcylinder and the isolated microcylinder. At very short times, the current is proportional to the surface area of the electrode, hence the response of the surface mounted microcylinder tends towards that of the fully isolated microwire. However, as time progresses and the thickness of the diffusion layer increases relative to the electrode radius, the importance of the diffusional blocking by the electrode support becomes a more signifcant factor. Consequently, the current at the surface

supported microwire electrode tends towards the response predicted for the hemi-cylindral electrode. However, even in the long time limit as the currents become quasi-steady state, due to the differing gemotries associated with the surface supported microwire and the hemi-cylindral electrode the currents predicted for the two systems do not converge to the same value. Table 5.3 presents the ratios of chronoamperometric currents of a fast one-electron transfer reaction at the different electrode geometries in the long time limit ($Dt/r_{el}^2 >> 1$), demonstrating that the geometric influence cannot be neglected when analysing electrochemical reactions at a microcylinder electrode.

Table 5.3: Geometry influence on the predicted quasi-steady state currents of the different microwire electrode geometries. Values respresent the long-time limit current ratios among the supported microwire, the isolated microwire and the hemi-microcylinder with equal radii

Geometry	Current ratio at long time
$i_{\text{supported}}/i_{\text{isolated}}$	0.545
$i_{\text{supported}}/i_{\text{hemi}}$	1.09
$i_{\text{hemi}}/i_{\text{isolated}}$	0.5

- ## Experimental

The reversible one-electron transfer redox couple of $FcCH_2OH/FcCH_2OH^+$ is used to demonstrate the current-time responses at the supported microwire electrode. Experimentally, $FcCH_2OH$ of 1.0 mM concentration (in 0.10 M KCl) is oxidised at a potential of 0.35 V vs. SCE for 10 s. The chronoamperograms obtained are then compared with the results of numerical simulation from the previous section.

The diffusion regimes alter during the course of the chronoamperogram.[34] In order to consider comparatively both the linear (1D) and radial (2D) diffusion regimes as well as to avoid the influence of convective force, it is important to determine the optimal time range for the comparison of the simulated and experimental data, as further described below.

Experimentally at transient time (t) of less than 0.3 s, there is a significant non-Faradaic contribution due to the build-up of charged species at the electrode. This can be seen from the chronoamperogram of 0.10 M KCl solution where the potential of 0.35 V vs. SCE is applied at the supported microwire (Figure 5.4). Consequently, t = 0.3 s was used as the short-time limit (t_{min}) for fitting of experimental data to simulation results.

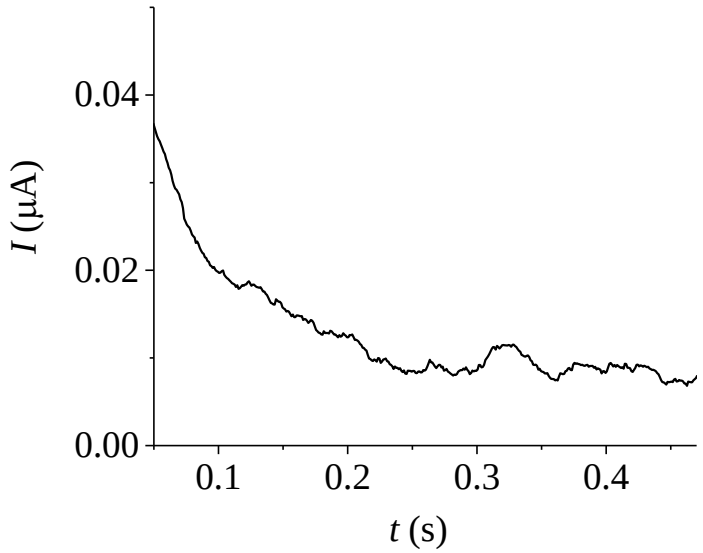


Figure 5.4: Chronoamperogram of 0.10 M KCl electrolyte solution; E = 0.35 V vs. SCE showing significant contribution from non-Faradaic currents at the experimental time of less than 0.3 s.

The long-time limit (t_{max}) as well as the quality of the fit between the experimental (I_{exp}) and simulated (I_{sim}) data is assessed based on the magnitude of the mean scaled absolute deviation (%MSAD) between the data sets. The %MSAD for N data points is defined as:

$$\%\text{MSAD} = \frac{1}{N}\sum_N \left|\frac{I_{\text{sim}} - I_{\text{exp}}}{I_{\text{exp}}}\right| \times 100 \qquad (5.6)$$

For the chronoamperometry of $FcCH_2OH$ oxidation, the experimental time range of 0.3 s – 3.8 s was found to give the lowest value of %MSAD of 0.31%, see Figure 5.5a. This time range is subsequently chosen for use in the following analysis.

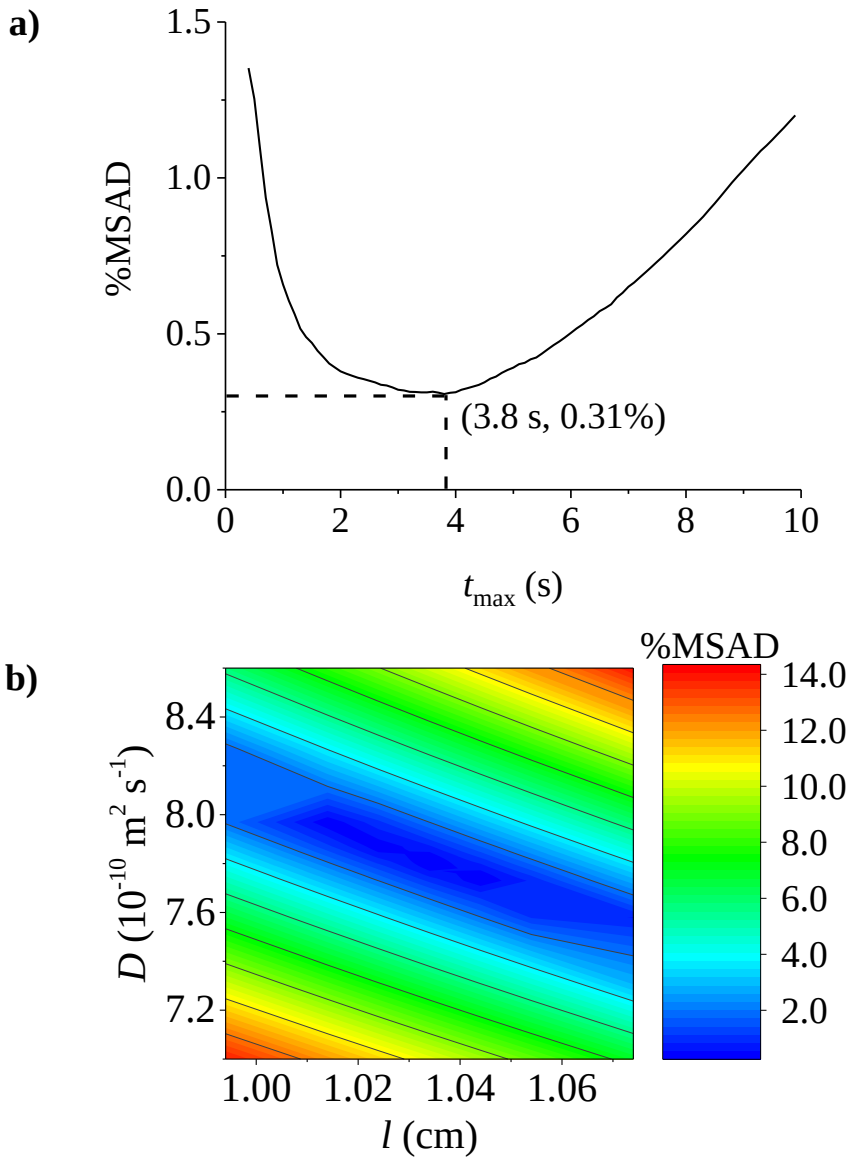


Figure 5.5: a) %MSAD as a function of long-time limits (t_{max}) showing a minimum of %MSAD of 0.31% when t_{max} is 3.8 s; **b)** %MSAD as a function of diffusion coefficient (D) and length of the supported wire electrode (l) showing a minimum of %MSAD of 0.29% when D and l are 3.8 s 7.81×10^{-10} m^2 s^{-1} and 1.034 cm respectively.

In accordance with eqn. 5.5, at high overpotentials the current-time responses of a reversible one-electron transfer process at a microcylinder electrode varies as a function of diffusion coefficient (D), concentration (c^*) of the redox-active species, the radius (r_{el}) and length (l) of the wire electrode. In present experimental case, the concentration of ferrocencemethanol and the radius of the electrode are precisely known to be 1.02 mM and 3.5 μm respectively. Note that the carbon fiber wire has its diameter as specified by the manufacturer (Goodfellow, UK) of 0.007 mm with the tolerances in the fiber diameter, number of strands, tex number and length of ±25%, ±10%, ±10% and +5% / -1% respectively.

There are however two unknown parameters, D and l, noting that the length l will vary slightly between electrode preparations (the question of the reproducibility of the wire length will be returned to later). Consequently, a best fit of the experimental data needs to be found using these two parameters, this best fit is found by searching for a local minimum in the %MSAD. The values of D and l which yield the lowest %MSAD of 0.31% are 7.81×10^{-10} m^2 s^{-1} and 1.034 cm respectively; see Figure 5.5b. The value of D obtained is in excellent accordance to that reported by Sun and Mirkin,[35] and Miao et al.[23] (7.8×10^{-10} m^2 s^{-1}).

Having determined the optimal transient times (0.3 s – 3.8 s) for the fitting of the simulated and experimental results, and the values of all the parameters required for the calculation of the current-time responses (c^*, r_{el}, D and l), the simulated and experimental chronoamperograms can then be compared as presented in Figure 5.6 below.

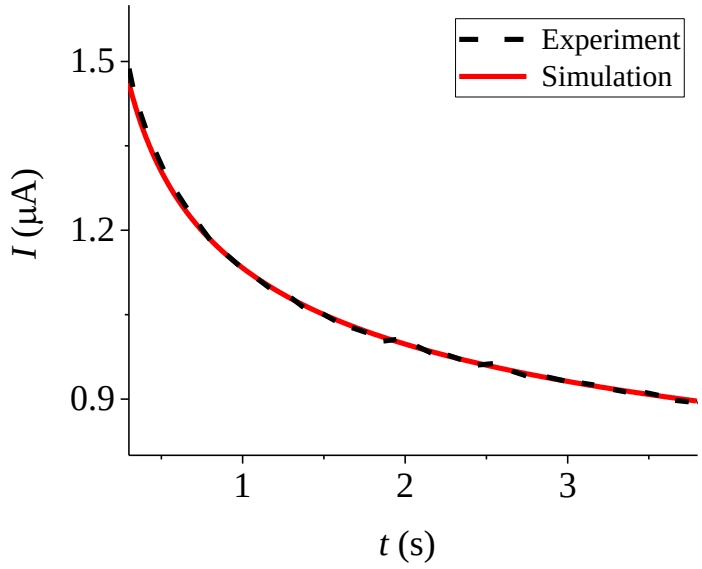


Figure 5.6: Comparison between the experimental (black, dashed line) and simulated (red, solid line) chronoamperograms of 1.0 mM $FcCH_2OH$ (+0.10 M KCl) oxidation, 298 K at the supported microcylinder electrode.

Having validated the simulated chronoamperometric response of the surface mounted microwire electrode and utilised this as a method to accurately determine the diffusion coefficient of the redox species ferrocenemethanol, the work now continues by looking at the voltammetric response of these surface mounted microwire electrodes.

5.4.2 Cyclic voltammetry

Simulation of the cyclic voltammetry for a fast one-electron transfer process is first performed, providing a working curve for the predicted peak currents at a supported microwire electrode for a reversible one-electron diffusion only redox process. Experimentally, the $FcCH_2OH/FcCH_2OH^+$ redox reaction is taken as the model system to study the cyclic voltammetric behaviour of the supported microwire electrode, and the results from simulation and experiments compared towards the end of this section.

- **Theory**

Figure 5.7a shows the current-potential responses for a fast one-electron transfer reaction simulated under different scan rates and Figure 5.7b compares the forward peak currents between the surface supported and isolated microwire electrodes. The peak current of the supported microwire are obtained from simulation. For the isolated microwire, the peak currents can be predicted by the following equation:[22]

$$I_{\mathrm{p}} = 2\pi nFc^{*}Dl(0.446p + 0.335p^{0.15}),\ p = \left(\frac{nFvr_{\mathrm{el}}^{2}}{RTD}\right)^{0.5} \qquad (5.7)$$

As shown in Figure 5.7b, the ratios of the peak currents between the supported and the isolated microwires $I_{\mathrm{p,supported}}$ / $I_{\mathrm{p,isolated}}$ vary as a function of a combined parameter $\frac{Fvr_{\mathrm{el}}^{2}}{RTD}$. Figure 5.7c and 5.7d provide two example concentration profiles collected at the forward peak potentials with $\log_{10}\left(\frac{Fvr_{\mathrm{el}}^{2}}{RTD}\right) = 3.5$ and $\log_{10}\left(\frac{Fvr_{\mathrm{el}}^{2}}{RTD}\right) = -4$, respectively. The combined parameter reflects the diffusion mode of the reactant. When the combined parameter is large, linear diffusion is observed as illustrated in Figure 5.7c, hence the current is proportional to the electrode surface area and thus the ratio $I_{\mathrm{p,supported}}$ / $I_{\mathrm{p,isolated}}$ tends to unity at large values of $\frac{Fvr_{\mathrm{el}}^{2}}{RTD}$. Conversely, when the value of the combined parameter decreases, the diffusion varies from linear to radial, as shown in Figure 5.7d. Diffusion to the bottom of the supported microcylinder is restricted due to the substrate and the geometry influence bemores more significant. At very small value of $\frac{Fvr_{\mathrm{el}}^{2}}{RTD}$, the ratio $I_{\mathrm{p,supported}}$ / $I_{\mathrm{p,isolated}}$ tends to 0.545, the same value as the ratio between two chronoamperometric currents listed in Table 5.3. The exact values of the $I_{\mathrm{p,supported}}$ / $I_{\mathrm{p,isolated}}$ ratio in Figure 5.7b are given Table 5.4. The

$I_{p,supported}$ / $I_{p,isolated}$ ratios for the irreversible electron-transfer system are further provided in Appendix A.

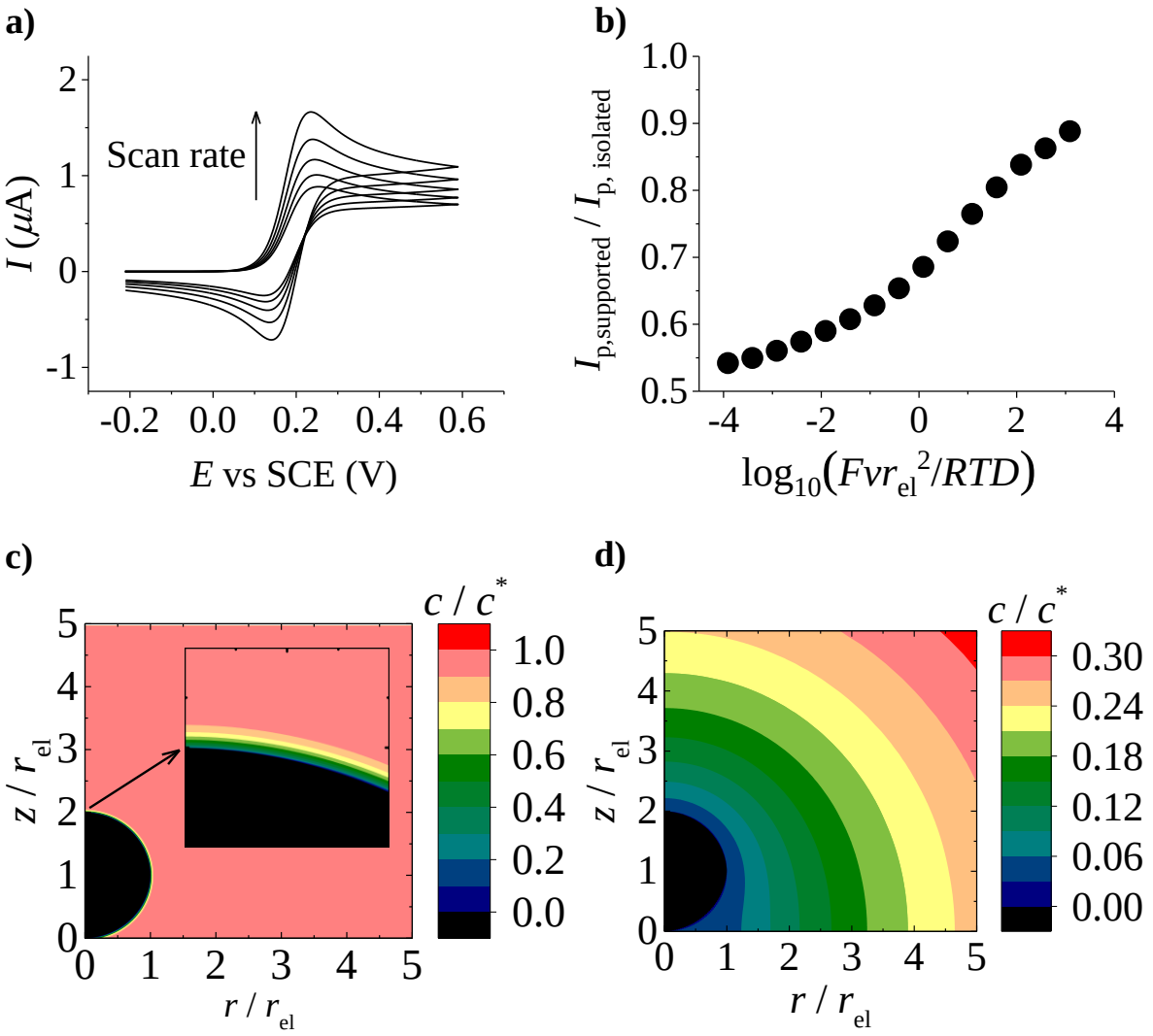


Figure 5.7: a) Cyclic voltammetry of a fast one-electron transfer reaction on the supported microwire electrode at different scan rates. From bottom to top, the scan rates are 25, 50, 100, 200 and 400 mV s^{-1}; **b)** The ratio of forward peak currents between the supported and isolated microwire electrodes, see Table 5.4 for exact values; **c)** Concentration profile of the reactant collected at the forward peak potential when $\log_{10}(Fvr_{el}^2/RTD)$ = 3.5; **d)** Concentration profile of the reactant collected at the forward peak potential when $\log_{10}(Fvr_{el}^2/RTD)$ = -4.

Table 5.4: The $I_{p,supported}$ / $I_{p,isolated}$ ratios for reversible one-electron transfer process at different $Fr_{el}^2 v/RTD$

$\log_{10}(Fr_{el}^2 v/RTD)$	$I_{p,supported}/I_{p,isolated}$
-3.91	0.545
-2.91	0.560
-2.41	0.574
-1.82	0.593
-1.41	0.608
-0.91	0.628
-0.41	0.654
0.09	0.686
0.59	0.724
1.09	0.765
1.59	0.804
2.09	0.838
3.09	0.888

- ## Experimental

Cyclic voltammetry of ferrocenemethanol ($FcCH_2OH$) of 1.0 mM concentration (in 0.10 M KCl) was measured (E = -0.2 → 0.6 → -0.2 V vs. Ag) at range of scan rates (25 – 400 mV s^{-1}). The previously determined values of diffusion coefficient (D) and length of wire electrode (l) of 7.81×10^{-10} m^2 s^{-1} and 1.034 cm respectively are used to analyse the voltammetric currents; refer to eqn. 5.7. As shown in Figure 5.8a, the experimental results show an excellent fit to the numerical data, with the plots of comparison of peak potentials and peak currents provided in Figure 5.8b. The results indicate that not only the quasi-steady

state currents, but the fabricated microwire electrodes give well-defined CVs for a reversible redox system, and that the working curve presented in Figure 5.7b together with the analytical expression given in eqn. 5.7 can be used to accurately predict the voltammetric peak currents of the supported microwire electrodes.

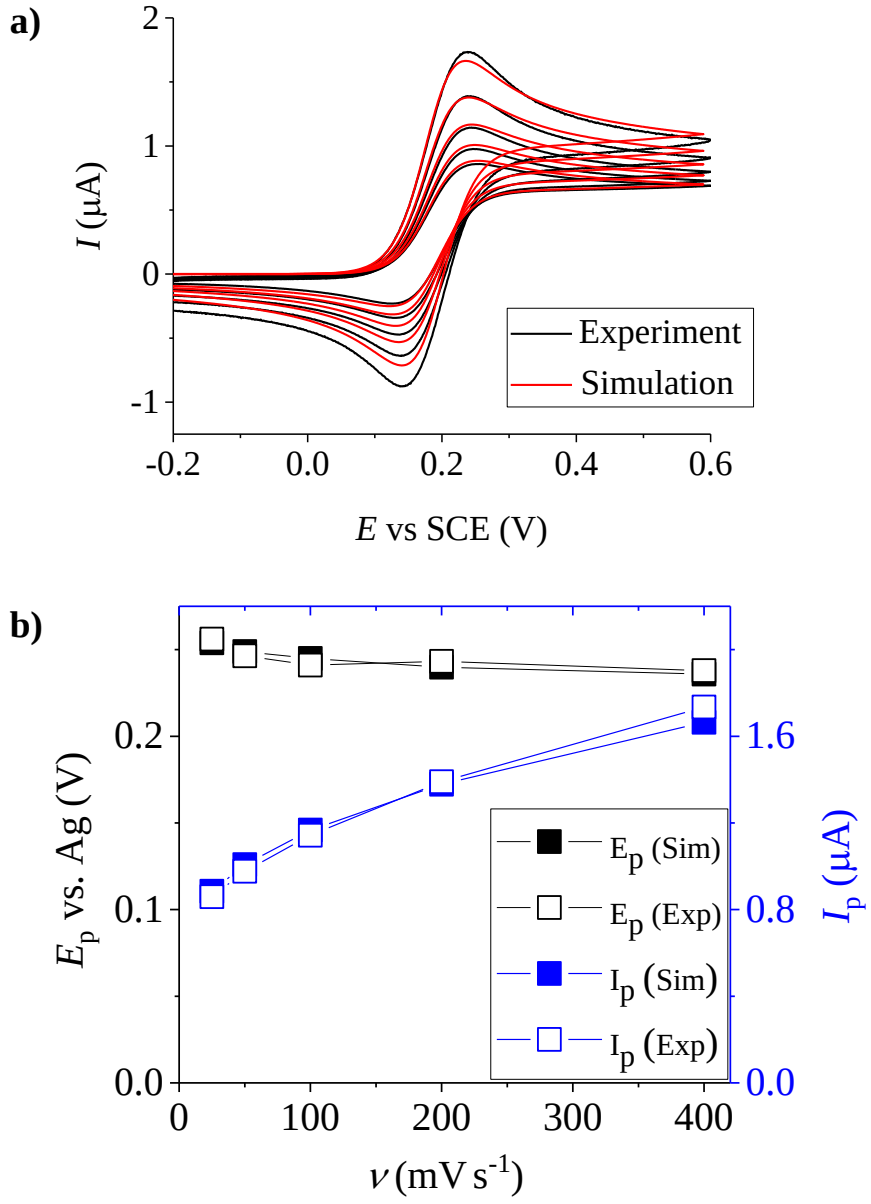


Figure 5.8: a) Comparison between the experimental (black) and simulated (red) cyclic voltammograms of 1.0 mM $FcCH_2OH$ (+0.10 M KCl) oxidation, ν = 25 - 400 mV s^{-1}, 298 K at the supported microcylinder electrode; **b)** Comparison between the experimental (open squares, □) and simulated (solid squares, ■) anodic peak potentials (E_p, black) and anodic peak currents (I_p, blue)

5.4.3 Reproducibility of electrodes

The above results have been presented for a supported microwire electrode. An important question arises as to the reproducibility of this cell design. Specifically, the variability in the electrode lengths between fabrications is of distinct importance. In the case that the electrochemical response of the wire is found to be highly reproducible, then within a certain error the electrode may be used without prior calibration of the wire length. The 1 cm carbon fiber wire electrodes were made by taping the Kapton tape on both sides of the carbon fiber. The error in the wire length arises due to the inherent variability of this process. The reproducibility of the electrode length and its resulting amperometric responses was tested using the well-characterised $FcCH_2OH$ as a model system.

Cyclic voltammetry of 1.0 mM $FcCH_2OH$ (in 0.10 M KCl) at the scan rate of 25 mV s^{-1} was recorded on three different electrodes with three scans each, see Figure 5.9. The oxidative peak potential remained at 0.246 V vs. SCE in all cases. The forward oxidative peak currents were 0.840 ± 0.005 μA within the electrode and 0.846 ± 0.039 μA between electrodes, giving the measurement errors of 0.6% and 4.6% within the electrode and between electrodes respectively. The length of the wires was calculated using eqn. 5.7 and the geometry factor ($I_{p,supported}$ / $I_{p,isolated}$) of 0.593 (Table 5.4: $\log_{10}(Fr_{el}^2 v/RTD)$ = -1.82) to be 1.004 ± 0.047 cm, showing the excellent reproducibility of the electrodes.

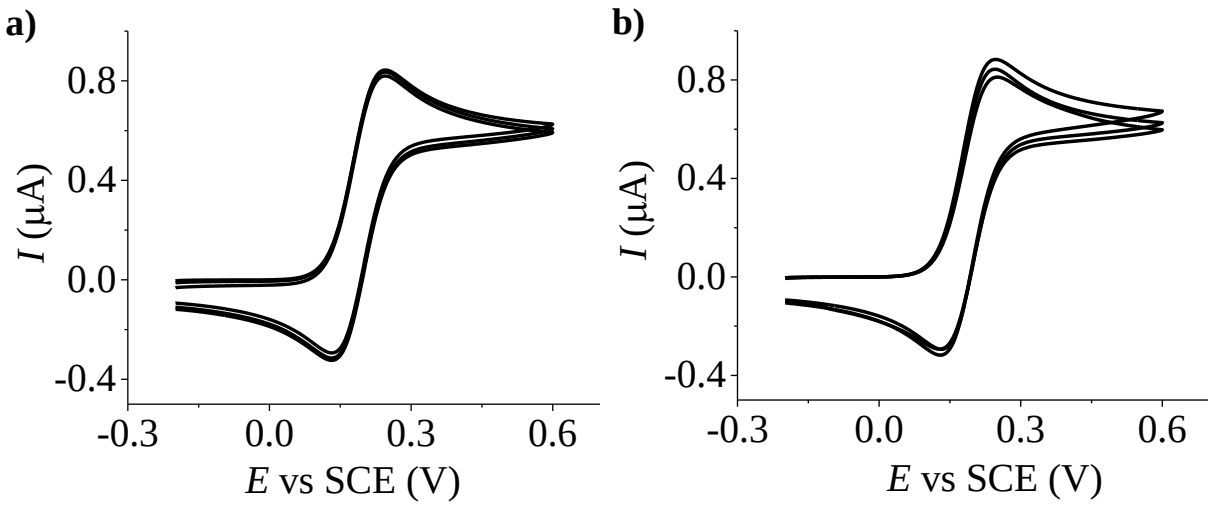


Figure 5.9: Cyclic voltammetry of 1.0 mM $FcCH_2OH$ oxidation in 0.10 M KCl at the supported microwire electrodes at the scan rate of 25 mV s^{-1}, 298 K; **a)** same electrode, multiple scans; **b)** different electrodes

5.4.4 Reduced glutathione (GSH) measurement

The supported microwire electrodes can further be applied to a more complicated system such as that of an electrochemically irreversible process. The system chosen for investigation herein is 5-thio-2-nitrobenzoate (TNB). This compound is commonly used in the analysis of thiol concentrations, most notably reduced glutathione (GSH); see eqn. 5.1. TNB oxidation is an irreversible process and is thought to follow a chemical-electrochemical-chemical or CEC mechanism.[36] At low pH, the thiol moiety of TNB has to be deprotonated (the first 'chemical' step). The deprotonated TNB then undergoes oxidation ('electrochemical' step), and the oxidised products dimerise to form DTNB (the last 'chemical' step).

- **Preliminary studies of TNB oxidation**

Cyclic voltammetry of 0.84 mM TNB oxidation is performed at a glassy carbon macro-electrode (GC; r_{el} = 1.49 ± 0.02 cm) at 298 K at the scan rates of 25, 50, 100, 200, 300 and

400 mV s^{-1}. The voltammograms are presented in Figure 5.10a and the peak currents plotted against the square root of scan rates in Figure 5.10b. The voltammograms obtained are subjected to Tafel analysis[7] giving the value of transfer coefficient (β) of 0.24. The diffusion coefficient (D) is then determined using eqn. 5.8[7] to be 1.36 x 10^{-9} ± 0.04 x 10^{-9} m^2 s^{-1}.

$$I_p = 0.496\sqrt{(1-\beta)}FA_e c^* \sqrt{\frac{FD\nu}{RT}} \qquad (5.8)$$

where I_p is the peak current. α, F, A_e, ν, R, T, $c^*$and D are the transfer coefficient, Faraday constant (96,485 C mol^{-1}), electrode surface area, scan rate, molar gas constant (8.314 J K^{-1} mol^{-1}), absolute temperature and bulk concentration and diffusion coefficient of the redox-active species, respectively.

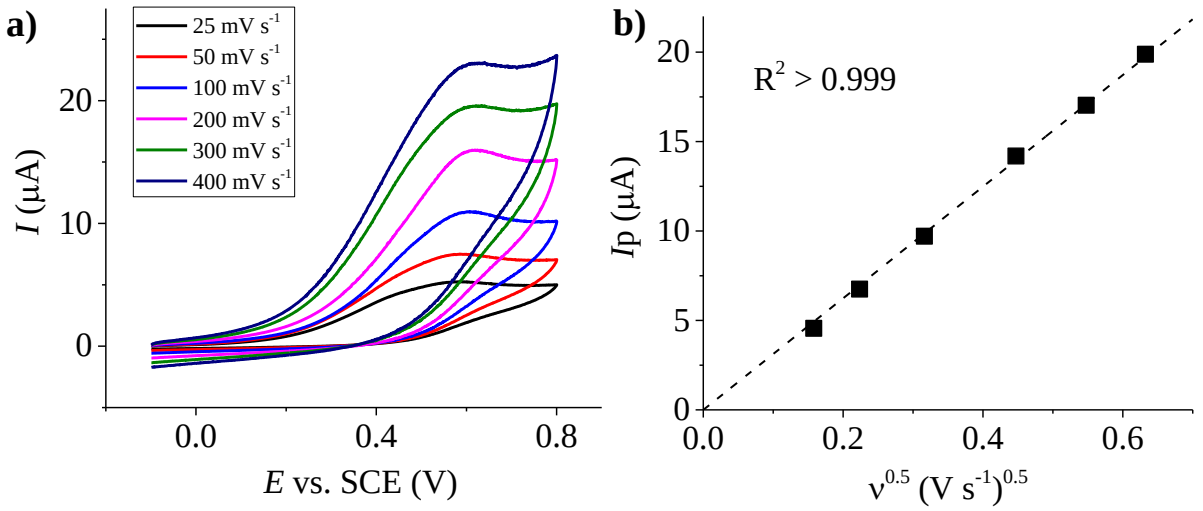


Figure 5.10: a) Cyclic voltammetry of 0.84 mM TNB oxidation at GC electrode at the scan rates of 25, 50, 100, 200, 300 and 400 mV s^{-1}; **b)** Voltammetric peak currents as a function of square root of scan rates.

Similar experiments were performed at the supported microwire electrode. The value of transfer coefficient (β) of TNB oxidation at the wire electrodes was determined to be 0.26, similar to the value obtained at the glassy carbon and that previously reported in literature.[36]

- **Enhanced sensitivity using supported carbon microwire electrodes**

Four different carbon electrodes, glassy carbon macrodisc (GC), carbon nanotube modified screen-printed (CNT-SPE), carbon microdisc (C-microdisc) and supported carbon fiber microwire (C-wire), are next investigated for their sensitivity towards the voltammetric measurement of TNB oxidation. This will be evaluated using the ratios of Faradaic to capacitative currents (i_F/i_C). The measurement of the i_F/i_C ratios is detailed below.

Capacitance of the electrodes is measured by cyclic voltammetry of blank electrolyte (0.10 M phosphate buffer pH 7.5, 10 mM EDTA) at the scan rate of 25 mV s^{-1}. The resulting amperometric current is due to the build-up of charge at the electrode surface. The capacitative current (i_C) is measured at 0.7 V vs. Ag. Subsequently, cyclic voltammetry of the oxidation of 168 μM TNB in 0.10 M phosphate buffer pH 7.5 at the scan rate of 25 mV s^{-1} is performed and the value of its peak current (i_F) at 0.7 V vs. Ag is noted. The ratios of Faradaic to capacitative currents (i_F/i_C) can then be determined.

Figure 5.11 displays the voltammograms of the oxidation of 168 μM TNB in 0.10 M phosphate buffer pH 7.5 at the scan rate of 25 mV s^{-1}, currents are normalised relative to the electrode geometric area. The ratios of Faradaic peak current (i_F) to non-Faradaic current (i_C) are observed to be 7.6 ± 0.2, 3.6 ± 0.1, 3.1 ± 0.2 and 33 ± 4 for GC (Figure 5.11a), CNT-SPE (Figure 5.11b), C-microdisc (Figure 5.11c) and C-microwire (Figure 5.11d) respectively.

It is predicted that the Faradaic peak currents at macrodisc electrodes vary linearly with the electrode area (r_{el}^2),[7] while the limiting currents at microdisc or microwire are dependent on the electrode radius ($\sim r_{el}$).[22] Capacitance, on the other hand in the absence of considering other contributing factors, is linearly dependent on the area for all types of electrodes.[7,37] Based on this knowledge, microdiscs and microwires are expected to show better sensitivity

than the macroelectrodes. The measurement at the microwire indeed shows significantly higher sensitivity (i.e. larger i_F/i_C) than the macroelectrodes, justifiable by the enhancement of the diffusion to the electrode and the reduction of the capacitance. The commercial microdisc electrodes however have unexpectedly large capacitance, likely reflecting the imperfect sealing of the electrodes and the occurrence of cracks potentially from the manufacturing processes.[16-18] Note that the cyclic voltammogram provided by the supplier presented in Appendix A2 also shows similar level of capacitance (1977 ± 441 μF cm^{-2}).[18]. Accordingly, it has been demonstrated herein the superiority of the supported microwires for the analysis of low concentration of analyte where the measurement is often found to be challenging due to the large capacitance.

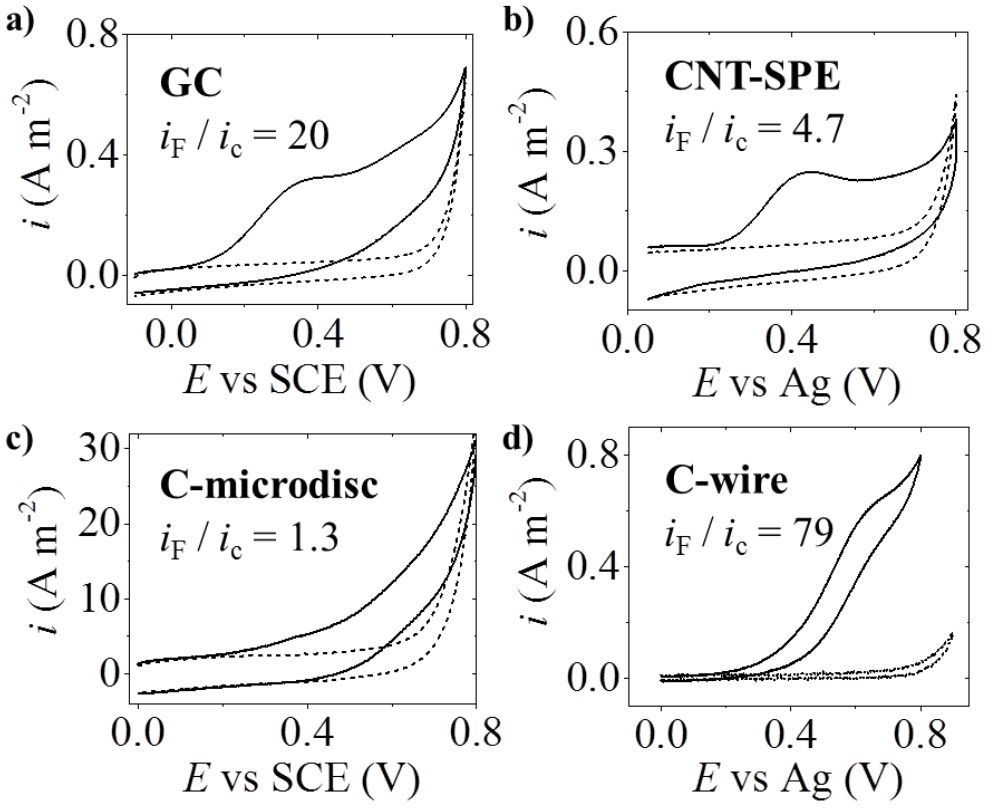


Figure 5.11: Cyclic voltammograms of blank 0.10 M phosphate buffer pH 7.5 (dashed lines) and 168 μM TNB in 0.10 M phosphate buffer pH 7.5 (solid lines) at the scan rate of 25 mV s^{-1} at different carbon electrodes: **a)** glassy carbon macrodisc (GC); **b)** carbon nanotube modified screen-printed (CNT-SPE); **c)** carbon microdisc (C-microdisc); **d)** supported carbon fiber microwire (C-wire). The currents are normalised by the electrode area.

Above, it has been demonstrated by linear sweep voltammetry that the microwire electrodes display significantly improved ratios of Faradaic to non-Faradaic currents compared to that of macrodisc electrodes, carbon nanotube modified electrodes and microdisc electrodes. Importantly due to the disposable nature of the designed electrodes, they can be easily adopted for practical applications.

- **Calibration curve**

Having demonstrated the enhanced voltammetric response of the microwires, next the ability of the microwires to quantitatively detect GSH is explored.

An excess amount of DTNB (168 μM) was used to react with 0, 5, 10, 20, 30, 45 and 65 μM of GSH in 0.10 M, pH 7.5 phosphate buffer in the presence of 10 mM ethylene-diaminetetraacetic acid (EDTA; to prevent GSH oxidation catalysed by metal ions impurity in the solutions[30]). The mixtures were left to react for 2 minutes to allow the reactions to go to completion, and hence producing 0, 5, 10, 20, 30, 45 and 65 μM of TNB. Cyclic voltammetry of the reaction mixtures were recorded and the peak currents [I (0.7 V) – I (0.3 V)] plotted against GSH concentrations, yielding a linear calibration plot ($R^2 > 0.99$) with the sensitivity of 0.7 nA μM^{-1} and limit of detection of 0.5 μM ($3s_B/m$); refer to Figure 5.12. Figure 5.12 further shows that other than TNB, no other species in the solution gives rise to the voltammetric response in the potential window studied.

Chronoamperometry was also recorded and the calibration plot of the quasi-steady state current at 10 s against GSH concentration gives the sensitivity of 0.7 nA μM^{-1} and the limit of detection of 1.3 μM ($3s_B/m$); refer to Figure 5.13.

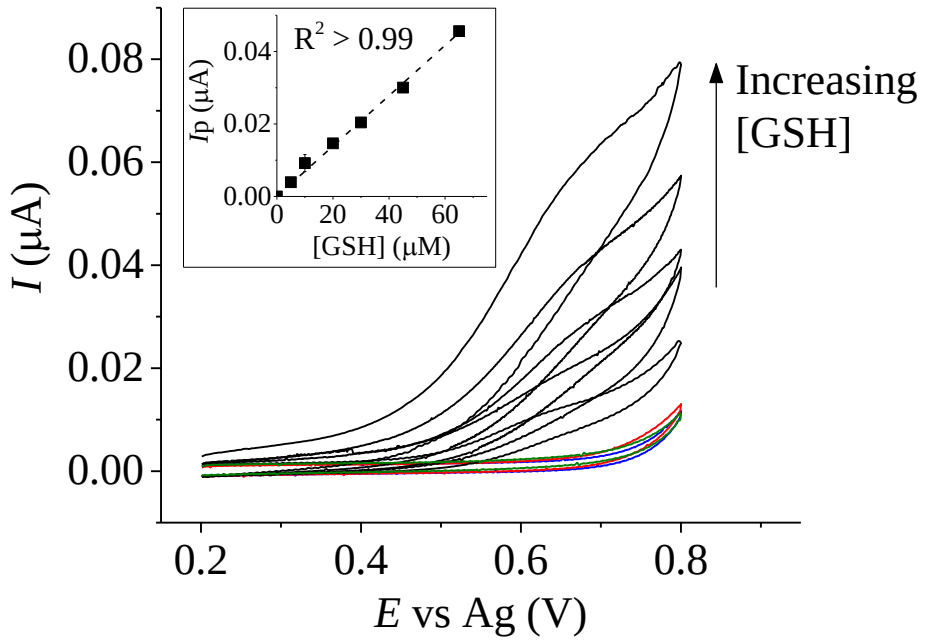


Figure 5.12: (Black) Cyclic voltammetry of 0, 5, 10, 20, 30, 45 and 65 μM of GSH reacted with 168 μM DTNB for 2 minutes to form equal concentrations of TNB at the supported microwire electrode. **(Blue)** Blank phosphate electrolyte. **(Green)** 60 μM GSH **(Red)** 168 μM DTNB. ν = 25 mV s^{-1}. 298 K. Inlay: calibration plot of voltammetric peak currents (I_p) against GSH concentration.

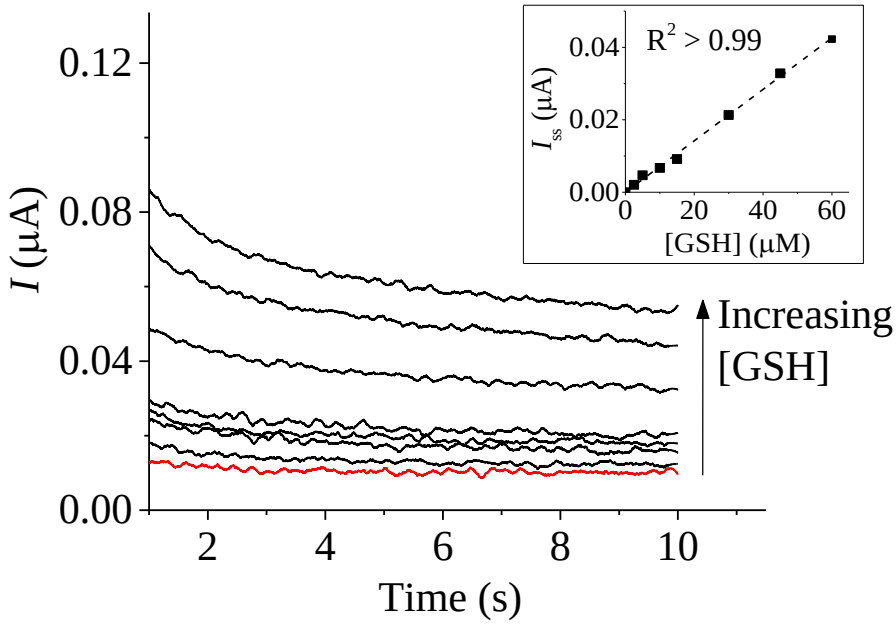


Figure 5.13: (Black) Chronoamperometry of 0, 5, 10, 20, 30, 45 and 65 μM of GSH reacted with 168 μM DTNB for 2 minutes to form equal concentrations of TNB at the supported microwire electrode. **(Red)** Blank electrolyte solution. 298 K. Inlay: calibration plot of quasi-steady state currents (I (t = 10 s)) against GSH concentration.

5.5 Conclusions

The fabricated supported microwires have been developed into an electrochemical sensor for the quantification of solution phase analytes at low micromolar concentrations. The theoretical models for the amperometric responses at the supported microwires are also developed for the first time in this work, reflecting the partially restricted diffusion of the analyte to the electrode blocked by the support. This sensor platform is reproducible, inexpensive and easily fabricated in-house without any requirement for specialized tools. The sensor requires only a small volume of samples (~150 μL) and show good reproducibility in electrochemical responses (±4.6%). It displays excellent performance with the systems of reversible $FcCH_2OH$ oxidation and irreversible TNB oxidation studied in this work. In particular, the latter allows the detection of reduced glutathione with sub-micromolar limit of detection. In addition to the electrochemical detection, a spectrophotometric assay is further developed for the detection of glutathione (both reduced and oxidised forms), presented in the following chapter.

Bibliography

(1) Ngamchuea, K.; Lin, C.; Batchelor-McAuley, C.; Compton, R. G. *Anal. Chem.* **2017**, *89*, 3780-3786.
(2) Privett, B. J.; Shin, J. H.; Schoenfisch, M. H. *Anal. Chem.* **2008**, *80*, 4499-4517.
(3) Hanrahan, G.; Patil, D. G.; Wang, J. *J. Environ. Monit.* **2004**, *6*, 657-664.
(4) Toghill, K. E.; Compton, R. G. *Int. J. Electrochem. Sci.* **2010**, *5*, 1246-1301.
(5) Harfield, J. C.; Batchelor-McAuley, C.; Compton, R. G. *Analyst* **2012**, *137*, 2285.
(6) Windmiller, J. R.; Wang, J. *Electroanalysis* **2013**, *25*, 29-46.
(7) Compton, R. G.; Banks, C. E. *Understanding Voltammetry*, 2nd ed.; Imperial College Press, London, UK, **2011**.
(8) Bond, A. M. *Analyst* **1994**, *119*, 1R.
(9) Craston, D. H.; Jones, C. P.; Williams, D. E.; El Murr, N. *Talanta* **1991**, *38*, 17-26.
(10) Xiong, L.; Goodrich, P.; Hardacre, C.; Compton, R. G. *Sens. Actuators, B* **2013**, *188*, 978-987.
(11) Sokolov, S. V.; Bartlett, T. R.; Fair, P.; Fletcher, S.; Compton, R. G. *Anal. Chem.* **2016**, *88*, 8908-8912.
(12) Rahman, A. R.; Guiseppi-Elie, A. *Biomed. Microdevices* **2009**, *11*, 701-710.
(13) Prieto, F.; Coles, B. A.; Compton, R. G. *J. Phys. Chem. B* **1998**, *102*, 7442-7447.
(14) Streeter, I.; Compton, R. G. *J. Phys. Chem. C* **2007**, *111*, 15053-15058.
(15) Ordeig, O.; del Campo, J.; Muñoz, F. X.; Banks, C. E.; Compton, R. G. *Electroanalysis* **2007**, *19*, 1973-1986.
(16) Wehmeyer, K. R.; Wightman, R. M. *J. Electroanal. Chem. Interfacial Electrochem.* **1985**, *196*, 417-421.
(17) Wipf, D. O.; Michael, A. C.; Wightman, R. M. *J. Electroanal. Chem. Interfacial Electrochem.* **1989**, *269*, 15-25.

(18) Cinková, K.; Clark, M.; Sokolov, S. V.; Batchelor-McAuley, C.; Švorc, Ľ.; Compton, R. G. *Electroanalysis* **2016**.
(19) Ellison, J.; Batchelor-McAuley, C.; Tschulik, K.; Compton, R. G. *Sens. Actuators, B* **2014**, *200*, 47-52.
(20) Batchelor-McAuley, C.; Ellison, J.; Tschulik, K.; Hurst, P. L.; Boldt, R.; Compton, R. G. *Analyst* **2015**, *140*, 5048-5054.
(21) Szabo, A.; Cope, D. K.; Tallman, D. E.; Kovach, P. M.; Wightman, R. M. *J. Electroanal. Chem.* **1987**, *217*, 417-423.
(22) Aoki, K.; Honda, K.; Tokuda, K.; Matsuda, H. *J. Electroanal. Chem.* **1985**, *182*, 267-279.
(23) Miao, W.; Ding, Z.; Bard, A. J. *J. Phys. Chem. B* **2002**, *106*, 1392-1398.
(24) Michelet, F.; Gueguen, R.; Leroy, P.; Wellman, M.; Nicolas, A.; Siest, G. *Clin. Chem.* **1995**, *41*, 1509-1517.
(25) Zappacosta, B.; Manni, A.; Persichilli, S.; Boari, A.; Scribano, D.; Minucci, A.; Raffaelli, L.; Giardina, B.; De Sole, P. *Clin. Biochem.* **2007**, *40*, 661-665.
(26) Franco, R.; Schoneveld, O. J.; Pappa, A.; Panayiotidis, M. I. *Arch. Physiol. Biochem.* **2007**, *113*, 234-258.
(27) Ballatori, N.; Krance, S. M.; Notenboom, S.; Shi, S.; Tieu, K.; Hammond, C. L. *Biol. Chem.* **2009**, *390*, 191-214.
(28) Lawrence, N.; Davis, J.; Compton, R. G. *Talanta* **2001**, *53*, 1089-1094.
(29) Szajewski, R. P.; Whitesides, G. M. *J. Am. Chem. Soc.* **1980**, *102*, 2011-2026.
(30) Ngamchuea, K.; Batchelor-McAuley, C.; Compton, R. G. *Chem. Eur. J* **2016**, *22*, 15937-15944.
(31) Ward, K. R.; Lawrence, N. S.; Hartshorne, R. S.; Compton, R. G. *J. Phys. Chem. C* **2011**, *115*, 11204-11215.
(32) Jiao, X.; Lin, C.; Young, N. P.; Batchelor-McAuley, C.; Compton, R. G. *J. Phys. Chem. C* **2016**, *120*, 13148-13158.
(33) Compton, R. G.; Laborda, E.; Ward, K. R. *Understanding Voltammetry: Simulation of Electrode Processes*; Imperial College Press, London, UK, **2013**.
(34) Xiong, L.; Aldous, L.; Henstridge, M. C.; Compton, R. G. *Anal. Methods* **2012**, *4*, 371-376.
(35) Sun, P.; Mirkin, M. V. *Anal. Chem.* **2006**, *78*, 6526-6534.
(36) Nekrassova, O.; Lawrence, N. S.; Compton, R. G. *Electroanalysis* **2003**, *15*, 1501-1505.
(37) Bard, A. J.; Faulkner, L. R. *Electrochemical Methods: Fundamentals and Applications*; Wiley, New York, USA, **2000**.

Chapter 6 Rapid method for the quantification of reduced and oxidised glutathione in human plasma and saliva

The previous chapter presented an electroanalytical method for reduced glutathione (GSH) detection. In this chapter, an alternative detection method is developed based on spectrophotometric measurements. This new method is able to determine the concentrations of both reduced (GSH) and oxidised glutathione (GSSG), and hence the GSH:GSSG ratios in human plasma and saliva samples. The assay is based on the masking of GSH in a GSH and GSSG mixture via a 1,4-addition reaction with *p*-benzoquinone (BQ), followed by enzymatic kinetic measurement. The enzyme, glutathione reductase, is highly specific to glutathione. Excess BQ can thus be easily removed by the addition of non-GSH thiols. The assay takes less than 2 min, is suitable for short timescale study and minimises the *in-vitro* underestimation of the GSH:GSSG ratio arising from the degradation of GSH and formation of GSSG. It is further demonstrated in this work that the stability of the total glutathione content (GSH + GSSG) and GSH in saliva is significantly greater than in plasma, encouraging the development of non-invasive saliva sensing.

The work presented in this chapter has been published in *Analytical Chemistry*.[1]

6.1 Introduction

An increase in the level of prooxidants, notably reactive oxygen species, relative to that of antioxidants in cells and tissues results in 'oxidative stress' which potentially leads to oxidative damage to important biological components such as DNA, proteins and lipids.[2] The level of oxidative stress can be assessed using marker compounds, such as glutathione. The change in the ratio of reduced (GSH) to oxidised glutathione (GSSG) has been reported to be diagnostic of various diseases such as cancers,[3] neurodegenerative diseases,[4] and cardiovascular diseases.[5] The primary aim of this chapter is thus to evaluate the levels of GSH, GSSG and hence the ratio between the two species in human plasma and saliva. Plasma is commonly used for health diagnosis, while saliva is a possible superior alternative offering the advantage of non-invasive sample collection. Saliva is particularly suitable for point-of-care analysis as well as for those with hemophobia and trypanophobia.

Plasma glutathione is known to decrease at a significant rate at room temperature *in-vitro* with a half-life of approximately 20 minutes.[6] The stability of salivary glutathione at room temperature however has not been reported. For diagnostic analysis, it is important that the concentrations of glutathione are accurately determined and reflect the 'true' concentrations in the human body. It is therefore favourable to use the biological medium which exhibits the slowest rate of glutathione degradation. To evaluate the reliability of glutathione concentrations measured as well as to explore the possibility of using saliva as a diagnostic medium, kinetic and recovery studies are further performed in this work. The stabilities of total glutathione and GSH in plasma and saliva samples are investigated alongside the formation of GSSG, for which a new methodology is developed.

At present, the contents of GSH and GSSG in biological samples can be determined by various means notably chromatographic methods,[7,8] capillary electrophoresis,[9,10]

electrochemical techniques,[11-13] nanoparticle-based colorimetric tests,[14] chemiluminescence,[15] spectrofluorimetric methods and spectrophotometric methods.[16,17] Among those, one of the most commonly used methods is the spectrophotometric enzymatic assay first developed by Tietze.[18] This colorimetric test, presented as part of Figure 6.1a, is based on the thiol-disulfide exchange reaction between GSH and the sulfhydryl reagent 5,5′-dithiobis(2-nitrobenzoic acid) (DTNB). The reaction produces a chromophore that strongly absorbs at the wavelength of 412 nm (5-thio-2-nitrobenzoate, TNB) and a mixed disulfide GS-TNB. GS-TNB is then reduced by the enzyme glutathione reductase (GR) to form another TNB and regenerate GSH. The recycle rate of GSH, which is proportional to the GSH level, is then measured by monitoring the rate of TNB formation at 412 nm. The method finds widespread use in part due to its low cost, convenience, high sensitivity, and low limit of detection of ca. 10 nM. The Tietze assay however measures the concentration of *total* glutathione, both reduced and oxidised forms, due to the catalytic action of the enzyme.

To determine the levels of GSH and GSSG, and hence the ratio between the two species, an extra step of masking of GSH is required prior to the enzymatic reactions. Currently, there are two widely-used thiol-masking reagents for uses in the enzymatic assay, *N*-ethylmaleimide (NEM)[18] and 2-vinylpyridine (2VP),[19] each of which has its own advantages and disadvantages. The former reacts with GSH almost instantaneously but is highly toxic and known to inhibit the activity of glutathione reductase used in the measurement assay. Consequently, any excess NEM has to be removed by column chromatography[20] or by multiple extractions with organic solvents[18,21] before performing the enzymatic cycling. This has led to the development of another thiol-masking agent, 2VP, which does not inhibit the enzyme, but nonetheless, has its own disadvantage of a very slow reaction with GSH. In particular, it takes ca. $20 - 60$ minutes for the reaction between GSH and 2VP to go to completion and hence fully mask all thiols from the sample.

In this chapter, a new GSH-masking reagent based on benzoquinone (BQ) is explored. BQ is much less toxic than NEM, and efficiently and almost instantaneously binds to the target thiol. More importantly, any excess BQ can be easily and quickly removed (< 20 s) by the method developed herein, see the enclosed box in Figure 6.1. It is thus a significant improvement as compared to the original NEM or 2VP assays, allowing rapid detection of both GSH and GSSG in biological samples.

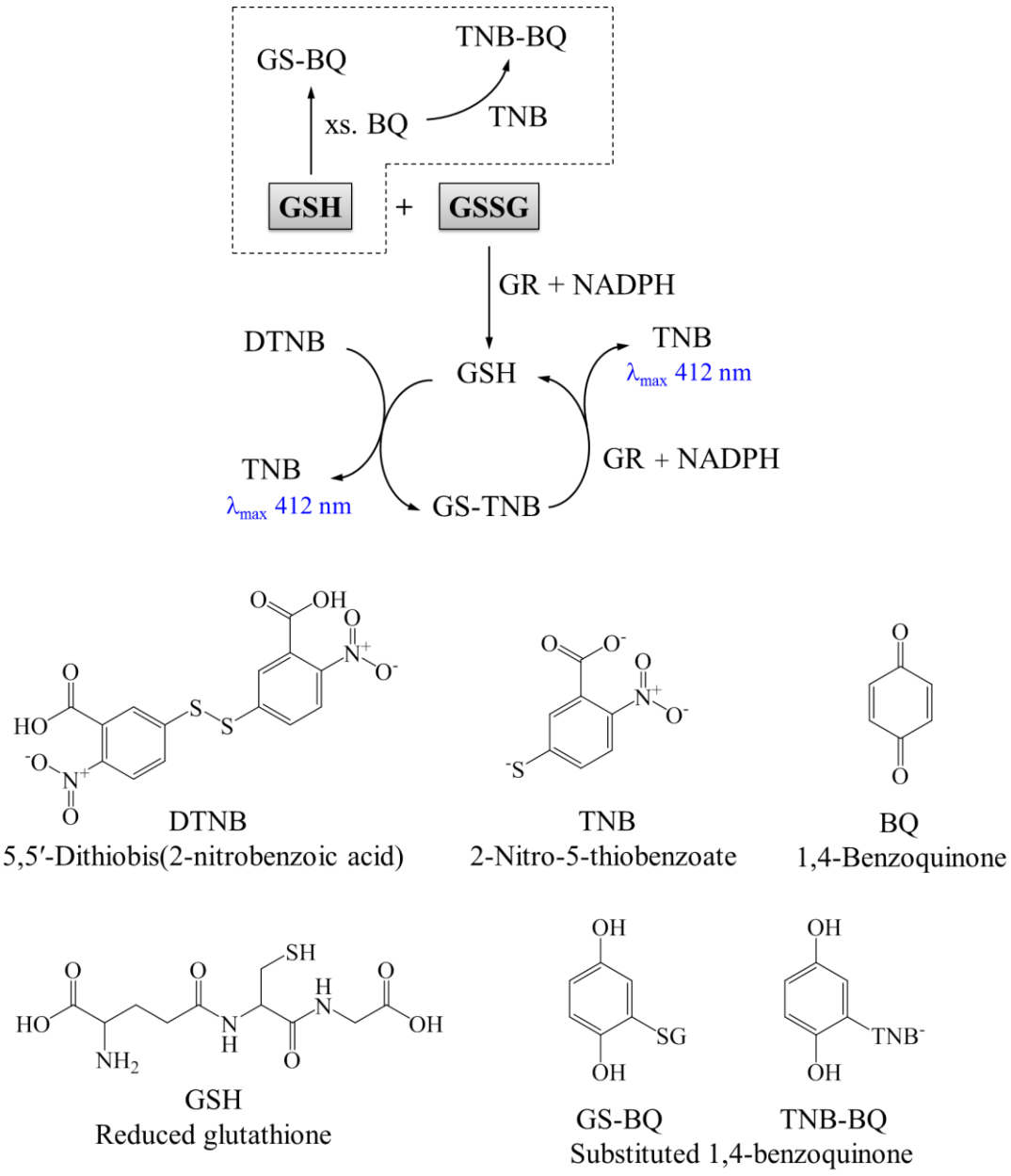


Figure 6.1: Schematic representation of the Tietze enzymatic kinetic assay, with the developed GSSG (BQ/TNB) assay in the enclosed box. The bottom of the figure shows the chemical structures of the relevant compounds.

6.2 Experimental

This section gives details of the source and storage of biological samples as well as the procedures for the measurements of GSH and GSSG, and the stability studies.

6.2.1 Biological samples

Plasma samples were supplied by ZenBio (NC, USA). The plasma was collected in acid citrate dextrose from consenting adult (male) donors with the average age of 36.5 (range: 20-57). The plasma was shipped frozen on dry ice and stored at -80 °C prior to use.[22] Saliva samples were kindly donated by laboratory colleagues without any known pathological conditions. Saliva was taken at least 1 hour after fasting using Salivette® and immediately stored at -20 °C.[23]

6.2.2 Measurement procedures

The concentrations of *total glutathione* (in GSH equivalents; [GSH] + 2[GSSG]) are measured using the Tietze enzymatic kinetic assay (Figure 6.1).[18] The Tietze assay is based on the reaction between GSH and 5,5′-Dithiobis(2-nitrobenzoic acid) (DTNB). The reaction produces 5-thio-2-nitrobenzoate (TNB; $\varepsilon_{\lambda=412\ nm}$ = 14,150 M^{-1} cm^{-1})[24] and a mixed disulfide (GS-TNB). GS-TNB is then reduced by glutathione reductase (GR) in the presence of NADPH to form another TNB and GSH. Any GSSG present in the sample is converted to GSH by GR at the beginning of the assay.

Subsequently, an aliquot of the sample is added to the solutions of DTNB and GR. After 30 s, NADPH is added to the solution mixtures. The absorbance at 412 nm (A_{412}) is then recorded for 120 s and the slope of A_{412} against time ($\mathrm{d}A_{412}/\mathrm{d}t$), which is linearly proportional to the concentration of total glutathione in the sample, is determined.

At the same time, the concentrations of *oxidised glutathione* (GSSG) are determined using the modified enzymatic assay developed in this work, referred to as *the GSSG (BQ/TNB) assay*. First, benzoquinone (BQ) is used to mask GSH in the samples. After the solution is well-mixed, TNB is added to the reaction mixture to remove excess BQ. An aliquot of the mixture is then transferred to a UV-vis cuvette, followed by the addition of DTNB, GR and NADPH. The spectrophotometric monitoring at 412 nm (A_{412}) is then performed as described above. The concentrations, temperature and pH are optimised below and the final protocol is presented in Figure 6.6.

The levels of *reduced glutathione* (GSH) can be calculated from the difference in concentrations of the total and oxidised glutathione.

6.2.3 Recovery study in plasma and saliva samples

Plasma and saliva samples are spiked with 15 μM, 50 μM (plasma only) and 100 μM GSH in final concentrations. The spiked samples are incubated at 25 °C and the concentrations of total, reduced and oxidised glutathione determined every 10 minutes for the total of 90 minutes using the Tietze assay together with the GSSG assay.

6.3 Results and discussions

The GSSG assay developed herein is based on the selected 1,4-addition ("Michael addition") of the GSH thiol in a mixture of GSH and GSSG to a quinone. After reaction, only the oxidised form of glutathione, GSSG, is left in the sample. The quinone-treated sample is then subjected to the Tietze enzymatic kinetic assay, which determines the concentration of the remaining GSSG. The assay is first optimised to explore the most efficient excess quinone scavenger and the thiol-masking quinone, as well as the most suitable reaction conditions: pH, temperature, reaction time and concentrations. The optimised assay is then validated

using variable concentrations of GSH, GSSG and mixtures of GSH and GSSG standards. Subsequently, the assay is applied to real biological samples including human plasma and saliva samples. Further applications of the assay to investigate the stability of the total glutathione and of GSH, as well as the formation of GSSG in plasma and saliva samples are then performed.

6.3.1 Assay optimisation

GSH standard solutions were subjected to the Tietze assay to determine the rate of TNB formation (s_0) for each concentration. Aliquots of the GSH solutions were then reacted with quinone, and the excess quinone removed by the addition of a non-GSH thiol, as detailed later. Afterwards, the quinone-treated solutions were subjected to the enzymatic measurement. The resulting rate of TNB formation (s_1) reveals the amount of GSH left unreacted. The proportion of GSH remained in the solution is calculated by $s_1/s_0 \times 100$ %. The amount of GSH removed by quinone is therefore $(1 - s_1/s_0) \times 100$ %.

Excess thiol-masking quinone in the solution has to be removed prior to the enzymatic measurements to prevent undesirable reactions between quinone and the TNB formed during enzymatic cycling. Due to the selectivity of the enzyme, this can be done by the addition of thiols other than GSH. The quinone-scavenging non-GSH thiol does not contribute to the rate of $\mathrm{d}A_{412}/\mathrm{d}t$.[25,26]

To identify the most suitable quinone-quenching reagent, four thiols which react rapidly with quinone including cysteine, 2-mercaptoethanesulfonate, 2-mercaptoimidazole and 2-nitro-5-thiobenzoate (TNB) were investigated, refer to Figure 6.2 for chemical structures of the relevant compounds. The first three thiols were supplied by commercial providers, while TNB was made by the addition of $NaBH_4$ to the solution of DTNB.

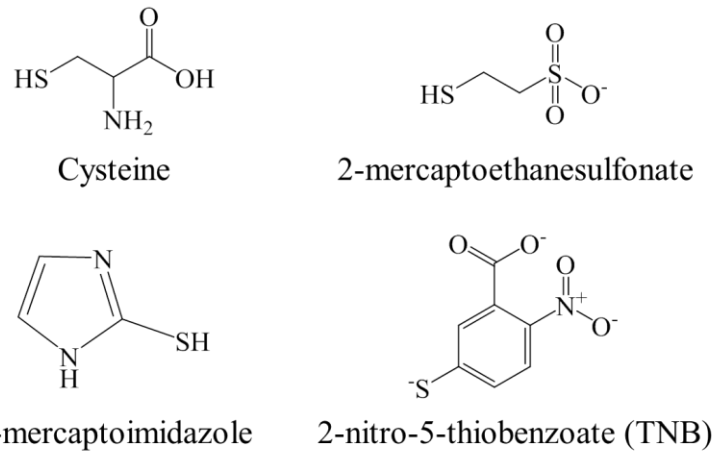


Figure 6.2: Structures of the quinone-quenching thiols investigated in this work; cysteine, 2-mercaptoethanesulfonate, 2-mercaptoimidazole and 2-nitro-5-thiobenzoate (TNB)

The solution of 40 μM GSH was treated with 300 μM benzoquinone, followed by 300 μM of the different thiols. The concentration of the remaining GSH was determined to find out the most efficient quinone-quenching reagent. In addition to GSH standards, the reactions between 20 μM GSSG and 300 μM benzoquinone, followed by 300 μM of the thiols were performed to determine whether the thiols added interferes with the GSSG (BQ/TNB) measurement assay.

It was found that 1.9 ± 0.2 %, 3.87 ± 0.07 %, 0.08 ± 0.07 % and 1.42 ± 0.05 % of GSH was left in the solution when cysteine, 2-mercaptoethanesulfonate, 2-mercaptoimidazole and TNB were used respectively. 2-mercaptoimidazole gives rise to the smallest amount of GSH being left unreacted in the solutions. However, it was found that when 20 μM GSSG was treated with 300 μM benzoquinone, followed by 300 μM of 2-mercaptoimidazole, no GSSG was recovered. This suggests either that the compound cannot quench benzoquinone or the compound itself interferes with the measurement assay. Meanwhile, TNB solution which can also mask off GSH efficiently has been proved not to interfere with the measurement of GSSG that > 99% of GSSG was recovered when 20 μM GSSG was treated with 300 μM

benzoquinone, followed by 300 μM TNB. TNB is thus used as a quinone-scavenger throughout the remainder of this work.

Next, it is important to identify a quinone compound which very efficiently removes free GSH from the system. Four quinone or quinone-like species with different substituents including 1,4-benzoquinone, 1,4-naphthoquinone, 2-chloro-1,4-benzoquinone and 2,6-dichloroquinone-4-chloroimide were investigated, see Figure 6.3 for structures of the compounds.

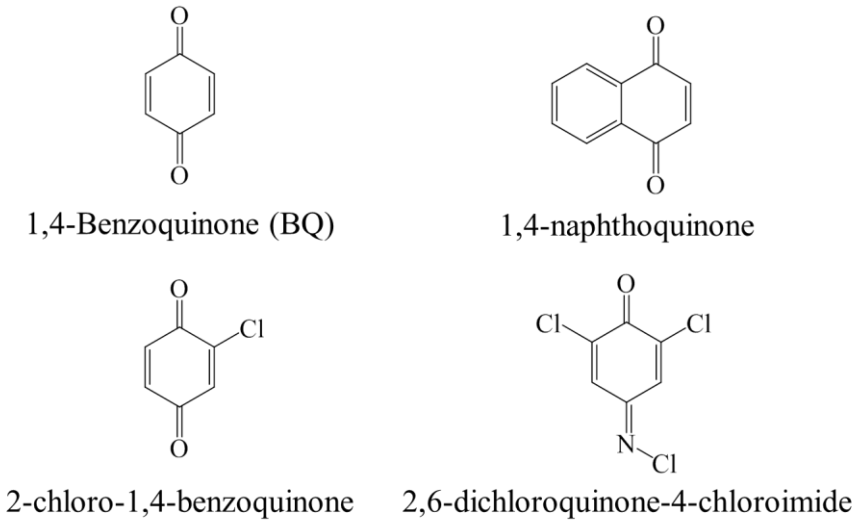


Figure 6.3: Structures of the quinones investigated in this work; 1,4-benzoquinone, 1,4-naphthoquinone, 2-chloro-1,4-benzoquinone and 2,6-dichloroquinone-4-chloroimide

The solutions of 40 μM GSH in the presence of 300 μM of different quinones (followed by 300 μM TNB) were studied. The concentration of the remaining GSH was determined to find out the most efficient thiol-masking quinone. The results show that 1.4 ± 0.1 %, 22.4 ± 0.6 %, 2.8 ± 0.1 % and 4.6 ± 0.3 % of free GSH remained in the solution when 1,4-benzoquinone, 1,4-naphthoquinone, 2-chloro-1,4-benzoquinone and 2,6-dichloroquinone-4-chloroimide were used respectively. It has been further shown that if excess benzoquinone is removed by

sufficient amount of TNB, GSSG concentration is not affected by the use of the reagent in the assay. Consequently, 1,4-benzoquinone (BQ) was chosen as the thiol-masking agent for the GSSG assay.

The reaction conditions including reaction time (between GSH and BQ), pH, temperature and concentrations are optimised next.

Reaction time. The reaction between BQ and GSH goes to completion in less than 20 s. Increasing the reaction time does not result in further masking of GSH i.e. no change in the 1.5 ± 0.2% of GSH remained in the solution.

Temperature. The reaction was studied at 0 °C, 25 °C and 40 °C. The amounts of GSH remained in the three temperatures studied were 1.6 ± 0.1 %, 1.4 ± 0.1 % and 1.7 ± 0.1 % at 0 °C, 25 °C and 40 °C respectively, and hence not distinguishably different within experimental errors. For convenience, the assay is therefore suggested to be performed at room temperature (25 °C).

pH. The reaction between BQ and GSH was studied at pH 1.0, 7.5 and 12.0. At pH 7.5 and 12.0, the masking of GSH was similarly efficient with 1.4 ± 0.1 % and 1.7 ± 0.1 % of GSH remained respectively. In contrast, > 44% of GSH was left unmasked in the solution at pH 1.0. The inefficient masking in acidic condition is thought to be due to the unfavourable 1,4-addition reaction between the protonated TNB and BQ. The higher amount of unmasked GSH equivalent at pH 12.0 as compared to at pH 7.5 is likely due to either the formation of a small amount of GSSG at very high pH[27] or the reaction of OH^- with BQ.[28] The reaction medium is therefore suggested to be at pH ~7.5 for the most efficient masking of GSH and so that additional pH adjustment when performing the enzymatic cycling is not required.

Concentrations. For 40 μM of GSH, 50 μM of BQ has been observed to be able to minimise the amount of remaining unmasked GSH to 1.5 ± 0.3 %, the lowest we can possibly obtain using the developed assay. Increasing the concentration of BQ further does not change the amount of GSH left in the solution. At the same time, the concentration of TNB has to be in excess of any remaining unreacted BQ to ensure none of BQ is left to interfere with the formation of TNB from enzymatic cycling.

6.3.2 Assay validation and calibration curves

In this section, the optimised GSSG (BQ/TNB) assay is validated. Standard solutions of variable concentrations: GSH, GSSG and GSH/GSSG mixtures were studied. First, GSH solutions were tested to evaluate whether the BQ/TNB assay efficiently removes GSH from the solutions. Second, GSSG solutions were studied to ensure that the BQ/TNB assay selectively masks GSH, and does not affect the concentration of GSSG. Third, the GSH/GSSG solution mixtures were studied to demonstrate that the BQ/TNB assay, together with the Tietze assay, can be used to quantify the amount of both GSH and GSSG, as well as the ratio between the two species accurately. Consequently, the standard solutions were subjected to the total glutathione (Tietze) and the GSSG assays. The rates of change in the absorbance at 412 nm ($\mathrm{d}A_{412}/\mathrm{d}t$) were measured in the absence of BQ/TNB (i.e. total glutathione assay) and were compared with those in the presence of the BQ/TNB (i.e. GSSG assay).

For all the solutions of GSH studied, the results of $\mathrm{d}A_{412}/\mathrm{d}t$, presented as a function of GSH concentration in Figure 6.4a, show the efficient depletion of free GSH in the BQ/TNB assay with less than 1.5% of GSH remaining in the solution after the reaction with BQ for all the concentrations studied. At the same time, the concentrations of GSSG in standard GSSG solutions were not altered by the presence of BQ and excess TNB within the experimental

errors of 1.8%; refer to Figure 6.4b. The sensitivity of GSSG measurement obtained in the presence of 50 μM BQ and 50 μM TNB, at the range 0 – 20 μM, is 0.307 ± 0.002 ms^{-1} μM^{-1}. The limit of detection [$c_{L(k=3)}$] is determined to be 0.02 μM.

The assay was further applied to the mixtures of GSH and GSSG. The reactions as well as the measurements were performed in buffered solution containing 10 mM EDTA. At this high concentration of EDTA, it has been reported that oxidation of GSH to GSSG in non-biological media does not occur within 3 hours with the experimental errors of less than ±2%.[29] The reference GSH:GSSG ratio in the solution can therefore be taken from the concentrations of GSH and GSSG used to prepare the solution. The ratios of GSH:GSSG measured using the assay are 98.7 ± 1.3 % of the actual ratios of GSH:GSSG in the solutions, as displayed as a scattered plot in Figure 6.4c, evidencing the high accuracy of the developed assay.

6.3.3 Assay limitation

As discussed above, there is an inherent error of ca. 1.5 % of the assay, the size of which is comparable to that reported for the 2VP assay.[19] The origin of the small amount of remaining GSH equivalent is unclear. One possibility is the conversion of a small amount of GSH to GSSG. Although literature reports suggest that no GSSG is formed from the reaction between BQ and GSH,[30,31] there may be a difference in the sensitivity of the technique used. Another possible route is the substitution reaction of TNB to the GS-BQ compound, resulting in the reformation of free GSH. However, this process is also unlikely due to TNB ($pK_{a,\ thiol}$ = 4.5)[32] being a much better leaving group than GS^- ($pK_{a,\ thiol}$ = 9.1).[33] No GSSG impurity is detected in the standard solutions as determined by titration with DTNB without the enzymatic cycling.

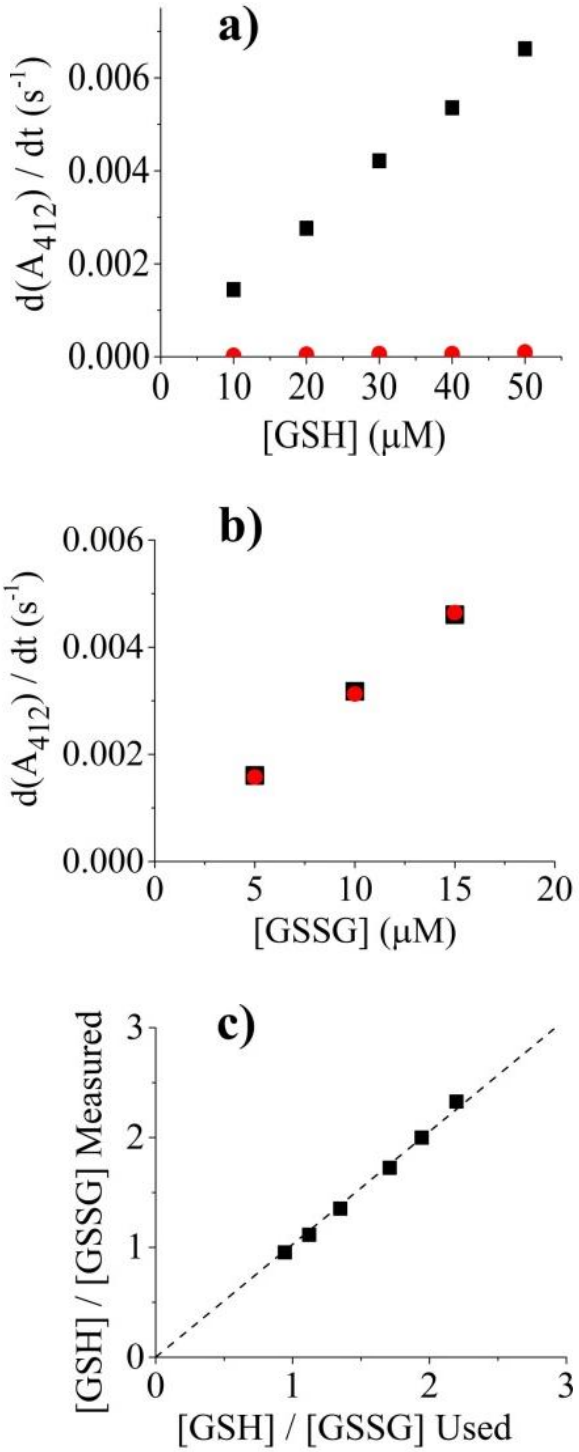


Figure 6.4: Calibration curves showing the rates of TNB formation (dA_{412}/dt, s^{-1}) determined by (**Black** (■)) Tietze assay using the conditions recommended by Rahman et al.[34]; (**Red** (●)) the GSSG (BQ/TNB) assay using 50 μM BQ, 50 μM TNB, 25 °C, pH 7.5 for variable concentrations of the solutions of **a)** GSH and **b)** GSSG. **c)** The GSH:GSSG ratios determined *vs.* the GSH:GSSG ratios used to prepare the solutions.

Due to the 1.5% error of the assay, the measurements of GSH:GSSG ratio is not recommended for systems whose ratios are expected to exceed ~67. Nonetheless, the concentrations of GSH, GSSG, as well as the ratio between the two species (i.e. oxidative status) in typical biological samples such as plasma and saliva are within the ranges that can be detected accurately (within 1.5% of the measurement error) using the developed assay, as will be evidenced in the following section.

6.3.4 Applications of the GSSG (BQ/TNB) assay

- **Quantification of GSH and GSSG in human plasma and saliva samples**

The optimised BQ/TNB assay has been validated against standard GSH and GSSG solutions. In this section, the assay will be used in the quantification of GSH and GSSG in biological samples. Two biological media are employed. One is the most commonly used medium for health diagnosis, namely plasma. The other is the clinically non-invasive alternative saliva.

In this work, the biological samples are assayed without deproteinisation. However, if the samples were to be deproteinised by the addition of acids,[34] the pH would need to be adjusted to ca. 7.5 prior to the measurement, simply by the addition of NaOH as the reaction between BQ and GSH is not efficient in acidic solution, as mentioned above. In addition, BQ can react with other thiols in the samples such as cysteine, homocysteine, as well as other nucleophiles and reducing agents. Therefore, a sufficient amount of BQ has to be added to ensure that the maximal possible amount of GSH in the sample has been masked by the BQ. For this reason, the amount of BQ used in biological samples for the measurement of GSSG is 185 μM (followed by 370 μM TNB), higher than the 50 μM (followed by 50 μM TNB) used for the standard solutions. The BQ concentration of 185 μM employed has been validated by the addition of increasing concentrations of GSH solutions to aliquots of the samples. The

concentration of BQ may be adjusted to suit various samples as long as the concentration of TNB is adjusted accordingly. The results are shown in Figures 6.5a and 6.5b for plasma and saliva respectively. The errors of the measurement (%GSH remained) are determined from the slopes of the amount of GSH remaining plotted against the amount of GSH added to be 0.7 ± 0.1 % and 0.1 ± 0.03 % for plasma and saliva respectively. The amount of GSH equivalent detected when no GSH is added reflects the concentration of GSSG initially present in the sample.

The assay has then been employed to quantify the amount of GSH and GSSG in plasma and saliva samples. The levels of GSH and GSSG found in plasma were 4.20 ± 0.12 μM and 1.99 ± 0.08 μM respectively, similar to the values reported in literature measured using HPLC.[35] In saliva, 3.14 ± 0.50 μM and 0.60 ± 0.15 μM were detected for GSH and GSSG respectively, consistent with the literature values determined by HPLC[36] and by chromatography / mass spectroscopy[37]. The assay has thus been proved to be able to accurately determine the concentrations of GSH and GSSG in plasma and saliva samples. More importantly, the developed technique is significantly quicker and less inexpensive than measurements by HPLC or mass spectroscopy. It also does not require specific training for use of the instrument.

The GSSG assay has been further validated to be highly specific to GSH that other thiols in biological samples, cysteine and homocysteine, give rise to an undetectable change in the slope of A_{412} against time ($\mathrm{d}A_{412}/\mathrm{d}t$).

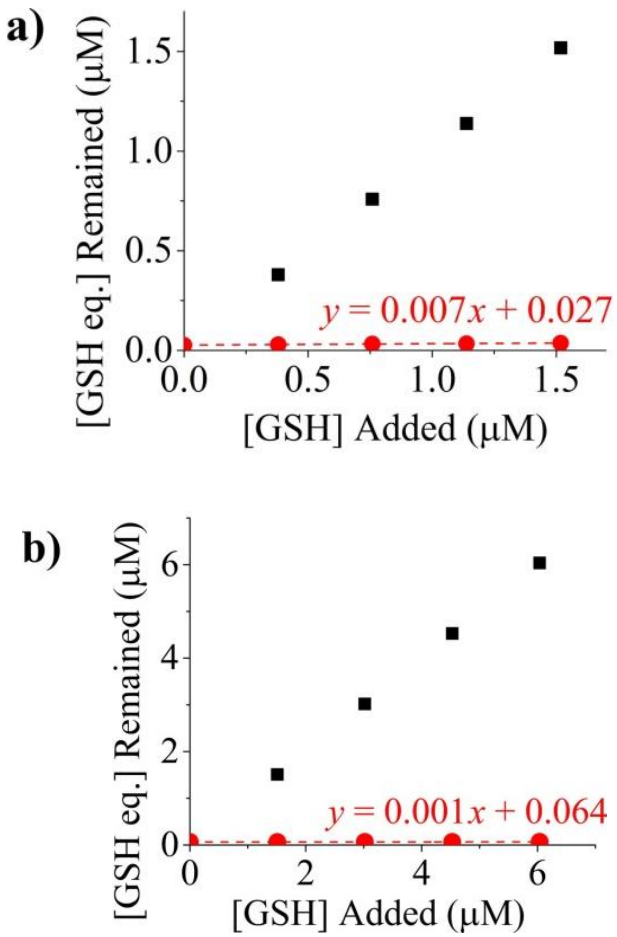


Figure 6.5: Validation of the GSSG (BQ/TNB) assay in **a)** plasma, and **b)** saliva. The black squares (■) and red circles (●) designate the amounts of GSH expected without the masking by BQ/TNB and the GSH measured with the GSSG (BQ/TNB) assay respectively. The equations displayed in the graphs are those for the lines of best-fit of the GSH concentrations measured with the GSSG (BQ/TNB) assay as a function of GSH added. The slopes of 0.007 and 0.001 give the errors of the measurements of 0.7% and 0.1% for plasma and saliva respectively.

For practical applications, the recommended protocol of the *GSSG (BQ/TNB)* assay for plasma and saliva samples is summarised in Figure 6.6. The protocol describes the reagents employed, the assay for the masking of GSH as well as the assay for enzymatic measurement of glutathione.

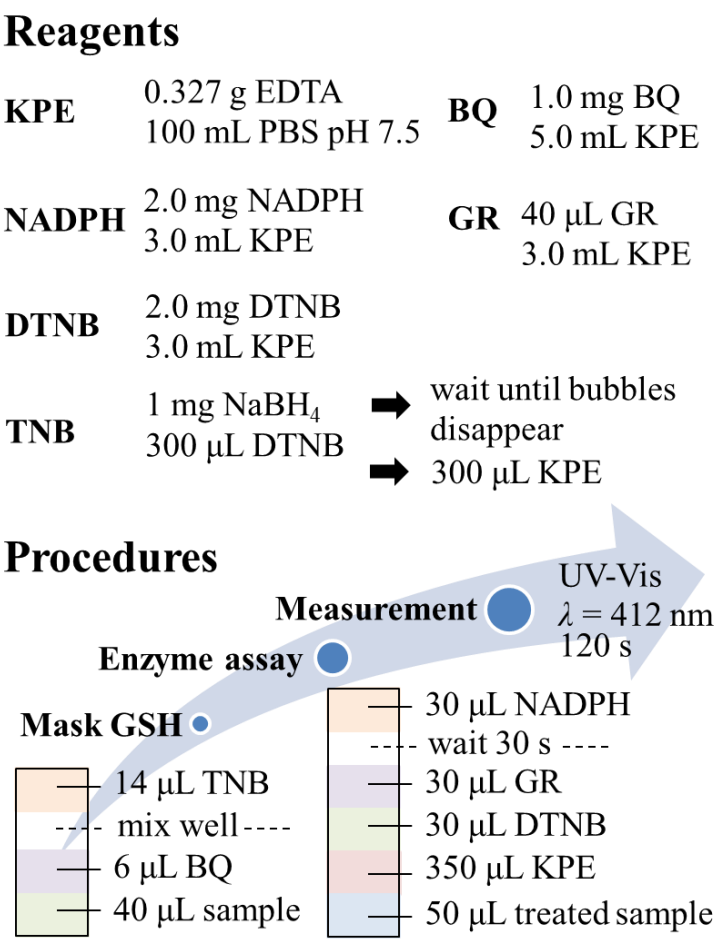


Figure 6.6: Protocol of *GSSG (BQ/TNB)* assay for plasma and saliva samples describing the concentrations of the reagents recommended and the procedures for the masking of GSH as well as the practice of the enzymatic measurement

- **Recovery of glutathione added to human plasma and saliva samples**

The amounts of GSH and GSSG were measured *in-vitro*. The concentrations of both species, however, have been reported to change with storage time.[6,38] Plasma GSH, in particular, has been reported to decay at a very fast rate at room temperature with a half-life of ca. 20 min.[6,38] The fast changes in GSH and GSSG concentrations in plasma potentially result in serious *in-vitro* artefacts. For saliva, on the other hand, there is no literature report on the stability of GSH and GSSG at room temperature. Although there are data showing that

salivary GSH is stable for up to 30 days at –20 °C.[23] Therefore, in order to study the stability of glutathione in saliva samples at room temperature as well as to investigate the effect of the medium (plasma *vs.* saliva) on the rates of changes in GSH and GSSG concentrations, recovery studies are performed next. The recovery study further highlights the key advantage of the short experimental time of the developed GSSG (BQ/TNB) assay. In contrast to the other existing enzymatic techniques for the measurement of GSH and GSSG, the newly developed BQ/TNB assay can be completed in 2 minutes and hence are suitable for uses in short timescale study.

In this study, plasma and saliva samples were spiked with the solutions of GSH to yield the initial GSH concentrations (at $t = 0$) of 15 μM and 100 μM in the spiked samples. The samples were then incubated at 25 °C and the concentrations of total glutathione, GSH and GSSG were determined every 10 minutes for the total time of 90 min. Note that the concentrations presented here are corrected for the concentrations of GSH and GSSG initially present in the sample, i.e. those initially present in the samples are treated as background concentrations and have been set to zero.

In the following discussions, we give values of the concentrations of total glutathione, GSH and GSSG after incubation at 25 °C for 20 minutes. The full set of concentrations measured every 10 min for the total of 90 min are presented as 'normalised' concentrations in Figure 6.7 for a clear comparison between the plasma and saliva, and between the different concentrations studied. The normalised concentration ($c_{\text{normalised}}$) is the concentration measured at time t ($c_{(t)}$) divided by the initial concentration ($c_{(t=0)}$); $c_{\text{normalised}} = c_{(t)} / c_{(t=0)}$. All concentrations are given as GSH equivalents which are equal to [GSH] + 2[GSSG] and 2[GSSG] for total glutathione and oxidised glutathione respectively.

Plasma. The concentrations of plasma glutathione change rapidly at both initial GSH concentrations studied (15 μM and 100 μM). At 15 μM initial GSH concentration after incubation at 25 °C for 20 min, the concentrations of total glutathione and GSH drop to 41% and 36%, while GSSG concentration rises to 5%. For the initial GSH of 100 μM, the concentrations of total glutathione and GSH are 73% and 60% after 20 min incubation respectively, while GSSG increases to 13%.

Saliva. The levels of salivary total glutathione, GSH and GSSG change very slowly with time. The total glutathione and GSH levels are stable within the errors of ±6% and ±3% for the initial GSH concentrations of 15 μM and 100 μM in the first 20 min of incubation. After 20 min, the changes in concentrations of total glutathione and GSH become more significant, reaching up to 20% after incubation for 90 min, the change of which is nonetheless much smaller than in plasma.

The significantly greater stability of saliva at room temperature (25 °C) offers the advantage of more reliable clinical information regarding antioxidant and the oxidative status of the cells compared to the information obtained from plasma currently used for the diagnosis.

The results of the stability studies presented in Figure 6.7 further show that the concentration of GSSG increases as a function of time, while the concentration of GSH decreases, suggesting there is a conversion of GSH to GSSG. However, the concentration of *total* glutathione also decreases with time. This implies that not all the consumption of GSH is due to the formation of GSSG. Consequently, to further explore the stability of GSH and GSSG in the samples, we additionally observed the speciation of the products at different initial GSH concentrations studied.

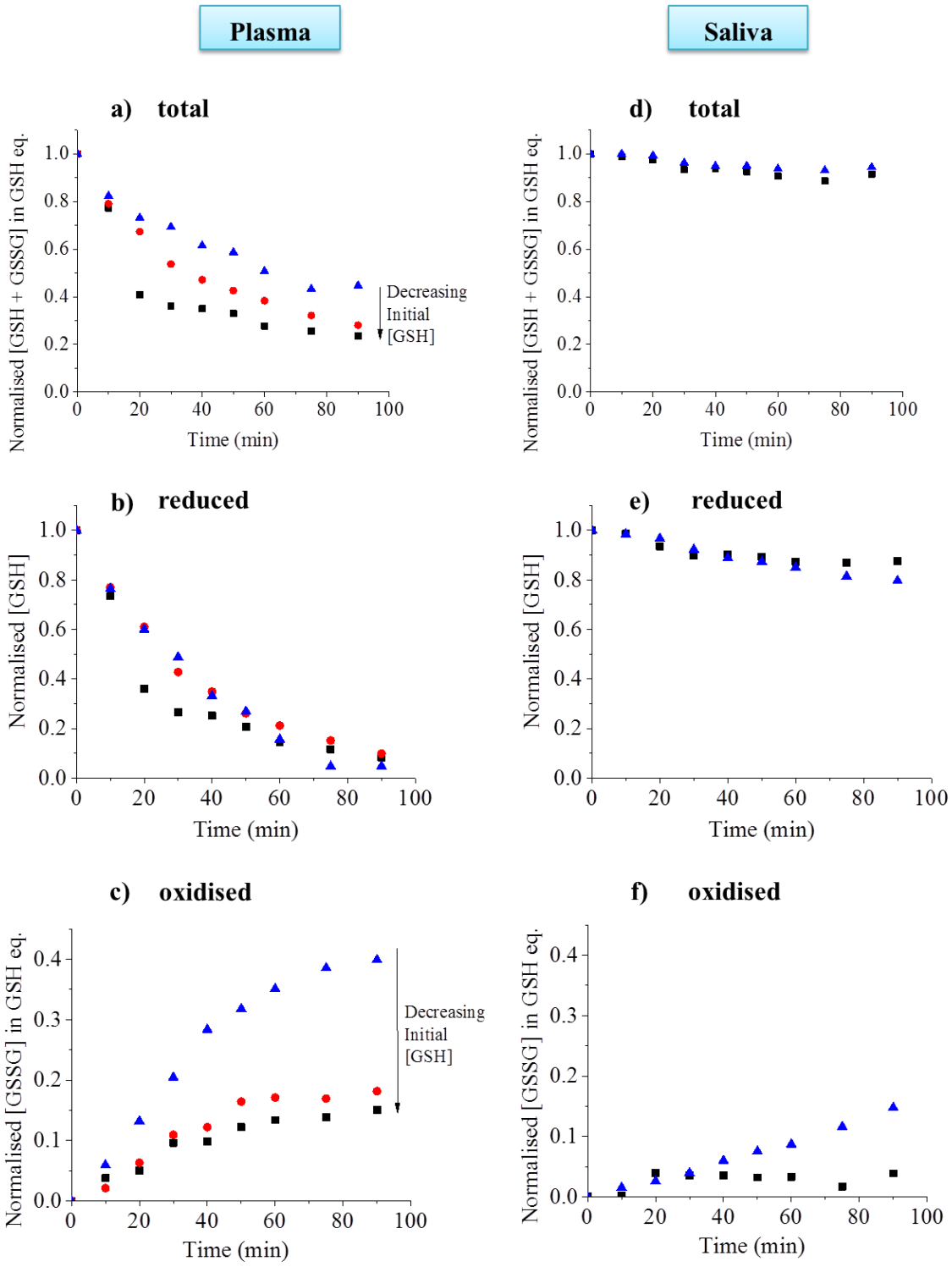


Figure 6.7: Plasma: changes in normalised concentrations ($c_{normalised} = c_{(t)}/c_{(t=0)}$) of **a)** total glutathione (GSH + GSSG), **b)** reduced glutathione (GSH) and **c)** oxidised glutathione (GSSG) as a function of time at different initial GSH concentrations spiked in plasma; **blue**: 100 µM, **red**: 50 µM, **black**: 15 µM. **Saliva:** changes in normalised concentrations of **d)** total glutathione (GSH + GSSG), **e)** reduced glutathione (GSH) and **f)** oxidised glutathione (GSSG) as a function of time at different initial GSH concentrations spiked in saliva; **blue**: 100 µM, **black**: 15 µM.

In saliva, the speciation of the products after incubation at 25 °C for 90 minutes, described in terms of the ratio of GSSG to other products, changes from 0.4 (4% : 9%) to 2.5 (15 % : 6%) for the initial concentration changes from 15 μM to 100 μM. On the other hand, the speciation changes of the products in plasma are 0.2 (15% : 77%) and 0.7 (40% : 55%) at the initial GSH concentrations of 15 μM and 100 μM respectively.

This result may be explained by the two possible routes of the loss of GSH from the system. First is the oxidation of GSH to GSSG catalysed by metal catalysts such as copper(II), further discussed in Chapter 7.[29] Second is the degradation of GSH into its amino acid constituents (glutamic acid, cysteine and glycine) catalysed by the enzyme γ-glutamyltransferase (GGT).[39] The concentrations of copper in plasma and saliva have been reported to be ca. 20 μM[40-42] and 1 μM[43] respectively, although there are papers reporting a wide range of copper contents in saliva from 0.8 μM to 12.0 μM.[44,45] Salivary and serum GGT activities have been reported to be 2.9 ± 1.0 units/L and 14.6 ± 5.8 units/L respectively.[46] The levels of copper as well as the activities of GGT in the two media are consistent with the results that salivary glutathione is, on the basis of these results, more stable than plasma. Consequently, this information together with the variable speciation of products observed support the hypotheses that both metal and biological catalysts play important roles in the loss of GSH as well as total glutathione from biological samples.

In addition to copper and GGT, the formation of mixed protein disulfides may also contribute to the loss of glutathione from biological samples. The total protein content in plasma (68.5 ± 1.0 mg/mL)[47] is two orders of magnitude higher than in saliva (0.68 ± 0.07 mg/mL),[48] consistent with the fact that the loss of glutathione in plasma happens much more rapidly than in saliva. However, note that the concentration of glutathione decreases rapidly in plasma

even when the samples are deproteinized, suggesting the significant roles of copper and GGT.[6]

After all, the results presented herein display potential problems in accurately determining the levels of glutathione in biological samples due to the *in-vitro* artefacts. At the same time, the results show that the problem is minimised in saliva, and hence emphasise that saliva offers greater advantage than plasma in terms of the stability of GSH and GSSG in addition to its non-invasive nature.

6.4 Conclusions

Benzoquinone (BQ) has been introduced as a new, rapid thiol-masking reagent for uses in the quantification of GSH and GSSG via the enzymatic recycling assay. Excess BQ is removed by the rapid reaction with TNB (made from the reduction of DTNB by $NaBH_4$), exploiting the selectivity of glutathione reductase. This developed assay can be completed within 2 minutes, in contrast to other techniques which require at least 30 minutes for reaction to go to completion (e.g. 2VP), or for the efforts required to remove excess chemical (e.g. NEM). The assay can be directly applied to biological samples such as plasma and saliva. The BQ/TNB assay is thus a significant improvement to the enzymatic cycling assay, which is the most widely-used technique for determination of glutathione. The new assay has been demonstrated to be particularly useful in situations where limited time is available for accurate analysis such as the diagnosis of plasma glutathione, the level of which decreases significantly with the half-life of ca. 5-20 minutes (half-life decreases with initial concentration), or the kinetic/stability study of glutathione levels in biological samples, such as the work done in this chapter. From this demonstration of application of the developed assay, it is further shown that the use of saliva is preferential for the determination of GSH, GSSG and the oxidative status in terms of the stability and the accurate representation of the

'true' values of these parameters in the body (i.e. minimised *in-vitro* effect in saliva than plasma) in addition to the non-invasive nature of its sampling. The process of copper(II)-catalysed GSH oxidation which contributes to the difference in glutathione stability in saliva and plasma samples will be investigated in the following chapter.

Bibliography

(1) Ngamchuea, K.; Batchelor-McAuley, C.; Compton, R. G. *Anal. Chem.* **2017**, *89*, 2901-2908.
(2) Sies, H. *Oxidative Stress*; Elsevier Science, Academic Press Inc., London, UK, **2013**.
(3) Pastore, A.; Federici, G.; Bertini, E.; Piemonte, F. *Clin. Chim. Acta* **2003**, *333*, 19-39.
(4) Schulz, J. B.; Lindenau, J.; Seyfried, J.; Dichgans, J. *Eur. J. Biochem.* **2000**, *267*, 4904-4911.
(5) Mills, B. J.; Weiss, M. M.; Lang, C. A.; Liu, M. C.; Ziegler, C. *J. Lab. Clin. Med.* **2000**, *135*, 396-401.
(6) Beutler, E.; Duron, O.; Kelly, B. M. *J. Lab. Clin. Med.* **1963**, *61*, 882-888.
(7) Reed, D. J.; Babson, J. R.; Beatty, P. W.; Brodie, A. E.; Ellis, W. W.; Potter, D. W. *Anal. Biochem.* **1980**, *106*, 55-62.
(8) Neuschwander-Tetri, B. A.; Roll, F. J. *Anal. Biochem.* **1989**, *179*, 236-241.
(9) Serru, V.; Baudin, B.; Ziegler, F.; David, J. P.; Cals, M. J.; Vaubourdolle, M.; Mario, N. *Clin. Chem.* **2001**, *47*, 1321-1324.
(10) Carru, C.; Zinellu, A.; Mario Pes, G.; Marongiu, G.; Tadolini, B.; Deiana, L. *Electrophoresis* **2002**, *23*, 1716.
(11) Harfield, J. C.; Batchelor-McAuley, C.; Compton, R. G. *Analyst* **2012**, *137*, 2285.
(12) Lee, P. T.; Goncalves, L. M.; Compton, R. G. *Sens. Actuators, B* **2015**, *221*, 962-968.
(13) Zaidi, S. A.; Shin, J. H. *Anal. Methods* **2016**, *8*, 1745-1754.
(14) Chen, Z.; Wang, Z.; Chen, J.; Wang, S.; Huang, X. *Analyst* **2012**, *137*, 3132-3137.
(15) Han, H.-Y.; He, Z.-K.; Zeng, Y.-E. *Microchim. Acta* **2006**, *155*, 431-434.
(16) Monostori, P.; Wittmann, G.; Karg, E.; Turi, S. *J. Chromatogr. B Analyt. Technol. Biomed. Life Sci.* **2009**, *877*, 3331-3346.
(17) Camera, E.; Picardo, M. *J. Chromatogr. B* **2002**, *781*, 181-206.
(18) Tietze, F. *Anal. Biochem.* **1969**, *27*, 502-522.
(19) Griffith, O. W. *Anal. Biochem.* **1980**, *106*, 207-212.
(20) Güntherberg, H.; Rost, J. *Anal. Biochem.* **1966**, *15*, 205-210.
(21) Giustarini, D.; Dalle-Donne, I.; Milzani, A.; Fanti, P.; Rossi, R. *Nat. Protoc.* **2013**, *8*, 1660-1669.
(22) Richie, J. P., Jr.; Skowronski, L.; Abraham, P.; Leutzinger, Y. *Clin. Chem.* **1996**, *42*, 64-70.
(23) Emekli-Alturfan, E.; Yarat, A.; Caliskan-Ak, E.; Pisiriciler, R.; Kuru, B.; Noyan, U. *J. Clin. Lab. Anal.* **2013**, *27*, 261-266.
(24) Riddles, P. W.; Blakeley, R. L.; Zerner, B. *Methods Enzymol.* **1983**, *91*, 49-60.
(25) Henderson, G. B.; Murgolo, N. J.; Kuriyan, J.; Osapay, K.; Kominos, D.; Berry, A.; Scrutton, N. S.; Hinchliffe, N. W.; Perham, R. N.; Cerami, A. *Proc. Natl. Acad. Sci. U. S. A.* **1991**, *88*, 8769-8773.
(26) Ngamchuea, K.; Batchelor-McAuley, C.; Cowen, P. J.; Williams, C.; Goncalves, L. M.; Compton, R. G. *Analyst* **2016**, *141*, 4707-4712.
(27) Eckert, K. G.; Eyer, P.; Sonnenbichler, J.; Zetl, I. *Xenobiotica* **2008**, *20*, 351-361.
(28) Lin, Q.; Li, Q.; Batchelor-McAuley, C.; Compton, R. G. *J. Phys. Chem. C* **2015**, *119*, 1489-1495.
(29) Ngamchuea, K.; Batchelor-McAuley, C.; Compton, R. G. *Chem. Eur. J* **2016**, *22*, 15937-15944.
(30) O'Brien, P. J. *Chem. Biol. Interact.* **1991**, *80*, 1-41.
(31) Brunmark, A.; Cadenas, E. *Chem. Biol. Interact.* **1988**, *68*, 273-298.
(32) Stewart, A. J.; Blindauer, C. A.; Berezenko, S.; Sleep, D.; Tooth, D.; Sadler, P. J. *FEBS J.* **2005**, *272*, 353-362.
(33) Kanchuger, M. S.; Byers, L. D. *J. Am. Chem. Soc.* **1979**, *101*, 3005-3010.
(34) Rahman, I.; Kode, A.; Biswas, S. K. *Nat. Protoc.* **2006**, *1*, 3159-3165.
(35) Michelet, F.; Gueguen, R.; Leroy, P.; Wellman, M.; Nicolas, A.; Siest, G. *Clin. Chem.* **1995**, *41*, 1509-1517.
(36) Zappacosta, B.; Manni, A.; Persichilli, S.; Boari, A.; Scribano, D.; Minucci, A.; Raffaelli, L.; Giardina, B.; De Sole, P. *Clin. Biochem.* **2007**, *40*, 661-665.

(37) Iwasaki, Y.; Hoshi, M.; Ito, R.; Saito, K.; Nakazawa, H. *J. Chromatogr. B Analyt. Technol. Biomed. Life Sci.* **2006**, *839*, 74-79.
(38) Jones, D. P.; Carlson, J. L.; Samiec, P. S.; Sternberg, P., Jr.; Mody, V. C., Jr.; Reed, R. L.; Brown, L. A. *Clin. Chim. Acta* **1998**, *275*, 175-184.
(39) Whitfield, J. B. *Crit. Rev. Clin. Lab. Sci.* **2001**, *38*, 263-355.
(40) Ward, A. F.; Mitchell, D. G.; Kahl, M.; Aldous, K. M. *Clin. Chem.* **1974**, *20*, 1199-1203.
(41) Aldor, Y.; Walach, N.; Modai, D.; Horn, Y. *Klin. Wochenschr.* **1982**, *60*, 375-377.
(42) Kurekci, A. E.; Alpay, F.; Tanindi, S.; Gokcay, E.; Ozcan, O.; Akin, R.; Isimer, A.; Sayal, A. *Epilepsia* **1995**, *36*, 600-604.
(43) Ayinampudi, B. K.; Narsimhan, M. *J. Oral Maxillofac. Pathol.* **2012**, *16*, 178-182.
(44) Dreizen, S.; Spies, H. A., Jr.; Spies, T. D. *J. Dent. Res.* **1952**, *31*, 137-142.
(45) Dejorge, F. B.; Canelas, H. M.; Dias, J. C.; Cury, L. *Clin. Chim. Acta* **1964**, *9*, 148-150.
(46) Jiménez-Alonso, J.; Sabio, J. M.; Rivera-Cívico, F.; Martín-Armada, M. a.; Rodríguez, M. Á.; Jáimez, L.; Castillo, M. a. J.; Sánchez-Román, J.; Castro, J. *Clin. Chim. Acta* **2003**, *334*, 225-231.
(47) Morris, B.; Courtice, F. C. *Q. J. Exp. Physiol. Cogn. Med. Sci.* **1955**, *40*, 127-137.
(48) Walsh, N. P.; Blannin, A. K.; Clark, A. M.; Cook, L.; Robson, P. J.; Gleeson, M. *J. Sports Sci.* **1999**, *17*, 129-134.

Chapter 7 The copper(II)-catalysed oxidation of glutathione

In this chapter, the kinetics and mechanisms of copper(II)-catalysed GSH oxidation are examined in the light of its biological importance and in the use of blood and/or saliva sample for GSH monitoring. The rates of 'free thiol' consumption in standard solutions were measured spectrophotometrically via reaction with DTNB, showing that GSH is not auto-oxidised by oxygen in the absence of a catalyst. In the presence of Cu^{2+}, reactions with two timescales were observed. The first step (short timescale) involves the fast formation of a copper-glutathione complex via the cysteine thiol. The second step (longer timescale) is the overall oxidation of GSH to GSSG catalysed by copper(II). When the initial concentrations of GSH are at least three-fold in excess of Cu^{2+}, the rate law is deduced to be $-\mathrm{d[thiol]/dt} = k[\text{copper–glutathione complex}][O_2]^{0.5}[H_2O_2]^{-0.5}$. The order of reaction with respect to O_2 of 0.5 reveals a pre-equilibrium prior to the rate-determining step of GSSG formation. In contrast to the effects of $[Cu^{2+}]$ and $[O_2]$, the rate of reaction decreases with increasing concentrations of GSH. This inverse relationship is proposed to be a result of competing formation of an inactive form of copper-glutathione complex (binding to glutamic and/or glycine moieties).

The work presented in this chapter has been published in *Chemistry – A European Journal*.[1]

7.1 Introduction

Glutathione is the most abundant thiol compound in animals and plants. Its reduced form functions as a cellular antioxidant, preventing oxidative damage caused by xenobiotic and endogenous reactive oxygen and nitrogen species. For this purpose, the level of reduced glutathione in biological subjects must be maintained, for example, at ca. 1.0 mM and 15 μM in human blood and saliva respectively.[2,3] Changes in reduced glutathione (GSH) concentrations in biological fluids are auxiliary diagnostic of health status as well as various diseases. The stability of GSH concentrations in the samples collected is thus highly important for the accuracy of blood and non-invasive saliva sensing technology.

There are several parameters which can affect the levels of reduced glutathione in biological systems. One of the influential factors, and the focus of this chapter, is the consumption of reduced glutathione via reactions, both stoichiometric and catalytic, with copper(II) ions. This reaction is of direct physiological relevance for certain diseases such as Wilson's disease, where the amount of copper(II) in blood is present in excess.[4,5] In such cases, haemolytic anemia may be induced by the decreased level of reduced glutathione. From the above reports, it may be proposed that the toxicity of copper is a consequence of glutathione and copper(II) reaction. However, the co-existence of glutathione and copper can inhibit the formation of reactive radicals by the stabilisation of copper(I) with reduced glutathione.[6,7] The presence of GSH has also been used as an anti-oxidant in the prevention of copper-dependent DNA damage.[8,9]

All of these properties are consequences of the formation of copper-glutathione complex and the depletion of reduced glutathione by oxidation reaction to its oxidised form, GSSG. Despite the biological importance, the mechanistic details of these processes have been unclear for decades. The previously suggested mechanisms include the simple redox process

of Cu^{2+} and GSH to Cu^{+} and GSSG.[10] The more complex mechanisms proposed involve detailed studies of the formation of different possible radical species due to much interest in the radical reactivity within the biological systems.[11,12] Studies based on GSSG formation and O_2 consumption have also been reported.[13] However, the stoichiometry as well as the kinetics of the reaction is unknown. Therefore, the re-evaluation of the fundamental mechanisms of GSH oxidation catalysed by Cu(II) is required.

In this work, only the situation where GSH is in excess is exclusively considered to focus on the 'catalytic' behaviour of copper(II) and to mimic physiological conditions where GSH is usually in large excess. The copper-glutathione complex formation is monitored by UV-vis spectrophotometry at a number of different times during the reaction. The concentrations of free thiols, including free GSH and GSH bound to copper(II) via the non-thiol sites, are determined by reactions with DTNB to form a coloured TNB species ($\varepsilon_{\lambda=412\ nm}$ = 14,150 cm^{-1}).[14] The change in absorbance values at 412 nm with experimental time is studied and the rate of consumption of free thiols assessed. The variation in rates as a function of different experimental parameters is analysed to yield the kinetics of the reaction.

The order of reaction with respect to the concentration of oxygen is determined and a pre-equilibrium step prior to the production of GSSG revealed. The intriguing apparent inverse relationship of the reaction rate with GSH concentrations is further observed. Consequently, this provides an insight into the formation and further rearrangement of copper-glutathione complexes. As a result, this chapter proposes the mechanisms of copper(II)-catalysed GSH oxidation which will help to gain better understandings of the role of GSH as well as copper(II) in biological systems.

7.2 Experimental methods

Copper-glutathione complex formation was monitored as a function of time using UV-vis spectrophotometry in the range of wavelengths of 250 nm to 1,000 nm.

The concentrations of reduced glutathione (GSH) were determined by the reaction with 5,5′-dithiobis(2-nitrobenzoic acid) (DTNB) producing a coloured product, TNB, which has a strong absorbance at 412 nm; refer to eqn. 7.1. The UV-vis spectra were recorded over the course of the experiment and the absorbance values at 412 nm plotted against time.

$$\text{DTNB} + \text{GSH} \longrightarrow \text{GS-TNB} + \text{TNB} \; (\varepsilon_{\lambda=412\ \text{nm}} = 14{,}150\ \text{cm}^{-1})\ ^{14} \qquad (7.1)$$

All the reactions involving glutathione and copper(II) took place in aqueous solution without the presence of other species such as buffers, which could potentially form a complex with copper. This potential interference is evidenced by the modelling of the speciation of copper(II) in the presence of phosphate buffer. For example, in a solution of 1 mM Cu^{2+} and 1 M PO_4^{3-} at pH 7, the concentrations of free Cu^{2+} and the main copper-complex formed ($CuHPO_4$) are simulated using Visual MINTEQ[15] to be 2.4×10^{-7} M and 1.0×10^{-3} M respectively.

Nonetheless, the measurement of free thiol concentration requires the presence of (phosphate) buffer for the thermodynamically-driven reaction of thiols with DTNB.[16] Hence, solutions of the reaction mixture (unbuffered) and DTNB (in phosphate buffer pH 7) were used and allowed to mix for 2 minutes prior to the measurements for absorbance at 412 nm.

7.3 Results and discussions

In this study, aqueous solutions of excess GSH and Cu^{2+} were allowed to mix in the absence or presence of O_2. The rates of the reactions were then determined by monitoring of either the changes in GSH concentrations or the copper-glutathione complex formation as a function of time. The kinetics of the reactions was investigated by analysing the dependence of the rates of GSH oxidation on the concentrations of Cu^{2+}, O_2 and GSH.

For the monitoring of GSH concentrations, the DTNB measurement method was first validated. Variable concentrations of standard GSH solutions (0.5 - 60 μM) were mixed with excess DTNB (87 μM) in phosphate buffer (pH 7). The UV-vis spectra of the reaction mixtures (2 minutes after mixing) and the linear calibration plot of absorbance values at 412 nm (A_{412}) as a function of GSH concentration are given in Figure 7.1. The absorbance value at 412 nm was also monitored for 10 minutes after GSH was mixed with DTNB. At t = 0 minute, A_{412} is ca. 4% lower than the stable value which is reached at ca. 2 minutes after mixing; refer to Figure 7.2. For all the following experiments, solutions of the reaction mixture (unbuffered) and DTNB (in phosphate buffer pH 7) were therefore mixed for 2 minutes prior to the measurements.

However, note that DTNB is not specific to GSH. The concentration of the species measured from A_{412} thus will be referred to as that of 'free thiols' or '–SH' throughout this chapter.

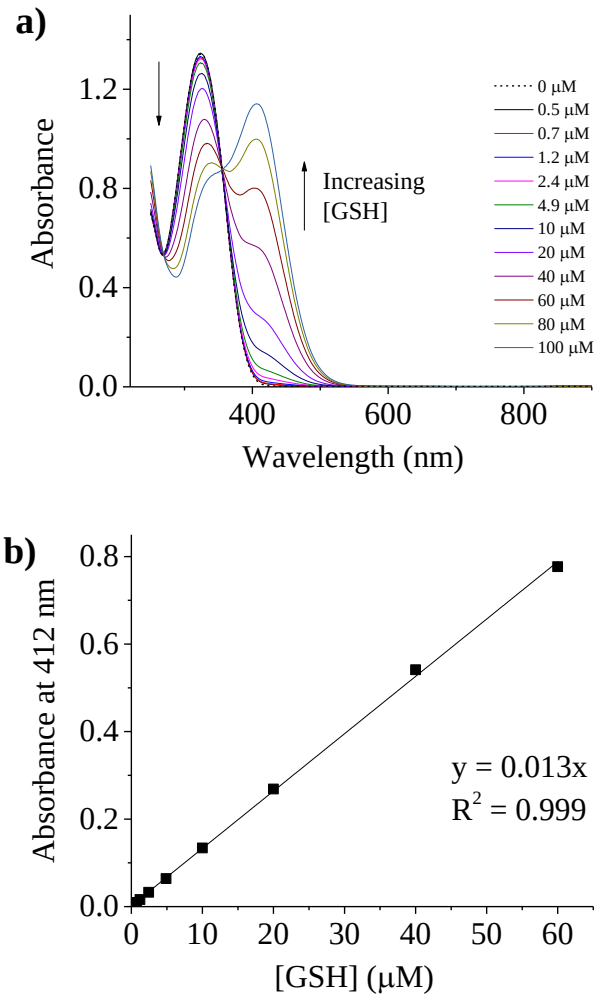


Figure 7.1: a) UV-visible spectra of the reaction mixture of varied concentrations of unbuffered GSH and 87 µM pH 7 buffered DTNB; **b)** Calibration plot of the absorbance values at 412 nm as a function of GSH concentration.

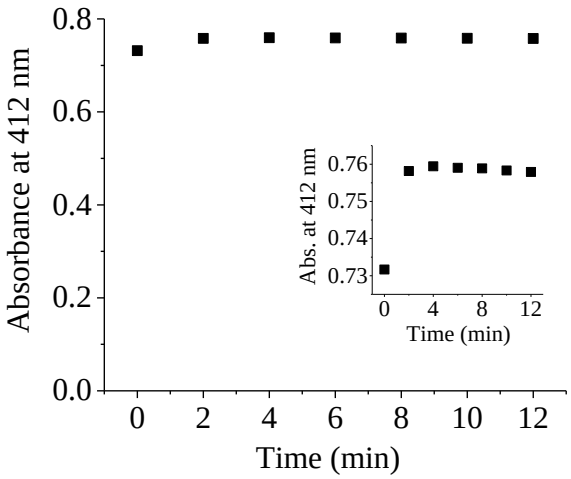


Figure 7.2: Absorbance values at 412 nm of the reaction mixtures of 87 µM DTNB and 60 µM GSH as a function of mixing time.

Using the validated DTNB method, buffered DTNB was added to aliquots of the reaction mixtures every 4 or 8 min to assess the levels of –SH in three different sets of experiments. First is the study of GSH auto-oxidation; that is the oxidation of GSH in the presence of O_2 but in the absence of Cu^{2+}. Second, the reaction between GSH and Cu^{2+} is investigated in the absence of O_2. Third, the oxidation of GSH is studied in the presence of both Cu^{2+} and O_2.

All the three situations above give rise to different patterns of reactivity and will be discussed next. In the following experiments performed in the presence of copper(II) catalyst, the kinetic data reveal two distinct timescales for the reactions. In the absence of O_2, the reaction occurring at a short timescale is referred to as step '*x*,' while that occurring at a long timescale is called step '*y*.' In the presence of O_2, steps 'X' and 'Y' designate the reactions occurring at short and long timescales respectively.

7.3.1 GSH oxidation in the presence of O_2, but in the absence of Cu^{2+}

The concentration of reduced glutathione in aqueous solution in the presence of atmospheric oxygen (0.27 mM O_2)[17] was measured as a function of time. The results showed that the GSH concentration is extremely stable in the absence of added metal catalysts, with the rate of GSH consumption as low as 6.6 ± 0.4 nM min^{-1} for the starting GSH concentration of 56 μM.

However, note that there is a ≤0.01 μM trace impurity of copper present in the solution (calculated from ≤0.0005% copper stated by Sigma-Aldrich). It was therefore further investigated if the slow oxidation of GSH observed in the absence of 'added' catalyst is a result of catalytic activity of the trace amount of copper(II) present. For this purpose, Cu^{2+} impurities in the GSH solution were removed by the addition of excess EDTA. The concentration of GSH in the reaction mixtures of 1.0 mM EDTA and 56 μM GSH was then

measured at different times. At these concentrations, over 99.99% of the Cu^{2+} ions are bound to EDTA (from the value of stability constant of the Cu(II)–EDTA complex formation of $10^{18.80}$) [18] and hence no longer available to participate in reactions with GSH. The result shows that the concentration of GSH is constant for the three hours studied with the experimental errors of less than ±2%. It thus can be deduced that a metal catalyst is required for GSH to be oxidised by oxygen at noticeable rates and that 'auto-oxidation' is unlikely, as reported previously by Warburg.[19] Furthermore, it is noted that the rate of GSH oxidation of 6.6 ± 0.4 nM min^{-1} for the 56 μM GSH solution (as presented at the beginning of this section) corresponds to sub-ten nanomolar concentration of Cu^{2+}, as estimated from the results that will be demonstrated later in Section 7.3.3a. The estimated concentration of Cu^{2+} is in good agreement with the manufacturer suggested concentration of the copper(II) impurities in solution.

7.3.2 GSH oxidation in the presence of Cu^{2+}, but in the absence of O_2

The concentrations of –SH were measured at different experimental times (every 4 or 8 minutes) after the deoxygenated solutions of Cu^{2+} and GSH were mixed in the absence of O_2. The experiments using 95 μM GSH and varied concentrations of Cu^{2+} (2.5 μM, 12.5 μM and 17.5 μM) were performed to study the stoichiometric ratio of Cu:GSH. Meanwhile, the fixed Cu^{2+} concentration of 5 μM and varied concentrations of GSH (56 μM, 85 μM and 110 μM) were used in the study of the effect of GSH concentrations on the rates of changes in –SH concentration.

The kinetic studies revealed two-step reactions (i.e. reactions with two different timescales). The first step, labelled as step '*x*' in Figure 7.3, showed a fast decrease in free thiols or –SH concentration when Cu^{2+} were added to the solution of GSH by the amount that is equal to one equivalent of Cu^{2+} used; please refer to Figure 7.3a.

Following the fast drop in –SH, there is a slow increase in –SH as time progresses, the process of which is referred to as 'step *y*.' The rate of –SH released from the Cu-SG complex in step *y* is dependent on the concentration of GSH; refer to Figure 7.3b.

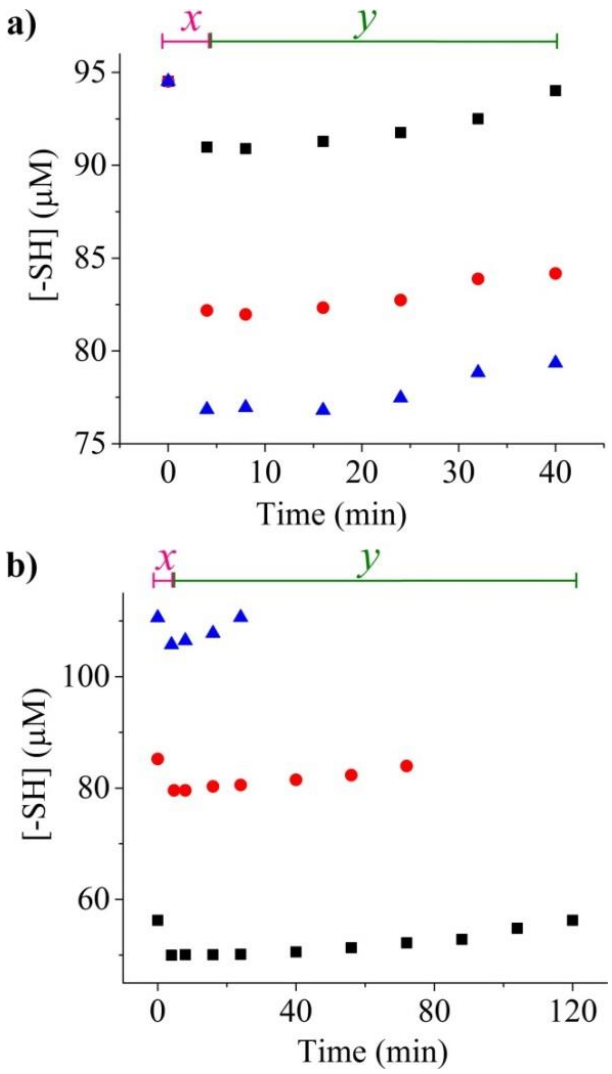


Figure 7.3: The concentrations of free thiols (–SH) at different experimental times for **a)** deoxygenated, 95 μM GSH, varied concentrations of Cu^{2+}: 2.5 μM (square), 12.5 μM (circle) and 17.5 μM (triangle); **b)** deoxygenated, 5 μM Cu^{2+}, varied concentrations of GSH: 56 μM (square); 85 μM (circle); 110 μM (triangle)

The decrease in –SH concentration observed in step *x* may be a result of either the fast oxidation of GSH to GSSG catalysed by Cu^{2+} or the formation of copper-glutathione complex via the thiol group; both processes of which would result in the loss of 'free' thiols. In order to elucidate this process further, the UV-vis spectra of different copper-glutathione complexes without the inclusion of DTNB were studied and are described next.

The UV-vis spectra of the species involved in the reaction were recorded and are displayed in Figure 7.4. Cu^{2+} and GSH showed no observable absorption in the wavelength range of interest, 250 - 350 nm.[20,21] GSSG exhibited a strong absorption at wavelengths below ~270 nm. The addition of Cu^{2+} to the solution of GSSG results in the reduction of absorbance in that region. This is possibly a result of the formation of Cu^{2+}- GSSG complex, which does not have strong absorption in this long-wavelength UV region. Proposed structures of Cu^{2+}–GSSG complexes have been reported. [22,23] Meanwhile, the strong absorption observed at 297 nm in the spectra of Cu^{2+} and GSH mixtures is ascribed as relating to the formation of copper-reduced glutathione complex,[19] the structure of which is unconfirmed and discrepancy exists in the literature. [24,25]

From the rapid increase in absorption at 297 nm when Cu^{2+} is added to the GSH solution and the stoichiometry between Cu^{2+} and GSH of 1:1 determined earlier, the fast drop in –SH concentration in step *x* is concluded to be a result of the formation of 1:1 Cu-SG complex via the cysteine moiety (eqn. 7.2).

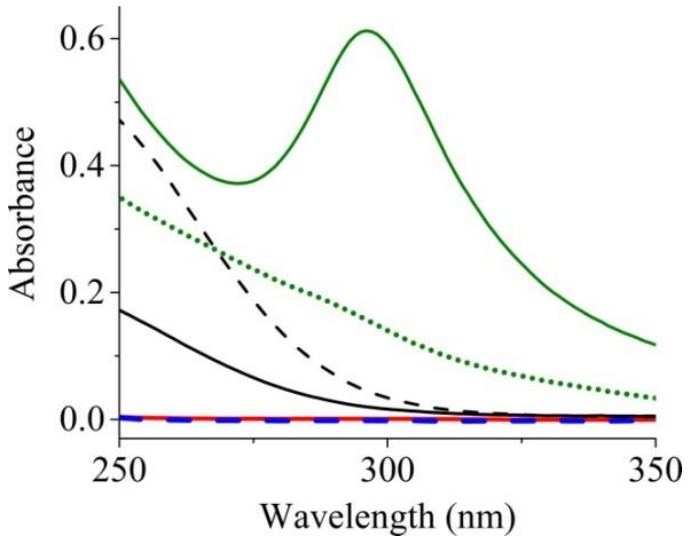


Figure 7.4: UV-vis spectra of 60 μM Cu^{2+} (red); 600 μM GSH (aq) (dashed blue); 300 μM GSSG (aq) (dashed black); 300 μM GSSG and 60 μM Cu^{2+} (aq) (solid black; remain unchanged with time); 600 μM GSH and 60 μM Cu^{2+} (aq) after mixing for 30 sec (dotted green) and 40 min (solid green)

An increase in free –SH concentration with time was observed in step *y* reaction (Figure 7.3b). This implies that there is a release of the thiol group initially bound to copper. We therefore propose the rearrangement of copper-glutathione complex from thiol-bound to glutamic/glycine-bound as the mechanism contributing to this phenomenon. The other routes such as the loss of Cu^{2+} availability in solutions have also been considered and were eliminated due to opposing evidences. Specifically, the alternative mechanisms were demonstrated to play a very minor role or not to be thermodynamically favourable. These alternative mechanistic pathways will be returned to towards the end of this section.

The rate of freeing the thiol groups depends on the concentration of GSH (step *y*, Figure 7.3b), suggesting the involvement of GSH and not simply the loss of Cu^{2+}. More importantly, this dependence on the GSH concentration indicates that the process proceeds via an intermolecular rather than intramolecular mechanism. Consequently, the copper-sulfur bond of the Cu-SG complex is concluded to be dissociated before the slow,

thermodynamically favourable re-combination of Cu with GSH through the glutamic and/or glycine moieties takes place (eqn. 7.3).

$$Cu^{2+} + GSH \underset{}{\overset{\text{fast}}{\rightleftharpoons}} Cu^{2+}\text{–}S(H)G \qquad (7.2)$$

$$Cu^{2+} + GSH \underset{}{\overset{\text{slow}}{\rightleftharpoons}} Cu^{2+}\text{–}GSH \qquad (7.3)$$

The existence of the rearrangement pathway for the copper-glutathione complex is further corroborated by the following observation made in the literature. It has been reported that GSH is a versatile ligand that can bind to GSH to glutamic moiety as well as the thiolate sulfur. [26] There is also a report on the complex formation between copper(II) and glutamic acid. [27] The versatility of GSH ligand is further demonstrated by the fast rate of exchange of GSH with Cu-SG which was reported to be 13 s^{-1}. [28] Furthermore, the rates of thiol oxidation processes catalysed by copper(II) are significantly different for different thiols such as glutathione and cysteine. [29] This indicates the involvement of the glutamic and/or glycine moieties in the formation of complex of copper(II).

7.3.3 GSH oxidation in the presence of both Cu^{2+} and O_2

Solutions of Cu^{2+} and GSH were mixed under different reaction conditions (detailed in separate sections below) in the presence of atmospheric (0.27 mM)[17] or saturated (1.24 mM)[30] oxygen. The concentrations of free –SH were monitored as a function of time. The results revealed two-step reactions (i.e. reactions with two different timescales) designated as X and Y (Figure 7.5), described next.

<u>Step X:</u> short timescale reactions

Solutions of fixed GSH concentration and varied concentrations of Cu^{2+} were mixed in the presence of atmospheric O_2 to yield the final concentrations of 56 μM GSH and 0 μM, 2 μM, 5 μM and 10 μM Cu^{2+}. Similar experiments were performed for a high GSH concentration (600 μM) with 0 μM, 60 μM, 150 μM and 300 μM Cu^{2+}. The concentrations of free –SH were monitored for 40 min after the solutions were mixed.

The plots of –SH against time in Figure 7.5 show that in the first step ("step X") there is a fast drop in concentration of –SH analogous to that observed earlier. However, the stoichiometry of Cu:GSH is now 1:2 (Figure 7.5), in contrast to the 1:1 observed in the absence of O_2 (Figure 7.3a).

The dependency of the stoichiometry on oxygen implies that GSH first forms a 1:1 Cu:SG complex via the thiol group of glutathione in a very fast timescale. The binding of the second GSH molecule to copper via the thiol group requires the presence of oxygen, suggesting that the 1:2 Cu:SG complex is relatively unstable without electron transfer with oxygen; refer to eqn. 7.4 and 7.5. The electron transfer results in the formation of one of the oxidised forms of the 1:2 Cu:SG complex. For the moment, we call this complex 'A,' the identity of which is proposed and presented later on in the text (Figure 7.12).

$$Cu^{2+}– S(H)G + GSH \rightleftharpoons G(H)S – Cu^{2+}– S(H)G \qquad (7.4)$$

$$G(H)S – Cu^{2+}– S(H)G + ½\ O_2 \overset{\text{fast}}{\rightleftharpoons} A + ½\ H_2O_2 \qquad (7.5)$$

<u>Step Y:</u> long timescale reactions

In this section, we will focus on the second step ("step Y") of the results obtained from the experiments performed in the previous section (refer to Figure 7.5). During step Y, there is a linear decrease in –SH concentration with time, suggesting the overall reaction is zeroth order. To investigate the kinetics of the slower step Y reaction, the concentrations of Cu^{2+}, O_2 and GSH were varied to evaluate how the rate depends on the concentration of each species.

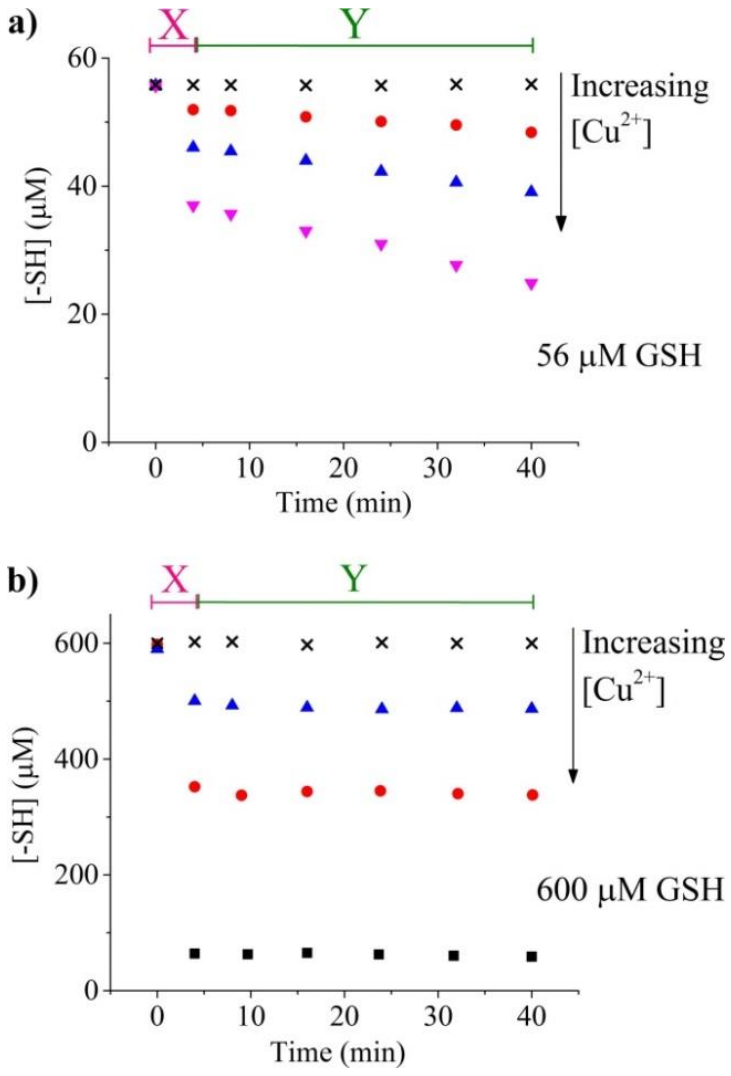


Figure 7.5: The concentrations of free thiols (–SH) at different experimental times; **a)** 56 μM GSH, atmospheric O_2, varied concentrations of Cu^{2+}: 0 μM (cross); 2 μM (red); 5 μM (blue); 10 μM (pink); **b)** 600 μM GSH, atmospheric O_2, varied concentrations of Cu^{2+}: 0 μM (cross); 60 μM (blue); 150 μM (red); 300 μM (black). For presentational purposes, only four of the Cu^{2+} concentrations studied are shown in each case.

a) Effect of [Cu^{2+}]

The rates of step Y were determined for a range of Cu^{2+} concentrations (0 nM, 25 nM, 50 nM, 2 μM, 5 μM, 10 μM and 15 μM) in the presence of 56 μM GSH under atmospheric oxygen. The plot of concentrations of –SH against time for some of the Cu^{2+} concentrations studied is given in Figure 7.5a. The rate of –SH depletion (-d[-SH]/dt) in step Y is plotted against Cu^{2+} concentrations as displayed in Figure 7.6. The result shows that the rate of GSH (–copper complex) oxidation increases with Cu^{2+} concentrations. Similar studies were performed for 100 μM GSH in the presence of atmospheric oxygen. It was also observed that the rate increases as the concentration of Cu^{2+} increases. However, the extents to which the rates increase with [Cu^{2+}] are different for the different GSH concentrations studied. Hence, the order of reaction with respect to concentration of Cu^{2+} cannot be readily determined. This likely arises due to involvement of Cu^{2+} in more than one reaction routes, as will be discussed later.

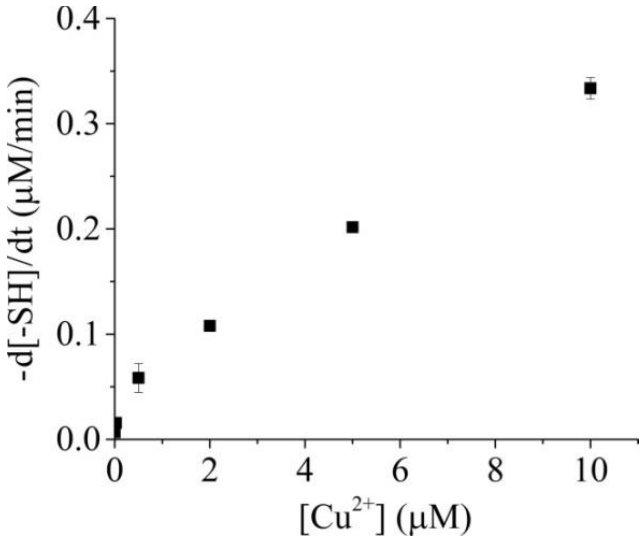


Figure 7.6: The rates of –SH depletion (-d[-SH]/dt) during step Y as a function of Cu^{2+} concentrations studied in the solutions containing 56 μM GSH and varied concentrations of Cu^{2+}: 0 nM, 25 nM, 50 nM, 2 μM, 5 μM, 10 μM and 15 μM, in the presence of atmospheric (0.27 mM) O_2.

b) Effect of [O_2]

Two different concentrations of O_2, atmospheric (0.27 mM) and saturated (1.24 mM), were used to study its effect on the rate of step Y. The results for the reaction mixtures of 56 μM GSH and 7.5 μM Cu^{2+} are shown in Figure 7.7. The rates of step Y reactions are 0.312 ± 0.008 μM min^{-1} and 0.718 ± 0.021 μM min^{-1} for atmospheric and saturated oxygen respectively. At the same time, similar experiments were performed for 100 μM GSH and 7.5 μM Cu^{2+} mixtures to give the step Y rates of 0.211 ± 0.006 μM min^{-1} and 0.464 ± 0.023 μM min^{-1} in the presence of atmospheric and saturated oxygen respectively. The results studied in both GSH concentrations indicate that the rate of step Y reaction is $(0.53 \pm 0.04)^{th}$ order with respect to the O_2 concentration.

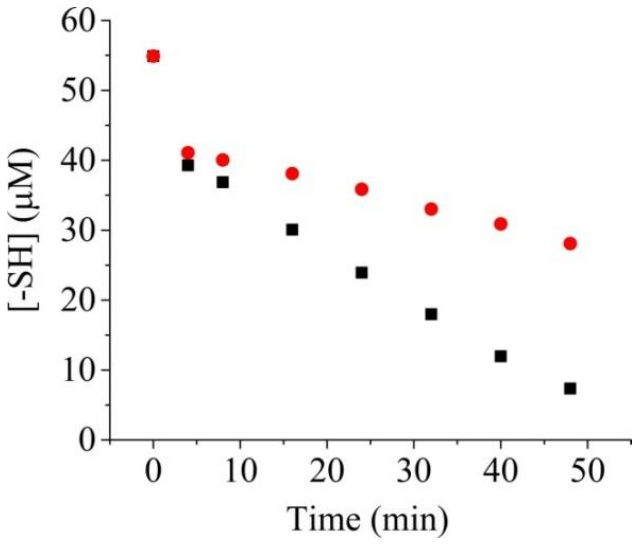


Figure 7.7: The concentration of free thiols (–SH) at different experimental times for the solution mixtures of 56 μM GSH, 7.5 μM Cu^{2+} and varied concentrations of O_2: atmospheric (0.27 mM) O_2 (red); saturated (1.24 mM) O_2 (black)

The results of kinetic studies suggest the clear positive dependence of the rate of GSH oxidation on both [Cu^{2+}] and [O_2]. This indicates the involvements of these two species in or prior to the rate-determining step (RDS).

More specifically, the kinetic studies showed that the rate of step Y reaction is proportional to the square root of O_2 concentration ($-d[-SH]/dt \propto [O_2]^{0.5}$). This relationship is consistent with a pre-equilibrium step involving the copper-glutathione complex ('A') and O_2 in the stoichiometric ratio of 2:1 to form another different complex with one less electron, 'B' (eqn. 7.6). This may be followed by the rate-determining conversion of 'B' to the final product of GSH oxidation, which has been reported to be GSSG [31] (eqn. 7.7). The derived rate law is given in eqn. 7.10.

$$A + \tfrac{1}{2} O_2 \underset{}{\overset{K}{\rightleftharpoons}} B + \tfrac{1}{2} H_2O_2 \qquad (7.6),$$

$$B \xrightarrow{k'} Cu^{2+} + GSSG \qquad (7.7),$$

$$K = \frac{[B][H_2O_2]^{0.5}}{[A][O_2]^{0.5}} \qquad (7.8),$$

$$\nu = k'[B] \qquad (7.9),$$

$$\nu = \frac{k'K[A][O_2]^{0.5}}{[H_2O_2]^{0.5}} \qquad (7.10),$$

where [i] denotes the concentration of species i. K is the equilibrium constant of the oxidation of 'A' to 'B' by O_2. ν and k' are the rate of reaction and rate constant for the conversion of 'B' to Cu^{2+} and GSSG respectively. [A] is the concentration of the 1:2 Cu-SG complex formed in excess of GSH, [A] is thus equivalent or proportional to the concentration of Cu^{2+}.

The suggested mechanism for step Y reaction is therefore consistent with the dependence of the rate of GSH oxidation on Cu^{2+} concentration.

c) Effect of [GSH]

The rates of the step Y reactions were investigated for varied concentrations of GSH in solutions containing 10 μM Cu^{2+} under atmospheric O_2. The rates of free thiol consumption (−d[−SH]/dt) are plotted against GSH concentration, as shown in Figure 7.8. The results show a *decreasing* rate of reaction as the concentration of GSH increases.

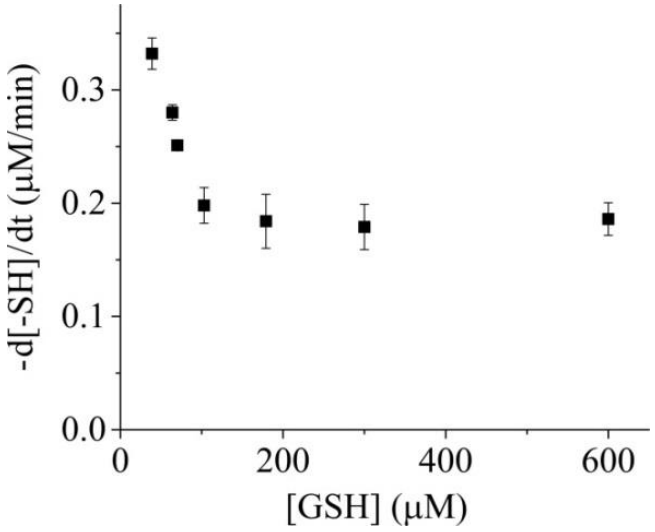


Figure 7.8: The rates of –SH depletion (-d[-SH]/dt) during step Y as a function of GSH concentrations studied in the solutions containing 10 μM Cu^{2+} and varied concentrations of GSH: 39 μM, 64 μM, 70 μM, 103 μM, 179 μM, 300 μM and 600 μM, in the presence of atmospheric (0.27 mM) O_2.

In contrast to the response to [Cu^{2+}] and [O_2], the rate of step Y reaction *decreases* with increasing concentration of GSH. The unusual behaviour suggests the existence of a competing, parallel reaction which becomes more favourable as the GSH concentration increases and outweighs the oxidation of GSH to GSSG at sufficiently high level of GSH.

Note that the lower consumption of –SH measured via DTNB reaction at high [GSH] suggests that the competing reaction results in the formation of a stable, inactive species with unbound thiol groups. This result is consistent with the rearrangement mechanism proposed for step *y* reaction.

In fact, there are at least two pathways which can potentially lead to the decrease in step Y reaction rate as the concentration of GSH increases. One is the rearrangement of copper-glutathione complex into a different form which is inactive to the catalytic oxidation of GSH, as proposed. The other is the reduction in Cu^{2+} concentration.

The availability of Cu^{2+} can be lost from the system via different means. First is the formation of copper complex with the product, GSSG. To investigate this process, the kinetic studies on the copper-glutathione complex formation were performed, as detailed with following. The changes in UV-vis spectra as a function of time were investigated for three different cases: GSSG + Cu^{2+}, GSH + Cu^{2+} (with and without O_2) and GSSG + GSH + Cu^{2+}, which unless stated otherwise studied under atmospheric oxygen.

The spectra of the 300 μM GSSG and 60 μM Cu^{2+} solution mixtures remained unchanged over the 40 min course of study. In contrast, the spectra of 600 μM GSH and 60 μM Cu^{2+} showed increasing absorbance at 297 nm as a function of time, refer to Figure 7.9. There is a small but insignificant difference in the rates in the absence and presence of O_2 (< 1%). The formation of this complex is thus predominantly independent of the O_2 concentration.

Addition of 300 μM GSSG to the 600 μM GSH and 60 μM Cu^{2+} mixtures results in ca. 15% reduction in Cu-GSH complex formation rates. Note that for the initial GSH concentration of 600 μM, the highest possible concentration of GSSG formed is 300 μM, the concentration of which is unlikely to be reached due to the equilibrium state and the loss of GSH in the formation of complexes. The small decrease in the rates of Cu-GSH complex formation even

with the large amount of GSSG added implies that GSSG is not the *dominant* factor that causes the reduction in GSH oxidation rates as the concentration of GSH increases. This indicates that although Cu^{2+} can form complexes with GSSG, in the presence of both GSH and GSSG, Cu^{2+} favourably binds to GSH. There is therefore a minor effect from Cu^{2+}–GSSG complex if formed.

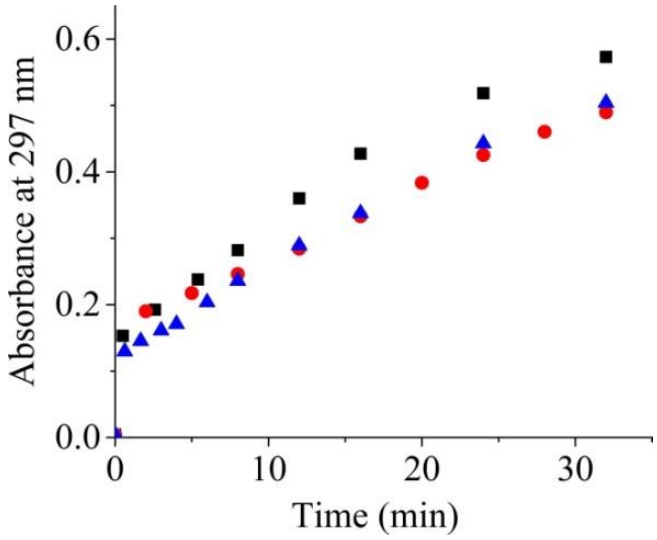


Figure 7.9: The values of absorbance at 297 nm as a function of experimental time. 600 μM GSH and 60 μM Cu^{2+} in the absence of O_2 (blue); 600 μM GSH and 60 μM Cu^{2+} in the presence of atmospheric O_2 (black); 600 μM GSH, 300 μM GSSG and 60 μM Cu^{2+} in the presence of atmospheric O_2 (red).

Additional evidence that GSSG has no observable effect on the rate of GSH oxidation was confirmed by the monitoring of –SH concentrations (via reactions with DTNB) as a function of experimental time in the absence and presence of added GSSG. Addition of GSSG to the GSH and Cu^{2+} mixtures results in no observable difference in the rate of GSH oxidation in comparison with that in the absence of added GSSG; refer to Figure 7.10. It can thus be concluded that GSSG has no or negligible effect on the rates of step 'Y' GSH oxidation.

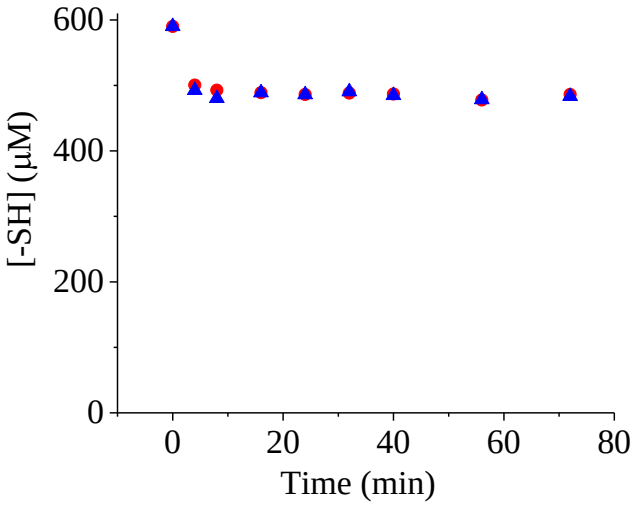


Figure 7.10: The concentrations of free thiols (–SH) at different experimental times for the solution mixtures of 600 μM GSH and 60 μM Cu^{2+} (red); 600 μM GSH, 300 μM GSSG and 60 μM Cu^{2+} (blue).

The second possible route for the loss of Cu^{2+} is the reactions of Cu^{2+} with other species in the solution such as H_2O_2 and the solvent, H_2O. The reaction of Cu^{2+} with H_2O_2 produces Cu^{+} and radical species, which are very reactive and can react with TNB to regenerate DTNB in a very fast timescale. Therefore, if there is a significant amount of H_2O_2 present in the solution, the absorbance at 412 nm (A_{412}) would decrease. However, the monitoring of A_{412} with time, as presented in Figure 7.11, suggests that this is not the case. A_{412} and hence the concentration of TNB remain constant with time. The amount of H_2O_2 (if formed) is thus very small and does not affect the rate of GSH oxidation. Meanwhile, the reaction of Cu^{2+} with H_2O may form copper oxides. This is however endergonic under the reaction conditions employed (calculated from the values of standard potentials of the half-reactions involved).[32] Therefore, there is no mechanisms, to the author's best knowledge, which can be responsible for the decreasing rates of GSH oxidation at higher GSH concentrations other than the

rearrangement of the copper-glutathione complex (cysteine thiol-bound) to its inactive form (glutamic/glycine-bound).

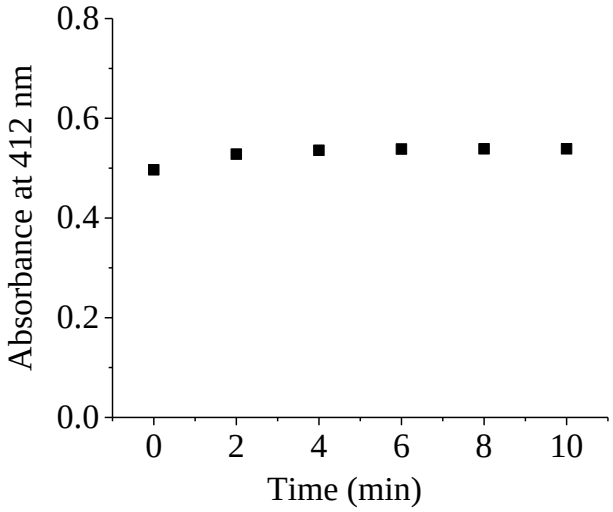


Figure 7.11: Absorbance values at 412 nm of the reaction mixtures of 87 μM DTNB, 60 μM GSH and 10 μM Cu^{2+} as a function of mixing time.

Following all the above information together with that obtained from the variation of GSH oxidation rates as a function of various experimental parameters, we propose a step-wise mechanism shown in Figure 7.12.

It has been reported that when the molar ratio of GSH:Cu^{2+} is equal to or greater than 3:1, corresponding to conditions in all of the experiments studied in this work, a GS-Cu(I)-SG complex is swiftly formed.[28,31] However, as discussed before in Section 7.3.3b that a pre-equilibrium step is required prior to the rate-determining formation of GSSG. We therefore tentatively propose the structure of 'A' as presented in Figure 7.12. Note that our proposed structure of 'A' has the same overall oxidation state as the GS-Cu(I)-SG complex previously reported.[28,31] The only difference is how the electrons might be distributed between copper and sulfur in the Cu-S bond. Following 'A,' the proposed structure of the intermediate oxidation product 'B,' is given in Figure 7.12.

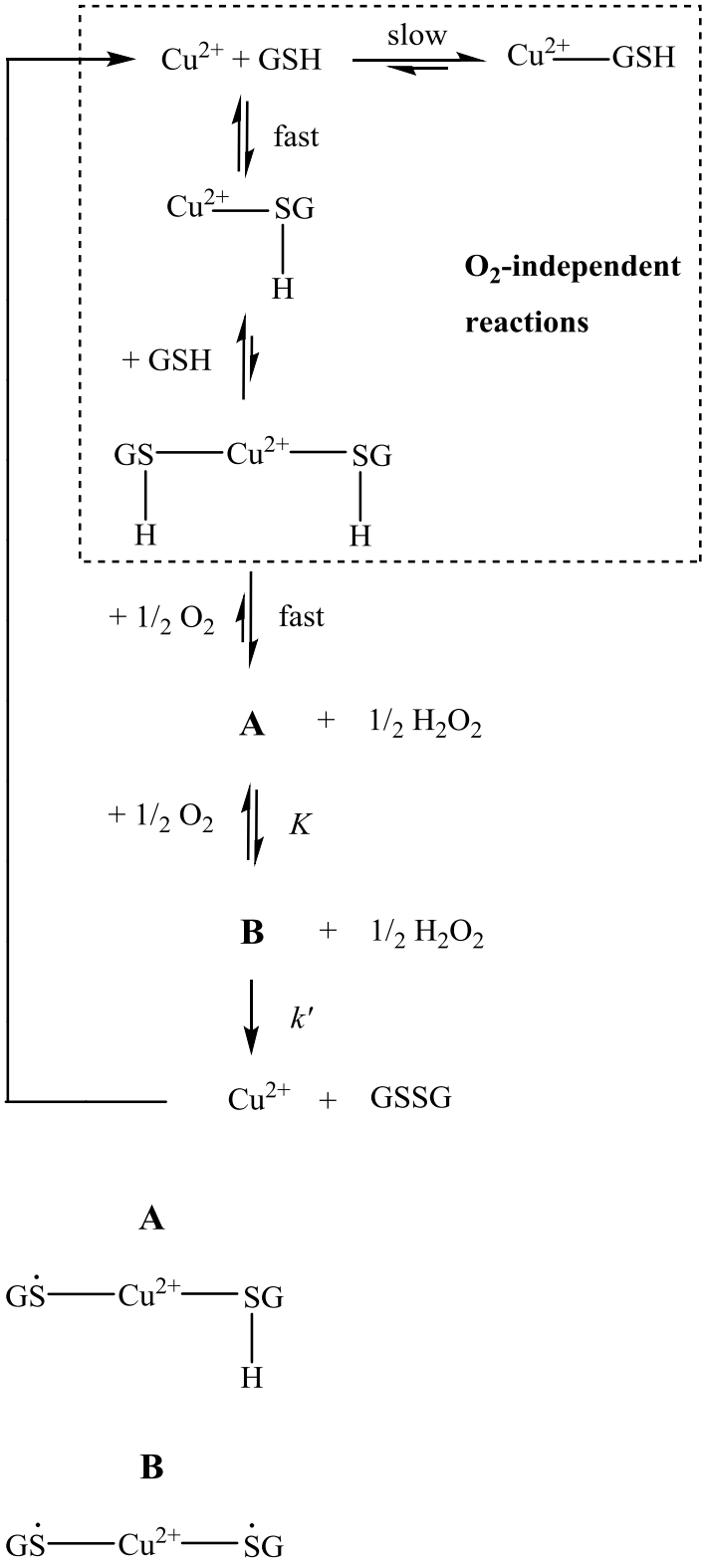


Figure 7.12: The proposed mechanisms for the oxidation of GSH catalysed by copper(II) and the proposed structures of the intermediate complexes ‘A’ and ‘B.’

7.4 Conclusions

The kinetics of glutathione oxidation reaction catalysed by copper(II) have been investigated and step-by-step mechanisms proposed. The results emphasise that GSH is *not* auto-oxidised by oxygen in the absence of a catalyst. In the presence of Cu^{2+}, two-step reactions were observed in both the absence and presence of O_2. The first steps (*x* and X) involve the formation of copper-glutathione complexes. In the absence of O_2, the stoichiometry of Cu:GSH complex is 1:1. With O_2 present, the 1:2 Cu:GSH complex is formed. The second step (Y) is the overall oxidation of GSH to GSSG catalysed by copper(II). The rates of GSH oxidation in the second step increase with increasing concentrations of the oxidising agent, O_2, and the catalyst, Cu^{2+}, but decrease when the concentration of GSH itself is increased. This inverse relationship is suggested to be a result of competing formation of an inactive form of copper-glutathione complex. In this work, we have thus provided insights into the mechanistic details of the copper(II)-catalysed oxidation of GSH. The understanding of this process will be beneficial towards the studies of the roles of copper and glutathione in biological systems as well as the development of sample preparation procedures for bioanalysis. With the measurement assay developed in the previous chapter and the understanding of the stability of glutathione in biological samples, we next investigate the potential of glutathione as a biomarker in the following chapter.

Bibliography

(1) Ngamchuea, K.; Batchelor-McAuley, C.; Compton, R. G. *Chem. Eur. J* **2016**, *22*, 15937-15944.
(2) Richie, J. P., Jr.; Skowronski, L.; Abraham, P.; Leutzinger, Y. *Clin. Chem.* **1996**, *42*, 64-70.
(3) Nassar, M.; Hiraishi, N.; Islam, M. S.; Otsuki, M.; Tagami, J. *J. Dent. Sci.* **2014**, *9*, 85-90.
(4) Deiss, A. *Ann. Intern. Med.* **1970**, *73*, 413.
(5) Osterberg, R.; Ligaarden, R.; Persson, D. *J. Inorg. Biochem.* **1979**, *10*, 341-355.
(6) Jiménez, I.; Speisky, H. *J. Trace Elem. Med Biol.* **2000**, *14*, 161-167.
(7) Hanna, P. M.; Mason, R. P. *Arch. Biochem. Biophys.* **1992**, *295*, 205-213.
(8) Milne, L.; Nicotera, P.; Orrenius, S.; Burkitt, M. J. *Arch. Biochem. Biophys.* **1993**, *304*, 102-109.
(9) Spear, N.; Aust, S. D. *Arch. Biochem. Biophys.* **1995**, *317*, 142-148.
(10) Carrasco-Pozo, C.; Aliaga, M. E.; Olea-Azar, C.; Speisky, H. *Bioorg. Med. Chem.* **2008**, *16*, 9795-9803.

(11) Speisky, H.; Gomez, M.; Carrasco-Pozo, C.; Pastene, E.; Lopez-Alarcon, C.; Olea-Azar, C. *Bioorg. Med. Chem.* **2008**, *16*, 6568-6574.
(12) Speisky, H.; Gomez, M.; Burgos-Bravo, F.; Lopez-Alarcon, C.; Jullian, C.; Olea-Azar, C.; Aliaga, M. E. *Bioorg. Med. Chem.* **2009**, *17*, 1803-1810.
(13) Kachur, A. V.; Koch, C. J.; Biaglow, J. E. *Free Radic. Res.* **1998**, *28*, 259-269.
(14) Riddles, P. W.; Blakeley, R. L.; Zerner, B. *Methods Enzymol.* **1983**, *91*, 49-60.
(15) Gustafsson, J. P. *Visual MINTEQ ver. 2.32*, Department of Land and Water Resources Engineering, Royal Institute of Technology, Stockholm, Sweden, **2005**.
(16) Szajewski, R. P.; Whitesides, G. M. *J. Am. Chem. Soc.* **1980**, *102*, 2011-2026.
(17) Battino, R.; Rettich, T. R.; Tominaga, T. *J. Phys. Chem. Ref. Data* **1983**, *12*, 163.
(18) Pecosk, R. L. *Anal. Chem.* **1953**, *25*, 561-564.
(19) Warburg, O. *Heavy Metal Prosthetic Groups and Enzyme Action*, Oxford University Press, New York, USA, **1949**.
(20) Zhang, N.; Zhou, Q.; Yin, X.; Zeng, D. *J. Solution Chem.* **2014**, *43*, 326-339.
(21) Areias, M. C.; Shimizu, K.; Compton, R. G. *Analyst* **2016**, *141*, 2904-2910.
(22) Shtyrlin, V. G.; Zyavkina, Y. I.; Ilakin, V. S.; Garipov, R. R.; Zakharov, A. V. *J. Inorg. Biochem.* **2005**, *99*, 1335-1346.
(23) Pederson, J. Z.; Steinkuhler, C.; Weser, U.; Rotilio, G. *BioMetals* **1996**, *9*, 3-9.
(24) Chow, S. T.; McAuliffe, C. A.; Sayle, B. J. *J. Inorg. Nucl. Chem.* **1975**, *37*, 451-454.
(25) Ahmed, M. *World Appl. Sci. J.* **2014**, *29*, 1357-1362.
(26) Krezel, A.; Bal, W. *Acta Biochim. Pol.* **1999**, *46*, 567-580.
(27) Bregier-Jarzebowska, R. *J. Solution Chem.* **2014**, *43*, 2144-2162.
(28) Corazza, A.; Harvey, I.; Sadler, P. J. *Eur. J. Biochem.* **1996**, *236*, 697-705.
(29) Smith, R. C.; Reed, V. D.; Hill, W. E. *Phosphorus Sulfur Silicon Relat. Elem.* **1994**, *90*, 147-154.
(30) Millero, F. J.; Huang, F.; Graham, T. B. *J. Solution Chem.* **2003**, *32*, 473-487.
(31) Aliaga, M. E.; Carrasco-Pozo, C.; López-Alarcón, C.; Speisky, H. *Transition Met. Chem.* **2010**, *35*, 321-329.
(32) Bard, A. J.; Parsons, R.; Jordan, J. *Standard Potentials in Aqueous Solution*, Marcel Dekker Inc., New York, USA, **1985**.

Chapter 8 Salivary glutathione in bipolar disorder

This chapter assesses the potential of salivary glutathione as a biomarker for bipolar disorder. Glutathione is an important cellular antioxidant whose levels are decreased in some studies of bipolar patients. Saliva provides a simple and feasible means of measuring glutathione but has not yet been applied to the study of bipolar patients. The purpose of the study is thus to compare the levels of salivary total glutathione (GSH+GSSG), its reduced (GSH) and oxidised (GSSG) forms, as well as the GSH:GSSG ratios in bipolar patients and healthy controls. Glutathione concentrations were measured using the enzyme kinetic essay developed in Chapter 6. Relative to controls, salivary levels of total glutathione, GSH and GSSG were found to increase in bipolar patients but the GSH:GSSG ratio was unchanged.

This work was done in collaboration with Professor Philip J. Cowen from the Psychiatry Department, University of Oxford. Some of the work presented in this chapter has been published in *Journal of Affective Disorders.*[1]

8.1 Introduction

Easily accessible biomarkers could be of great value in the diagnosis and management of mood disorders. Oxidative stress has been implicated in the pathophysiology of bipolar disorder and several measures of this process, often utilising enzymes measured in blood, have been explored in bipolar patients.[2,3]

Glutathione is a major endogenous free radicle scavenger, and its lessened availability can increase vulnerability to cellular oxidative stress.[2] A number of studies have measured glutathione concentrations in blood and brain in patients with bipolar disorder but the findings have been somewhat inconsistent, as summarised in Table 8.1. For example, glutathione levels in blood plasma and red blood cells have been reported both as being lowered and unchanged.[3-5] One post-mortem work has found lowered glutathione in cerebral cortex from bipolar patients,[6] though this has not been confirmed in magnetic resonance spectroscopy studies which are able to measure glutathione concentrations in the living brain.[7,8]

In chapter 6, a novel method of analysing glutathione in saliva using an enzyme kinetic assay was described.[9] The determination is rapid and the stability of glutathione in saliva is greater than that in plasma due to decreased GSH degradation.[9] Salivary glutathione therefore offers the possibility of an easily accessible biomarker for bipolar patients. The aim of this work is to carry out a study examining glutathione levels in saliva in patients with bipolar disorder compared to a group of healthy controls.

Table 8.1: Literature on glutathione for bipolar disorder

Medium	Species	Methods	Concentrations in bipolar patients relative to controls	*p*-value	[ref]
Blood plasma	Total (GSH+GSSG)	GR/DTNB	lower	0.012	[3]
	GSSG	2-VP, GR/DTNB	higher	0.0001	
	GSH	-	lower	< 0.0001	
	GSH:GSSG	-	lower	< 0.0001	
Blood plasma	Total (GSH+GSSG)	GR/DTNB	no significant difference	0.51	[5]
Red blood cell	Total (GSH+GSSG)	GR/DTNB	lower	< 0.001	[4]
	GSSG	NEM, GR/DTNB	no significant difference	0.288	
	GSH	-	lower	< 0.001	
Anterior cingulate cortex	GSH	^{1}H-MRS	no significant difference	0.213	[7]
Medial prefrontal	GSH	^{1}H-MRS	no significant difference	-	[8]
Occipital cortex	GSH	^{1}H-MRS	no significant difference	-	[8]
Post-mortem prefrontal cortex	Total (GSH+GSSG)	GR/DTNB	lower	≤ 0.05	[6]
	GSSG	2-VP, GR/DTNB	lower	≤ 0.05	
	GSH	-	lower	≤ 0.05	
	GSH:GSSG	-	no significant difference	-	

Detection methods:

GR/DTNB: Tietze enzymatic assay (previously described in Chapter 6), 2-VP: 2-vinylpyridine (a GSH-masking reagent), NEM: *N*-ethylmaleimide (a GSH-masking reagent), ^{1}H-MRS: proton magnetic resonance spectroscopy.

8.2 Experimental procedures

8.2.1 Study setting

The saliva and blood samples used in this study were collected by Professor Philip J. Cowen and Clare Williams from the Department of Psychiatry, University of Oxford.

Participants with bipolar disorder were patients of the Oxford Health NHS Foundation Trust. They were approached by research facilitators attached to clinical teams and asked if they would like to participate in the study which involved a clinical assessment and donation of saliva sample. Healthy control participants were recruited by advertisement. All participants gave full, written informed consent to the study which was approved by the West of Scotland Research Ethics Service.

8.2.2 Patients and controls

Two independent studies were performed in this work. In the first study, we recruited 16 patients with bipolar disorder and 15 healthy controls, and only saliva samples were collected using *cotton* Salivettes (detailed in Section 8.2.4). In the second study, 10 bipolar patients and 10 healthy controls were recruited. Both saliva and blood samples were collected in the second study, and the saliva samples collected using *synthetic* polystyrene Salivettes (detailed in Section 8.2.4).

All participants were assessed for DSM-IV diagnoses using the Standard Clinical Interview for Diagnostic and Statistical Manual for Mental Health Disorders—Fourth Edition).[10] Current mood was assessed using the Young Mania Rating Scale (YMRS)[11] and the Hamilton Depression Ratings Scale (HAM-D).[12] Healthy controls were required not to have any Axis 1 DSM-IV disorder (e.g. depression, schizophrenia, social phobia).

8.2.3 Demographic data

Patients and controls were well matched for age and gender. The demographic data are summarised in Table 8.2 and Table 8.4 for the first and second independent studies respectively.

8.2.4 Sample collection and storage

Subjects consumed no food or drink at least one hour prior to sampling. 5 mL venous blood samples were taken into ethylenediaminetetraacetic acid (EDTA) bottles and frozen whole. Blood samples were stored at -70 °C prior to analysis. Richie et al.[13] have reported that the concentration of glutathione in human blood sample is stable for up to 20 days when the blood is frozen at -70 °C.

Saliva samples were taken directly after the blood sample using either a cotton Salivette® (in the first study) or a synthetic polystyrene Salivette® (in the second study) with the participant subjects seated. The Salivette remained in the oral cavity for 1 minute. The saliva was then centrifuged at 1000g for 2 minutes and the saliva stored at -20^{o}C[14] for no more than 7 days before assay.

8.2.5 Glutathione quantification

Assays were carried out blind to diagnosis. Saliva samples were used as received without any pre-treatments or modifications. Blood samples were haemolysed immediately prior to the determination of glutathione concentration by mixing 1,990 μL of 0.01 M phosphate/5 mM EDTA buffer (pH 7.5) with 10 μL of whole blood.

Reduced, oxidised and total glutathione were measured using the assay developed in Chapter 6. Briefly, total glutathione (GSH + GSSG) concentrations were determined using

the Tietze enzymatic kinetic assay[15,16] together with the method of standard addition.[17] All solutions were made in 0.10 M phosphate buffer at pH 7.5 containing 10 mM EDTA. First, 50 μL of the saliva sample, 30 μL of 1.68 mM DTNB and 30 μL of 40 μL/3.0 mL GR were added respectively to a cuvette containing 350 μL of the phosphate buffer. After 30 seconds, 30 μL of 0.80 mM NADPH was then added. The absorbance at 412 nm was then recorded for 60 seconds. The above procedures were repeated for each sample but with increasing GSH concentrations added to the assay to perform standard additions.

The concentrations of oxidised glutathione (GSSG) were measured using the *GSSG (BQ/TNB) assay*, refer to Chapter 6. First, reduced glutathione (GSH) was masked by the reaction with benzoquinone. The benzoquinone-treated samples were then subjected to Tieze measurements as described above. The result yields the concentrations of GSSG. GSH concentrations were calculated from the subtraction of GSSG concentrations from the concentration of total glutathione. The ratio of GSH:GSSG which is an indicator of oxidative status was also calculated.[2]

8.2.6 Data analysis

8.2.6.1 Student's *t*-test

The unpaired Student's *t*-test (two-tailed; eqn. 8.1) is used to assess the statistical difference in age and glutathione concentrations between the bipolar and the control groups. This is described next.

Consider two independent samples x_1 and x_2 of size n_1 and n_2 from two normal populations with means $\overline{x_1}$ and $\overline{x_2}$, and variances s_1^2 and s_2^2 respectively. In the case that equal variance is assumed ($s_1^2 = s_2^2$), the test statistic *t* can be calculated by:[18]

$$t = \frac{\overline{x_1} - \overline{x_2}}{s_p \sqrt{\frac{1}{n_1} + \frac{1}{n_2}}} \tag{8.1}$$

s_p is defined as:

$$s_p = \sqrt{\frac{(n_1 - 1)s_{x1}^2 + (n_2 - 1)s_{x2}^2}{n_1 + n_2 - 2}} \tag{8.2}$$

where $n_1 + n_2 - 2$ is the degrees of freedom.

The test is then based on hypothesis testing where a null hypothesis (H_0) is assumed.[19,20] The null hypothesis in this case is the mean values of the two sample groups being equal (H_0: $\overline{x_1} = \overline{x_2}$).

The *t* value is compared with the critical value, t^*. H_0 is rejected if:

$$|t| > t^* \tag{8.3}$$

For a two-tailed test, t^* is defined as the t-value which gives the probability of rejecting H_0 when it is true of 2.5% at each end of the normal distribution (for the significant level (σ) of 0.05 set in this work), refer to Figure 8.1.

The *p*-value (the sum of the two tail areas in Figure 8.1) quantifies the possibility that H_0 is true. If *p*-value is smaller than the significant level (σ) of 0.05, H_0 is rejected with less than 5% chance that this is the incorrect rejection of H_0. The result is thus considered to be statistically significant when *p*-value is less than 0.05.[18]

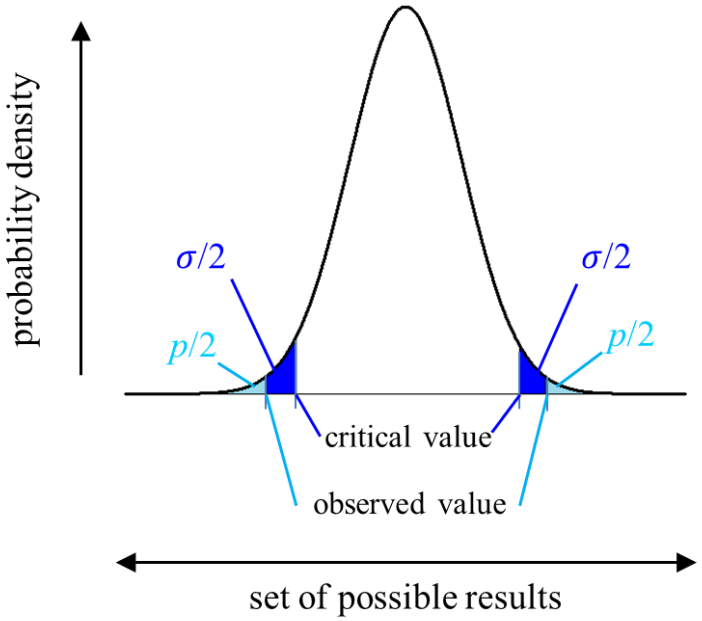


Figure 8.1: Normal distribution of the set of possible results (*t* from Student's *t*-test, χ^2 from chi-square test and *r* from Pearson correlation test) and graphical illustration to the relation between the significance level (σ), critical value (e.g. t^* from Student's *t*-test) and *p*-value (*p*) for a two-tailed test.

8.2.6.2 Chi-square test

The chi-square (χ^2) test is a nonparametric test which determines whether there is a significant association between two variables. The variables are summarised into a contingency table (a type of frequency distribution table where the two variables are shown simultaneously). χ^2 can then be determined from the relationships between rows and columns:[18]

$$\chi^2 = \sum_{i=0}^{n_1} \sum_{j=0}^{n_2} \frac{(O_{ij} - m_{ij})^2}{O_{ij}} \qquad (8.4)$$

where O_{ij} and m_{ij} are the observed and expected frequency counts of the i^{th} row and j^{th} column of the contingency table. m_{ij} can be calculated from

$$m_{ij} = \frac{N_i N_j}{N} \quad (8.5)$$

where N_i and N_j are the total values in the i^{th} row and j^{th} column respectively. N is the table grand total.

The calculated χ^2 is then compared with the critical value $(\chi^2)^*$. The condition for the critical value is the same as that of t^* explained in the previous section. If the observed χ^2 is greater than $(\chi^2)^*$, the null hypothesis is rejected.

Chi-square is used in this work to confirm that there is no statistical difference in gender between the bipolar and the control groups. The null hypothesis (H_0) in this case is that the gender is independent of the sample group i.e. the gender distribution in the bipolar and the control groups is the same. The high *p*-values of 0.808 and 0.329 (much greater than the significant level (σ) of 0.05) for the gender tests in the first and second studies, presented in Table 8.2 and Table 8.4 respectively, suggests that the gender distribution is indeed *not* different between the two groups.

8.2.6.3 Pearson correlation coefficient

The correlation between salivary glutathione concentrations and the sample volume, as well as the correlation between saliva and blood glutathione (discussed later in Section 8.3.2.2) are assessed by Pearson correlation coefficient (*r*). Pearson correlation measures the strength of linear relationship between two normally distributed variables.[21] The value of *r* varies from -1 to 1, and can be calculated according to eqn. 8.6. A positive value of *r* indicates a positive linear relationship (i.e. positively correlated). A negative value suggests the variables are negatively correlated. The closer the value of $|r|$ is to 1, the stronger the linear dependence. *r* can be calculated by:[18]

$$r = \frac{\sum_{i=1}^{n}(x_i - \bar{x})(y_i - \bar{y})}{\sqrt{\sum_{i=1}^{n}(x_i - \bar{x})^2}\sqrt{\sum_{i=1}^{n}(y_i - \bar{y})^2}} \quad (8.6)$$

where n is the sample size. x_i and y_i are the i^{th} data points of variables x and y with the mean values of $\bar{x}$ and $\bar{y}$ respectively.

8.3 Results

Two independent studies herein investigate the possibility of salivary glutathione as a biomarker for bipolar disorder. The factors influencing the amount of salivary glutathione detected were particularly considered in the second study, including the loss of material to the collection tools and the hydration level of the subjects. Blood glutathione concentrations were further determined, and the correlation with salivary contents was evaluated.

8.3.1 First study – salivary glutathione

The first saliva study included a total of 16 bipolar patients and 15 healthy control subjects. The two groups did not statistically differ in terms of age and gender, summarised in Table 8.2. The concentrations of total, reduced and oxidised glutathione determined in the stimulated saliva samples are presented in Table 8.3. Figure 8.2 shows the distribution of salivary glutathione concentrations in the different samples of bipolar and control groups.

The contents of total glutathione are statistically higher in bipolar patients than in healthy controls (p = 0.049). Reduced and oxidised glutathione levels are also higher in bipolar patients although not statistically significant (reduced: p = 0.076, oxidised: p = 0.132). No significant correlations of salivary glutathione with age (p = 0.409) or medication (lithium: p = 0.668) were observed.

Table 8.2: Demographic and clinical characteristics of the subjects participating in the 1st study

	Controls (*n*=15)	**Bipolar (*n*=16)**	***p*-value**
Mean age, years (S.D.)[a]	34.3 (9.8)	38.4 (10.3)	0.258[b]
Male sex, *n* (%)	5 (33.3%)	7 (43.8%)	0.567[c]
Bipolar Type I, *n* (%)	-	12 (75%)	-
Lithium, *n* (%)	-	4 (25%)	-

[a] S.D.: standard deviation

[b] Two-tailed Student's *t*-test

[c] Chi-square (χ^2)

Table 8.3: Salivary glutathione concentrations in bipolar patients vs. controls of the 1st study. GSSG concentrations are expressed in GSH equivalents (1GSSG = 2GSH).

	Controls (*n*=15)	**Bipolar (*n*=16)**	***p*-value[b]**
Total glutathione: GSH + GSSG, μM (S.D.)[a]	1.5 (1.1)	2.7 (2.0)	0.049
Reduced glutathione: GSH, μM (S.D.)	1.0 (0.9)	1.7 (1.2)	0.076
Oxidised glutathione: GSSG, μM (S.D.)	0.5 (0.4)	1.0 (1.1)	0.132
Ratio of GSH : GSSG (S.D.)	2.7 (3.7)	3.2 (4.3)	0.726

[a] S.D.: standard deviation

[b] Two-tailed Student's *t*-test

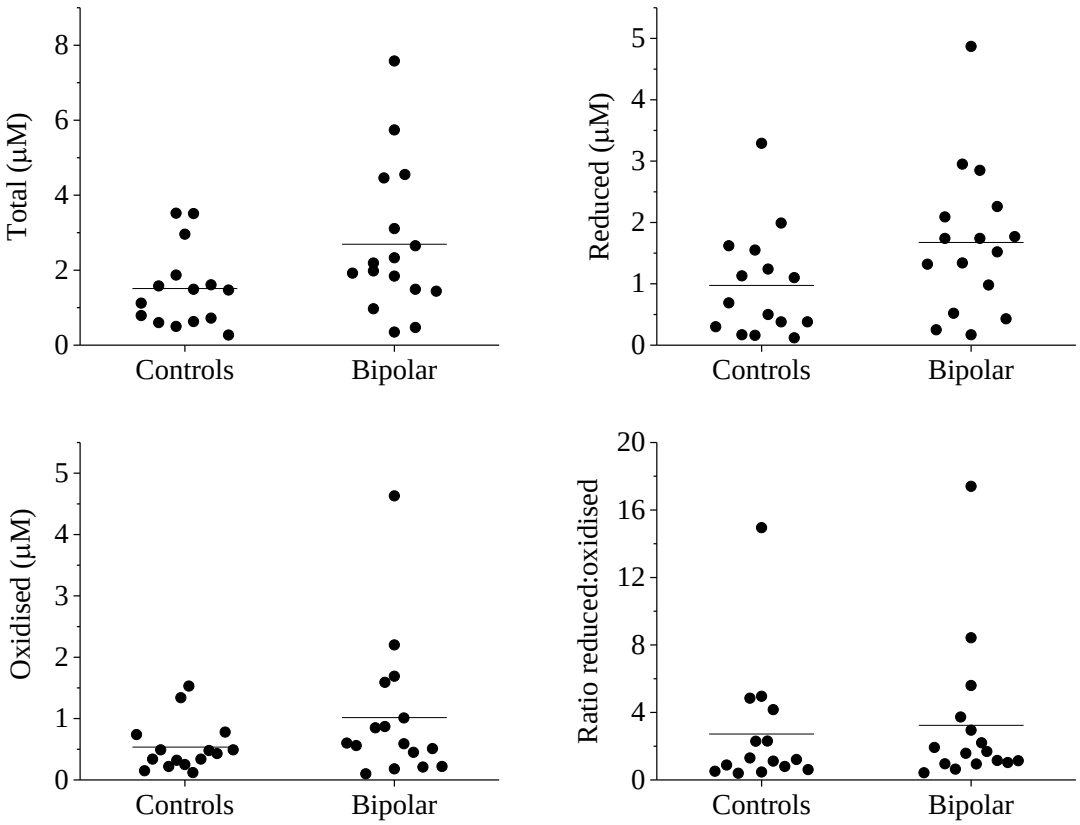


Figure 8.2: Scattered plots and mean (horizontal lines) of salivary glutathione concentrations: total (GSH+GSSG), reduced (GSH), oxidised (GSSG) and ratio of reduced to oxidised (GSH:GSSG) in healthy control group and bipolar patients of the 1st study. GSSG concentrations are expressed in GSH equivalents (1GSSG = 2GSH).

8.3.2 Second study – salivary and blood glutathione, and the effects of collection tools

In the first study (Section 8.3.1) and in salivary glutathione literature,[17,22,23] most of the saliva samples were collected using *cotton* Salivettes. The device facilitates the stimulated collection of whole saliva. However, cotton based sampling may affect some of the salivary composition levels because of the binding of analytes to cotton.[24] In order to avoid the binding of analytes to the collection devices, non-cotton based materials such as polystyrene and polyester may be preferable.[25] This section will first demonstrate the effects of the

collection tools on the concentration of reduced glutathione (GSH) detected. The re-evaluation of the potential of salivary glutathione as a biomarker of bipolar disorder will next be performed. The correlation between saliva and blood glutathione levels is further investigated.

8.3.2.1 Effects of collection tools on salivary glutathione concentrations

In this section, the difference between cotton and synthetic polystyrene Salivettes is investigated using standard reduced glutathione (GSH) solutions as well as real saliva samples.

In the case of standard solutions, 1.0 μM of GSH in phosphate buffer pH 7.0 was used. First, the GSH solution with the initial volumes of 245, 980 or 1,960 μL was exposed to cotton Salivette swab. The solution was left on the cotton swab for a varied time between 0 - 60 minutes. The soaked cotton swab was then centrifuged at the supplier recommended speed of 1000g for 1 minute. The extracted liquid, whose volume was smaller than the initial volume, was then subjected to GSH measurement by the Tietze method.[17] The amount of GSH recovered from the swab is quantified by the percentage (%) recovery defined as:

$$\% \text{ recovery} = c_f / c_i \times 100\ \% \qquad (8.7)$$

where c_i and c_f refer to the concentrations of glutathione measured before and after being exposed to the swabs respectively.

Figure 8.3 shows that the recovery of GSH from cotton swab is always lower than 100%, even in the case that the Salivettes are centrifuged immediately after collection. Figure 8.3a also demonstrates the decrease of glutathione recovery as a function of exposure time (t), with only ca. 20% of GSH recovered in the worst case (245 μL initial volume and 60 min exposure time). In real applications where there is an unavoidable varying delay in the

transfer of samples from collection points such as clinic or hospital to the analysis laboratory, the delay can give rise to significant errors.

From Figure 8.3a, it can also be seen that the percentage recovered from the cotton swabs also depends on the initial volumes used. The dependency on the initial volume makes it not possible to correct for the loss of GSH, especially in saliva collection experiments where initial volumes are unknown. Consequently, the use of a cotton-based tool induces random errors to saliva analysis especially for substances which have high a affinity to bind to cotton.

As a comparison to the cotton Salivette, synthetic polystyrene Salivette was studied. In contrast to the cotton, polystyrene yields ca. 100% recovery of the material (Figure 8.3b), suggesting that polystyrene may be a better alternative for saliva collection.

The effect of the collection tools on the concentrations of glutathione detected was further investigated in real saliva samples. The subjects were given the cotton and polystyrene swabs to chew for 1 minute. The stimulated saliva samples were then extracted from the swabs by centrifuging at 1000g for 1 minute. Whole unstimulated saliva collected by spitting were also studied in comparison. As glutathione concentrations vary from sample to sample, the results are presented as 'normalised GSH concentration' where the GSH concentration in whole unstimulated saliva is normalised to 1, and the GSH levels in stimulated saliva collected from the same subject are scaled accordingly. When collecting stimulated saliva using the cotton Salivette, the glutathione measured were 81 ± 2% (t = 0 minute) and 83 ± 7% (t = 10 minutes) of that detected in unstimulated saliva (Figure 8.3c). On the other hand when polystyrene Salivette was used, the levels of GSH detected were 101 ± 8 % (t = 0 minute) and 107 ± 6 % (t = 10 minutes) of the whole unstimulated saliva level (Figure 8.3c). The comparable results in whole unstimulated saliva and stimulated saliva obtained using

polystyrene Salivette further evidence that polystyrene swab is a suitable saliva collection tool for glutathione analysis.

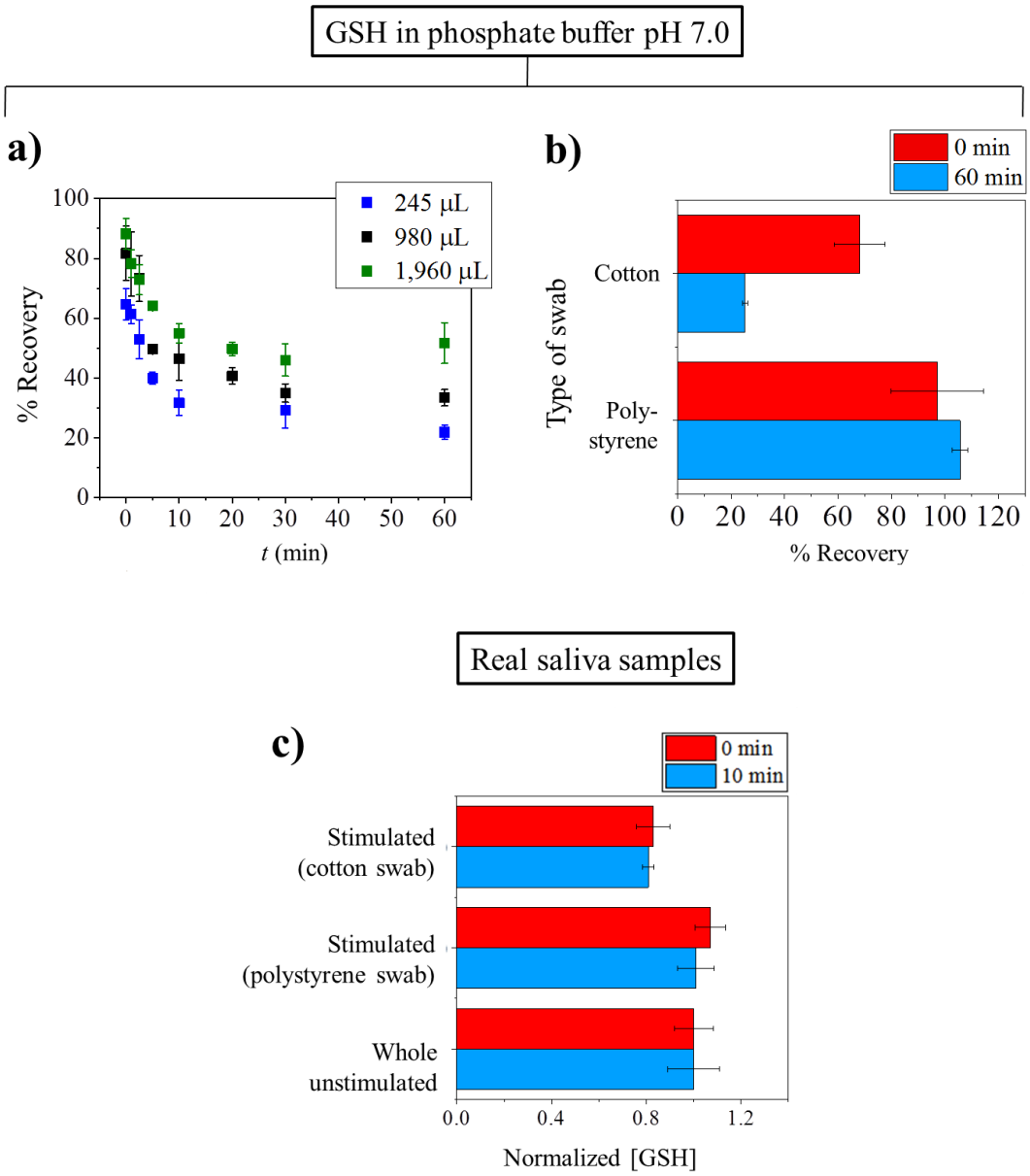


Figure 8.3: The effects of collection tools on the recovery of glutathione. **a)** The amount of glutathione recovered from cotton swab as a function of time between collection and centrifugation retrieval of the samples. **b)** The bar graph showing the significantly higher recovery of glutathione from synthetic polystyrene Salivette as compared with cotton Salivette at two different exposure times (*t*) of 0 min (**red**) and 60 min (**blue**). **c)** The concentrations of glutathione in real saliva samples: whole unstimulated saliva collected by spitting directly into a container and stimulated saliva collected by cotton Salivette and polystyrene Salivette at two different exposure times (*t*) of 0 min (**red**) and 10 min (**blue**).

8.3.2.2 Salivary and blood glutathione in bipolar disorder

In the first study, the saliva samples were collected using *cotton* Salivettes. Glutathione however has been demonstrated above to adsorb onto the surface of cotton swabs.[26] Importantly, the amount of glutathione lost to the cotton cannot be easily predicted, depending on a number of unknown and variable parameters (volume, initial concentration and saliva/cotton contact duration).[26] Alternatively, synthetic polystyrene Salivettes showed almost 100% recovery of glutathione[26] and hence were employed for the collection of saliva throughout the following studies.

In addition to the effect of collection tool, the volume of saliva collected was found to vary between individuals. Saliva samples were collected herein by giving the synthetic swabs to participants to chew for 1 minute. The samples were then extracted from the chewed swabs by centrifuging at the speed of 1000g for 2 minutes. The variation in the saliva volume collected likely reflect the hydration level (often affected by medication) of the subjects, and may cause additional uncertainties to the measurement of glutathione. Consequently, the correlation between salivary glutathione concentrations and the volume of the saliva extracted was evaluated. A total number of 10 bipolar patients and 10 control subjects were studied. The details of the subjects' demographic and clinical characteristics are summarised in Table 8.4.

Table 8.4: Demographic and clinical characteristics of the subjects participating in the 2nd study

	Controls (*n*=10)	**Bipolar (*n*=10)**	***p*-value**
Mean age, years (S.D.)[a]	36.7 (9.7)	36.3 (8.2)	0.922[b]
Male sex, *n* (%)	4 (40)	2 (20)	0.329[c]
Bipolar Type I, *n* (%)	-	4 (40)	-
Lithium, *n* (%)	-	5 (50)	-

[a] S.D.: standard deviation

[b] Two-tailed Student's *t*-test

[c] Chi-square (χ^2)

A significant negative correlation was observed between the volume of saliva collected and the total and reduced glutathione concentrations (total and reduced: r = -0.7, p = 0.001), see Figure 8.4. For oxidised glutathione, a negative correlation with volume was also observed, although not statistically significant (oxidised: r = -0.4, p = 0.10).

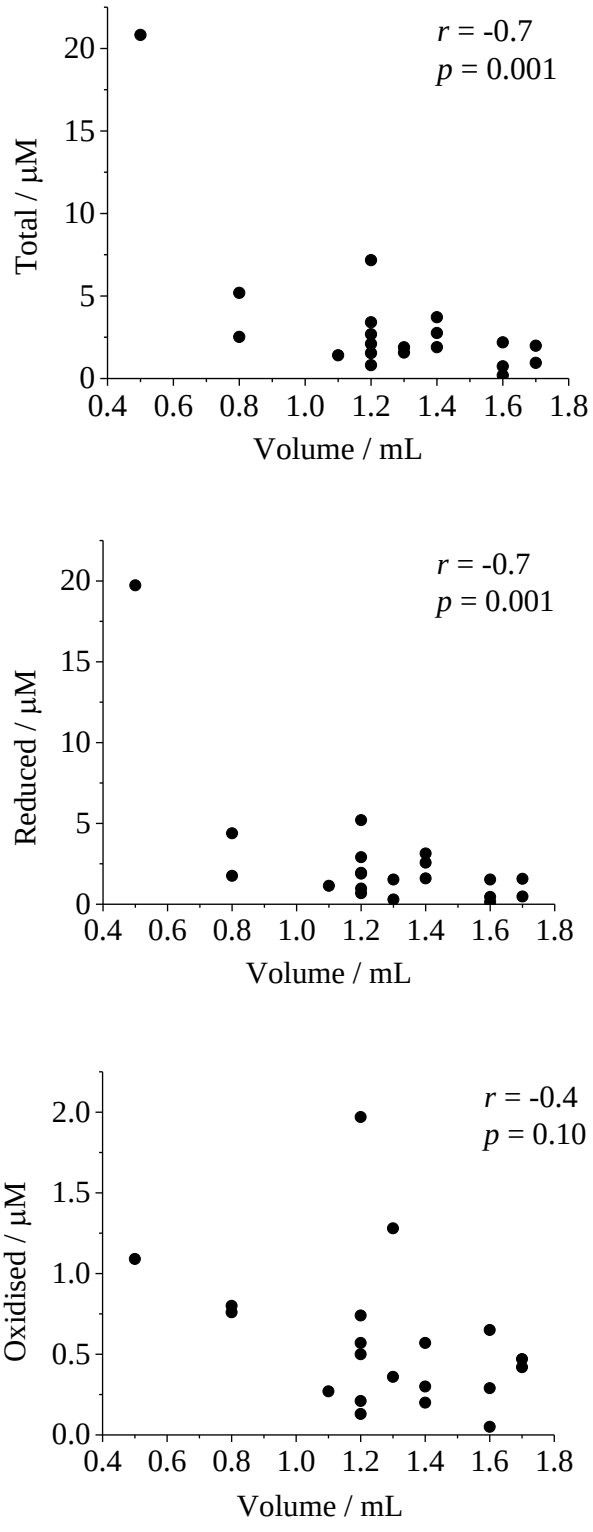


Figure 8.4: Correlations between salivary glutathione concentrations (total, reduced and oxidised) and the volume of saliva collected

The negative correlations between glutathione concentrations and the volume of saliva suggests that the measurement in 'concentrations' may primarily reflect the subject's hydration level, and thus hinder the determination of the target glutathione. Consequently, to eliminate the influence of the amount of water in the oral cavity, the *absolute* number of glutathione molecules is used instead of concentrations. The conversion between the two quantities can be done according to eqn. 8.8:

$$\text{Number of glutathione (mol)} = \text{Concentration (mol/L)} \times \text{Volume (L)} \qquad (8.8)$$

Using the improved collection method together with the correction for the variation in volume (eqn. 8.8), the potential of salivary glutathione as a biomarker for bipolar disorder was re-evaluated. Table 8.5 and Figure 8.5 summarise the amount of salivary glutathione measured. The numbers of total (GSH+GSSG) and reduced glutathione (GSH) are significantly higher in the bipolar group than the controls (total: $p = 0.029$, reduced: $p = 0.048$). The number of oxidised glutathione (GSSG) is also higher in the bipolar group, although not statistically significant (oxidised: $p = 0.134$). The results of the 2nd study are in good agreement with the 1st study that the salivary glutathione levels are likely to be elevated in bipolar patients.

The concentrations of glutathione were also determined in whole blood samples of all the subjects in this 2nd study; refer to Table 8.4 for demographic and clinical details. There was *no* significant difference in blood glutathione levels between bipolar and control groups (bipolar: 1169 ± 422 μM, control: 1161 ± 398 μM, $p = 0.97$). No significant correlations between saliva and blood glutathione were observed ($p > 0.6$).

Table 8.5: Salivary glutathione levels presented as the *number of moles* in bipolar patients vs. controls of the 2nd study

	Controls (*n*=10)	**Bipolar (*n*=10)**	***p*-value[b]**
Total glutathione: GSH + GSSG, nmol (S.D.)[a]	2.1 (1.2)	4.5 (2.9)	0.029
Reduced glutathione: GSH, nmol (S.D.)	1.6 (1.1)	3.6 (2.8)	0.048
Oxidised glutathione: GSSG, nmol (S.D.)	0.5 (0.3)	0.9 (0.7)	0.134
Ratio of GSH : GSSG (S.D.)	3.9 (3.6)	5.8 (5.0)	0.350

[a] S.D.: standard deviation

[b] Two-tailed Student's *t*-test

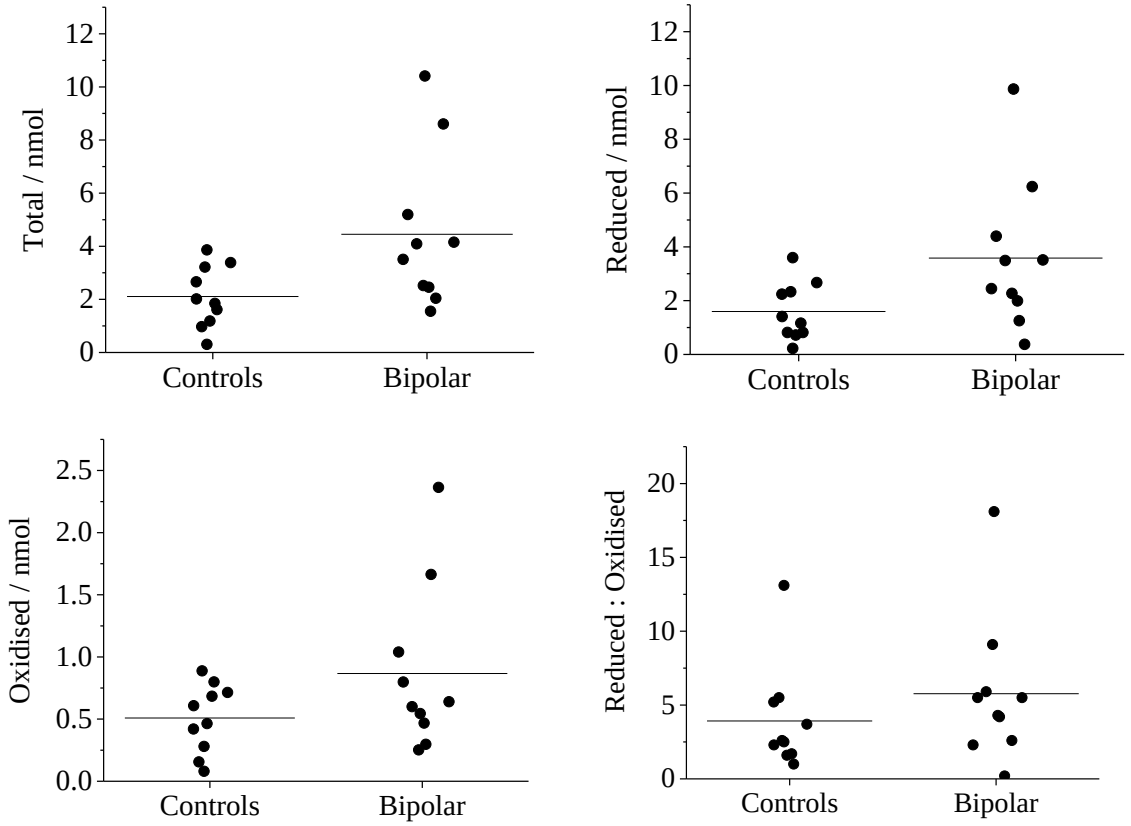


Figure 8.5: Scattered plots and mean (horizontal lines) of salivary glutathione in *number of moles*: total (GSH+GSSG), reduced (GSH), oxidised (GSSG) and ratio of reduced to oxidised (GSH:GSSG) in healthy control group and bipolar patients of the 2nd study.

8.4 Discussion

In this study, we found raised salivary levels of total (GSH + GSSG) and reduced glutathione (GSH) in bipolar patients compared to healthy controls. However the ratio of GSH:GSSG was unchanged. Since the latter has been suggested to represent a measure of oxidative status,[2] our results suggest that in saliva at least there does not appear to be evidence for oxidative stress in medicated bipolar patients in a relatively euthymic state.

The increase in salivary glutathione in bipolar patients observed herein is different from previous studies in other biological media, which have either reported no significant change or a decrease in glutathione levels, as summarised in Table 8.1. In particular, Rosa et al.[3] reported that plasma GSH levels were decreased while those of GSSG were increased. A similar finding was obtained by Raffa et al.[4] studying glutathione in the red blood cells of medicated bipolar patients. On the other hand, Tunçel et al.[5] found a tendency to increased plasma total glutathione levels in medicated bipolar patients although the result was not statistically significant. The measurements of glutathione in plasma however are likely to be undermined due to the fast rate of degradation *in-vitro*, as discussed in Chapter 6. No studies of salivary glutathione in bipolar patients have been reported before.

A decrease in glutathione levels in bipolar patients was also observed in prefrontal cortex of post-mortem samples from bipolar patients compared to matched controls; however, the ratio of GSH:GSSG was unaltered.[6] Two *in-vivo* studies of bipolar patients did not find any difference in brain GSH levels between bipolar patients and healthy controls.[7,8]

The increase in salivary GSH and GSSG may reflect the different origin of saliva glutathione from that in blood. Indeed, we found no significant correlation between glutathione measured in saliva and that in whole blood. In addition to antioxidant activity, glutathione has been

suggested to be involved in glutamatergic neurotransmission by potentially inducing glutamate release.[27] Glutamate is a major excitatory neurotransmitter in the brain, and the abnormal glutamate functions have been reported to be related to bipolar and other mood disorders.[28,29] The change in glutathione levels may also relate to the abnormalities of γ-aminobutyric acid (GABA) in bipolar disorder.[30]

8.5 Conclusions

The finding of increased total (GSH + GSSG) and reduced glutathione (GSH) in bipolar patients was statistically significant, suggesting the potential of salivary glutathione as a biomarker for the disorder. The origin of this increase however still remains unknown. It is possible that saliva glutathione is not representative of glutathione levels in tissues more related to bipolar disorder, for example the central nervous system, but may be involved in processes indirectly connected with bipolar disorder. This work further demonstrates that the assay developed in Chapter 6 for salivary glutathione measurements is simple and feasible, allowing easy, swift and non-invasive testing of both GSH and GSSG in bipolar patients.

Bibliography

(1) Ngamchuea, K.; Batchelor-McAuley, C.; Williams, C.; Godlewska, B. R.; Sharpley, A. L.; Cowen, P. J.; Compton, R. G. *J. Affect. Disord.* **2018**, *238*, 277-280.
(2) Berk, M.; Kapczinski, F.; Andreazza, A. C.; Dean, O. M.; Giorlando, F.; Maes, M.; Yucel, M.; Gama, C. S.; Dodd, S.; Dean, B.; Magalhaes, P. V.; Amminger, P.; McGorry, P.; Malhi, G. S. *Neurosci. Biobehav. Rev.* **2011**, *35*, 804-817.
(3) Rosa, A. R.; Singh, N.; Whitaker, E.; de Brito, M.; Lewis, A. M.; Vieta, E.; Churchill, G. C.; Geddes, J. R.; Goodwin, G. M. *Psychol. Med.* **2014**, *44*, 2409-2418.
(4) Raffa, M.; Barhoumi, S.; Atig, F.; Fendri, C.; Kerkeni, A.; Mechri, A. *Prog. Neuropsychopharmacol. Biol. Psychiatry* **2012**, *39*, 371-375.
(5) Tuncel, O. K.; Sarisoy, G.; Bilgici, B.; Pazvantoglu, O.; Cetin, E.; Unverdi, E.; Avci, B.; Boke, O. *Psychiatry Res.* **2015**, *228*, 688-694.
(6) Gawryluk, J. W.; Wang, J. F.; Andreazza, A. C.; Shao, L.; Young, L. T. *Int. J. Neuropsychopharmacol.* **2011**, *14*, 123-130.
(7) Lagopoulos, J.; Hermens, D. F.; Tobias-Webb, J.; Duffy, S.; Naismith, S. L.; White, D.; Scott, E.; Hickie, I. B. *J. Psychiatr. Res.* **2013**, *47*, 412-417.
(8) Godlewska, B. R.; Yip, S. W.; Near, J.; Goodwin, G. M.; Cowen, P. J. *Psychopharmacology (Berl.)* **2014**, *231*, 327-332.
(9) Ngamchuea, K.; Batchelor-McAuley, C.; Compton, R. G. *Anal. Chem.* **2017**, *89*, 2901-2908.

(10) First, M. B.; Spitzer, R. L.; Gibbon, M.; Williams, J. B. W. *Structured Clinical Interview for DSM-IV Axis I Disorders-Clinical Version (SCID-CV)*; American Psychiatric Press. Washington, DC., USA, **1997**.
(11) Young, R. C.; Biggs, J. T.; Ziegler, V. E.; Meyer, D. A. *Br. J. Psychiatry* **1978**, *133*, 429-435.
(12) Hamilton, M. *J. Neurol. Neurosurg. Psychiatry* **1960**, *23*, 56-62.
(13) Richie, J. P., Jr.; Skowronski, L.; Abraham, P.; Leutzinger, Y. *Clin. Chem.* **1996**, *42*, 64-70.
(14) Emekli-Alturfan, E.; Yarat, A.; Caliskan-Ak, E.; Pisiriciler, R.; Kuru, B.; Noyan, U. *J. Clin. Lab. Anal.* **2013**, *27*, 261-266.
(15) Tietze, F. *Anal. Biochem.* **1969**, *27*, 502-522.
(16) Rahman, I.; Kode, A.; Biswas, S. K. *Nat. Protoc.* **2006**, *1*, 3159-3165.
(17) Ngamchuea, K.; Batchelor-McAuley, C.; Cowen, P. J.; Williams, C.; Goncalves, L. M.; Compton, R. G. *Analyst* **2016**, *141*, 4707-4712.
(18) Fowler, J.; Cohen, L.; Jarvis, P. *Practical Statistics for Field Biology*; Wiley, Chichester, UK, **2013**.
(19) Lang, T. A.; Secic, M. *How to Report Statistics in Medicine: Annotated Guidelines for Authors, Editors, and Reviewers*; American College of Physicians, Philadelphia, USA, **2006**.
(20) Ramachandran, K. M.; Tsokos, C. P. *Mathematical Statistics with Applications*; Elsevier Science, **2009**.
(21) Zou, K. H.; Tuncali, K.; Silverman, S. G. *Radiology* **2003**, *227*, 617-622.
(22) Almadori, G.; Bussu, F.; Galli, J.; Limongelli, A.; Persichilli, S.; Zappacosta, B.; Minucci, A.; Paludetti, G.; Giardina, B. *Head Neck* **2007**, *29*, 648-654.
(23) Zappacosta, B.; Persichilli, S.; De Sole, P.; Mordente, A.; Giardina, B. *Arch. Oral Biol.* **1999**, *44*, 485-488.
(24) Shirtcliff, E. A.; Granger, D. A.; Schwartz, E.; Curran, M. J. *Psychoneuroendocrinology* **2001**, *26*, 165-173.
(25) Hodinka, R. L.; Nagashunmugam, T.; Malamud, D. *Clin. Diagn. Lab. Immunol.* **1998**, *5*, 419-426.
(26) Ngamchuea, K.; Chaisiwamongkhol, K.; Batchelor-McAuley, C.; Compton, R. G. *Analyst* **2018**, *143*, 81-99.
(27) Chin, T. Y.; Chueh, S. H.; Tao, P. L. *Acta Pharmacol. Sin.* **2006**, *27*, 853-860.
(28) Jun, C.; Choi, Y.; Lim, S. M.; Bae, S.; Hong, Y. S.; Kim, J. E.; Lyoo, I. K. *Exp. Neurobiol.* **2014**, *23*, 28-35.
(29) Sanacora, G.; Treccani, G.; Popoli, M. *Neuropharmacology* **2012**, *62*, 63-77.
(30) Soares, J. C.; Young, A. H. *Bipolar Disorders: Basic Mechanisms and Therapeutic Implications*; Cambridge University Press, Cambridge, UK, **2016**.

Chapter 9 Understanding electroanalytical measurements in authentic human saliva leading to the detection of salivary uric acid

This chapter shifts the focus of this thesis to another potential biomarker present in saliva, uric acid. An electroanalytical method for the detection of salivary uric acid is developed herein, together with the investigations of the electrochemical behaviour of the commonly used redox mediators, ferrocenemethanol **(**$FcCH_2OH$**)** and ferrocyanide ($[Fe(CN)_6]^{4-}$), in authentic saliva samples. First, we show that $FcCH_2OH$ and $[Fe(CN)_6]^{4-}$ display well-defined voltammetry in undiluted saliva at a carbon microdisc electrode without the addition of any supporting electrolyte. The $FcCH_2OH$ oxidation is shown not to be altered by the medium apart from the steady-state currents which change according to the viscosity of the solvent. In contrast, the voltammetry of $[Fe(CN)_6]^{4-}$ oxidation in authentic saliva is significantly different from that in synthetic saliva or aqueous electrolyte. It is demonstrated that the electrode is partially blocked by organic molecules or other electrochemically inert species when placed in authentic saliva samples. The distortion in voltammetry thus reflects the different surface sensitivity of the two processes. Ohmic drop is proved to be minimal at microelectrodes even without added electrolyte. Finally, we demonstrate that uric acid which is a potential biomarker for gout, oral cavity cancer and other several diseases can be directly detected in authentic saliva at a carbon microelectrode with the interference of ascorbic acid and dopamine of no more than 10%.

The work presented in this chapter has been published in *Sens. Actuators, B.*[1]

9.1 Introduction

Saliva is a complex bodily fluid consisting of a variety of diagnostically useful components.[2] Saliva specimens can be easily collected via non-invasive means, are readily available and easily stored at lower temperatures than blood samples.[3,4] The results reported in Chapter 8 on the use of salivary glutathione as a biomarker for bipolar disorder further demonstrates the potential of saliva as an alternative diagnostic fluid. Certain metabolites (such as glutathione reported in Chapter 6) also display greater stability in saliva than blood plasma, potentially reducing errors arising from *in-vitro* artefacts.[5,6] Consequently, saliva analysis may be preferred over traditional blood measurements in particular at point-of-care sites and for long-term self-monitoring purposes.

To facilitate the use of saliva as a diagnostic auxiliary, inexpensive and reliable analytical assays are required. In this work, electroanalytical methods are studied, developed and validated for applications in human saliva samples. *Authentic* saliva however is a complex medium and the electroanalytical performance of many redox-active species can be significantly different from their behaviour in standard aqueous electrolytes. Even *synthetic* saliva, as will be demonstrated, can be a poor model medium. Potential issues surrounding electrochemical measurements in authentic saliva include the fouling of electrode surface, the variation between different samples in terms of their viscosity and hence the diffusion coefficients of the analytes, as well as the presence of dissolved interfering molecules. [7]

Herein, the deviation of electrochemical responses in authentic saliva from those seen in other inorganic electrolytes is investigated using the standard redox probes: ferrocenemethanol/ferroceniummethanol and ferrocyanide/ferricyanide. Both systems are often used as redox mediators in biosensors.[8-10] The understanding of these redox processes in authentic saliva is thus highly important for accurate measurements in biological and

medical samples. Analysis of the voltammograms at a microdisc electrode reveals the physical origins underlying the altered responses in authentic saliva. Importantly using the two redox processes above, we demonstrate that well-defined voltammetry can be obtained directly in *undiluted* authentic saliva without any pre-treatment or modification of the samples.

With understanding of the characteristics of electroanalytical measurements in authentic saliva, this work then moves on to the detection of uric acid in saliva samples. Salivary uric acid has displayed potential as a biomarker for gout,[11] renal disease,[12] oral cavity cancer,[13,14] obesity, hypertension and metabolic syndrome[15,16] as well as type 2 diabetes.[17] Its concentration has further been used in the monitoring of the efficiency of treatment of chronic gout arthropathy[18] and hyperuricemia,[19] and in the estimation of oxidative stress produced by smoking and periodontitis.[20,21] Statistically significant positive correlations between the concentrations of uric acid in saliva and blood have been established.[15,19] Detection of salivary uric acid has been made using microfluidics,[22,23] capillary electrophoresis,[11,12] colorimetry,[24] spectrophotometry,[25] chromatography[26] and biosensors.[27] A number of electrochemical methods are available for the detection of uric acid.[28-33] However, only a few methodologies have been validated with authentic saliva and in those cases the saliva samples were greatly diluted in inorganic buffers.[34] In this work, an electroanalytical method for the detection of uric acid is developed and applied to authentic whole saliva without dilution or any modification of the samples via the use of a carbon microdisc electrode.

9.2 Experimental

9.2.1 Electrode set-up

Electrochemical experiments were performed using a standard three electrode setup. A carbon microdisc (33 μm diameter, BASi) and a platinum mesh were used as working and counter electrodes respectively. A leakless Ag/AgCl (in 3.4 M KCl, eDAQ) was used as a reference electrode in order to prevent contamination of the samples by chloride ions, which could otherwise affect the responses measured.[35]

9.2.2 Ferrocenemethanol and ferrocyanide oxidation

Synthetic or authentic saliva samples containing 1.0 mM ferrocenemethanol ($FcCH_2OH$) were prepared by directly dissolving 0.5 mg of $FcCH_2OH$ (s) into 2.30 mL of the samples. Cyclic voltammetry of $FcCH_2OH$ oxidation was first scanned anodically before being reversed back in the potential range of -0.2 - 0.8 V at the scan rate of 10 mV s^{-1}.

Similar experiments were performed with ferrocyanide ($[Fe(CN)_6]^{4-}$). The samples containing 1.0 mM ferrocyanide were prepared by dissolving 1.0 mg of $K_4[Fe(CN)_6]\cdot 3H_2O$ (s) in 2.37 mL of synthetic or authentic saliva samples.

9.2.3 Uric acid, ascorbic acid and dopamine oxidation

Cyclic voltammetry of uric acid, ascorbic acid and dopamine oxidation in synthetic or authentic saliva was recorded by scanning the potential anodically from -0.2 V to 1.0 V, then reversed back to -0.2 V at the scan rate of 10 mV s^{-1}. In authentic saliva specimens, standard addition method was used to determine the levels of the relevant species in the samples.

9.3 Results and discussion

Herein, the characteristics of electrochemical measurements in authentic saliva are first investigated. An assay for the detection of uric acid is then developed and validated in authentic undiluted saliva specimens.

9.3.1 Investigations of the electrochemical behaviour in *authentic* vs. *synthetic* saliva

The electrochemical performances of ferrocenemethanol / ferrocenium methanol and ferrocyanide/ferricyanide redox systems are investigated in authentic saliva and the results compared with that in synthetic saliva and standard electrolytes.

a) Ferrocenemethanol ($FcCH_2OH$) oxidation

The oxidation of 1.0 mM ferrocenemethanol ($FcCH_2OH$) in 0.10 M KCl solution, in synthetic saliva and in authentic saliva was investigated at a carbon microdisc electrode at a scan rate of 10 mV s^{-1}. The use of microdisc electrodes minimises the contribution of capacitative currents and allows under favourable conditions the measurement of the electron-transfer kinetics of the redox couple. The resulting cyclic voltammograms presented in Figure 9.1 display steady-state behaviour with the steady-state currents (mean ± standard deviation) of 6.4 ± 0.1, 6.6 ± 0.1 and 4.2 ± 0.1 nA in 0.10 M KCl, synthetic saliva and authentic saliva respectively. From these mass-transport limited currents and using eqn. 9.1,[36] the diffusion coefficients of $FcCH_2OH$ in the differing media were determined to be $8.1 \pm 0.1 \times 10^{-10}$ (comparable to literature[37,38]), $8.3 \pm 0.1 \times 10^{-10}$ and $5.3 \pm 0.1 \times 10^{-10}$ m^2 s^{-1} respectively.

$$I_{ss} = 4nFcDr_e \qquad (9.1)$$

where I_{ss} is the steady-state current, n is the number of electron transferred per molecule and F is the Faraday constant (96,485 C mol^{-1}). c and D are the bulk concentration and the diffusion coefficient of the redox-active species respectively. r_e is the radius of the electrode determined using $[Ru(NH_3)_6]^{3+}$ reduction[39] to be 20.5 ± 0.1 μm (Appendix B1).

Diffusion coefficient (D) varies approximately with the inverse of the solution viscosity (η) for sufficiently large molecules according to the Stokes-Einstein equation:

$$D = \frac{k_B T}{6\pi\eta r} \qquad (9.2)$$

where k_B is the Boltzmann constant, T the absolute temperature and r the radius of the diffusing particle.

The viscosity of synthetic saliva is approximated to be similar to that of pure water at 25 ^oC. Authentic saliva showed a variation in viscosity, with the average being ca. 1.1-1.3 times higher than that of pure water at 25 ^oC.[40] The higher viscosity of authentic saliva is due to the presence of mucin and other macromolecules.[41] The lower diffusion coefficient observed in authentic saliva as compared with synthetic saliva is thus consistent with the higher viscosity of the former.

For one-electron transfer systems, as in the case of $FcCH_2OH$ oxidation, the rate of electron transfer can be analysed using mass-transport corrected Tafel analysis. In the irreversible limit (eqn. 9.3),[36] a plot of $\ln\left(\frac{I_{ss}}{I} - 1\right)$ against E gives a slope of $\frac{\alpha F}{RT}$ for a one-electron transfer process and hence the experimental transfer coefficient (α) can be determined. In the reversible limit (eqn. 9.4),[42] the electrochemical flux is controlled by the Nernst equation, and hence no kinetic information can be obtained. In this reversible limit, a plot of $\ln\left(\frac{I_{ss}}{I} - 1\right)$

against E gives the slope of a constant value of $\frac{F}{RT}$, hence yielding an experimentally determined *apparent* transfer coefficient of 1 (equalling the number of electrons transferred).

$$\textbf{Irreversible limit:} \quad \ln\left(\frac{I_{ss}}{I} - 1\right) = \frac{\alpha F}{RT}\left(E - E_f^0\right) + \ln\left(\frac{-I_{ss}}{FA_e k^0 c}\right) \tag{9.3}$$

$$\textbf{Reversible limit:} \quad \ln\left(\frac{I_{ss}}{I} - 1\right) = \frac{F}{RT}\left(E - E_f^0\right) + \ln\left(\frac{D_{\text{reduced}}}{D_{\text{oxidised}}}\right) \tag{9.4}$$

where I_{ss} and I are the steady-state and transient currents respectively. R is the molar gas constant (8.314 J mol^{-1} K^{-1}). E and E_f^0 are the applied potential and formal potential respectively. A_e is the geometric surface area of the electrode and k^0 the rate of electron transfer. D_{reduced} and D_{oxidised} are the diffusion coefficients of the reduced and oxidised species respectively.

For the oxidation of $FcCH_2OH$, the experimentally determined apparent transfer coefficient (α) was 1.06 ± 0.04 in all the electrolytes and real samples studied, indicating the electron transfer is electrochemically reversible under all conditions; see inlay in Figure 9.1. The voltammograms of $FcCH_2OH$ oxidation are the same to within 2 mV in all media with the half-wave potentials ($E_{½}$) at 0.226 ± 0.002 V (vs. Ag/AgCl).

In this section, we have thus demonstrated that well-defined voltammetric responses of $FcCH_2OH$ can be obtained in undiluted unmodified authentic saliva samples, and that the responses observed were electrochemically reversible. However, the magnitude of the steady-state currents varies according to the viscosity of the samples. The $FcCH_2OH/FcCH_2OH^+$ system is thus recommended for use as a redox mediator in sensors for saliva applications, but a calibration curve of $FcCH_2OH$ steady-state currents vs. concentrations of the target analytes should be obtained directly in the saliva samples to prevent errors from the variation in the viscosity of the medium.

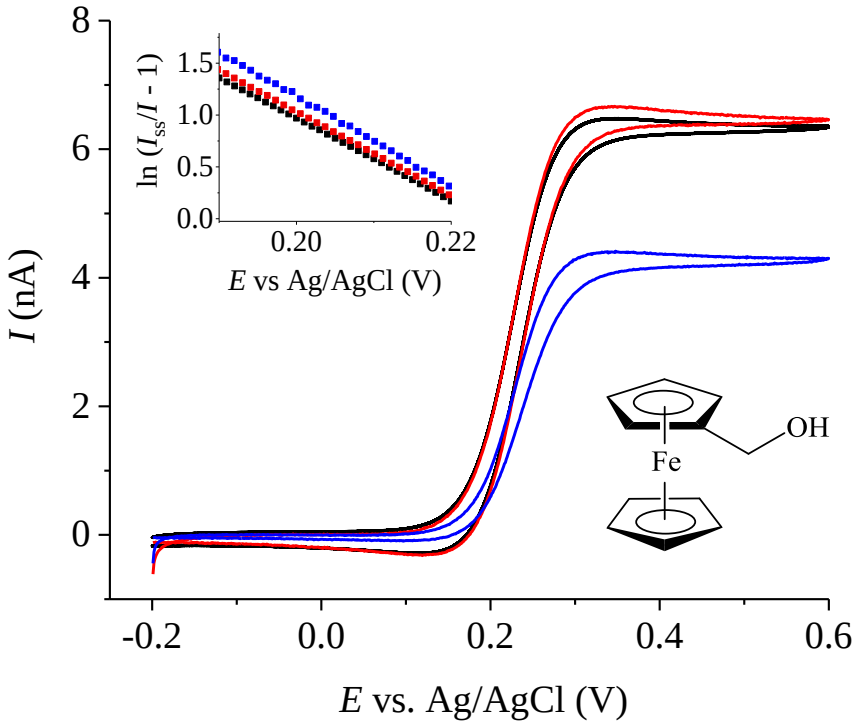


Figure 9.1: Cyclic voltammetry of 1.0 mM ferrocenemethanol ($FcCH_2OH$) oxidation in 0.10 M KCl (**black**), synthetic saliva (**red**) and authentic saliva (**blue**) at a carbon microdisc working electrode; scan rate of 10 mV s^{-1}. The inlay shows the results of mass-transport corrected analyses. The chemical structure of ferrocenemethanol is given on the right-hand side of the figure.

b) Ferrocyanide ($[Fe(CN)_6]^{4-}$) oxidation

The oxidation of 1.0 mM ferrocyanide ($[Fe(CN)_6]^{4-}$) in 0.10 M KCl, in synthetic saliva and in authentic saliva was next investigated at a carbon microdisc electrode (scan rate of 10 mV s^{-1}). Figure 9.2a shows the resulting voltammograms. The steady-state currents were 5.4 ± 0.1, 5.1 ± 0.2 and 4.5 ± 0.2 nA, corresponding to the diffusion coefficients of $6.8 \pm 0.1 \times 10^{-10}$ (comparable to literature[43,44]), $6.4 \pm 0.3 \times 10^{-10}$ and $5.7 \pm 0.3 \times 10^{-10}$ in 0.10 M KCl, synthetic and authentic saliva respectively. The slower diffusion in authentic saliva is consistent with the more viscous nature of the sample as discussed above. However, in authentic saliva, the oxidation of $[Fe(CN)_6]^{4-}$ is found to be voltammetrically distorted

with the oxidation requiring the applications of higher over-potentials ($E_{½}$ = 0.25 V) as compared with 0.10 M KCl and synthetic saliva ($E_{½}$ = 0.22 V). The apparent transfer coefficient (α) of $[Fe(CN)_6]^{4-}$ oxidation in authentic saliva is 0.8 ± 0.1, lower than the value of 1.0 ± 0.1 in 0.10 M KCl and synthetic saliva and thus suggests the more electrochemically *irreversible* nature of the oxidation in authentic samples; see inlay in Figure 9.2a.

The above voltammetry was conducted directly in undiluted saliva samples. To further elucidate the origin of the relatively slow kinetics in authentic saliva, a carbon microdisc electrode was first immersed in authentic saliva samples under open circuit potential. The electrode was then transferred to a solution containing only 1.0 mM $[Fe(CN)_6]^{4-}$ and 0.10 M KCl where cyclic voltammetry was again recorded. The resulting voltammograms are shown in Figure 9.2b and demonstrate that the redox process becomes more *irreversible* as the electrode was immersed in authentic saliva for longer time prior to the oxidation of $[Fe(CN)_6]^{4-}$ in standard 0.10 M KCl solutions; $E_{½}$ of 0.22, 0.29 and 0.32 V after 0, 1 and 5 minutes immersion respectively. This is an indication that the exposure of electrode to authentic saliva results in the adsorption of electrochemically inert components (such as organic molecules, proteins, etc.) or the assembly of charged species on the electrode surface. The former effectively decreases the electroactive surface area of the electrode.[45] The latter hinders the mass transport of $[Fe(CN)_6]^{4-}$ ions to the electrode due to electrostatic repulsion between negatively charged species and hence alters the electrochemical responses observed.

Similar experiments were performed for ferrocenemethanol (electrically neutral) and no changes in the voltammograms were observed from prolonged exposure of the electrode in authentic saliva samples. The hypothesis of the negatively charged species on the electrode surface was further tested using the positively charged redox probe, hexaammineruthenium (III) ($[Ru(NH_3)_6]^{3+}$), Appendix B2. The cyclic voltammograms of

$[Ru(NH_3)_6]^{3+}$ reduction in both authentic and synthetic saliva are fully reversible with the electron transfer coefficient of 1.0 within ±5% error, see Appendix B2. Therefore out of the three redox systems tested, ferrocenemethanol and hexaammineruthenium (III) which are electrically neutral and positive respectively did not show the difference in the reversibility of the voltammetry in authentic saliva as compared with synthetic saliva. On the other hand, the voltammograms of the negatively charged ferrocyanide ($[Fe(CN)_6]^{4-}$) become more irreversible in authentic saliva. The results are thus not inconsistent with the proposed hypothesis of the negatively charged species on the electrode surface.

The difference in the effects of authentic saliva on the oxidation of ferrocyanide from that of ferrocenemethanol or hexaammineruthenium also likely reflects the inner-sphere *vs.* outer-sphere electron transfer behaviours of the processes. Although ferrocyanide is often considered to be a good redox probe, the electron transfer is known to exhibit surface sensitivity[46] and is perhaps best viewed as a fast inner-sphere redox process. The characteristics of these redox processes in authentic saliva, in particular the decrease in the steady-state currents due to the increased viscosity and the change in the electron transfer kinetics of ferrocyanide oxidation, should be considered when employed as standard redox probes in real saliva samples.

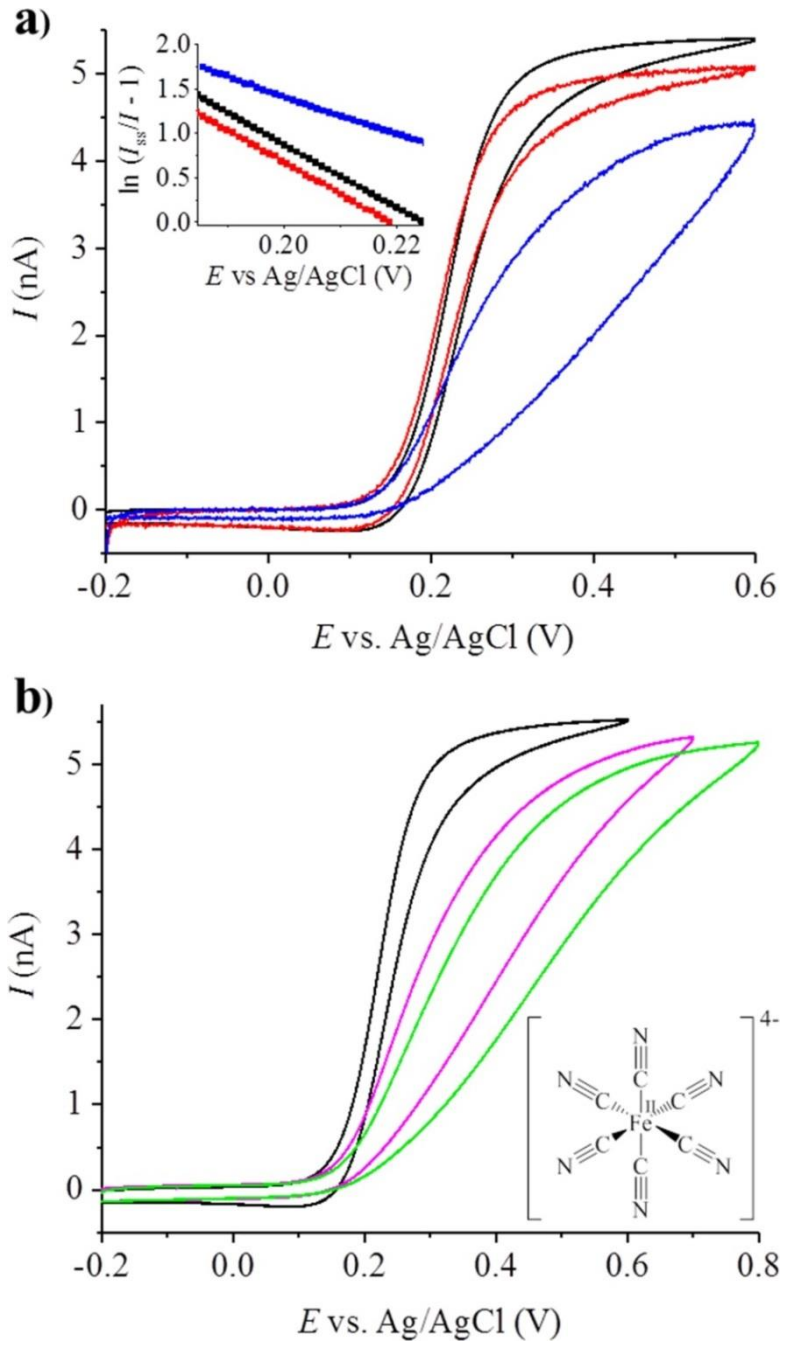


Figure 9.2: Cyclic voltammetry of 1.0 mM ferrocyanide ($[Fe(CN)_6]^{4-}$) oxidation **a)** performed directly in 0.10 M KCl (**black**), synthetic saliva (**red**) and authentic saliva (**blue**) with the inlay showing the results of mass-transport corrected Tafel analyses; **b)** in 0.10 M KCl after the carbon microdisc working electrode was immersed in authentic saliva for 0 minute (**black**), 1 minute (**pink**) and 5 minutes (**green**). Scan rate of 10 mV s^{-1}.

9.3.2 Salivary uric acid detection

In the previous sections, the electrochemical behaviour of often used redox markers has been investigated in authentic saliva demonstrating that electrochemical measurements can be made using a microelectrode without the addition of supporting electrolyte. Importantly, due to the small magnitude of the currents (<10 nA) passed at the microelectrode the requirement of using added excess supporting electrolyte is completely relaxed.[47,48] The ionic strength of human authentic saliva is 44.6 ± 11.6 mM.[49] The fact that the voltammetric response of ferrocenemethanol is found to be essentially unaltered apart from a change in the associated diffusion coefficient provides strong evidences that the voltammetric distortions observed for the other molecular species arises due to sensitivity of the redox processes to the electrode surface, and not from issues associated with ohmic drop. In the absence of ferrocenemethanol results, the observed distorted voltammograms for the other molecular probes might be erroneously ascribed as relating to ohmic drop effects through the solution.

Having demonstrated the ability to perform electroanalysis directly in authentic saliva samples, in this section, we next focus on the detection of salivary uric acid which is a potential biomarker for gout,[11] oral cavity cancer[13,14] and other several diseases.[15-17]

The cyclic voltammetry of authentic saliva sample at a carbon microdisc electrode shows an oxidative peak at ~0.7 V (Figure 9.3, inlay). The oxidation at this potential likely corresponds to uric acid (UA), ascorbic acid (AA) or dopamine (DA); see Appendix B3. However in authentic human saliva, AA and DA are present at very low concentrations of ca. 1.4 ± 0.3 μM[50] and < 0.5 nM[51] respectively, compared with the concentration of ca. 200-300 μM of UA.[52-54] Consequently, when measured using the carbon microdisc electrode, UA will be the dominant contributor to the electrochemical current with the interferences from AA and DA contributing no more than ~10%.

Figure 9.3 presents the cyclic voltammograms of 120 μM UA added to synthetic and authentic saliva at a carbon microdisc electrode at the scan rate of 10 mV s^{-1}; see Appendix B3 for the voltammograms of AA and DA. The oxidation of UA (as well as AA and DA) has been reported to be a 2-electron transfer process [55]. The steady-state current for UA oxidation in synthetic saliva was 1.4 ± 0.1 nA at a microdisc electrode radius 20.5 ± 0.1 μm, corresponding to the diffusion coefficient of $7.4 \pm 0.5 \times 10^{-10}$ m^2 s^{-1}. The half-wave potential ($E_{½}$) was observed at 0.47 ± 0.01 V and the apparent transfer coefficient (α) determined using eqn. 9.3 to be 0.48 ± 0.02 for UA oxidation in synthetic saliva.

In authentic saliva, the oxidation wave of UA is shifted from that of synthetic saliva to a more positive potential by ~100 mV likely due to partial blocking of the electrode as previously discussed. The sloping of the oxidative currents at high potentials is due to the earlier onset of solvent decomposition. In the determination of UA concentrations in authentic saliva, the steady-state currents may be influenced by the variation in the viscosity between different samples and possibly also the differing effects of molecular interferences. The method of standard additions was thus employed. The standard additions of UA to authentic saliva samples give linear responses of the peak currents ($I_p = I_{0.7\,V} - I_{0.2\,V}$) as a function of concentrations with the sensitivity of 8.8 ± 0.8 pA μM^{-1}. In the particular sample studied, the concentration of UA was determined to be 192 ± 7 μM (mean ± standard deviation). However, it should be noted that there is also a possible ca. 10% error as a result of the AA and DA interferences. The levels of salivary UA measured are in good agreement with the range of independent values reported in literature.[52-54] The limit of detection ($3s_B/m$) of UA in the authentic saliva samples studied is 20 μM.

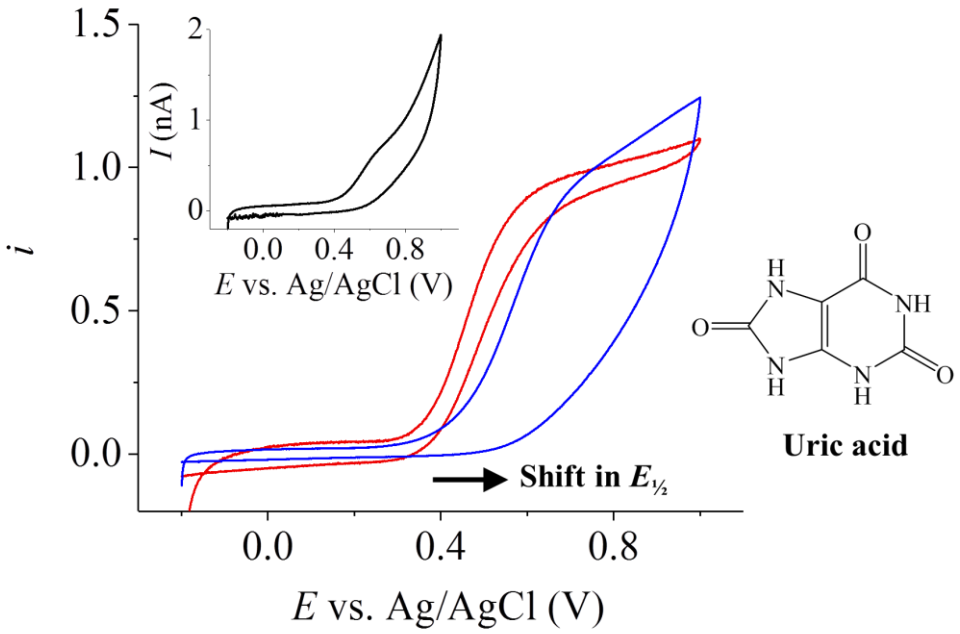


Figure 9.3: Normalised cyclic voltammograms of 120 µM uric acid oxidation in synthetic saliva (**red**) and authentic saliva (**blue**) showing the shift in the half-wave potentials ($E_{½}$). The inlay is the voltammogram of blank, unmodified authentic saliva. Carbon microdisc working electrode; scan rate of 10 mV s^{-1}. The chemical structure of uric acid is also given in the figure.

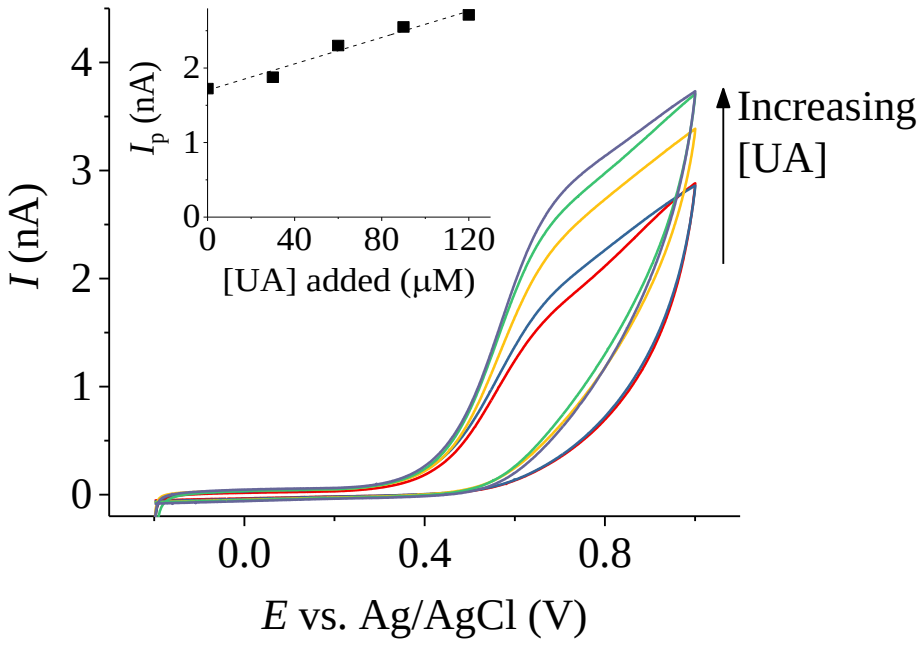


Figure 9.4: Cyclic voltammetry of increasing concentrations of uric acid added to authentic saliva samples at a carbon microdisc working electrode at the scan rate of 10 mV s^{-1}. The inlay shows the peak currents measured ($I_p = I_{0.7\ V} - I_{0.2\ V}$) as a function of concentrations added.

9.4 Conclusions

Steady-state voltammograms were observed at a carbon microdisc electrode for the oxidation of ferrocenemethanol ($FcCH_2OH$) and ferrocyanide ($[Fe(CN)_6]^{4-}$) in authentic human saliva without pre-treatment or modification of the samples. In the case of $FcCH_2OH$, the responses are electrochemically *reversible* in authentic saliva, synthetic saliva and aqueous KCl electrolyte, although the steady-state currents are ~20-30% smaller in authentic samples due to their higher viscosities. In contrast, the voltammogram of $[Fe(CN)_6]^{4-}$ oxidation becomes more *irreversible* in authentic saliva probably as a result of partial blocking of the electrode by organic interferences, reflecting the surface sensitivity of the two redox processes. We have thus demonstrated the different electrochemical behaviours in authentic saliva of the two common redox probes as well as highlighted the importance of the validation of any developed assays in *authentic* saliva, as opposed to synthetic saliva. Importantly, we developed an electroanalytical method via the use of a carbon microdisc electrode for the detection of salivary uric acid. The method has been directly validated in authentic saliva specimens and is suitable for salivary diagnostic applications.

Bibliography

(1) Ngamchuea, K.; Batchelor-McAuley, C.; Compton, R. G. *Sens. Actuators, B* **2018**, *262*, 404-410.
(2) Hofman, L. F. *J. Nutr.* **2001**, *131*, 1621s-1625s.
(3) Richie, J. P., Jr.; Skowronski, L.; Abraham, P.; Leutzinger, Y. *Clin. Chem.* **1996**, *42*, 64-70.
(4) Emekli-Alturfan, E.; Yarat, A.; Caliskan-Ak, E.; Pisiriciler, R.; Kuru, B.; Noyan, U. *J. Clin. Lab. Anal.* **2013**, *27*, 261-266.
(5) Ngamchuea, K.; Batchelor-McAuley, C.; Compton, R. G. *Anal. Chem.* **2017**, *89*, 2901-2908.
(6) Ngamchuea, K.; Batchelor-McAuley, C.; Compton, R. G. *Chem. Eur. J* **2016**, *22*, 15937-15944.
(7) Ngamchuea, K.; Chaisiwamongkhol, K.; Batchelor-McAuley, C.; Compton, R. G. *The Analyst* **2018**, *143*, 81-99.
(8) Weber, C.; Gauda, E.; Mizaikoff, B.; Kranz, C. *Anal. Bioanal. Chem.* **2009**, *395*, 1729-1735.
(9) Chen, P.; Peng, Y.; He, M.; Yan, X. C.; Zhang, Y.; Liu, Y. N. *Int. J. Electrochem. Sci.* **2013**, *8*, 8931-8939.
(10) Li, G.; Liao, J. M.; Hu, G. Q.; Ma, N. Z.; Wu, P. J. *Biosens. Bioelectron.* **2005**, *20*, 2140-2144.
(11) Guan, Y. Q.; Chu, Q. C.; Ye, J. N. *Anal. Bioanal. Chem.* **2004**, *380*, 913-917.
(12) Guan, Y. Q.; Wu, T.; Ye, J. N. *J. Chromatogr. B* **2005**, *821*, 229-234.
(13) Salian, V.; Demeri, F.; Kumari, S. *Clin. Cancer Invest. J.* **2015**, *4*, 516.
(14) Giebultowicz, J.; Wroczynski, P.; Samolczyk-Wanyura, D. *J. Oral Pathol. Med.* **2011**, *40*, 726-730.

(15) Soukup, M.; Biesiada, I.; Henderson, A.; Idowu, B.; Rodeback, D.; Ridpath, L.; Bridges, E. G.; Nazar, A. M.; Bridges, K. G. *Diabetol. Metab. Syndr.* **2012**, *4*, 14.
(16) Choromańska, K.; Choromańska, B.; Dąbrowska, E.; Bączek, W.; Myśliwiec, P.; Dadan, J.; Zalewska, A. *Postepy Hig. Med. Dosw.* **2015**, *69*.
(17) Al-Rawi, N. H. *Diab. Vasc. Dis. Res.* **2011**, *8*, 22-28.
(18) Zhao, J.; Huang, Y. *Clin. Chim. Acta* **2015**, *450*, 115-120.
(19) Shibasaki, K.; Kimura, M.; Ikarashi, R.; Yamaguchi, A.; Watanabe, T. *Metabolomics* **2012**, *8*, 484-491.
(20) Fatima, G.; Uppin, R. B.; Kasagani, S.; Tapshetty, R.; Rao, A. *J. Adv. Oral Res.* **2016**, *7*, 24-28.
(21) Banu, S.; Jabir, N. R.; Mohan, R.; Manjunath, N. C.; Kamal, M. A.; Kumar, K. R.; Zaidi, S. K.; Khan, M. S.; Tabrez, S. *J. Periodontol.* **2015**, *86*, 431-439.
(22) Chang, C. P.; Nagel, D. J.; Velasquez, M. T.; Zaghloul, M. E. *Biosens. Bioelectron.* **2011**, *26*, 4155-4161.
(23) Cardoso, V. F.; Catarino, S. O.; Martins, P.; Rebouta, L.; Lanceros-Mendez, S.; Minas, G. *Conf. Proc. IEEE Eng. Med. Biol. Soc.* **2009**, *2009*, 5879-5882.
(24) Blicharz, T. M.; Rissin, D. M.; Bowden, M.; Hayman, R. B.; DiCesare, C.; Bhatia, J. S.; Grand-Pierre, N.; Siqueira, W. L.; Helmerhorst, E. J.; Loscalzo, J.; Oppenheim, F. G.; Walt, D. R. *Clin. Chem.* **2008**, *54*, 1473-1480.
(25) Hawkins, G. R.; Zipkin, I. *J. Dent. Res.* **1961**, *40*, 721-&.
(26) Inoue, K.; Namiki, T.; Iwasaki, Y.; Yoshimura, Y.; Nakazawa, H. *J. Chromatogr. B* **2003**, *785*, 57-63.
(27) Kim, J.; Imani, S.; de Araujo, W. R.; Warchall, J.; Valdes-Ramirez, G.; Paixao, T. R.; Mercier, P. P.; Wang, J. *Biosens. Bioelectron.* **2015**, *74*, 1061-1068.
(28) Bagheri, H.; Pajooheshpour, N.; Jamali, B.; Amidi, S.; Hajian, A.; Khoshsafar, H. *Microchem. J.* **2017**, *131*, 120-129.
(29) Yang, B.; Wang, H.; Du, J.; Fu, Y.; Yang, P.; Du, Y. *Colloids Surf., A* **2014**, *456*, 146-152.
(30) Pandurangachar, M.; Kumara Swamy, B. E.; Chandrashekar, B. N.; Gilbert, O.; Sherigara, B. S. *J. Mol. Liq.* **2011**, *158*, 13-17.
(31) Nancy, T. E. M.; Kumary, V. A. *Electrochim. Acta* **2014**, *133*, 233-240.
(32) Zhang, R.; Jin, G.-D.; Chen, D.; Hu, X.-Y. *Sens. Actuators, B* **2009**, *138*, 174-181.
(33) Bing Li, N.; Mei Niu, L.; Qun Luo, H. *Microchim. Acta* **2005**, *153*, 37-44.
(34) Ramírez-Berriozabal, M.; Galicia, L.; Gutiérrez-Granados, S.; Cortes, J. S.; Herrasti, P. *Electroanalysis* **2008**, *20*, 1678-1683.
(35) Ngamchuea, K.; Clark, R. O. D.; Sokolov, S. V.; Young, N. P.; Batchelor-McAuley, C.; Compton, R. G. *Chem. Eur. J.* **2017**, *23*, 16085-16096.
(36) Compton, R. G.; Banks, C. E. *Understanding Voltammetry*, 2nd ed.; Imperial College Press, 2011, p 444.
(37) Sun, P.; Mirkin, M. V. *Anal. Chem.* **2006**, *78*, 6526-6534.
(38) Ngamchuea, K.; Lin, C.; Batchelor-McAuley, C.; Compton, R. G. *Anal. Chem.* **2017**, *89*, 3780-3786.
(39) Wang, Y.; Limon-Petersen, J. G.; Compton, R. G. *J. Electroanal. Chem.* **2011**, *652*, 13-17.
(40) NordbÖ, H.; Darwish, S.; Bhatnagar, R. S. *Eur. J. Oral Sci.* **1984**, *92*, 306-314.
(41) Hatton, M. N.; Levine, M. J.; Margarone, J. E.; Aguirre, A. *J. Oral Maxillofac. Surg.* **1987**, *45*, 496-499.
(42) Klymenko, O. V.; Compton, R. G. *J. Electroanal. Chem.* **2004**, *571*, 207-210.
(43) Klymenko, O. V.; Evans, R. G.; Hardacre, C.; Svir, I. B.; Compton, R. G. *J. Electroanal. Chem.* **2004**, *571*, 211-221.
(44) Konopka, S. J.; McDuffie, B. *Anal. Chem.* **2002**, *42*, 1741-1746.
(45) Kätelhön, E.; Cheng, W.; Batchelor-McAuley, C.; Tschulik, K.; Compton, R. G. *ChemElectroChem* **2014**, *1*, 1057-1062.
(46) Swaddle, T. W. *Chem. Rev.* **2005**, *105*, 2573-2608.
(47) Clark, R. O. D.; Ngamchuea, K.; Batchelor-McAuley, C.; Compton, R. G. *Electroanalysis* **2017**, *29*, 1418-1425.
(48) Li, X.; Batchelor-McAuley, C.; Laborda, E.; Compton, R. G. *Chem. Eur. J* **2017**, *23*, 15222-15226.
(49) Larsen, M. J.; Pearce, E. I. F. *Arch. Oral Biol.* **2003**, *48*, 317-322.
(50) Shetty, S. R.; Babu, S.; Kumari, S.; Prasad, R.; Bhat, S.; Fazil, K. A. *South Asian J. Cancer* **2013**, *2*, 142-144.
(51) Okumura, T.; Nakajima, Y.; Matsuoka, M.; Takamatsu, T. *J. Chromatogr. B: Biomed. Sci. Appl.* **1997**, *694*, 305-316.
(52) Castagnola, M.; Cabras, T.; Lupi, A.; Manca, I.; Onnis, G.; Piras, V.; Soro, V.; Tambaro, S.; Messana, I.; Denotti, G.; Fadda, M. B.; Gambarini, G. *Biol. Rhythm Res.* **2002**, *33*, 213-222.
(53) Lomonaco, T.; Ghimenti, S.; Biagini, D.; Bramanti, E.; Onor, M.; Bellagambi, F. G.; Fuoco, R.; Di Francesco, F. *Microchem. J.* **2018**, *136*, 255-262.
(54) Bakhtiari, S.; Toosi, P.; Samadi, S.; Bakhshi, M. *Med. Princ. Pract.* **2017**, *26*, 57-60.
(55) Kamel, M. M.; Abdalla, E. M.; Ibrahim, M. S.; Temerk, Y. M. *Can. J. Chem.* **2014**, *92*, 329-336.

Chapter 10 Electrochemical detection of silver nanoparticles

Chapters 5-9 focussed on glutathione and uric acid detection and the application of salivary compounds as biomarkers. In addition to molecular species such as glutathione and uric acid, saliva can be used to investigate the potential toxicity of nanoparticles. Chapter 10 first develops electrochemical methods to detect silver nanoparticles, before the techniques are applied to saliva samples in Chapter 11.

In this chapter, the detection and the investigations of silver nanoparticles (AgNPs) oxidative dissolution are performed by two electrochemical techniques: nano-impacts and anodic stripping voltammetry. The former allows the detection of *individual* nanoparticles, while the latter detect the particle *ensembles*. In nano-impact measurements, the AgNP undergoes *complete* oxidation upon impact at a suitably potentiostated electrode. The frequency of the nanoparticle-electrode collisions observed as current-transient spikes depends on the electrolyte identity, its concentration and the potential applied at the working electrode. From the frequency, the rate of AgNP oxidation as compared with the timescale the AgNP is in electrical contact with the electrode can be inferred, and hence is indicative of the relative kinetics of the oxidation process. Primarily based on these results, the rate-determining process of silver oxidation on the nanoparticle is proposed to be the initial formation of the silver (I) nucleus.

The work presented in this chapter has been published in *Chemistry – A European Journal*.[1]

10.1 Introduction

The use of electrochemical techniques to determine the concentrations, volumes and surface areas of nanoparticles has been widely reported in literature.[2,3] Among these, anodic stripping voltammetry[4,5] is one of the most widely-used methods. Anodic stripping voltammetry has also been used in the characterisation of core-shell[6] and alloy nanoparticles,[7] the determination of the surface energy of single nanoparticles[8] and the extent of nanoparticles agglomeration.[9] There are however limitations to this technique arising from agglomeration/aggregation of the nanoparticles on the electrode surface upon the evaporation of solvent and a variation of the possible diffusion regimes.[9-11] In addition, the peak height and peak position alter in the presence of different capping agents,[12] electrolytes,[13] nanoparticle surface coverage and the size of the nanoparticle itself.[11,14,15]

As an alternative to stripping voltammetry, single nanoparticle collisions or the 'nano-impact' technique can be used in the detection of *individual* nanoparticles.[16-18] Nano-impacts have been utilised in extensive applications such as the detection of femtomolar levels of nanoparticles[19] and the investigations of nanoparticle catalytic activity.[20-25] Upon impact (collision) with a suitably potentiostated electrode, the redox-active nanoparticles may be oxidised or reduced, resulting in current-transient spikes.[26] Knowledge of how this processes varies as a function of potential can under suitable conditions and upon assumption of a mechanism allow the kinetics of the nano-redox event to be inferred.[27,28] For an ideal system of nanoparticles diffusing freely in the solution, a number of studies have discussed the relations between the *frequency* of the spikes,[16] the first passage time of the impact[29] and the concentration of the nanoparticles in the suspension. In practice, however, the observed spike frequency can be markedly influenced by the electrolyte used.[30]

This work studies the oxidative dissolution events of citrate-capped silver nanoparticles (AgNPs). AgNPs are extensively used in commercial products from textiles to antimicrobial and biomedical applications. A large quantity of AgNPs are released into the environment and there are concerns about health risks and environmental damage.[31] Electrochemical methods provide simple, quick and easy measurements of the AgNPs' sizes and concentrations. However, due to the issues raised above regarding the variation in the amperometric responses in different media, it is essential to understand the fundamental/physical mechanisms of the AgNPs oxidation that takes place at the electrode interface. The electrochemical response of AgNPs oxidation is studied herein using the novel nano-impact technique along with anodic stripping voltammetry. With the aim of understanding the rate-determining process of the AgNPs oxidation, the effects of the electrolytes (KNO_3, KCl, KBr and KI) and their concentrations on the stripping voltammograms and nano-impacts spikes are investigated. From this study, we gain physical insight into the initiation and the rate-determining process of the AgNPs oxidation at the electrode surface.

In the nano-impact measurements, the total charge transferred during each current-transient spike directly relates to the *number* of constituent electroactive atoms or molecules of the nanoparticles, irrespective of their shape[32] or the presence of capping agents.[12] This is different from other techniques that measure the length scale of the particles such as transmission electron microscopy (TEM). In the comparison of the sizes determined using TEM to that obtained from electrochemical measurements, careful inference of the particle volume from the two-dimensional TEM images is emphasised in this work. In particular, consideration of the particle shape is taken into account as (large) metal nanoparticles exhibit a significant extent of faceting.[33] From the careful analysis of 180 TEM images and over 5,000 spikes, this work provides evidences for the *complete* oxidation of the AgNPs upon the

impact at a suitably potentiostated electrode although the frequency of the nano-impact spikes is *lower* than the predicted diffusion-limited fluxes.

10.2 Experimental

10.2.1 Chemical reagents

Spherical 50 nm diameter citrate-AgNPs (NanoXact, 0.02 mg/mL silver, 2 mM sodium citrate) were obtained from Nanocomposix, USA. All other reagents are as described in Chapter 4.

10.2.2 Sizing of the AgNPs

Transmission electron microscopy (TEM, 300 kV JEOL 3000F microscope) was used to determine the size of the AgNPs, detailed in Chapter 4.

10.2.3 Stability of the AgNPs in different electrolytes

The stabilities of AgNPs in 20 mM KNO_3, KCl, KBr or KI electrolyte solutions were studied via UV-vis measurements, detailed in Chapter 4. The UV-vis spectra of the AgNPs in the different electrolytes were recorded in the range of wavelength (λ) of 250 – 800 nm as a function of time for a total of 20 minutes.

10.2.4 Anodic stripping voltammetry

Anodic stripping experiments were performed with a µAutolab Type III potentiostat (Utrecht) using a glassy carbon working electrode (3 mm diameter, BASi, USA) and a platinum mesh counter electrode. A leakless Ag/AgCl (in 3.4 M KCl, eDAQ) or a saturated calomel electrode (BASi, USA) was used as a reference electrode.

Prior to use, the glassy carbon electrode was polished to a mirror finish using a water-alumina slurry (1.0 µm, 0.3 µm and 0.05 µm; Buehler, USA) on soft lapping pads (Buehler, USA). A

5 μL aliquot of the 48.2 pM AgNPs suspension was then dropcast onto the surface of the glassy carbon electrode and allowed to dry under a flowing nitrogen atmosphere. The AgNP-modified glassy carbon electrode was transferred to the electrolyte solution under studies (KNO_3, KCl, KBr or KI). The system was then subjected to cyclic voltammetric measurements initially scanning anodically in the potential range of -0.4 V to 1.2 V vs. SCE at the scan rate of 10 mV s^{-1}.

10.2.5 Nano-impacts

Nano-impact experiments were performed with a low noise potentiostat that was built in-house.[34] A carbon microdisc (33 μm diameter, IJ Cambria Scientific Ltd, UK) and a platinum mesh were used as working and counter electrodes respectively. A leakless Ag/AgCl (in 3.4 M KCl, eDAQ) or a saturated calomel electrode (BASi, USA) was used as a reference electrode.

Cyclic voltammetric measurements initially scanning anodically in the potential range of -0.4 V to 1.2 V vs. SCE at the scan rate of 10 mV s^{-1} were performed in the solutions containing 12 pM AgNPs and varied supporting electrolytes (KNO_3, KCl, KBr and KI).

Note that the anodic stripping voltammetry and nano-impact measurements in all KNO_3 and in KCl solutions at and below 5 mM concentrations are performed against a leakless Ag/AgCl reference electrode (E = -0.039 V vs. SCE) to prevent the contamination of Cl^-, which would affect the position of the anodic stripping voltammetry. Otherwise, the voltammetric measurement is performed against a standard calomel reference electrode (SCE). All the results below are presented as *vs. SCE* for clear comparison.

10.3 Results

The AgNPs are first characterised using transmission electron microscope (TEM), where the nanoparticle's volume as inferred from two-dimensional TEM images is discussed in detail (Section 10.3.1). Next, the stability of the AgNPs in different electrolyte solutions is demonstrated by UV-vis measurements as a function of time (Section 10.3.2). The oxidation of AgNPs is then studied using anodic stripping voltammetry and the nano-impact method. The factors influencing the resulting electrochemical responses are investigated, in particular the effects of the electrolyte concentrations (Section 10.3.3) and the presence of different anions (Section 10.3.4).

10.3.1 TEM analysis of AgNPs

The commercial spherical citrate-capped AgNPs were characterised by transmission electron microscope (TEM). It was observed that although described as spherical, the shapes of the AgNPs are not that of a perfect sphere. In other words, the circularity of the two-dimensional images is less than unity. Figure 10.1 gives examples of the resulting nanoparticle images.

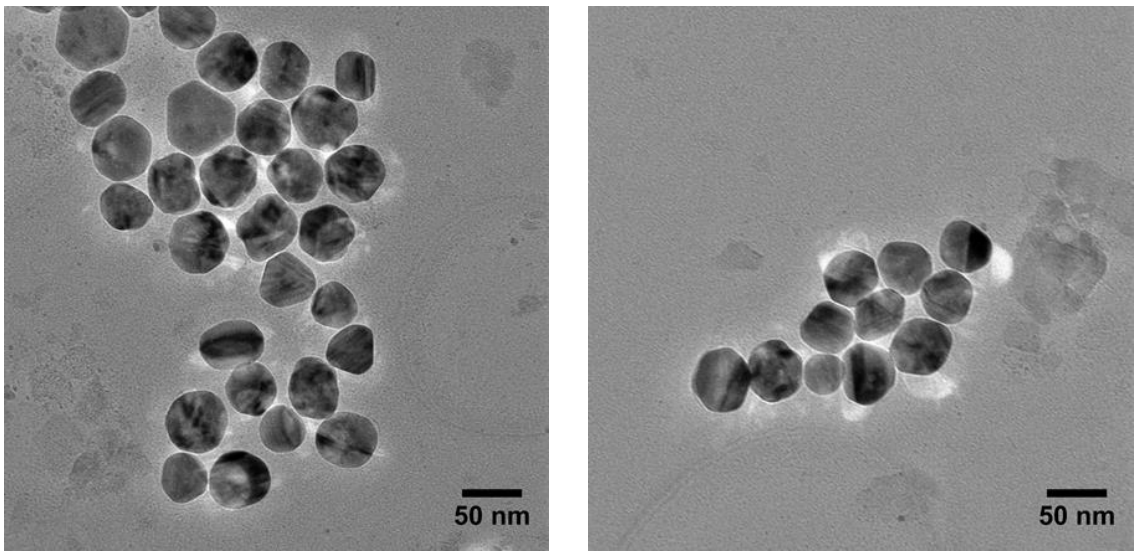


Figure 10.1: TEM images of AgNPs (50 nm Silver Nanospheres, NanoXact (0.02 mg/mL), NanoComposix, USA)

This is true not only for this batch of commercial AgNPs, the citrate-capped AgNPs employed in other electrochemical studies, both home-made via citrate reduction and commercial products from different sources, show a significant level of non-sphericity,[35-38] often due to the presence of various facets.[33] As the particles are not perfect spheres, there is ambiguity in the determination of the particle 'radius'. Notably, any inaccuracy in the radius measurement gives rise to a significantly large error in volume, as the volume scales with the third power of radius. Importantly, in terms of comparison with the experimental nano-impact electrochemical data, it is the volume rather than the length scale that is required.

In order to estimate the volume of the AgNPs more accurately, the resulting two-dimensional TEM images of AgNPs are classified into circular (Figure 10.2b), hexagonal (Figure 10.2c) and 'other' ambiguous shapes (Figure 10.2d). However, we comment that the circularity of a particle 2D projection in an image is generally a poor indicator of a particle's inscribed volume compared to that of a sphere. From the analysis of 180 nanoparticles, it was found for this sample that the particles are approximately equally distributed between the three classes of particle shapes. It is approximated that circular and hexagonal images correspond to spherical and icosahedral particles respectively.[38] For hexagonal images, all three diagonals are measured and the average is taken as the diameter of the circumscribed sphere. In the case of nanoparticles with ambiguous shapes, the maximal diameter is used to describe the circumscribed sphere. The circumscribed volume is determined and the actual volume of the nanoparticles (V_{NP}) of the different shapes is calculated according to the following equation:

$$V_{\mathrm{NP}} = \frac{4\pi R_{\mathrm{c}}^3}{3} \times f \qquad (10.1)$$

where R_c is the radius of the sphere circumscribing the nanoparticle. f is a correction factor accounting for the overestimation of the nanoparticle volume from the radius of the circumscribed sphere.

The values of f are 1 and 0.605 for spherical and icosahedral nanoparticles respectively.[38] In the case of nanoparticles with ambiguous shapes, the f-factor is likely to be much smaller than 0.605 of the highly symmetric icosahedron and is chosen semi-arbitrarily to be 0.5 in the present work. This value of 0.5 is relatively conservative given the distinct non-sphericity of some of the particles imaged and has recently been validated by electron tomography (or three-dimensional transmission electron microscopy, 3D-TEM) to be a reasonably good approximation.[39] The actual f value depends on the exact shapes of the nanoparticles and cannot be determined from the two-dimensional images alone.

In the following sections, the TEM sizes are compared with the volumes determined via nano-impact measurements. Accordingly, the size of the AgNPs as measured from the TEM data is thus converted via Faradays first law and presented in term of an *equivalent total charge* (Q_{equiv}). In the case that the entire AgNP is oxidised, the charge transferred per nanoparticle (Q_{NP}) can be calculated according to:

$$Q_{\mathrm{NP}} = \frac{\rho z F}{A_r} V_{\mathrm{NP}} \qquad (10.2)$$

where z is the number of electrons transferred per atom. z = 1 for silver oxidation. F is the Faraday constant (96,485 C mol^{-1}). A_r is the atomic mass of silver (107.9 g mol^{-1}) and ρ is the density of silver (10.5×10^6 g m^{-3}).[40]

Figure 10.2a presents the size distribution of the AgNPs as estimated from the TEM images and presented in terms of the expected *equivalent* charges as analysed by two different

approaches. First is the 'general analysis' where no correction is made to account for the irregularity of the nanoparticles. Second is the 'detailed analysis' where the AgNPs are characterised into spherical (f = 1), icosahedral (f = 0.605) and other ambiguous shapes (f = 0.5). The size distributions of the different shapes are presented in the inlay in Figure 10.2a. Compared with the detailed analysis (Q_{equiv} = 3.9×10^{-13} ± 1.6×10^{-13} C, corresponds to equivalent spherical radii of 21 ± 3 nm), the charges are more biased to higher values when using the general analysis (Q_{equiv} = 5.3×10^{-13} ± 2.1×10^{-13} C, corresponds to spherical radii of 24 ± 3 nm). The discrepancy in Q_{equiv} of the two approaches of ~30% arises due to the overestimation of the volume of the non-spherical particles. The importance of detailed analysis of the size of the AgNPs will be further highlighted in Section 10.3.4.2 where we compare the charges of the AgNPs oxidation upon impact at the electrode to the sizes characterised by TEM.

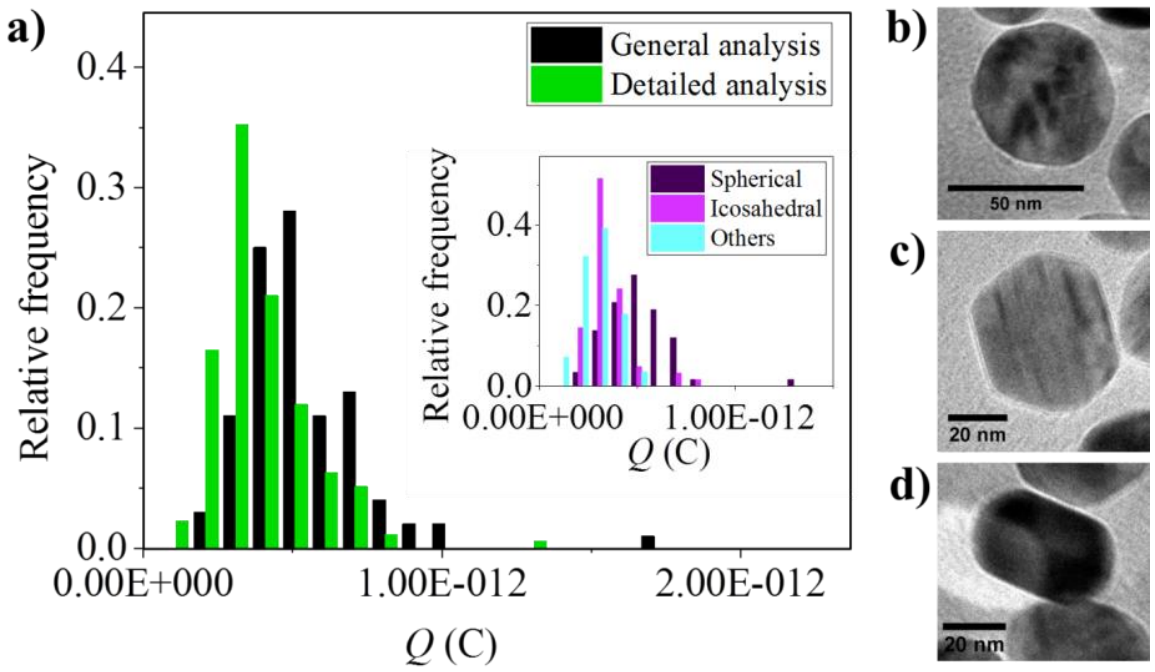


Figure 10.2: **a)** A histogram showing the size distribution (presented as charges (Q_{equiv}); see eqn. 10.2) of AgNPs determined by TEM and analysed using two different approaches: 'general analysis' and 'detailed analysis' as explained in the text. Examples of **b)** spherical, **c)** icosahedral and **d)** ambiguous shapes of AgNPs.

10.3.2 Stability of the AgNPs in different electrolytes

Repeated UV-visible spectra were recorded over 20 min after the suspensions of 12 pM AgNPs were mixed with 20 mM of KNO_3, KCl, KBr or KI electrolytes. The resulting spectra are displayed in Figure 10.3. Silver nanoparticle suspensions exhibit a strong plasmonic peak at ~400 nm. The peak's exact position, shape and magnitude are sensitive to not only the nanoparticles size and geometry but also their local environment.[41] Consequently, this peak can be used to monitor the nanoparticle suspensions stability. In all the electrolytes studied, the wavelength at maximum absorbance (λ_{max}) of the AgNPs is 423.3±0.7 nm and the magnitude of maximum absorbance (Abs_{max}) remained constant throughout the 20 min studied. This evidences the stability of the particles under these ionic conditions.

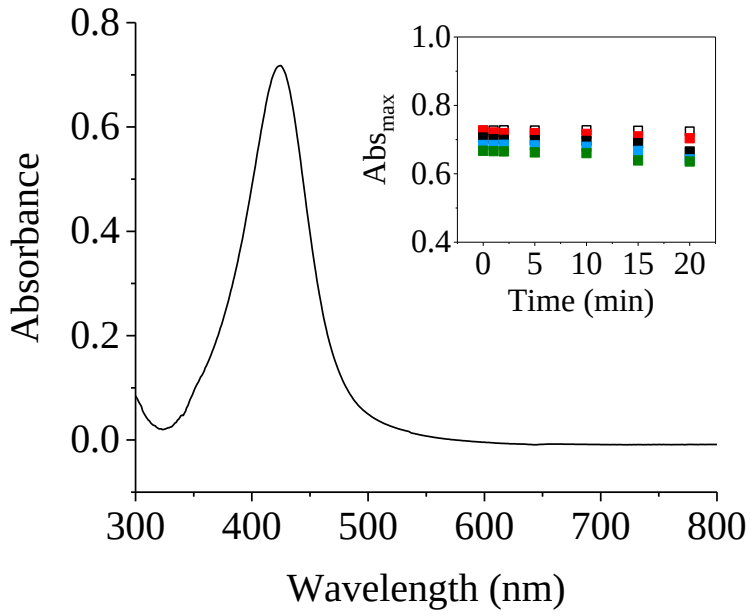


Figure 10.3: A representative UV-vis spectrum of 12 pM AgNPs suspension. The inlay shows the maximum absorbance (Abs_{max}) as a function of time in deionised water (**open squares**), and 20 mM of KNO_3 (**red**), KCl (**black**), KBr (**blue**) and KI (**green**).

10.3.3 AgNPs oxidation: the effects of the electrolyte concentrations

This section focuses on the effect of the electrolyte concentrations (≤ 20 mM) towards the amperometric responses of AgNPs oxidation. Two electrolytes KNO_3 and KCl are studied. The AgNPs oxidation events are first studied using anodic stripping voltammetry, then second by the nano-impact technique.

10.3.3.1 Anodic stripping voltammetry

AgNPs were first immobilised on the surface of glassy carbon electrode by dropcasting 2.4×10^{-16} moles of the AgNPs (7.8×10^{-10} moles of Ag atoms) on a 3 mm diameter electrode, yielding a surface coverage of ca. 4.5% by area. The glassy carbon electrode modified with the AgNPs was then subjected to cyclic voltammetry measurement in KNO_3 or KCl electrolytes of varied concentrations (0-20 mM).

Figure 10.4 displays the anodic stripping voltammograms of AgNPs in the different concentrations of electrolytes studied. In the absence of added electrolyte, the stripping voltammogram shows a broad anodic peak at 0.57 V vs. SCE. In KNO_3 solutions, the oxidative stripping takes place at 0.38 ± 0.07 V vs. SCE for all the concentrations studied. The anodic stripping of AgNPs in KCl solutions occurs at 0.21, 0.17, 0.14 and 0.11 V vs. SCE for 1, 5, 10 and 20 mM KCl respectively. The plot of the peak potential (E_p) against $\log_{10}([Cl^-])$ gives a slope of 76 ± 8 mV, the value of which is discussed below. Note that the stripping in KCl occurs at less positive potentials than in KNO_3 and the potential is further lowered with increasing concentrations of Cl^-.

In comparing the two responses, given that the quantity of the AgNPs immobilised on the electrode surface is the same, the extent of agglomeration/aggregation and the diffusion regimes can be inferred to be comparable.[9] In addition, both KCl and KNO_3 have the same

ionic strength at equal concentrations. Hence, the difference in the measured peak potentials arises from the influence of the anions. In KNO_3 solution and in the absence of any complexing agents, the AgNPs are oxidised to Ag^+. On the other hand, the products of silver oxidation in the presence of Cl^- ions are likely AgCl(s) or at higher chloride complexes such as $AgCl_2^-$.[42] For an oxidation involving one Cl^- ion per Ag atom, a shift in the anodic stripping peak of 59 mV per a unit of $\log_{10}([Cl^-])$ is expected according to the Nernst equation.[43] The plot of the anodic peak potentials (E_p) against $\log_{10}([Cl^-])$ however gives a slope of 76 ± 8 mV. This may be evidence for the participation of more than one Cl^- ions per Ag atom, and thus suggests the (partial) formation of $AgCl_2^-$ or other higher halide complexes. The standard electrode potential of Ag(s)/Ag^+(aq) and Ag(s)/AgCl(s) are 0.80 and 0.22 V vs. SHE respectively.[44] The negative shifts in the stripping peak potential in the presence of chloride predominantly reflects the more thermodynamically favourable oxidation of AgNPs in KCl than KNO_3, and more so at higher concentrations of Cl^-.

The amount of charge transferred during oxidation of the large ensemble of nanoparticles in all electrolytes are of similar order of $1.6\times10^{-5} \pm 4.8\times10^{-6}$ C, corresponding to 22 ± 6 % of the immobilised AgNPs being oxidised. The incomplete oxidation is likely a result of the particles agglomeration/aggregation on the electrode surface as arising from nanoparticle/electrode connectivity issues.[10] Previous experimental work utilising gold-silver contacts has evidenced the presence of poor electrical contact between nanoparticles in an agglomerate.[45] For the same coverage of AgNPs immobilised on the electrode surface, the oxidation of AgNPs in the presence of Cl^- ions gives rise to a much sharper anodic stripping peak than in KNO_3 or deionised water (Figure 10.4). To further investigate the difference of AgNP oxidation in KNO_3 and KCl, the oxidative dissolution of *individual* AgNP is studied next using the nano-impact technique.

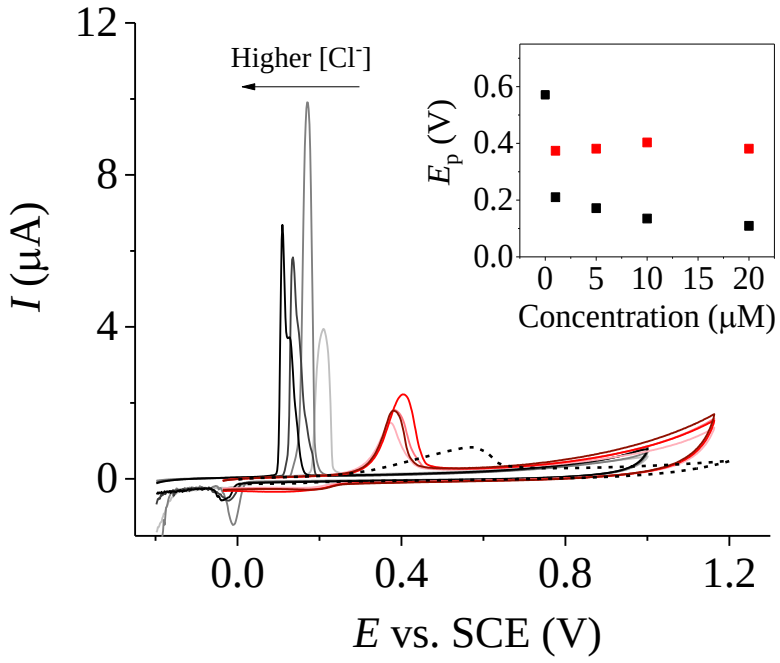


Figure 10.4: Anodic stripping voltammograms of 2.4×10^{-16} moles of AgNPs dropcasted on a 3 mm diameter glassy carbon electrode (surface coverage of 4.5%) in deionised water (dashed line), 1, 5, 10 and 20 mM KNO_3 (pale pink → dark red), and 1, 5, 10 and 20 mM KCl (grey → black). The inlay shows the plot of the position of the anodic stripping peaks (E_p) as a function of electrolyte concentrations.

10.3.3.2 Nano-impacts: single nanoparticle-electrode collisions

The oxidation of AgNPs is next studied via the nano-impact technique. In contrast to anodic stripping voltammetry, nano-impacts allow the detection of individual nanoparticles, eliminating the complication that may arise from different diffusion regimes or particle aggregation/agglomeration on the electrode surface after drop-casting.[9]

In the literature a number of works have sought to look at the potential dependency of a nano-impact event, focusing on both destructive [28,30] and mediated processes[46,47], where the influence of the electrode potential upon the observed impact frequency has also been highlighted.[30,47] However, with only a few notable exceptions[48,49] these works typically

involve nano-impact studies performed using chronoamperometry at a series of fixed potentials, in the present work cyclic voltammetry is employed to study the effect of the applied potentials simultaneously with obtaining nanoparticle size information (as derived from the total charge under a spike) and impact frequency of the particles in a single measurement.

The suspensions of 12 pM AgNPs in 0, 1, 5 or 20 mM of KNO_3 or KCl were subjected to cyclic voltammetry measurements at a carbon microdisc electrode at the scan rate of 10 mV s^{-1}. Figure 10.5 presents the representative cyclic voltammograms showing nano-impact spikes of AgNPs oxidation in 1, 5 and 20 mM KCl (Figures 10.5a-c), and 1, 5 and 20 mM KNO_3 (Figures 10.5d-f). Inlayed in Figures 10.5a-f are images showing the representative spikes shapes for the oxidative events, the duration of these feature is 10-20 ms. However, this timescale reflects the speed of the used electronics and not the course of the nano-impact event at the interface. In the present study the focus of the work is to determine the magnitude (charge) of the individual impact events and not the structure of the spike itself.

Without added electrolyte, no oxidative spikes are observed although the solution contains ~0.5 mM of citrate from the AgNP stock solution, results not shown. The previous section has demonstrated that AgNPs can be oxidised (anodic stripping) in the absence of electrolyte with the peak potential at 0.57 V vs. SCE. The fact that no spikes are observed suggests that the oxidation of any impacting AgNPs in the absence of electrolyte is very slow as compared to the time the AgNPs are in electrical contact with the electrode.

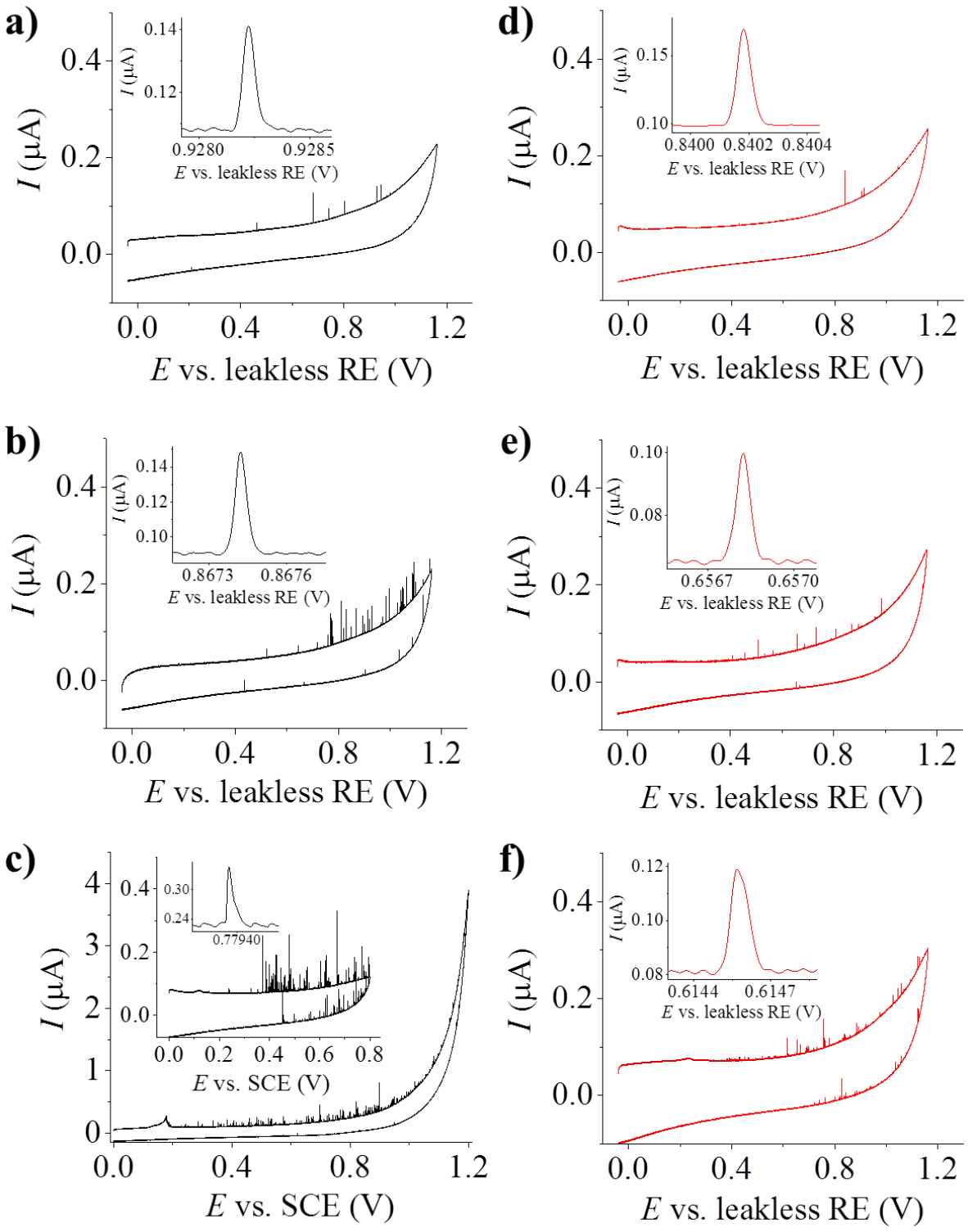


Figure 10.5: Representative cyclic voltammograms showing nano-impact spikes of 12 pM AgNPs in **a)** 1 mM KCl, **b)** 5 mM KCl, **c)** 20 mM KCl, **d)** 1 mM KNO_3, **e)** 5 mM KNO_3 and **f)** 20 mM KNO_3. Carbon microdisc (20.5 μm radius) working electrode. Scan rate of 10 mV s^{-1}.

In the presence of added supporting electrolyte, nano-impact spikes are observed at potentials more positive than the stripping potentials of AgNPs in the relevant electrolytes. In order to investigate the effect of the applied potentials on the size and frequency of the nano-impact spikes, the resulting voltammograms are sub-divided into smaller potential ranges of 0.1 V intervals. However, this analysis is restricted to the measurement of spikes observed in the forward scan. The use of higher electrode potentials can result in a decrease in the observed impact frequency. This influence can be seen from comparing the nano-impact spikes of AgNPs in 20 mM KCl subjected to the maximum potentials of 1.2 V (Figure 10.5c) and 0.8 V vs. SCE (Inlay in Figure 10.5c). No spikes are observed in the backward cathodic scan of the former while the latter shows a significant number of features. This suggests that at very high potentials, reactive (possibly radical, peroxide or O_2/H^+)[50,51] species that can oxidise the AgNPs within the diffusion layers may be formed. As a result, only the spikes observed in the forward scans are considered for analysis.

The area under each spike relates to the amount of charge transferred during a single nanoparticle oxidation event. At all potentials higher than the stripping potential, the average measured charges are in excellent agreement with the size (volume) determined using transmission electron microscope; see Figure 10.6a. This implies that if a nano-impact event occurs at a sufficiently biased electrode then the oxidation of the individual AgNP goes to completion. The evidence of the *complete* dissolution of the AgNPs is further provided and discussed in detail towards the end of Section 10.3.4.2.

In addition to the size of the nanoparticles, the frequency of the spikes (the number of spikes per second) is analysed for each of the 0.1 V potential intervals (equivalent to 10 s at the scan rate of 10 mV s^{-1}). Figure 10.6b presents the frequency of the nano-impact spikes taking place in 5 and 20 mM of KNO_3 or KCl as a function of applied potentials. Note that at 1 mM,

the frequencies are significantly lower than at 5 and 20 mM of the same electrolytes and very low such that no statistically relevant information can be extracted.

The frequency of the nanoparticle-electrode collisions increases with increasing potentials. Furthermore, at both 5 mM and 20 mM, the frequency in KCl is significantly (by up to a factor of 7) higher than in KNO_3, this is in agreement with reports by Krause et al.[30] from chronoamperometric results. The increase in frequency with the applied potentials and the higher frequencies in KCl than in KNO_3 may arise from either the difference in the mass-transport flux of AgNPs to the electrode or the rate of the AgNPs oxidation at the electrode. The former is not feasible and will be discussed in detail in Section 10.4. The latter can be limited by a number of factors and full insight cannot be deduced from this result alone. In the next section, we will further investigate the roles of Cl^- and other halide ions in the rate-determining step.

10.3.4 AgNPs oxidation: the effect of the electrolyte anion identity

In the previous section, it was observed that there is a substantial difference in the frequency of nano-impact spikes with the use of either KCl or KNO_3 as the supporting electrolyte, thus suggesting the important role of Cl^- in the rate-determining process of AgNPs oxidation. In this section, Br^- and I^- are further investigated in comparison to Cl^-. The AgNPs are first subjected to anodic stripping voltammetry to study the effect of the anions towards the stripping potential of AgNP oxidation. Nano-impacts are then performed to investigate the oxidation process at a single nanoparticle scale.

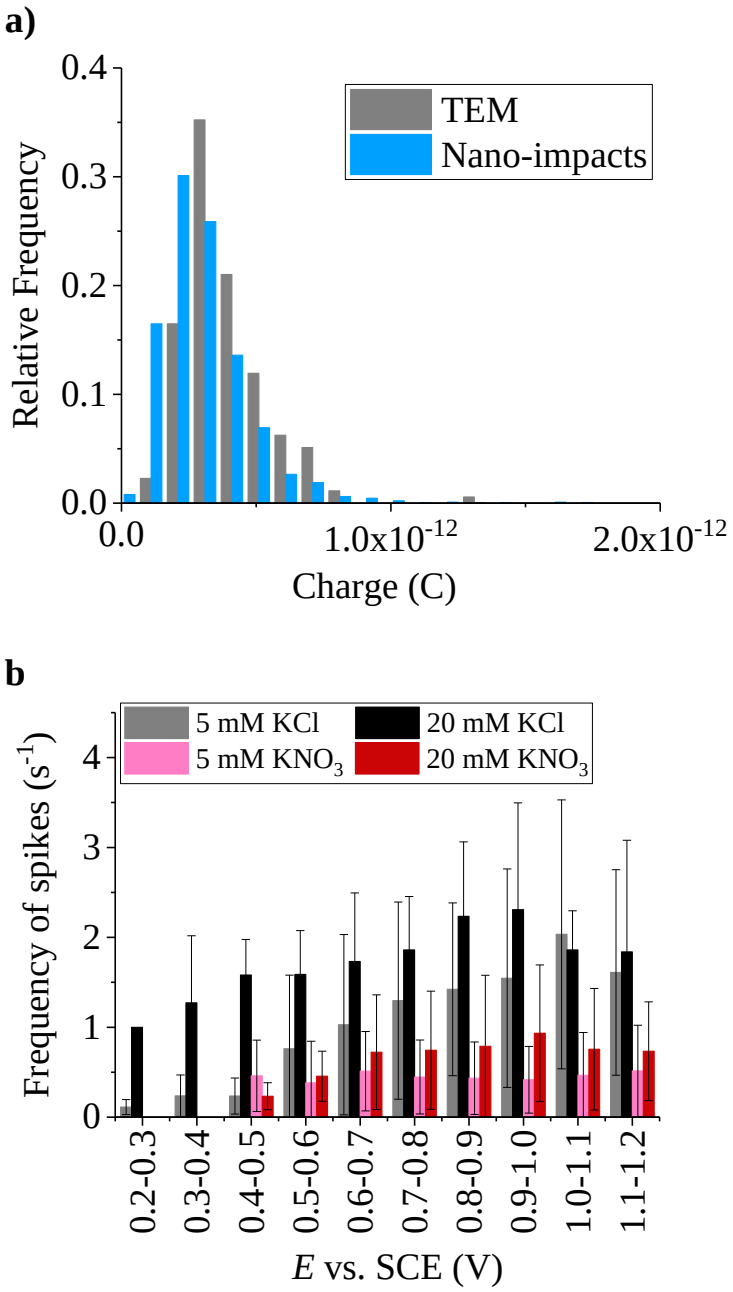


Figure 10.6: **a)** The histograms display the distribution of AgNPs sizes calculated from the charge transfer of nano-impact spikes in 5 mM and 20 mM KNO_3 and KCl, compared with the sizes determined by TEM. **b)** The bar graph showing the frequency of nano-impact spikes of 12 pM AgNPs oxidation events in 5 mM and 20 mM KNO_3 and KCl electrolyte solutions.

10.3.4.1 Anodic stripping voltammetry

The glassy carbon electrode modified with AgNPs as already described in Section 10.3.3.1 was subjected to cyclic voltammetric measurements in 20 mM of KNO_3, KCl, KBr or KI. Figure 10.7 displays the anodic stripping voltammograms of AgNPs in the different electrolytes studied. The positions of the oxidative peaks are 0.37, 0.11, -0.02 and -0.24 V vs. SCE for KNO_3, KCl, KBr and KI respectively. The more negative peak potential of KI as compared to other electrolytes implies the relative 'ease' (see below) of silver oxidation in the presence of I^-.

For all the electrolytes studied herein, the difference in the standard reaction Gibbs energy (ΔG_r^0) of the AgNPs oxidation is a result of the formation of the different oxidation products, see below.

$$Ag(s) + X^-(aq) \xrightarrow{\triangle G_r^0} e^- + AgX(s) \qquad (10.3)$$

$$Ag(s) \xrightarrow{\triangle G_1^0} e^- + Ag^+(aq) \qquad (10.4)$$

$$Ag^+(aq) + X^-(aq) \overset{\triangle G_2^0}{\rightleftharpoons} AgX(s) \qquad (10.5)$$

$$\Delta G_r^0 = \Delta G_1^0 + \Delta G_2^0 \qquad (10.6)$$

$$\Delta G_2^0 = RT \ln(K_{sp}) \qquad (10.7)$$

where R and T are the molar gas constant (8.314 J mol^{-1} K^{-1}) and absolute temperature respectively. K_{sp} is the solubility product constant. For AgCl, AgBr and AgI in aqueous solutions at 25°C under atmospheric pressure, the values of $\log(K_{sp})$ are -9.8, -12.3 and -16.0 respectively.[52]

$$AgX\,(s) \overset{K_{sp}}{\rightleftharpoons} Ag^{+}\,(aq) + X^{-}\,(aq) \qquad (10.8)$$

$$K_{sp} = (a_{Ag^{+}})(a_{X^{-}}) = (\gamma_{Ag^{+}}[Ag^{+}])(\gamma_{X^{-}}[X^{-}]) \qquad (10.9)$$

where a_j and γ_j are the activity and activity coefficient of species j respectively. The square brackets designate the concentrations of the relevant species. Assuming $\gamma = 1$ for both Ag^{+} and X^{-}, K_{sp} can be approximated:

$$K_{sp} \cong [Ag^{+}][X^{-}] \qquad (10.10)$$

The inlay in Figure 10.7 shows that the peak potential of the anodic stripping of AgNPs in KX electrolytes increases linearly with $\log(K_{sp})$ of the AgX products, suggesting the dependence of the peak position on the thermodynamic properties of the oxidation process. The peak of this oxidative stripping wave varies in a near Nernstian manner shifting ~57mV per decade in $\log(K_{sp})$.

In addition, the oxidation of AgNPs in the presence of any halide ions gives rise to a much sharper anodic stripping peak than in KNO_3 or deionised water, similar to the results discussed before in Section 10.3.3.1 (Figure 10.4). The sharper peak suggests the faster rate of oxidation of the AgNPs in the presence of halides. The difference in the rates of AgNPs oxidation in the presence of different halides cannot be determined from the anodic stripping voltammetry alone. Accordingly, the nano-impacts of AgNPs are studied in the presence of different anions, the results of which will yield the physical insights into the oxidation of silver at the electrode interface.

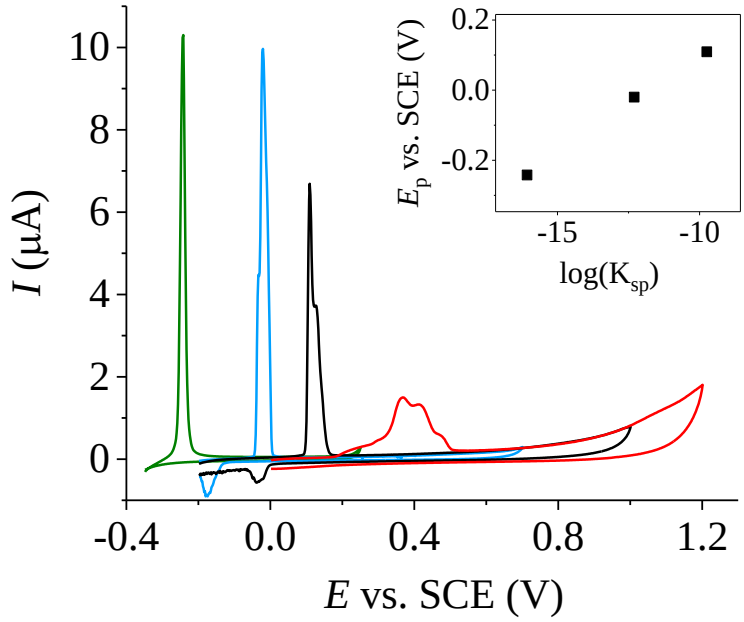


Figure 10.7: Anodic stripping of 2.4×10^{-16} moles of AgNPs dropcasted on a 3 mm diameter glassy carbon electrodes (surface coverage of 4.5%) in 20 mM of KNO_3 (**red**), KCl (**black**), KBr (**blue**) and KI (**green**); scan rate 10 mV s^{-1}. The **inlay** shows the peak potentials of AgNPs oxidation in different electrolytes plotted against the logarithm of the solubility constant ($\log(K_{sp})$) of AgX, where X is the different anions studied. The position of the oxidation peak in the presence of halides varies with ~57 mV per decade in $\log(K_{sp})$.

10.3.4.2 Nano-impacts: single nanoparticle collisions

Having evidenced the difference in the stripping potentials of AgNPs in the absence and presence of different electrolytes, next the nano-impact responses of AgNPs are investigated in 20 mM of KNO_3, KCl, KBr and KI. The suspensions of 12 pM AgNPs in 20 mM of varied electrolytes were subjected to cyclic voltammetry measurements at a carbon microdisc electrode at the scan rate of 10 mV s^{-1}.

For KNO_3 and KCl, the potentials were swept from 0 V to 1.2 V and back to 0 V vs. SCE. In the case of KBr and KI, the maximum potentials were limited to 0.7 V and 0.22 V vs. SCE

respectively due to the oxidation of Br^- and I^- at higher potentials, and the nano-impact spikes would be masked by the oxidative responses of Br^- and I^-. More importantly, any Br_2 (E^0 = 1.06 V vs. SHE) or I_2 (E^0 = 0.54 V vs. SHE) formed would likely spontaneously oxidise the silver nanoparticles (E^0 = 0.07 and -0.15 V vs. SHE for oxidation to AgBr and AgI respectively),[44] decreasing the number of AgNPs available for the nano-impact measurements and hence result in the underestimation of the frequency of spikes.

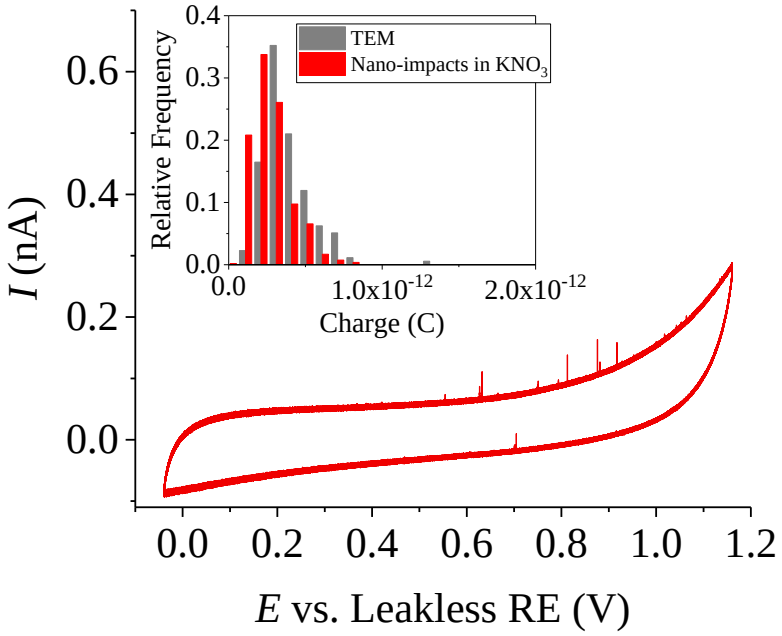
Figure 10.8 presents the representative cyclic voltammograms showing nano-impact spikes of AgNPs oxidation in 20 mM of KNO_3 (Figure 10.8a), KCl (Figure 10.8b), KBr (Figure 10.8c) and KI (Figure 10.8d).

Also observable in these voltammograms are small stripping peaks associated with the oxidation of nanoparticles that have accumulated at the electrode between experiments. The position of these stripping peaks as a function of the anion identity is in excellent agreement with the results obtained from the drop-cast experiments (Figure 10.7). In stripping experiments the finite nature of the amount of material initially present on the electrode leads to the voltammetric oxidation event only occurring at low electrode potentials. For a given salt no spikes are observed at potentials less positive than the stripping peak potentials. Moreover, the spikes are observed to onset at only tens of millivolts beyond the stripping peak. This delayed onset is consistent with being due to the relatively slow oxidation of the nanoparticle (after initiation of the process) at low overpotentials, such an interpretation is consistent with the results presented by Tschulik.[28]

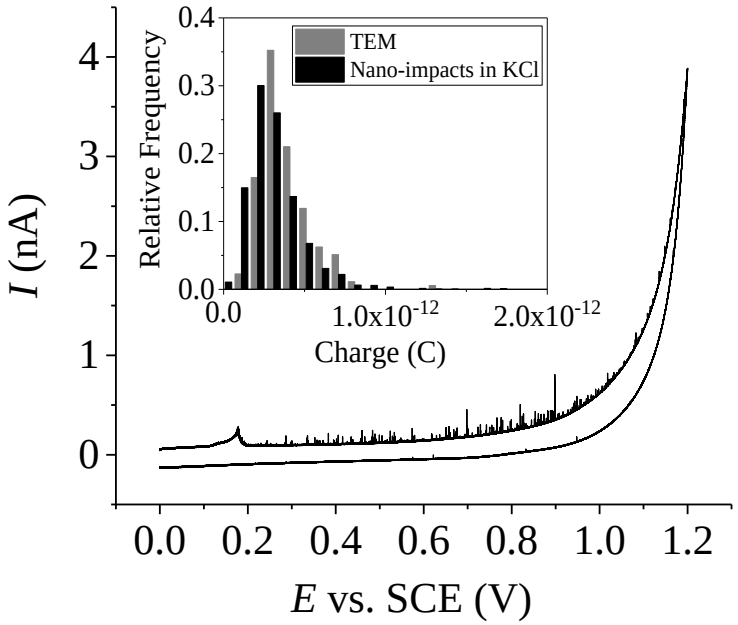
The amount of charge transferred is determined from the area under the spikes. The average and distribution of charges determined via nano-impact measurement is in excellent agreement with TEM, see histograms in the inlays of Figures 10.8a, 10.8b, 10.8c and 10.8d for the nano-impacts taking place in KNO_3, KCl, KBr and KI respectively.

The charges transferred are in the order of $3.2 \times 10^{-13} \pm 1.8 \times 10^{-13}$ C for all the electrolytes at all the potentials above the stripping potentials. This corresponds to >80% of the expected charge as determined from the detailed TEM analysis (conservatively estimated as Q_{equiv} = $3.9 \times 10^{-13} \pm 1.6 \times 10^{-13}$ C).

a)



b)



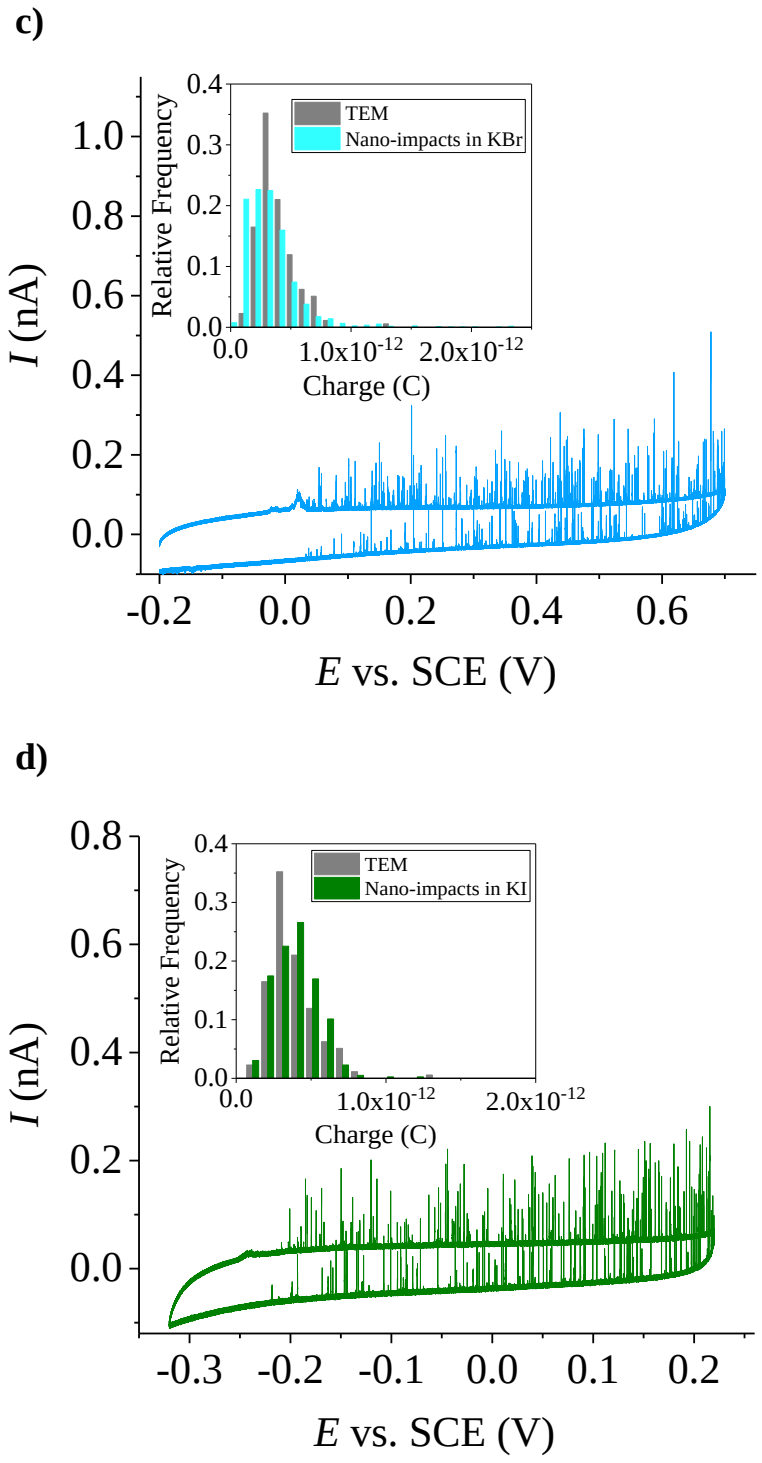


Figure 10.8: Representative cyclic voltammograms showing nano-impact spikes of 12 pM AgNPs in 20 mM of **a)** KNO_3; **b)** KCl; **c)** KBr; **d)** KI. The inlays display the distribution of AgNPs sizes calculated from the charge transfer of nano-impact spikes compared with the sizes determined using TEM. Carbon microdisc (20.5 µm radius) working electrode. Scan rate of 10 mV s^{-1}.

However, due to the ambiguity associated with obtaining a volume from a 2D image, the bias of nano-impact experiments towards the detection of smaller nanoparticles (due to their higher associated diffusion coefficient),[53] the insensitivity of the magnitude of this charge to the applied potential and the identity of the electrolyte, it is concluded that the data – within the accuracy of the presented work – is *fully consistent with* arising from the complete oxidation of the silver nanoparticles at the electrode surface. Hence, once the AgNPs reach a sufficiently biased electrode, they are completely oxidised. In terms of nanoparticle sizing any error in the volume measurement is minimised when converted to that of a length scale. From the charge histograms, it is further shown that not only the average value, but nano-impacts also provide an accurate determination of the size distribution (standard deviation) of the nanoparticles, in excellent agreement with TEM measurements (see Figure 10.6a and the inlays of Figure 10.8 a-d).

A number of independent studies, including the present work, report the *complete* oxidation of the AgNPs upon the impact at a sufficiently biased electrode.[12,28,32,45] Meanwhile, the incomplete oxidation is reported in some cases, in particular for particles of larger sizes.[35,36] In both cases these experiments were performed using a nitrate based electrolyte and, as evidenced above, this may *not* be the optimal conditions under which to study oxidative silver nanoparticle impacts. Furthermore, as discussed in Section 10.3.1 for relatively large nanoparticles (d > 20 nm), the shape of the AgNPs deviates from that of a sphere and the volume estimated from the two-dimensional TEM images is significantly lower than the circumscribed sphere. This missing volume of the particles may partially be the origin of the discrepancy in the sizes of AgNPs obtained from the nano-impact and TEM measurements reported in some cases.

In addition to the size of the nanoparticles, the frequency of nano-impact spikes is next evaluated. Figure 10.9 presents the resulting frequencies in different electrolytes at varied potentials. In the presence of Cl^-, Br^- or I^-, the frequencies of the collision events are significantly higher than in KNO_3, and the frequency increases with increasing potentials. These differences in frequencies are discussed in detail in Section 10.4.

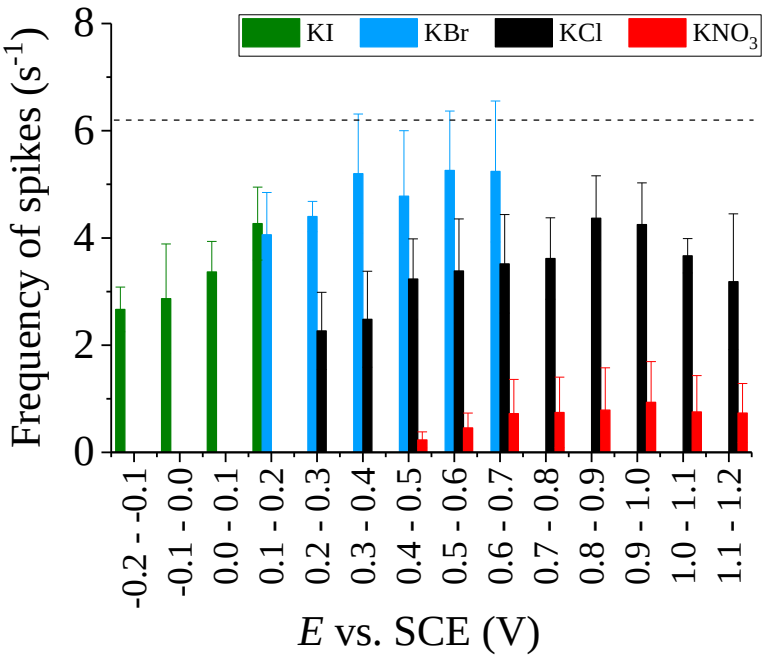


Figure 10.9: The bar graph showing the frequency of nano-impact spikes of AgNPs oxidation events. The dash line marks the diffusion-limited frequency of 6.2 s^{-1} predicted for the collisions of 12 pM AgNPs with a 20.5 μm radius microdisc electrode, using the AgNPs circumscribed radius of 24 nm. The different colours of the bar graphs designate the nano-impact of AgNPs in 20 mM of different supporting electrolytes: (**green**) KI, (**blue**) KBr, (**black**) KCl and (**red**) KNO_3.

10.3.5 Adsorption of silver nanoparticles onto a glass surface

The microdisc electrode employed in the nano-impact measurements is surrounded by an insulating glass sheath. Upon the immersion of the electrode into the nanoparticle suspension, the AgNPs may stick to the surface of the glass resulting in lower frequencies of spikes than predicted, discussed further in the next section.

The adsorption of AgNPs on a glass surface was studied by allowing the suspensions of 12 pM AgNPs in 20 mM of KNO_3 or KCl solutions to adsorb on a microscope glass slide as a function of time. The modified slide was then gently washed with deionised water and allowed to dry. The AgNPs adsorbed on the surface of a glass slide were observed under an optical microscope (Zeiss Axio Examiner.A1, Germany) using a 20× air objective (numerical aperture = 0.5, EC Plan-Neofluar, Germany). The number of AgNPs on the glass surface is analysed using the Python package Trackpy 0.3.2.[54]

In addition to the experimental studies, the expected numbers of AgNPs colliding with a unit area of the glass surface are approximated using the Cottrell equation:

$$j = \frac{nF\sqrt{D}c^*}{\sqrt{\pi t}} \tag{10.11}$$

where j is the number of AgNPs (moles) colliding with 1 m^2 of the glass surface at time t. n = 1, F is the Faraday constant (96,485 C mol^{-1}) and c^* is the concentration of the AgNPs. D is the diffusion coefficient of the AgNPs calculated using the Stokes-Einstein equation:[55,56]

$$D = \frac{k_B T}{6\pi\eta r_{NP}} \tag{10.12}$$

where k_B is the Boltzmann constant, T is the absolute temperature, η is the viscosity of solvent and r_{NP} is the radius of the nanoparticle. For the 24 nm radius AgNPs, the diffusion coefficient (D) is 1.0×10^{-11} m^2 s^{-1}.

Figure 10.10 shows that the number of AgNPs adsorbed on a glass surface is very similar in KNO_3 and KCl solutions, and the amount of the particles adsorbed increases with time. However in both electrolytes, the amounts of the AgNPs adsorbed are approximately an order

of magnitude smaller than the predicted values, as presented in Figure 10.10. This result will be further discussed in the next section.

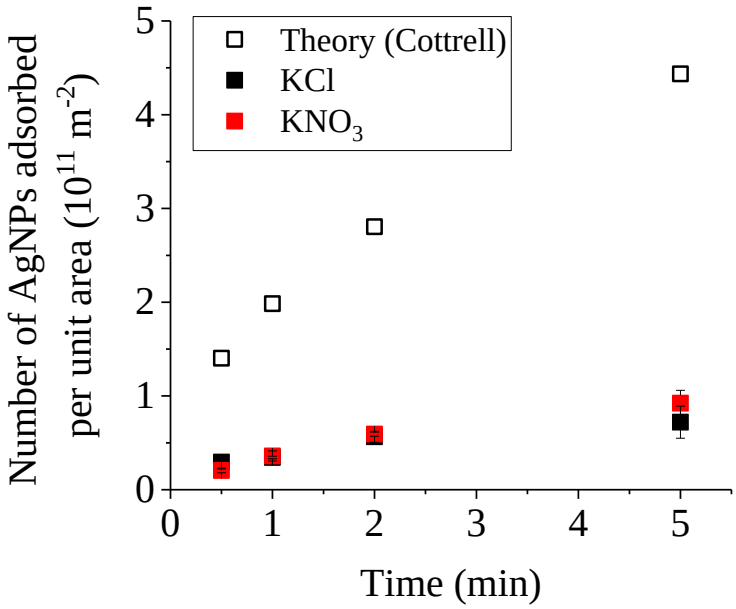


Figure 10.10: The numbers of AgNPs adsorbed on a glass surface (from the suspensions of 12 pM AgNPs) as a function of time: theoretically predicted (**open squares**), experimentally observed in 20 mM KCl (**black squares**) and in 20 mM KNO_3 (**red squares**).

10.4 Discussion

The results of the nano-impact studies presented in Sections 10.3.3.2 and 10.3.4.2 will be discussed in detail in this section to gain insight into the oxidative mechanisms of AgNPs oxidation. The frequency of the nano-impact spikes may be governed by three parameters including the flux of the nanoparticles to the electrode, the quality and time of electrical contact between the electrode and the nanoparticles, and the participation of the anions. Each point is discussed below.

First, there are three possible means of mass transport of the particles to the electrode: diffusion, migration and convection. Convection is assumed to be negligible as the oxidation

of the AgNPs passes only a small current such that no significant temperature or density gradient is built up.[57] Migration is also unlikely to be a dominant factor as the change in the concentration of charged species at the electrode surface is very small as, for a single collision event, only one AgNP is oxidised releasing ~5.3 attomoles of Ag. The surface charges (zeta-potentials) of the AgNPs are also very similar in KNO_3 and KCl electrolytes: -38 ± 1 mV, -28 ± 1 mV, -25 ± 5 mV and -16 ± 3 mV in 0 mM, 5 mM, 20 mM and 40 mM electrolyte respectively. Hence any electrostatic interaction such as the interaction between the electric double layer of the electrode and the Fermi level of the nanoparticle[58] are expected to be similar in all the electrolytes studied herein. The most important and relevant path of mass transport in this work is thus diffusion.

For nanoparticles moving freely in solution by Brownian motion, the diffusion-limited flux (J) of the nanoparticles to a microdisc electrode is expressed by the Shoup-Szabo equation:[59]

$$J = 4Dcr_{\mathrm{e}}f(\tau) \qquad (10.13)$$

where c is the particle number concentration (particles m^{-3}), r_{e} is the radius of the microdisc electrode.

$$f(\tau) = 0.7854 + 0.8862\tau^{-1/2} + 0.2146e^{\left(0.7823\tau^{-1/2}\right)} \qquad (10.14)$$

τ is the dimensionless time;

$$\tau = \frac{4Dt}{r_{\mathrm{e}}^2} \qquad (9.15)$$

t is the time parameter. D is the diffusion coefficient of the nanoparticle which can be estimated by the Stokes-Einstein equation (eqn. 10.12)[55,56]

The carbon microdisc electrode is made of a carbon microfiber surrounded with an insulating glass sheath of 2 mm radius. In the extreme case where all the AgNPs that reach the glass sheath stick to its surface, the flux of the AgNPs to the electroactive disc surface (J^{S}) is reduced to:[60]

$$J^{S} = J\frac{r_{e}}{2r_{s}} \qquad (10.16)$$

where r_e is the radius of the microdisc electrode, r_s is the radius of the insulating glass sheath, and J is the flux described in equation 10.13.

The carbon microdisc electrode used in this work has been characterised using the well-defined ruthenium hexamine ($[Ru(NH_3)_6]^{3+}/[Ru(NH_3)_6]^{2+}$) redox system[61] to have the disc radius (r_e) of 20.5 ± 0.1 μm; refer to Appendix B1. The insulating glass sheath radius (r_s) is 2.0 mm.

The sizes of AgNPs in 20 mM of KNO_3, KCl, KBr and KI have been demonstrated in Section 10.3.2 to be the same in all electrolytes throughout the entire period of the experiments (≤ 20 min). The viscosities of aqueous solutions containing 20 mM of salts are less than 0.04% higher than that of pure water (890.3 μPa s).[62,63] Consequently, the diffusion coefficients (D) are approximated to be ca. $1.1\times10^{-11} \pm 1.2\times10^{-12}$ m^2 s^{-1} using the AgNP (circumscribed) radius of 24 ± 3 nm of the AgNPs. In solution, the solvation of AgNPs has to be considered. The hydrodynamic radius of the AgNPs is determined using dynamic light scattering (DLS z-average) to be 30 ± 6 nm. Based on the hydrodynamic radius, the diffusion coefficients is $8.2\times10^{-12} \pm 1.3\times10^{-12}$ m^2 s^{-1}.

The diffusion-limited fluxes are calculated according to equation 10.13 to be 6.2 ± 0.7 s^{-1} and 4.9 ± 0.8 s^{-1} using the core and hydrodynamic radius respectively. The fluxes accounting for

the 100% adsorption of the AgNPs on the insulating sheath calculated according to equation 10.16 are $0.032 \pm 0.004\ s^{-1}$ and $0.025 \pm 0.004\ s^{-1}$ using the core and hydrodynamic radius respectively.

From the results presented in Figure 10.9, the nano-impacts of AgNPs in 20 mM KBr at very high potentials yield the frequency of spikes of $5.2 \pm 1.3\ s^{-1}$, close to the expected diffusional limit (within experimental error) of ca. $5\ s^{-1}$. However for most other cases (Figures 10.6b and 10.9), the observed spike frequencies are apparently lower than the predicted diffusion-limited value, up to an order of magnitude lower for KNO_3 and KCl at the low 5 mM concentration.

In Section 10.3.5, we demonstrate that less than 20% of the AgNPs that arrive at the glass surface are adsorbed, and that there is no difference in the adsorption rate between the AgNPs in KNO_3 and in KCl solutions. The observed frequencies are also significantly higher than that predicted for the case of full adsorption of AgNPs on the insulating glass sheath. Consequently, it is unlikely that the lower frequency observed is due to the loss of the material to the surrounding environments such as the insulating glass sheath around the electrode and the container. The lower frequency thus suggests that not every AgNP arriving at the electrode surface is oxidised. It is useful to reflect that for other experimental setups reported in the literature a variation in the frequency of the observed spikes as a function of the electrode potential has been reported.[64,65] However, for the present case it is challenging to interpret the variation of the nano-particle impact frequency, as a function of the anion identity, as relating to changes in the nanoparticle mass-transport. Consequently, in light of the results discussed above that the difference in the frequencies of nanoparticle-electrode collisions is *not* a result of the difference in the flux of the AgNPs to the electrode.

Next, we consider the quality and the timescale of the electrical contact between the particles and the electrode. In terms of the charges of the nanoparticles, the surface charges are similar between AgNPs in KNO_3 and KCl, as discussed above. The equal surface charges measured in both KNO_3 and KCl solutions also suggest that no modification is made to the surface of the AgNPs, and that citrate ions may remain as capping agents. Therefore, there should be no difference in the quality and time of contacts.

The difference in the frequency must then arise from the involvement of the anions in the oxidation of AgNPs, in particular during its rate-determining process. The lower frequency in the case of KNO_3 suggests that not all of the AgNPs that arrive at the electrode have been oxidised, implying that the rate at which the AgNPs are oxidised is slower than the time the AgNPs stay at the electrode. The higher frequency of the nano-impact spikes in potassium halide solutions suggests that the halide ions (X^-) accelerate the rate-determining process of the AgNPs oxidation. This altered mechanism is also in part reflected in the altered shape of the voltammetric stripping wave (Figure 10.7). The processes that involve anions are the diffusion of X^- *to* the AgNPs, the diffusion of X^- *into* the AgNPs, and the nucleation and growth of AgX.

It is shown in Figure 10.9 that the frequency of the collision events is not distinctly different (within experimental errors) between the different halides. If any, the frequency in the presence of Cl^- is lower than that of Br^- and I^-. This result infers that the diffusion of X^- to the AgNPs is *not* the rate-determining step of the AgNPs oxidation as the diffusion coefficients of the ions follow the opposite order. The diffusion of X^- into AgNPs or the propagation of the formation of Ag(I) products from the surface into the core of the particles is also *not* a possible initial rate-determining process as once the AgNP is oxidised, the

reaction goes to completion (Figure 10.6a and Inlays in Figure 10.8). The use of faster electronics may resolve the kinetics of this growth stage.

In the light of the above – and partially in analogy to pitting corrosion[66] – we propose that the AgNP oxidation follows a nucleation growth type mechanism such that the observation of an oxidation event is preceded by the stochastic formation of a nucleus of argentous species (Ag^+, AgCl, AgBr or AgI). This initial oxidation event must occur during electrical contact of the nanoparticle to the electrode surface. Accordingly, the sensitivity of the impact frequency towards the nature and concentration of the supporting electrolyte anions reflects the altered rate of this stochastic process. The higher formation constants for the halide/Ag+ complexes likely make the initiation process more favourable. After initiation, the subsequent rates of the nanoparticle oxidation, as reflected in the resulting spike shapes, may either arise from the nanoscale growth and dissolution of the material or alternately may relate to the nanoscopic motion of the nanoparticle (and hence its electrical connectivity) adjacent to the electrochemical interface.

10.5 Conclusions

The ability of the nano-impact technique to investigate the relative kinetics of nanoparticle oxidative dissolution is demonstrated in this work, by comparing the rate of the oxidation to the timescale the particles remain in electrical contact with the electrode and hence the frequency of spikes. The frequency is influenced by the electrolyte's identity and concentrations as well as the applied potentials. In the presence of anions that bind strongly to the oxidation product such as Ag(I) in the oxidative dissolution of AgNPs, the thermodynamically favourable product formation shifts the anodic stripping peaks to more negative potentials and enhance the frequency of spikes. Notably, the *complete* oxidation of AgNP upon impacting at a sufficiently biased electrode is demonstrated. The importance of

rigorous evaluation of the particle volume from two-dimensional transmission electron microscope (TEM) images is emphasised. Exact determination of a nanoparticle volume from a 2D image is not possible, leading to ambiguity in the sizing. This is particularly important when the TEM size is required for comparison with techniques which yield the atomic content of the particles as opposed to the length scale. In the nano-impact measurements, the total charge transferred under each spike is *not* influenced by the electrolyte nor the potential applied at the working electrode. On this basis, we gain physical insights into the oxidation of AgNPs at the electrode surface and reveal that the rate-determining process is the formation of the first oxidised Ag(I) products (similar to pit initiation). The fundamental understanding of this process facilitates the choice of electrolytes in various applications. For example, the determination of the size of AgNPs at low electrolyte concentrations can be achieved by nano-impact measurements at any high over-potential in the presence of e.g. 1 mM of Cl^-, the concentration of which is present in natural river and drinking water. In the next chapter, it will be further demonstrated that electrochemical nano-impacts as well as anodic stripping voltammetry can be used to study the behaviour of AgNPs in biological (saliva) samples in the absence of intentionally added supporting electrolyte.

Bibliography

(1) Ngamchuea, K.; Clark, R. O. D.; Sokolov, S. V.; Young, N. P.; Batchelor-McAuley, C.; Compton, R. G. *Chem. Eur. J.* **2017**, *23*, 16085-16096.
(2) Murray, R. W. *Chem. Rev.* **2008**, *108*, 2688-2720.
(3) Economou, A.; Arrigan, D. W. M.; Campo, J.; Reddy, S. M.; Lunte, S.; Thompson, M.; Kranz, C.; Compton, R.; O'Riordan, A.; Banks, C. *Electrochemical Strategies in Detection Science (Chapter 5)*; Royal Society of Chemistry, **2015**.
(4) Copeland, T. R.; Skogerboe, R. K. *Anal. Chem.* **1974**, *46*, 1257A-1268a.
(5) Ellis, W. D. *J. Chem. Educ.* **1973**, *50*, A131.
(6) Tschulik, K.; Ngamchuea, K.; Ziegler, C.; Beier, M. G.; Damm, C.; Eychmueller, A.; Compton, R. G. *Adv. Funct. Mater.* **2015**, *25*, 5149-5158.
(7) Plowman, B. J.; Sidhureddy, B.; Sokolov, S. V.; Young, N. P.; Chen, A.; Compton, R. G. *ChemElectroChem* **2016**, *3*, 1186-1186.
(8) Neumann, C. C. M.; Batchelor-McAuley, C.; Tschulik, K.; Toh, H. S.; Shumbula, P.; Pillay, J.; Tshikhudo, R.; Compton, R. G. *ChemElectroChem* **2014**, *1*, 87-89.
(9) Toh, H. S.; Batchelor-McAuley, C.; Tschulik, K.; Uhlemann, M.; Crossley, A.; Compton, R. G. *Nanoscale* **2013**, *5*, 4884-4893.

(10) Cloake, S. J.; Toh, H. S.; Lee, P. T.; Salter, C.; Johnston, C.; Compton, R. G. *ChemistryOpen* **2015**, *4*, 22-26.
(11) Ward Jones, S. E.; Campbell, F. W.; Baron, R.; Xiao, L.; Compton, R. G. *J. Phys. Chem. C* **2008**, *112*, 17820-17827.
(12) Toh, H. S.; Jurkschat, K.; Compton, R. G. *Chem. Eur. J* **2015**, *21*, 2998-3004.
(13) Dai, X.; Compton, R. G. *Electroanalysis* **2005**, *17*, 1325-1330.
(14) Ivanova, O. S.; Zamborini, F. P. *J. Am. Chem. Soc.* **2010**, *132*, 70-72.
(15) Giovanni, M.; Pumera, M. *Electroanalysis* **2012**, *24*, 615-617.
(16) Sokolov, S. V.; Eloul, S.; Katelhon, E.; Batchelor-McAuley, C.; Compton, R. G. *Phys. Chem. Chem. Phys.* **2016**, *19*, 28-43.
(17) Cheng, W.; Compton, R. G. *TrAC, Trends Anal. Chem.* **2014**, *58*, 79-89.
(18) Pumera, M. *ACS Nano* **2014**, *8*, 7555-7558.
(19) Sokolov, S. V.; Bartlett, T. R.; Fair, P.; Fletcher, S.; Compton, R. G. *Anal. Chem.* **2016**, *88*, 8908-8912.
(20) Zhao, L. J.; Qian, R. C.; Ma, W.; Tian, H.; Long, Y. T. *Anal. Chem.* **2016**, *88*, 8375-8379.
(21) Ying, Y. L.; Ding, Z.; Zhan, D.; Long, Y. T. *Chem. Sci.* **2017**, *8*, 3338-3348.
(22) Zhou, X.; Xu, W.; Liu, G.; Panda, D.; Chen, P. *J. Am. Chem. Soc.* **2010**, *132*, 138-146.
(23) Guo, Z.; Percival, S. J.; Zhang, B. *J. Am. Chem. Soc.* **2014**, *136*, 8879-8882.
(24) Xiao, X.; Bard, A. J. *J. Am. Chem. Soc.* **2007**, *129*, 9610-9612.
(25) Bard, A. J.; Zhou, H.; Kwon, S. J. *Isr. J. Chem.* **2010**, *50*, 267-276.
(26) Stevenson, K. J.; Tschulik, K. *Curr. Opin. Electrochem.* **2017**.
(27) Haddou, B.; Rees, N. V.; Compton, R. G. *Phys. Chem. Chem. Phys.* **2012**, *14*, 13612-13617.
(28) Saw, E. N.; Kratz, M.; Tschulik, K. *Nano Res.* **2017**, *10*, 3680-3689.
(29) Eloul, S.; Kätelhön, E.; Batchelor-McAuley, C.; Tschulik, K.; Compton, R. G. *J. Electroanal. Chem.* **2015**, *755*, 136-142.
(30) Krause, K. J.; Brings, F.; Schnitker, J.; Katelhon, E.; Rinklin, P.; Mayer, D.; Compton, R. G.; Lemay, S. G.; Offenhausser, A.; Wolfrum, B. *Chem. Eur. J.* **2017**, *23*, 4638-4643.
(31) Panyala, N. R.; Peña-Méndez, E. M.; Havel, J. *J. Appl. Biomed.* **2008**, *6*.
(32) Bartlett, T. R.; Sokolov, S. V.; Plowman, B. J.; Young, N. P.; Compton, R. G. *Nanoscale* **2016**, *8*, 16177-16181.
(33) de Mello Donegá, C. *Nanoparticles: Workhorses of Nanoscience*; Springer Berlin Heidelberg, Germany, **2014**.
(34) Batchelor-McAuley, C.; Ellison, J.; Tschulik, K.; Hurst, P. L.; Boldt, R.; Compton, R. G. *Analyst* **2015**, *140*, 5048-5054.
(35) Ustarroz, J.; Kang, M.; Bullions, E.; Unwin, P. R. *Chem. Sci.* **2017**, *8*, 1841-1853.
(36) Oja, S. M.; Robinson, D. A.; Vitti, N. J.; Edwards, M. A.; Liu, Y.; White, H. S.; Zhang, B. *J. Am. Chem. Soc.* **2017**, *139*, 708-718.
(37) Li, X.; Lenhart, J. J.; Walker, H. W. *Langmuir* **2010**, *26*, 16690-16698.
(38) Sokolov, S. V.; Batchelor-McAuley, C.; Tschulik, K.; Fletcher, S.; Compton, R. G. *Chem. Eur. J.* **2015**, *21*, 10741-10746.
(39) Little, C. A.; Batchelor-McAuley, C.; Young, N. P.; Compton, R. G. Shape and size of non-spherical silver nanoparticles: implications for calculating nanoparticle number concentrations; *Manuscript submitted for publication*.
(40) Lide, D. R. *CRC Handbook of Chemistry and Physics: A Ready-Reference Book of Chemical and Physical Data*; CRC Press, USA, **1995**.
(41) Esteban, R.; Taylor, R. W.; Baumberg, J. J.; Aizpurua, J. *Langmuir* **2012**, *28*, 8881-8890.
(42) Toh, H. S.; Batchelor-McAuley, C.; Tschulik, K.; Compton, R. G. *Analyst* **2013**, *138*, 4292-4297.
(43) Compton, R. G.; Banks, C. E. *Understanding Voltammetry*, 2nd ed.; Imperial College Press, UK, **2011**.
(44) Bard, A. J.; Parsons, R.; Jordan, J. *Standard Potentials in Aqueous Solution*; Taylor & Francis, UK, **1985**.
(45) Brasiliense, V.; Patel, A. N.; Martinez-Marrades, A.; Shi, J.; Chen, Y.; Combellas, C.; Tessier, G.; Kanoufi, F. *J. Am. Chem. Soc.* **2016**, *138*, 3478-3483.
(46) Ly, L. S. Y.; Batchelor-Mcauley, C.; Tschulik, K.; Kätelhön, E.; Compton, R. G. *J. Phys. Chem. C* **2014**, *118*, 17756-17763.
(47) Liu, Y.; Austen, B. J. J.; Cornwell, T.; Tilbury, R. D.; Buntine, M. A.; O'Mullane, A. P.; Arrigan, D. W. M. *Electrochem. Comm.* **2017**, *77*, 24-27.
(48) Li, X.; Batchelor-Mcauley, C.; Whitby, S. A. I.; Tschulik, K.; Shao, L.; Compton, R. G. *Angew. Chem. Int. Ed.* **2016**, *55*, 4296-4299.
(49) Percival, S. J.; Zhang, B. *J. Phys. Chem. C* **2016**, *120*, 20536-20546.
(50) Liu, J.; Hurt, R. H. *Environ. Sci. Tech.* **2010**, *44*, 2169-2175.
(51) Plowman, B. J.; Tschulik, K.; Walport, E.; Young, N. P.; Compton, R. G. *Nanoscale* **2015**, *7*, 12361-12364.

(52) Alexander, R.; Ko, E. C. F.; Mac, Y. C.; Parker, A. J. *J. Am. Chem. Soc.* **1967**, *89*, 3703-3712.
(53) Lees, J. C.; Ellison, J.; Batchelor-McAuley, C.; Tschulik, K.; Damm, C.; Omanovic, D.; Compton, R. G. *ChemPhysChem* **2013**, *14*, 3895-3897.
(54) Allan, D.; Caswell, T.; Keim, N.; van der Wel, C., *Trackpy v0.3.2*; Zenodo, Geneva, Switzerland, **2016**.
(55) Sutherland, W. *Philosophical Magazine Series 6* **1905**, *9*, 781-785.
(56) Einstein, A. *Ann. Phys. (Berlin)* **1905**, *322*, 549-560.
(57) Ngamchuea, K.; Eloul, S.; Tschulik, K.; Compton, R. G. *Anal. Chem.* **2015**, *87*, 7226-7234.
(58) Peljo, P.; Manzanares, J. A.; Girault, H. H. *Chem. Sci.* **2017**, *8*, 4795-4803.
(59) Shoup, D.; Szabo, A. *J. Electroanal. Chem. Interfacial Electrochem.* **1982**, *140*, 237-245.
(60) Eloul, S.; Compton, R. G. *ChemElectroChem* **2014**, *1*, 917-924.
(61) Wang, Y.; Limon-Petersen, J. G.; Compton, R. G. *J. Electroanal. Chem.* **2011**, *652*, 13-17.
(62) Kestin, J.; Sokolov, M.; Wakeham, W. A. *J. Phys. Chem. Ref. Data* **1978**, *7*, 941-948.
(63) Hai-Lang; Shi-Jun. *J. Chem. Eng. Data* **1996**, *41*, 516-520.
(64) Patel, A. N.; Martinez-Marrades, A.; Brasiliense, V.; Koshelev, D.; Besbes, M.; Kuszelewicz, R.; Combellas, C.; Tessier, G.; Kanoufi, F. *Nano Lett.* **2015**, *15*, 6454-6463.
(65) Kang, M.; Perry, D.; Kim, Y. R.; Colburn, A. W.; Lazenby, R. A.; Unwin, P. R. *J. Am. Chem. Soc.* **2015**, *137*, 10902-10905.
(66) Burstein, G. T.; Liu, C.; Souto, R. M.; Vines, S. P. *Corros. Eng., Sci. Technol.* **2013**, *39*, 25-30.

Chapter 11 The fate of silver nanoparticles in authentic human saliva

In this chapter, the physicochemical properties of silver nanoparticles (AgNPs) in human whole saliva are investigated. In authentic saliva samples, AgNPs exhibit a great stability with over 70% of the nanomaterial remaining intact after a 24-hour incubation in the presence of ~0.3 mM dissolved oxygen. The small loss of AgNPs from the saliva sample has been demonstrated to be a result of two processes: agglomeration/aggregation (not involving oxygen) and oxidative dissolution of AgNPs (assisted by oxygen). In authentic saliva, AgNPs are also shown to be more inert both chemically (silver oxidative dissolution) and electrochemically (electron transfer at an electrode) than in synthetic saliva or aqueous electrolytes. Based on the chemical persistence (over a 24-hour study) of AgNPs in saliva, it is predicted that the AgNPs are less likely to cause serious harm to the oral cavity. However, this persistence may enable their transport to other environments.

The work presented in this chapter has been published in *Nanotoxicology*.[1]

11.1 Introduction

As one of the most commonly used nanoparticles, a considerable quantity of nano-silver has been accumulated in water, soil, plants and animals in the food chain.[2-4] Silver nanoparticles (AgNPs) are further introduced in the processing, packaging of food containers and the food itself,[5,6] as well as in drug delivery and biomedical applications.[7] Direct exposure of the oral cavity to AgNPs is thus unavoidable. Diseases and abnormal activities of internal organs as a result of oral exposure to AgNPs have been reported.[8-11] The local susceptibility to damage caused by AgNPs in the oral cavity however has not been investigated. In this work, the physicochemical behaviour of AgNPs is studied *in-vitro* in human whole saliva.

The metabolic process that gives rise to the toxicity of AgNPs has yet to be fully elucidated. The potential causes of AgNPs toxicity are suggested to be the interaction with the cell walls, the release of silver(I) ions (Ag^+) and the generation of reactive oxygen species (e.g. H_2O_2, $^{\bullet}O_2^-$, etc.), leading potentially to damage of DNA and important proteins.[12-15] The toxic pathways mentioned above are strongly dependent on the chemical environments such as pH, concentrations of electrolytes and the presence of molecules that could interact with the silver or reactive oxygen species.[16]

In the oral cavity, saliva is the major component for the maintenance of oral health. It is composed of ca. 99% water, inorganic and organic substances, enzymes, mucus and glycoproteins.[17,18] The pH of saliva is ~6.8. To understand the toxicity of AgNPs to the oral cavity, one needs to directly investigate the course and fate of AgNPs in saliva. Hitherto only synthetic saliva, to the best of the authors' knowledge, has been used to study the properties of the AgNPs.[19,20] The work presented herein however shows that the chemical and electrochemical behaviours of relevant species in synthetic saliva are significantly different from authentic saliva.

The physicochemical properties including size, concentration, stability, integrity and electroactivity of AgNPs in human whole saliva are evaluated and discussed on the basis of electrochemical and spectrophotometric arguments. The dissolution and hence toxicity of these materials is intimately associated with their redox behaviours. The electrochemical responses of AgNPs oxidation are investigated in authentic saliva samples in comparison with synthetic saliva and standard potassium chloride (KCl) solutions. The oxidation process is studied by two techniques: anodic stripping and nano-impact electrochemistry (single particle coulometry). The solution-phase stability and chemical activity of the AgNPs are investigated by UV-visible spectrophotometric measurements.

11.2 Experimental

11.2.1 Chemical reagents and saliva samples

Silver nanoparticles (AgNPs) capped with citrate, branched polyethylenimine (BPEI), polyethylene glycol (PEG), polyvinylpyrrolidone (PVP) and lipoic acid were obtained from Nanocomposix, USA.

11.2.2 Anodic stripping voltammetry

Anodic stripping measurements were performed using a glassy carbon working electrode (3.0 mm diameter, BASi, USA), a platinum mesh counter electrode and a leakless Ag/AgCl (in 3.4 M KCl, eDAQ) reference electrode. Prior to use, the glassy carbon working electrode was polished using alumina powders (1.0 µm, 0.3 µm and 0.05 µm respectively; Buehler, USA) on soft lapping pads (Buehler, USA). A 5 µL aliquot of the suspension containing 48 pM of citrate-capped AgNPs was then dropcast onto the glassy carbon electrode surface. The AgNPs-modified electrode was allowed to dry under a flowing nitrogen atmosphere and then transferred to the standard KCl solutions of different concentrations (0, 1.0, 5.0, 10.0 and

20.0 mM), synthetic saliva or authentic saliva. The system was subjected to cyclic voltammetry measurements initially scanning anodically in the potential range of -0.2 V to 1.0 V vs. leakless reference electrode at the scan rate of 10 mV s^{-1}.

11.2.3 Nano-impacts

Nano-impact experiments were performed with a low noise potentiostat that was built in-house.[21] The measurements were done using a standard three electrode setup in a 25 °C thermostated Faraday cage. A carbon microdisc (33 μm diameter, BASi), a leakless Ag/AgCl (in 3.4 M KCl, eDAQ) and a platinum mesh were used as working, reference and counter electrodes respectively.

Cyclic voltammetry was initially scanned anodically in the potential range of -0.2 V to 1.0 V vs. leakless Ag/AgCl electrode at the scan rate of 10 mV s^{-1} in the 20 mM KCl solution, synthetic saliva or authentic saliva containing 12 pM citrate-capped AgNPs.

11.2.4 Spectrophotometric measurements

Silver nanoparticles capped with different molecules were incubated in synthetic saliva or authentic saliva at 25 °C in the absence or presence of atmospheric oxygen (~0.3 mM), and the UV-visible spectra recorded as a function of time.

11.2.5 Characterisation of AgNPs

All the silver nanoparticles used in this work were characterised using transmission electron microscope. The characterisation of citrate-capped AgNPs has been previously presented in Chapter 10, yielding the average radius of 21 ± 3 nm (Q_{equiv} = 3.9 × 10^{-13} ± 1.6 × 10^{-13} C from the 'detailed analysis' of TEM images, as described in Section 10.3.1). The sizes of AgNPs capped with BPEI, lipoic acid, PEG and PVP were sized by Dr. Her Shuang Toh,

presented in ref. 22, to have the average radii of 15.0 ± 1.6 nm, 13.5 ± 3.9 nm, 9.6 ± 2.0 nm and 13.5 ± 1.9 nm respectively.[22]

11.3 Results and discussion

The oxidation of AgNPs is first investigated electrochemically via anodic stripping voltammetry and nano-impact technique. The chemical stability, agglomeration/aggregation and oxidative dissolution of the AgNPs are then studied by UV-visible spectrophotometry and dark-field microscopy.

11.3.1 Anodic stripping voltammetry of AgNPs

In anodic stripping studies, an aliquot of AgNPs suspension consisting of 2.4×10^{-16} moles of the nanoparticles was dropcast onto the surface of a freshly polished glassy carbon electrode to yield a coverage (projected surface area of AgNPs:electrode) of ca. 4.5%. The modified electrode was allowed to dry under a flowing nitrogen atmosphere. The AgNP-modified electrode was then transferred to authentic saliva, synthetic saliva or standard KCl solutions (0, 1.0, 5.0, 10.0 and 20.0 mM), where the electrode was subjected to cyclic voltammetry measurements initially scanning anodically in the potential range of -0.2 V to 1.0 V vs. Ag/AgCl (in 3.4 M KCl) leakless reference electrode at the scan rate of 10 mV s^{-1}.

Figure 11.1 presents the voltammograms of AgNP anodic stripping in the different samples. A well-defined oxidative response of AgNPs can be obtained in authentic whole saliva without any pre-treatment or added supporting electrolyte. The anodic stripping peak potentials appear at ~0.18 V in both synthetic and authentic saliva, which is the same potential as the oxidation of AgNP in 1.0 mM KCl solution. At higher chloride concentrations, the positions of the anodic stripping peaks occur at less positive potentials, as previously discussed in Chapter 10.[23,24]

In standard KCl solutions for all the concentrations studied, the total charge (Q) transferred during the oxidation of the immobilised AgNPs was in the range of $1.6 \times 10^{-5} \pm 5 \times 10^{-6}$ C, corresponding to 22 ± 6 % of the expected charge (~7.5×10^{-5} C, as previously discussed in Chapter 10). In synthetic saliva, the charge transferred was $1.2 \times 10^{-5} \pm 1 \times 10^{-6}$ C, comparable to that obtained in the KCl solutions. However, the observed charge transferred in authentic saliva was $2.1 \times 10^{-6} \pm 6.0 \times 10^{-7}$ C significantly smaller than in the other cases.

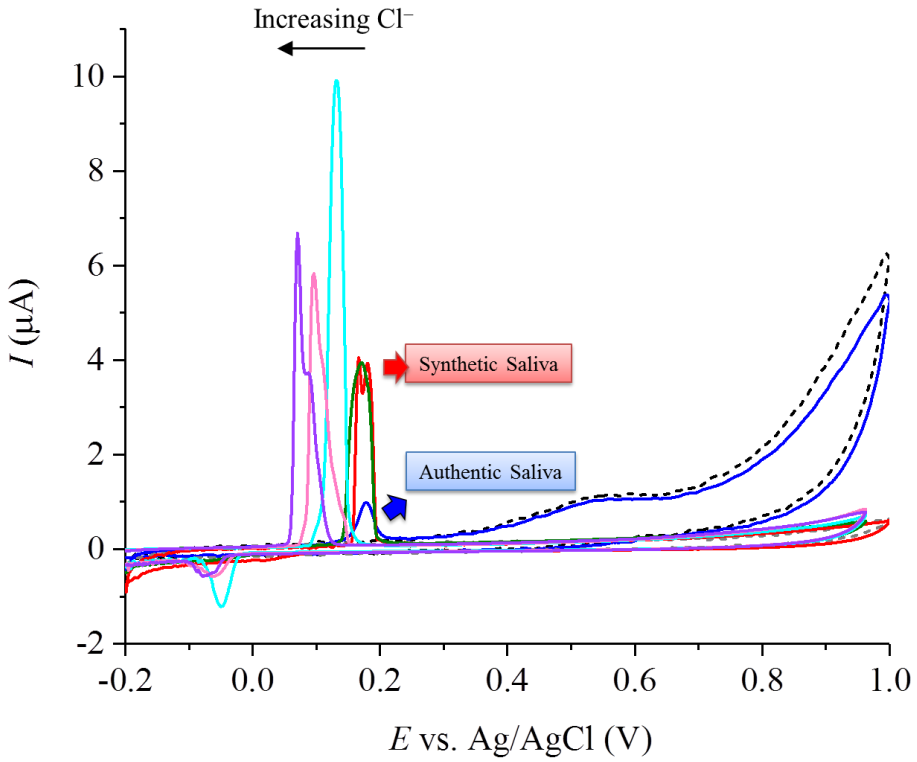


Figure 11.1: Anodic stripping voltammograms of silver nanoparticles (AgNPs) immobilised on the surface of a glassy carbon electrode in potassium chloride solutions: 1.0 mM (**green**), 5.0 mM (**light blue**), 10.0 mM (**pink**) and 20.0 mM (**purple**), synthetic saliva (**red**), and authentic saliva (**dark blue**). Scan rate of 10 mV s^{-1}. Dashed lines show the voltammograms of synthetic saliva (**grey**) and authentic saliva (**black**) at a blank, unmodified electrode.

In all cases, the charges observed experimentally were smaller than the predicted value. This is due to the agglomeration/aggregation of the AgNPs on the electrode surface,[25] and is part

of the reason why nano-impact, an *in-situ* technique, will be further performed along with anodic stripping voltammetry. The agglomeration/aggregation however takes place during the drying of the AgNPs suspension on the electrode prior to being exposed to the samples, and hence cannot contribute to the difference in the responses between authentic and synthetic saliva.

The other potential causes of the small anodic stripping charges observed in authentic saliva samples are ***i*)** the loss of AgNPs from the electrode surface and ***ii*)** the more electrochemically inert nature of AgNPs in authentic saliva. The effect of the former is first investigated. The AgNPs-modified electrode was left in authentic saliva samples for different times (0, 5 and 10 minutes) prior to performing anodic stripping. The results in Figure 11.2 show that the charges observed are independent of the exposure time, evidencing the minimal loss of material from the electrode surface. Therefore, the small stripping charge suggests the more electrochemically inert nature of AgNPs in authentic saliva, *vide infra*.

11.3.2 Nano-impacts of AgNPs

In addition to anodic stripping voltammetry, nano-impact experiments were performed to study the electrochemical responses of AgNPs oxidation *in-situ*. In solution, AgNPs diffuse freely by virtue of Brownian motion. In the event that a AgNP arrives at the electrode held at a suitable potential (E > ~0.2 V), the AgNP is fully oxidised resulting in a current-transient spike, refer to Chapter 10.[22,23,26-28] The charge transfer for each spike corresponds to the size of the AgNPs, while the diffusion-limited frequency of spikes is indicative of the concentration and agglomeration state of AgNPs in the suspension.

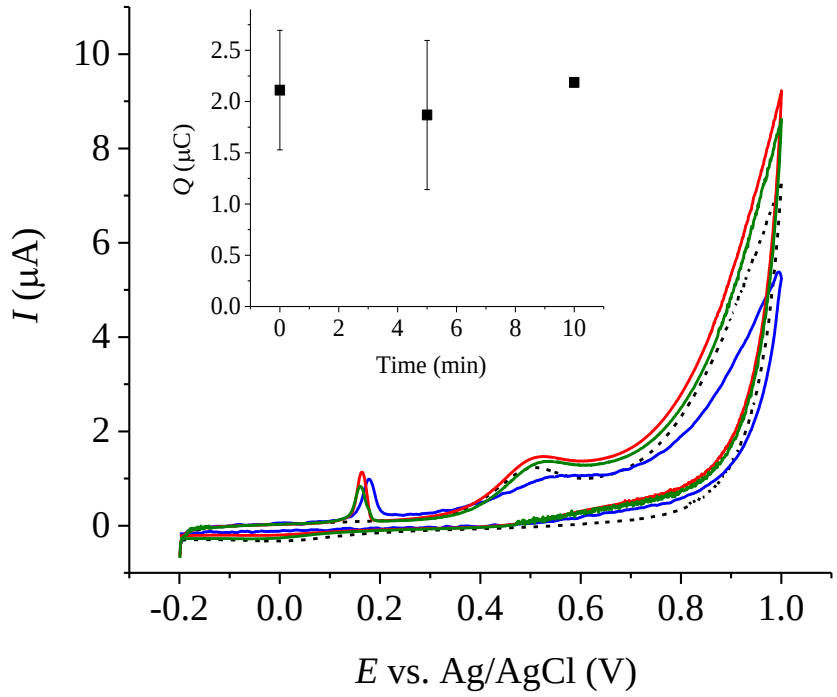


Figure 11.2: Cyclic voltammograms showing the peaks at ~0.18 V of AgNPs anodic stripping in authentic saliva samples after the AgNPs immobilised on the glassy carbon electrode are exposed to the sample prior to anodic stripping for 0 minute (**blue**), 5 minutes (**red**) and 10 minutes (**green**). Dashed line shows the voltammogram of authentic saliva in absence of the AgNPs. Scan rate of 10 mV s^{-1}.

Figure 11.3 displays examples of cyclic voltammetry responses of a carbon microdisc electrode (33 μm diameter) immersed in a 12 pM AgNP suspension, and the inlays clarify the representative spike shapes. In 20.0 mM KCl, the spikes were observed at the frequency of 4.6 ± 0.6 s^{-1} (diffusion-limited frequency: 6.2 s^{-1}) with the average charge transferred per spike of $3.2 \times 10^{-13} \pm 2.3 \times 10^{-13}$ C. These charges correspond to *complete* oxidation of the AgNPs (c.f. $Q_{\text{equiv}} = 3.9 \times 10^{-13} \pm 1.6 \times 10^{-13}$ C from TEM analysis) as previously discussed in Chapter 10. In synthetic saliva, the features were similar to that in 20.0 mM KCl with the frequency of spikes of 4.1 ± 2.2 s^{-1} and the average charge per spike of $3.1 \times 10^{-13} \pm 2.1 \times 10^{-13}$ C.

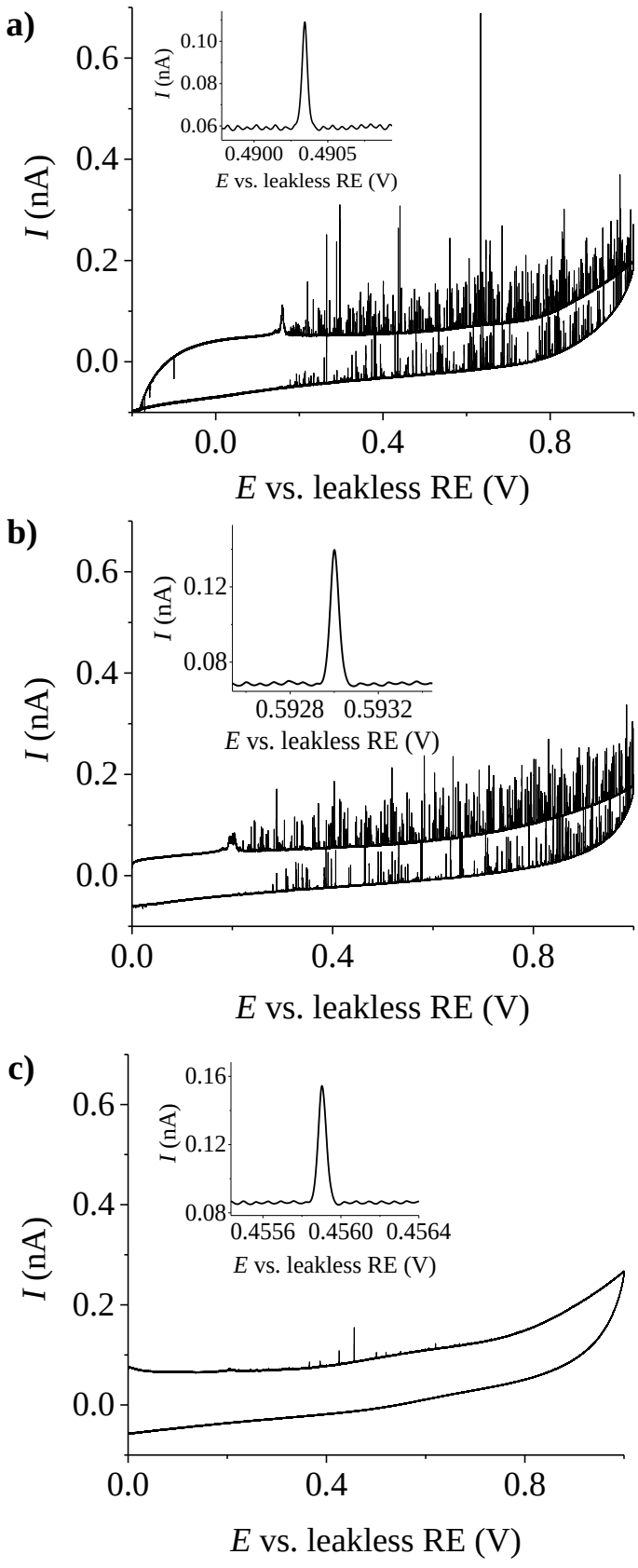


Figure 11.3: Cyclic voltammograms showing AgNPs nano-impact spike features in **a)** 20.0 mM KCl, **b)** synthetic saliva and **c)** authentic saliva diluted by a factor of 100 in synthetic saliva. The **inlays** show representative shapes of the current-transient spikes as a result of single AgNP oxidation.

In contrast, *no spikes* were observed in authentic saliva samples. A small number of current-transient spikes with a frequency of $0.13 \pm 0.08\ s^{-1}$ were observed when authentic saliva was diluted (using synthetic saliva) by a factor of 100. The mean charge transferred per spike in diluted authentic saliva sample is also found to be significantly smaller, $1.9 \times 10^{-13} \pm 1.3 \times 10^{-13}$ C. The small charges and low response rate of AgNPs oxidation further support the hypothesis that AgNPs are relatively oxidatively inert in authentic saliva. Additional evidences and mechanisms are proposed below.

11.3.3 Stability of AgNPs in saliva

The stability of AgNPs in saliva specimens was further investigated by spectrophotometry. AgNPs display plasmonic responses where the position (λ_{max}) and the magnitude of the peak (maximum absorbance; Abs_{max}) are related to size and concentration of the particles respectively.[29] Consequently, the AgNPs were incubated in synthetic and authentic saliva at 25 ^{o}C, and the spectra recorded as a function of time.

Figure 11.4 presents the absorption spectra of the AgNPs in synthetic and authentic saliva samples before and after four hours incubation in the absence and presence of atmospheric oxygen (~0.3 mM dissolved oxygen).[30] In synthetic saliva in the presence of dissolved oxygen, the maximum absorbance and hence the number of AgNPs in the sample (according to Beer-Lambert law) decreased by 81% in four hours.[29] In authentic saliva, the concentration of AgNPs also decreased in the first four hours in the presence of oxygen, but to a much smaller extent of 27%.

To investigate the effect of oxygen on the disappearance of AgNPs, oxygen was removed from the samples by a strong flow of argon gas into the samples prior to the addition of AgNPs. After the elimination of oxygen, the AgNPs UV-vis signals still decreased but to much smaller extents of 45% and 11% losses of AgNPs after 4 hours incubation in synthetic

and authentic saliva respectively (Figure 11.4). This indicates that there are (by a factor of ~3-4) more intact AgNPs left in authentic saliva than in synthetic saliva when the AgNPs are incubated in the samples for the same duration. The responses did not decrease further when left for longer (24 hours). The spectrophotometric results thus evidence the greater stability of AgNPs in authentic saliva samples as compared with synthetic saliva.

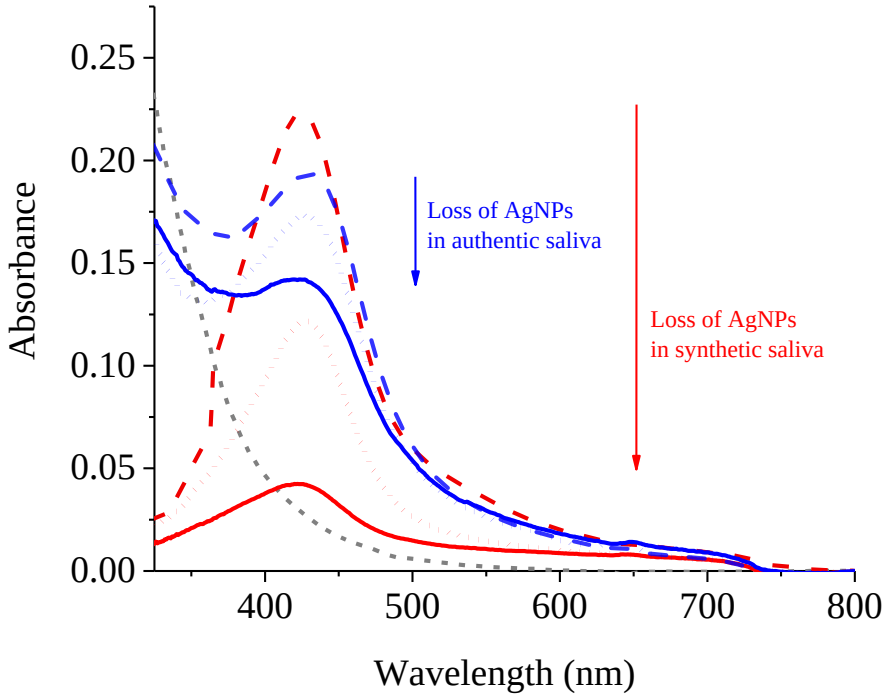
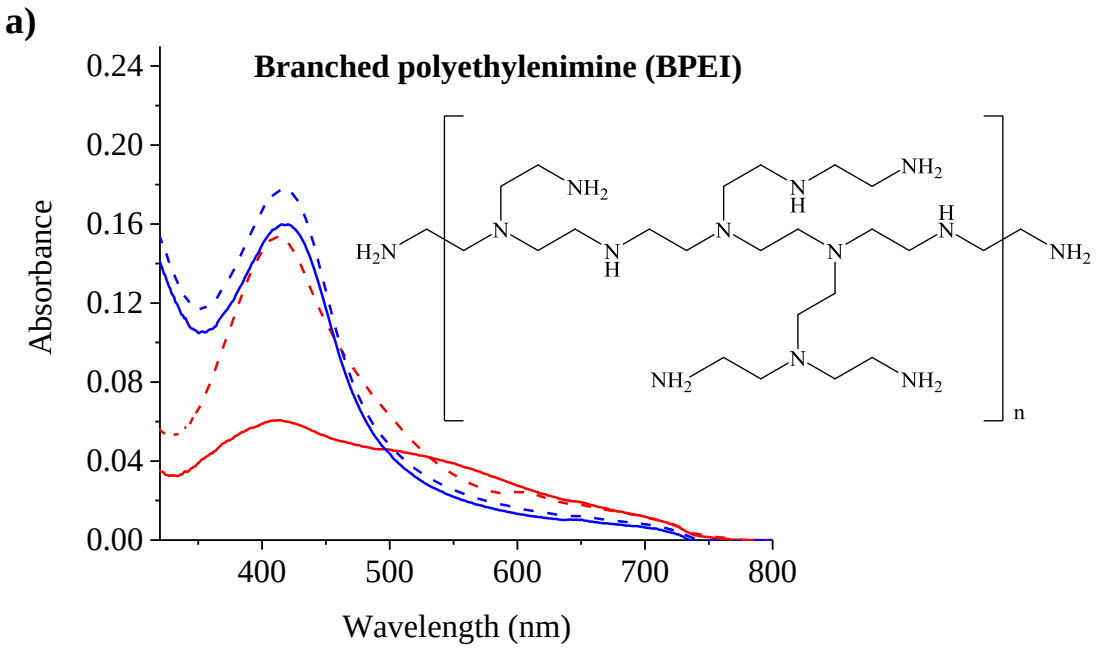
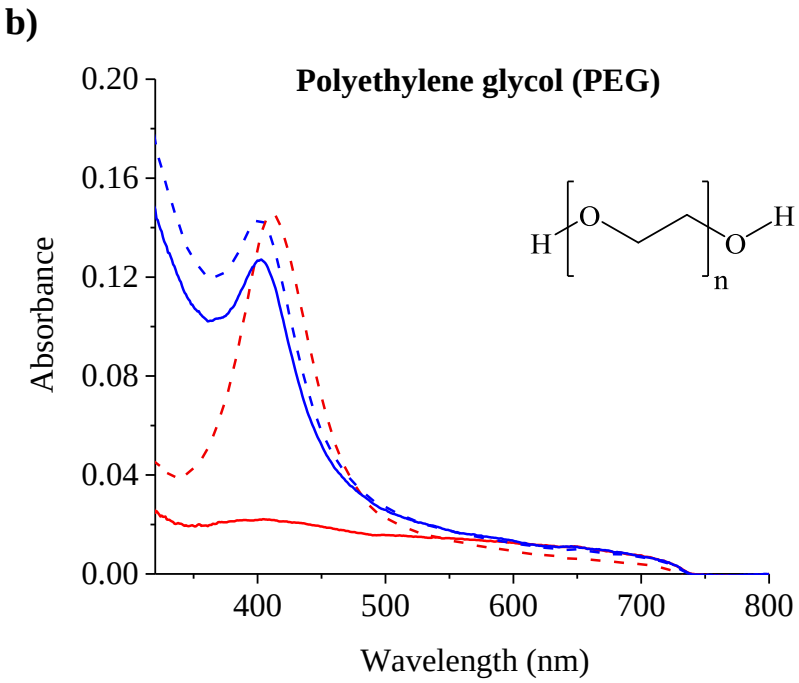


Figure 11.4: UV-visible spectra of blank authentic saliva (**grey, dashed line**), and AgNPs after incubation in synthetic saliva (**red**) and authentic saliva (**blue**) for 0 hr (**dashed lines**), 4 hr in the presence of atmospheric oxygen (**solid lines**) and 4 hr in the absence of oxygen (**dotted lines**)

In the above work, citrate-capped AgNPs were used experimentally. Similar spectrophotometric experiments were performed for AgNPs capped with different molecules including branched polyethylenimine (BPEI), polyethylene glycol (PEG), polyvinylpyrrolidone (PVP) and lipoic acid. The AgNPs were incubated in synthetic and authentic saliva in the presence of atmospheric oxygen, and the UV-vis spectra recorded for four hours. The results are presented in Figure 11.5. In synthetic saliva, the losses of AgNPs after 4-hour

incubation under atmospheric oxygen were 61%, 85%, 4% and 30% for BPEI, PEG, PVP and lipoic acid respectively. In authentic saliva, there were 10%, 11%, 3% and 7% losses of AgNPs capped with BPEI, PEG, PVP and lipoic acid respectively. Consequently, it has been shown that AgNPs were significantly more stable in authentic saliva than in synthetic saliva for all the different capping agents studied.





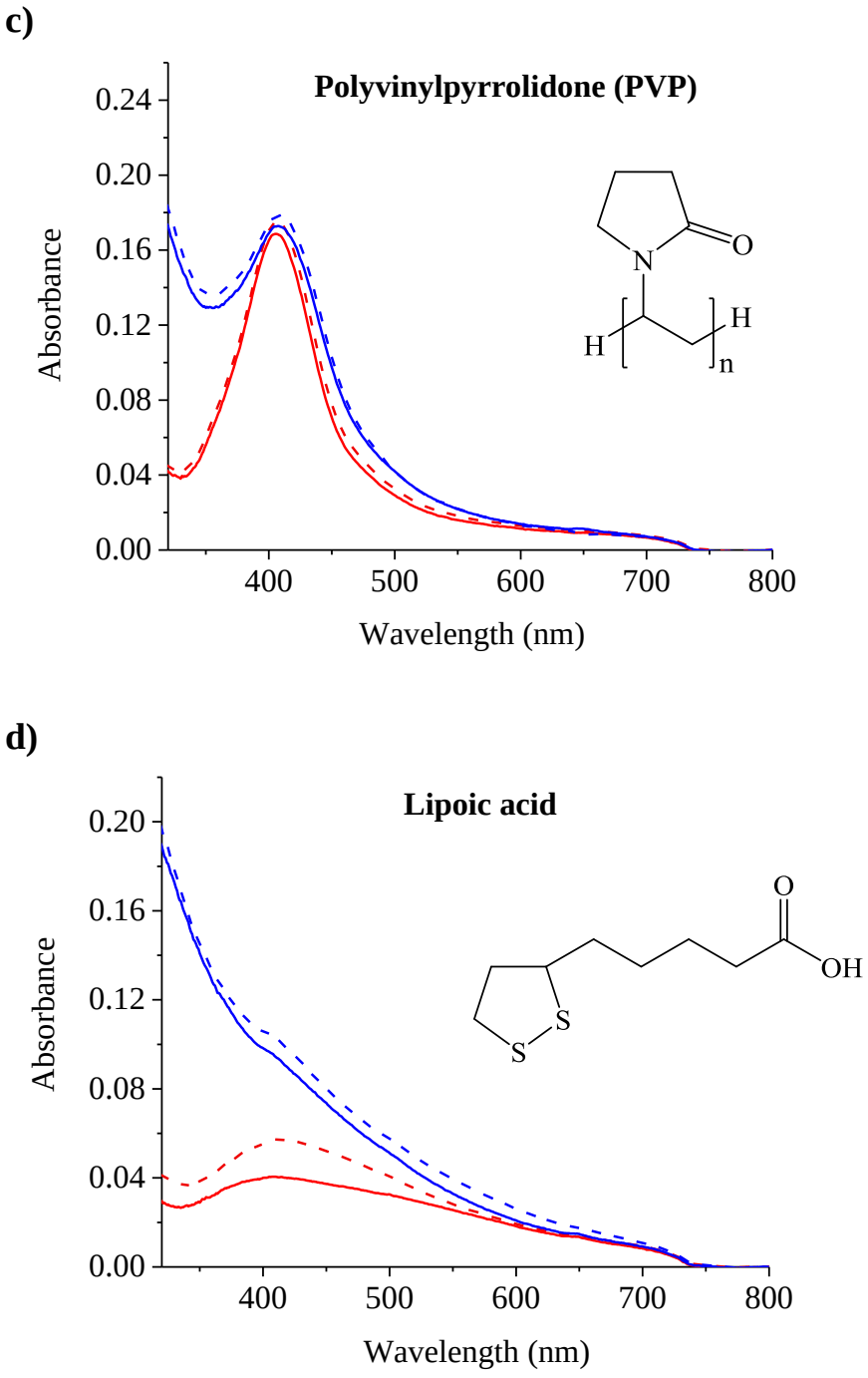


Figure 11.5: UV-vis spectra of AgNPs capped with different molecules **a)** branched polyethylenimine (BPEI), **b)** polyethylene glycol (PEG), **c)** polyvinylpyrrolidone (PVP) and **d)** lipoic acid in synthetic saliva (**red**) and authentic saliva (**blue**) after 0 hour (**dashed line**) and 4 hours (**solid line**) incubation at 25 ^{o}C in the presence of atmospheric oxygen.

11.3.4 Physical origins of the stability of AgNPs in saliva

The possible origins of the loss of AgNPs UV-vis signal may relate to the agglomeration/ aggregation and/or the dissolution of AgNPs. The latter likely only occurs in the presence of dissolved oxygen as shown by the cyclic voltammograms of authentic saliva in Figure 11.6 that in the absence of oxygen, no reductive peaks were observed. On the other hand, a clear reductive response was observed in the presence of atmospheric oxygen (~0.3 mM dissolved oxygen).[30] This suggests that the species reduced in saliva is predominantly oxygen and only a negligible amount of other species of a reduceable nature is present. Consequently, it suggests that oxygen is the main component in authentic saliva that could contribute to the dissolution of AgNPs.

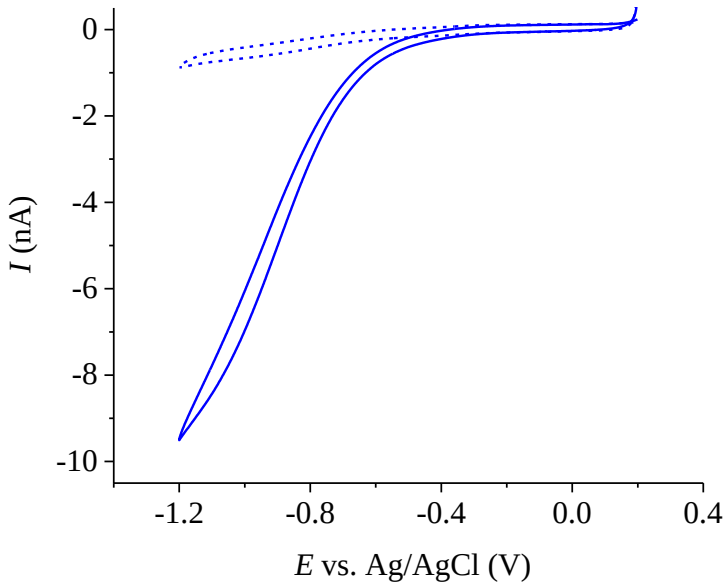


Figure 11.6: Cyclic voltammograms of authentic saliva reduction in the absence (**dashed line**) and presence (**solid line**) of atmospheric oxygen at a carbon microdisc electrode (33 μm diameter). Scan rate of 10 mV s^{-1}.

In the absence of oxygen, the loss of AgNPs is attributed to the agglomeration/aggregation of the particles.[19,20] It has been demonstrated in Figure 11.4 that after the elimination of oxygen, the loss of AgNPs from the samples was still observed, although to a smaller extent. Importantly, this loss of AgNPs was still smaller in authentic saliva compared with synthetic saliva. The results thus indicate that both agglomeration/aggregation and oxidative dissolution play important roles in the instability of the AgNPs in solution-phase. The results also indicate that the agglomeration/aggregation of AgNPs progresses to a smaller extent in authentic saliva as compared to synthetic saliva. This conclusion was further corroborated by the observation of the AgNP sizes in authentic *vs.* synthetic saliva under dark-field microscope.

Figure 11.7 shows the images of AgNPs in synthetic saliva (11.7a) and authentic saliva (11.7b) taken at 10 minutes after mixing. In synthetic saliva, the sizes of the AgNPs are significantly larger than in authentic saliva, indicating the greater extent of agglomeration/aggregation in synthetic saliva.

Thus far, the main observations on authentic saliva are that first the voltammetric oxidation of large ensembles of nanoparticles is inhibited in saliva. Second, the frequency of individual nanoparticle oxidations from the solution phase is significantly decreased in the presence of saliva. Moreover even in highly diluted authentic saliva samples, only small oxidative events are observed. Third, the UV-vis studies evidence a low rate of loss of the AgNPs in authentic saliva and that this loss of signal arises from both agglomeration and oxidative dissolution of the nanomaterial. In the presence of oxygen, AgNPs may undergo thermodynamically favorable oxidative dissolution to form Ag^+ and reactive oxygen species, likely via the following reaction pathways.[16]

$$\tfrac{1}{2}\,O_2 + H^+ + Ag(s) \longrightarrow Ag^+ + \tfrac{1}{2}\,H_2O_2 \qquad (11.1)$$

$$Ag(s) + \tfrac{1}{2}\,H_2O_2 + H^+ \longrightarrow Ag^+ + H_2O \qquad (11.2)$$

The dissolution of AgNPs, in particular the products formed in the process, has been suggested to be one of the origins of the toxicity of AgNPs to biological systems including microorganisms, animals and humans.[12-14] The toxicity of silver nanoparticles as compared with the bulk silver is thought to result from the efficient divergent diffusion of hydrogen peroxide (H_2O_2) away from the particle surface, before it can be reduced further to water.[15]

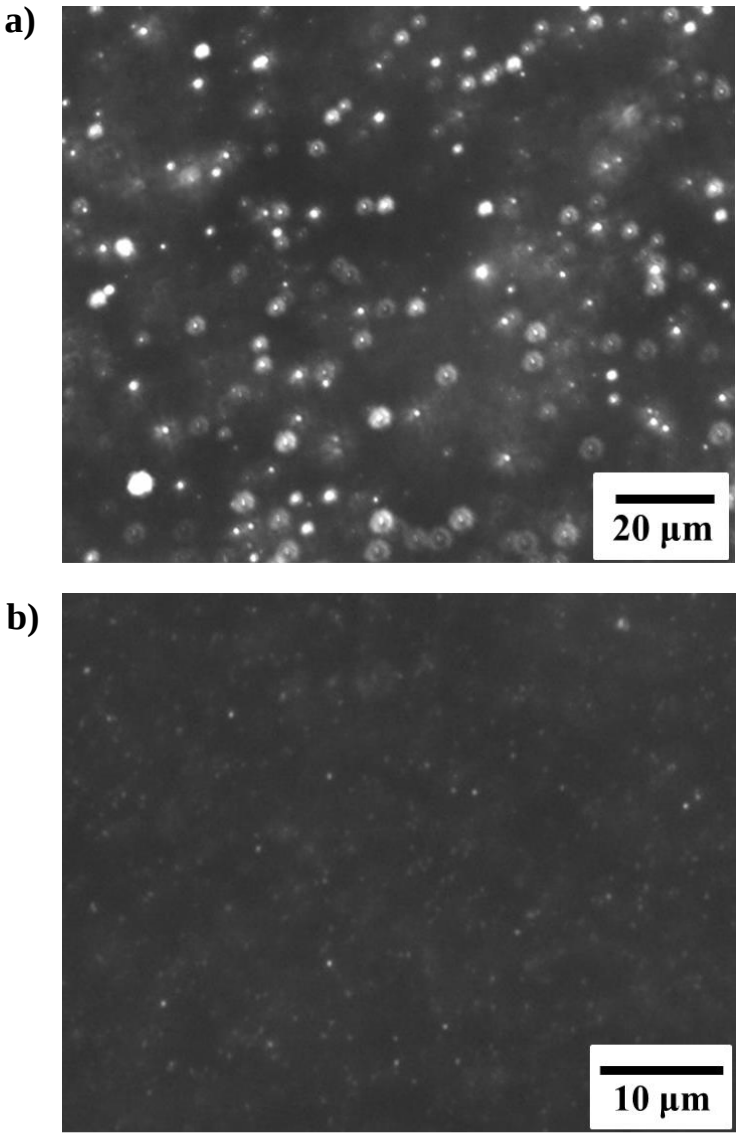


Figure 11.7: Dark-field microscopic images of AgNPs in **a)** synthetic saliva and **b)** authentic saliva.

These observations are consistent with the behaviour of the nanoparticles in authentic saliva being altered from synthetic saliva or aqueous solutions due to a change in their local chemical environment. This most likely arises from the adsorption of proteins,[31] large organic fragments or other macromolecules present in authentic saliva onto the surface of the nanoparticles. The surface agents introduce steric stabilisation, and hence preventing the formation of clusters. The presence of large organic layer on the AgNPs surface would also be consistent with the redox AgNP dissolution process being inhibited as demonstrated by both the UV-vis and electrochemical studies above, resulting in the greater stability of AgNPs in authentic saliva.

11.4 Conclusions

This work proves on the basis of the conservation of the nanoparticles integrity that AgNPs are relatively stable in authentic human whole saliva, as compared with synthetic saliva or aqueous solutions. The formation of Ag^+ and possibly reactive oxygen species in saliva are significantly lower. The presence of AgNPs in the oral cavity, whether by accident or intended for biodiagnostic, therapeutic or drug delivery applications,[7] is thus to a first approximation predicted not to cause serious harm to the oral cavity. As AgNPs remain intact in authentic saliva samples, it is likely that the particles would pass through the oral cavity into the other parts of the body in their original forms. However ingestion could be one route by which AgNPs may accumulate in liver, spleen and kidney as observed in laboratory animals,[4,32,33] causing diseases and abnormal activities of the organs.[8-11] Finally, based on these results any method validations or *in-vitro* studies related to oral cavity are also recommended to be performed in authentic saliva, as opposed to synthetic saliva because of the significant difference in the physicochemical properties of chemical species in the two media.

Bibliography

(1) Ngamchuea, K.; Batchelor-McAuley, C.; Compton, R. G. *Nanotoxicology* **2018**, *12*, 305-311.
(2) Gottschalk, F.; Sonderer, T.; Scholz, R. W.; Nowack, B. *Environ. Sci. Technol.* **2009**, *43*, 9216-9222.
(3) Harris, A. T.; Bali, R. *J. Nanopart. Res.* **2008**, *10*, 691-695.
(4) Lankveld, D. P.; Oomen, A. G.; Krystek, P.; Neigh, A.; Troost-de Jong, A.; Noorlander, C. W.; Van Eijkeren, J. C.; Geertsma, R. E.; De Jong, W. H. *Biomaterials* **2010**, *31*, 8350-8361.
(5) Mackevica, A.; Olsson, M. E.; Hansen, S. F. *J. Nanopart. Res.* **2016**, *18:5*.
(6) Carbone, M.; Donia, D. T.; Sabbatella, G.; Antiochia, R. *J. King Saud Univ. - Sci.* **2016**, *28*, 273-279.
(7) Austin, L. A.; Mackey, M. A.; Dreaden, E. C.; El-Sayed, M. A. *Arch. Toxicol.* **2014**, *88*, 1391-1417.
(8) Tiwari, R.; Singh, R. D.; Khan, H.; Gangopadhyay, S.; Mittal, S.; Singh, V.; Arjaria, N.; Shankar, J.; Roy, S. K.; Singh, D.; Srivastava, V. *Nanotoxicology* **2017**, *11*, 671-686.
(9) Heydrnejad, M. S.; Samani, R. J.; Aghaeivanda, S. *Biol. Trace. Elem. Res.* **2015**, *165*, 153-158.
(10) Kim, Y. S.; Song, M. Y.; Park, J. D.; Song, K. S.; Ryu, H. R.; Chung, Y. H.; Chang, H. K.; Lee, J. H.; Oh, K. H.; Kelman, B. J.; Hwang, I. K.; Yu, I. J. *Part. Fibre Toxicol.* **2010**, *7*, 20.
(11) Jeong, G. N.; Jo, U. B.; Ryu, H. Y.; Kim, Y. S.; Song, K. S.; Yu, I. J. *Arch. Toxicol.* **2010**, *84*, 63-69.
(12) AshaRani, P. V.; Low Kah Mun, G.; Hande, M. P.; Valiyaveettil, S. *ACS nano* **2009**, *3*, 279-290.
(13) Carlson, C.; Hussain, S. M.; Schrand, A. M.; Braydich-Stolle, L. K.; Hess, K. L.; Jones, R. L.; Schlager, J. J. *J. Phys. Chem. B.* **2008**, *112*, 13608-13619.
(14) Foldbjerg, R.; Dang, D. A.; Autrup, H. *Arch. Toxicol.* **2011**, *85*, 743-750.
(15) Batchelor-McAuley, C.; Tschulik, K.; Neumann, C. C. M.; Laborda, E.; Compton, R. G. *Int. J. Electrochem. Sci.* **2014**, *9*, 1132-1138.
(16) Liu, J.; Hurt, R. H. *Environ. Sci. Technol.* **2010**, *44*, 2169-2175.
(17) de Almeida Pdel, V.; Gregio, A. M.; Machado, M. A.; de Lima, A. A.; Azevedo, L. R. *J. Contemp. Dent. Pract.* **2008**, *9*, 72-80.
(18) Ngamchuea, K.; Chaisiwamongkhol, K.; Batchelor-McAuley, C.; Compton, R. G. *Analyst* **2018**, *143*, 81-99.
(19) Pindakova, L.; Kasparkova, V.; Kejlova, K.; Dvorakova, M.; Krsek, D.; Jirova, D.; Kasparova, L. *Int. J. Pharm.* **2017**, *527*, 12-20.
(20) Walczak, A. P.; Fokkink, R.; Peters, R.; Tromp, P.; Herrera Rivera, Z. E.; Rietjens, I. M.; Hendriksen, P. J.; Bouwmeester, H. *Nanotoxicology* **2013**, *7*, 1198-1210.
(21) Batchelor-McAuley, C.; Ellison, J.; Tschulik, K.; Hurst, P. L.; Boldt, R.; Compton, R. G. *Analyst* **2015**, *140*, 5048-5054.
(22) Toh, H. S.; Jurkschat, K.; Compton, R. G. *Chem. Eur. J* **2015**, *21*, 2998-3004.
(23) Ngamchuea, K.; Clark, R. O. D.; Sokolov, S. V.; Young, N. P.; Batchelor-McAuley, C.; Compton, R. G. *Chem. Eur. J.* **2017**, *23*, 16085-16096.
(24) Toh, H. S.; Batchelor-McAuley, C.; Tschulik, K.; Compton, R. G. *Analyst* **2013**, *138*, 4292-4297.
(25) Cloake, S. J.; Toh, H. S.; Lee, P. T.; Salter, C.; Johnston, C.; Compton, R. G. *ChemistryOpen* **2015**, *4*, 22-26.
(26) Bartlett, T. R.; Sokolov, S. V.; Plowman, B. J.; Young, N. P.; Compton, R. G. *Nanoscale* **2016**, *8*, 16177-16181.
(27) Saw, E. N.; Kratz, M.; Tschulik, K. *Nano Res.* **2017**, *10*, 3680-3689.
(28) Brasiliense, V.; Patel, A. N.; Martinez-Marrades, A.; Shi, J.; Chen, Y.; Combellas, C.; Tessier, G.; Kanoufi, F. *J. Am. Chem. Soc.* **2016**, *138*, 3478-3483.
(29) Ngamchuea, K.; Batchelor-McAuley, C.; Sokolov, S. V.; Compton, R. G. *Anal. Chem.* **2017**, *89*, 10208-10215.
(30) Truesdale, G. A.; Downing, A. L.; Lowden, G. F. *J. Chem. Technol. Biotechnol.* **2007**, *5*, 53-62.
(31) Duran, N.; Silveira, C. P.; Duran, M.; Martinez, D. S. *J. Nanobiotechnol.* **2015**, *13*, 55.
(32) Tang, J.; Xiong, L.; Wang, S.; Wang, J.; Liu, L.; Li, J.; Yuan, F.; Xi, T. *J. Nanosci. Nanotechnol.* **2009**, *9*, 4924-4932.
(33) Jia, J.; Li, F.; Zhou, H.; Bai, Y.; Liu, S.; Jiang, Y.; Jiang, G.; Yan, B. *Environ. Sci. Technol.* **2017**, *51*, 9334-9343.

Chapter 12 Overall conclusions

Saliva plays a major role in maintaining normal functions of the oral cavity. The concentrations of many salivary compounds also reflect the state of several systemic diseases. The functions of saliva and the possible use of saliva in medical applications have been summarised in chapter 3. The detection of salivary biomarkers offers alternative diagnostic methods suitable for point-of-care and long term self-monitoring. This thesis develops sensors for the detection of some salivary biomarkers, and presents the work done in collaboration with medical researchers to realise the practical use of the developed sensor in *real* patients.

First of all, the assays for glutathione quantification are developed using electrochemical and spectrophotometric techniques. In the electrochemical detection, a new electrode design based on the surface-supported carbon microfiber is implemented. The characterisation method using ferrocenemethanol and the theoretical model describing the amperometric responses at the supported cylindrical electrode (with restricted diffusion near the substrate surface) are further developed. This new electrode design minimises the capacitative currents, improves the limit of detection and can be widely used for many other electroanalytical applications.

The spectrophotometric assay improves the selectivity towards glutathione via the use of enzyme glutathione reductase. This assay has been applied and validated in authentic saliva and blood samples. The assay allows the measurements of both GSH (reduced glutathione) and GSSG (oxidised glutathione), and hence the ratio between the two species which is indicative of oxidative stress. The developed methodology can be completed in less than 2 minutes. This assay is further employed in the investigations of glutathione as a biomarker

for bipolar disorder. The result shows the significantly higher levels of glutathione in bipolar patients than in healthy controls, indicating the potential of salivary glutathione as a biomarker for the disorder.

Glutathione also shows significantly greater stability in saliva (half-life of > 90 minutes) than in blood plasma (half-life of ~5-20 minutes), further demonstrating the advantage of saliva over blood samples. The difference in the stability of glutathione in the two media is likely due to the difference in the levels of Cu^{2+}. Cu^{2+} can form a copper-glutathione complex and oxidise GSH to GSSG. The mechanisms and the kinetics of these complex reactions are investigated. Importantly, this work emphasises that GSH is not auto-oxidised by oxygen in the *absence* of metal or biological catalysts.

Another salivary biomarker considered in this thesis is uric acid. This compound is potentially diagnostic of gout, oral cavity cancer and other several diseases. An electrochemical assay is developed for the quantification of uric acid. The use of a microelectrode in this assay minimises the ohmic drop, allowing direct measurement in undiluted authentic human saliva *without* the need for the addition of supporting electrolyte.

In addition, this work demonstrates the significantly different electrochemical responses in *authentic* compared to *synthetic* saliva. This difference is highlighted and elucidated using ferrocenemethanol and ferrocyanide, which are two commonly used redox mediators. The former displays well-defined voltammetry in both synthetic and authentic saliva samples. Distortion of voltammetry in authentic saliva is observed in the latter, demonstrating the partial blocking of the electrode surface by organic species in saliva and reflecting the surface sensitivity of the process. In order to minimise the influence of electrode fouling on the measured responses, the surface-insensitive ferrocenemethanol is thus a better redox probe for saliva analysis.

Finally, this thesis develops electrochemical methods for the detection of silver nanoparticles. In particular, the oxidative dissolution of *individual* silver nanoparticles (AgNPs) is investigated using nano-impacts. The AgNPs undergo *complete* oxidation upon the impact at a suitably potentiostated electrode, the evidence of which is highly important for any further development of electrochemical single nanoparticle detection. The sensitivity of the nano-impact frequency towards the nature and concentration of the supporting electrolyte anions allows the determination of the rate-determining step of the oxidation process. It is found that the AgNP oxidation follows a nucleation growth type mechanism with the rate-determining step being the initial stochastic formation of a silver (I) nucleus.

The physicochemical properties of silver nanoparticles (AgNPs) are then investigated in authentic human whole saliva using the developed electrochemical techniques, together with spectrophotometric studies. The results demonstrate the electrochemically and chemically inert nature of AgNPs in authentic saliva samples. The stability of AgNPs in saliva suggests that AgNPs are not likely to cause serious harm to the oral cavity. However, these nanoparticles may be transported to other parts of the body where the chemical environments could be more susceptible to the release of the toxic Ag^+ and reactive oxygen species.

In summary, this thesis has presented methods developed for the detection of salivary biomarkers and demonstrated the auxiliary diagnostic application of the salivary compounds. In particular, simple and easy-to-use sensors have been developed for the detection of glutathione, uric acid and silver nanoparticles. The sensors have been applied to and validated in authentic saliva samples. The glutathione sensor, in particular, has been employed in the quantification of glutathione as a biomarker for bipolar disorder.

Appendix A

A1 Cyclic voltammetry at a supported microwire electrode in the irreversible electron-transfer limit

Similar to Figure 5.7b in the main text, the geometry influence on the supported microwire electrode for an irreversible reaction is also explored under different diffusion conditions, referred by the combined parameter Fvr_{el}^2/RTD. Figure A1 shows the working curve of the $I_{p,supported}$ / $I_{p,isolated}$ ratios as a function of $\log_{10}(Fvr_{el}^2/RTD)$ and the exact values are listed in Table A1 for reference. The peak currents used below are collected from numerical simulation. Different from the reversible case discussed in the main text, for the irreversible one-electron transfer reaction, the reaction rate of the reactant on the electrode surface is described by the Butler-Volmer equation:

$$-D\left.\frac{\partial c}{\partial n}\right|_{\text{surf}} = -k_0 \exp\left(\frac{\beta F(E-E_f)}{RT}\right) c_{\text{surf}} + k_0 \exp\left(-\frac{\alpha F(E-E_f)}{RT}\right)(1-c_{\text{surf}}) \qquad \text{(A1)}$$

where k_0 is the standard heterogeneous rate constant. α and β are transfer coefficients and $\alpha + \beta = 1$. For the fully irreversible case, k_0 is selected to be a small value compared to the diffusion rate D/r_{el} ($k_0 < 0.01D/r_{el}$) and both α and β are selected to be 0.5 (in fact, for the fully irreversible condition, any change of the values of α, β and k_0 will not influence the peak current ratios). As shown in Figure A1, the transition from the radial diffusion where the reaction is significantly affected by the geometry to the linear diffusion where the reaction is mainly determined by the electroactive surface area rather than the exact geometry is also found for an irreversible one-electron-transfer reaction.

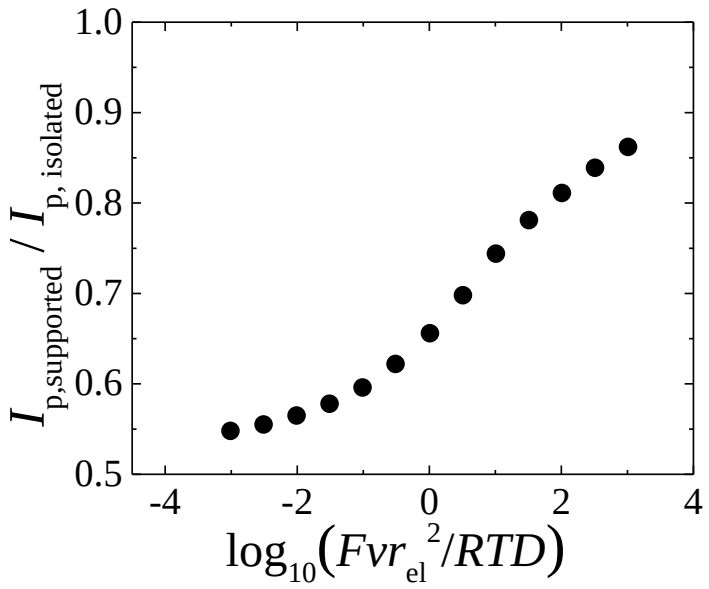


Figure A1: The $I_{p,supported}$ / $I_{p,isolated}$ ratios for irreversible one-electron transfer process at different $Fr_{el}^{2}v/RTD$.

Table A1: The $I_{p,supported}$ / $I_{p,isolated}$ ratios for irreversible one-electron transfer process at different $Fr_{el}^{2}v/RTD$

$\log_{10}(Fr_{el}^{2}v/RTD)$	$I_{p,supported}/I_{p,isolated}$
-3.01	0.548
-2.51	0.555
-2.01	0.565
-1.51	0.578
-1.01	0.596
-0.51	0.622
0.01	0.656
0.51	0.698
1.01	0.744
1.51	0.781
2.01	0.811
2.51	0.839
3.01	0.862

A2 Cyclic voltammetry at a microdisc electrode as provided by the supplier

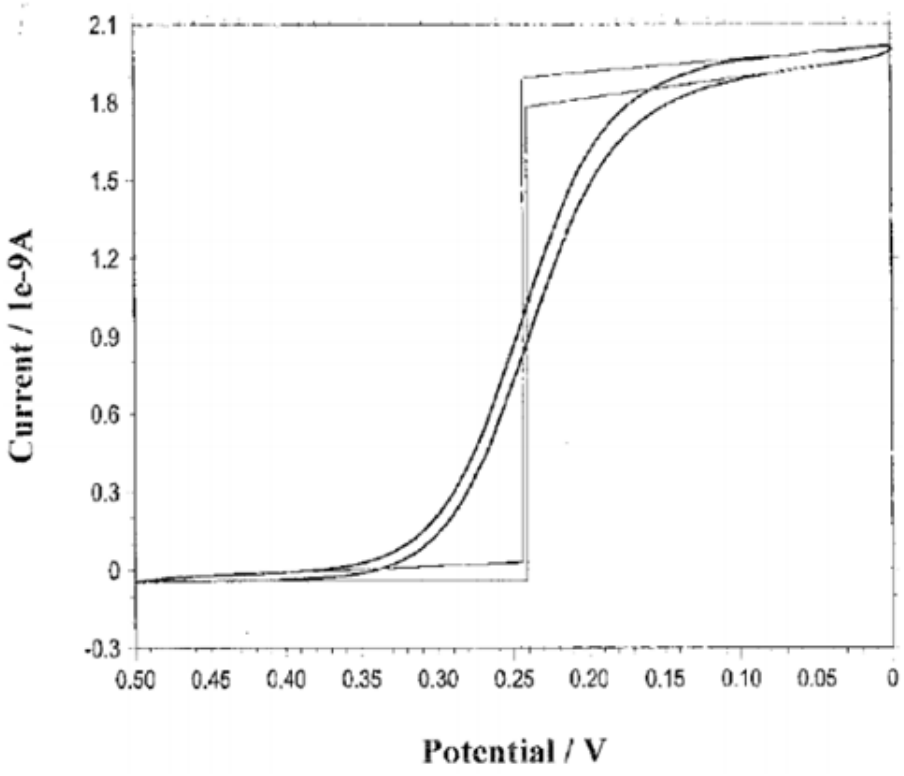


Figure A2: Cyclic voltammogram of 2 mM $K_3Fe(CN)_6$ in 1 M KNO_3 measured at the scan rate of 0.2 V s^{-1} at a commercial microdisc electrode with a radius of 3.5 μm. This image is provided by the supplier along with the commercial microdisc electrode.

Appendix B

B1 Characterisation of the carbon microdisc electrode

The surface area of the carbon microdisc working electrode used throughout this work was determined using the voltammetric responses of 1.0 mM $[Ru(NH_3)_6]^{3+}$ reduction in the presence of 0.1 M KCl. The steady state current (I_{ss}) observed was 6.67 ± 0.03 nA. The radius of the electrode (r_e) was then determined using equation (9.1) as provided in the main text to be 20.5 ± 0.1 μm, using the diffusion coefficient (*D)* of the redox species at 25 °C of 8.43×10^{-10} m^2 s^{-1} [1].

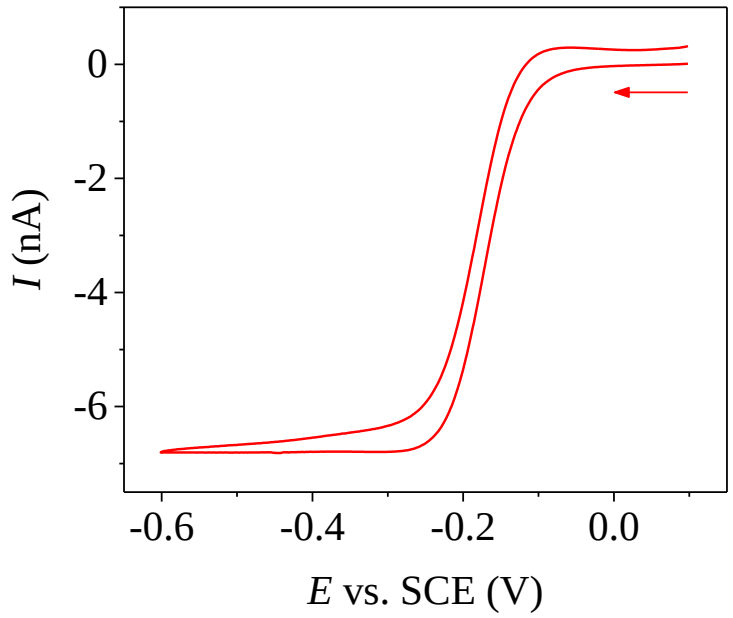


Figure B1: Cyclic voltammetry of 1.0 mM $[Ru(NH_3)_6]^{3+}$ reduction in 0.1 M KCl at the carbon microdisc electrode at the scan rate of 10 mV s^{-1}; 25 °C.

B2 Cyclic voltammetry of hexaammineruthenium(III) reduction in authentic *vs.* synthetic saliva

The normalised cyclic voltammograms of 1.0 mM $[Ru(NH_3)_6]^{3+}$ reduction in authentic and synthetic saliva are presented in Figure B2. In both media, the voltammograms are fully reversible with the electron transfer coefficient of 1.0 within ±5% error.

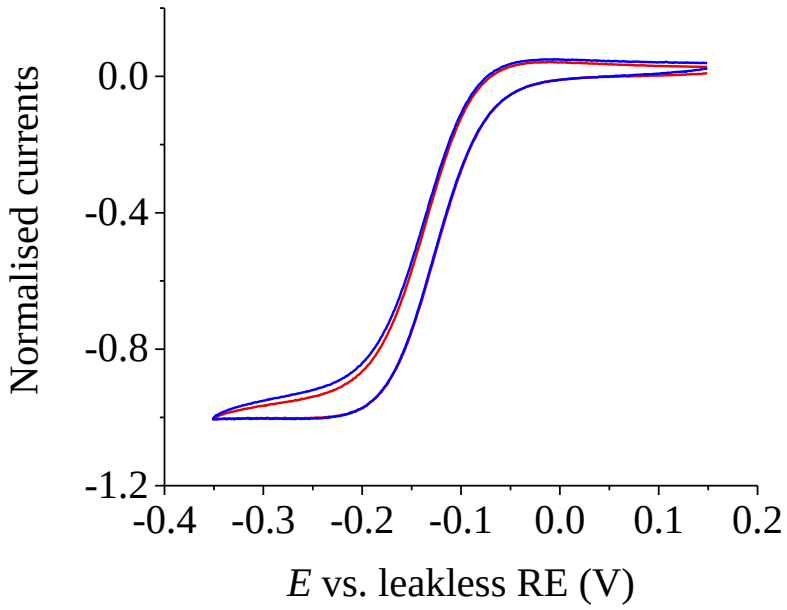


Figure B2: Normalised cyclic voltammetry of 1.0 mM $[Ru(NH_3)_6]^{3+}$ reduction in synthetic (**red**) and authentic saliva (**blue**) at a carbon microdisc electrode; scan rate of 10 mV s^{-1}.

B3 Cyclic voltammetry of uric acid, ascorbic acid and dopamine

The oxidation of 120 μM uric acid (UA), ascorbic acid (AA) and dopamine (DA) was first studied in synthetic saliva at a carbon microdisc electrode at the scan rate of 10 mV s^{-1} (Figure B3). The oxidation of these compounds has been reported to be a 2-electron transfer process.[2] The steady-state currents of UA, AA and DA were 1.4 ± 0.1, 1.7 ± 0.1 and 1.8 ± 0.2 nA, corresponding to the diffusion coefficients of $7.4 \pm 0.5 \times 10^{-10}$, $9.0 \pm 0.5 \times 10^{-10}$ and $9.5 \pm 1.1 \times 10^{-10}$ m^2 s^{-1} respectively. The half-wave potentials ($E_{½}$) were observed at 0.47, 0.37 and 0.24 V and the apparent transfer coefficients (α) determined to be 0.48 ± 0.02, 0.35 ± 0.01 and 0.52 ± 0.04 for UA, AA and DA respectively.

In authentic saliva, the background currents increase significantly at high potentials and hence no steady-state currents of UA, AA or DA oxidation could be observed. The waves of UA, AA and DA oxidation in authentic saliva shifted from that of synthetic saliva to more positive potentials by ~100 - 200 mV due to the partial blocking of the electrode; see main text for UA, and Figures B4 and B5 for AA and DA respectively.

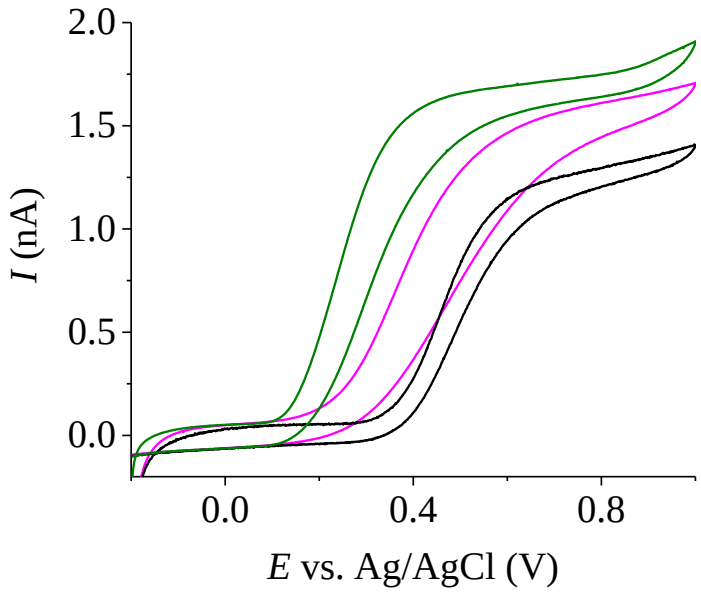


Figure B3: Cyclic voltammetry of 120 µM uric acid (**red**), ascorbic acid (**black**) and dopamine (**green**) in synthetic saliva. Carbon microdisc working electrode; scan rate of 10 mV s^{-1}.

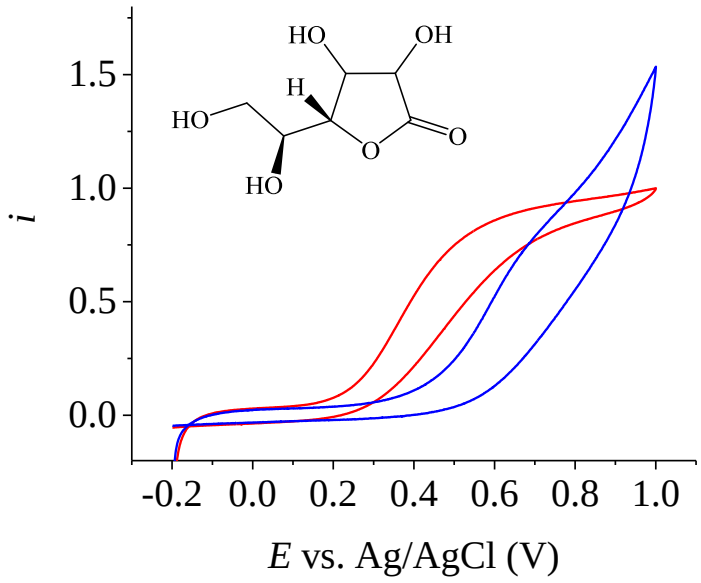


Figure B4: Normalised cyclic voltammograms of 120 µM ascorbic acid (AA) added to synthetic saliva (**red**) and authentic saliva (**blue**) at a carbon microdisc working electrode; scan rate of 10 mV s^{-1}.

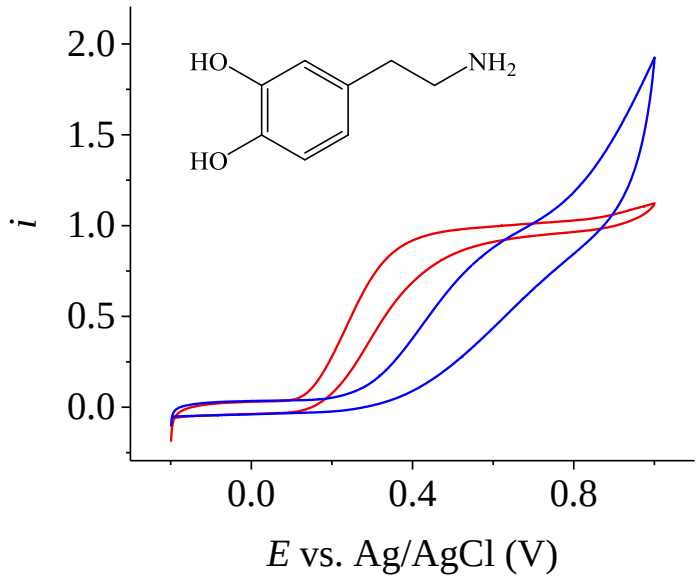


Figure B5: Normalised cyclic voltammograms of 120 μM dopamine (DA) added to synthetic saliva (**red**) and authentic saliva (**blue**) at a carbon microdisc working electrode; scan rate of 10 mV s^{-1}.

Bibliography

(1) Wang, Y.; Limon-Petersen, J. G.; Compton, R. G. *J. Electroanal. Chem.* **2011**, *652*, 13-17.
(2) Kamel, M. M.; Abdalla, E. M.; Ibrahim, M. S.; Temerk, Y. M. *Can. J. Chem.* **2014**, *92*, 329-336.